Characterization of the mechanical and morphological properties of cortical bones by nanoindentation and Atomic Force Microscopy

Sebastián Jaramillo Isaza

To cite this version:

Sebastián Jaramillo Isaza. Characterization of the mechanical and morphological properties of cortical bones by nanoindentation and Atomic Force Microscopy. Biomechanics [physics.med-ph]. Université de Technologie de Compiègne, 2014. English. NNT : 2014COMP2150 . tel-01143875

HAL Id: tel-01143875
https://theses.hal.science/tel-01143875

Submitted on 20 Apr 2015

Par **Sébastian JARAMILLO ISAZA**

Characterization of the mechanical and morphological properties of cortical bones by NanoIndentation and Atomic Force Microscopy

Thèse présentée pour l'obtention du grade de Docteur de l'UTC

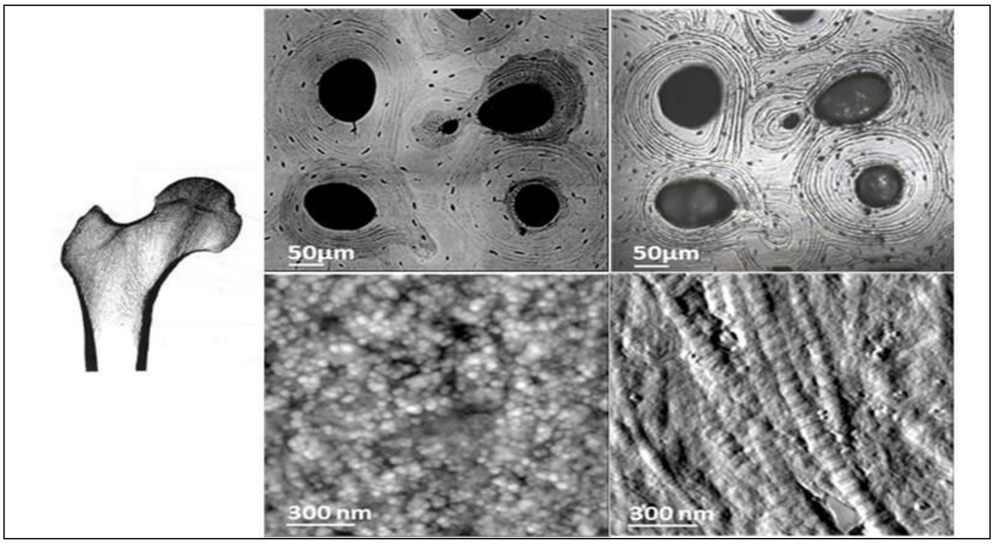

Soutenue le 28 octobre 2014
Spécialité : BioEngineering, BioMechanics and BioMaterials

D2150

A dissertation submitted to fulfil the requirements for the degree of
Doctor of Philosophy of the Université de Technologie de Compiègne (UTC)

Disciplinary fields: BioEngineering, BioMechanics and BioMaterials

Characterization of the mechanical and morphological properties of cortical bones by NanoIndentation and Atomic Force Microscopy

by:

Sebastián JARAMILLO ISAZA

Thesis defended the 28th October 2014 in front of the jury composed by:

Jean-Luc LOUBET (President of the jury)
Jean-Marie CROLET (Dissertation Referee)
Elisa BUDYN (Dissertation Referee)
Miguel CERROLAZA (Dissertation Examiner)
Sabine BENSAMOUN (Dissertation Examiner)
Marie-Christine HO BA THO (Supervisor)
Pierre-Emmanuel MAZERAN (Co-supervisor)
Karim EL-KIRAT (Co-supervisor)

Thesis prepared and defended within:

Laboratory of BioMechanics and BioEngineering (BMBI)
UMR CNRS 7338

Laboratory of Mechanics (ROBERVAL)
UMR CNRS 7337

Université de Technologie de Compiègne (UTC)
Centre de Recherches de Royallieu
Rue Personne de Roberval
BP 20529
Compiègne Cedex
France

Jury members:

Monsieur **Jean-Luc LOUBET**, *Senior Researcher, Ecole Centrale de Lyon, Laboratory of Tribology and Systems Dynamics, UMR 5513, France.*

Monsieur **Jean-Marie CROLET**, *Full Professor, Institut Supérieur d'Ingénieurs de Franche-Comté ISIFC, Laboratory of Mathematics of Beçanson, UMR 6623, France.*

Madame **Elisa BUDYN**, *Professor, École Normale Supérieure de Cachan, Laboratory of Mechanics and Technology (LMT), UMR 8535, France.*

Monsieur **Miguel CERROLAZA**, *Full Professor, Universitat Politècnica de Catalunya, International Center for Numerical Methods in Engineering CINME, Spain.*

Mademoiselle **Sabine BENSAMOUN**, *Researcher CNRS, Université de Technologie de Compiègne, Laboratory of Biomechanics and Bioengineering, UMR 7338, France.*

Madame **Marie-Christine HO BA THO**, *Full Professor, Université de Technologie de Compiègne, Laboratory of Biomechanics and Bioengineering, UMR 7338, France.*

Monsieur **Pierre-Emmanuel MAZERAN**, *Assistant Professor, HDR, Université de Technologie de Compiègne, Laboratory of Mechanical systems Roberval, UMR 7337, France.*

Monsieur **Karim EL-KIRAT**, *Assistant Professor, HDR, Université de Technologie de Compiègne, Laboratory of Biomechanics and Bioengineering, UMR 7338, France.*

Abstract

Bone is a dynamical, anisotropic, hierarchical, inhomogeneous and time-dependent biological material. At the micro and nano scales, their mechanical and structural characterizations are still being a challenging topic.

Nanoindentation and Atomic Force Microscopy are used to assess the mechanical and morphological characteristics of cortical bones. Time-dependent, elastic and plastic mechanical properties were computed using the nanoindentation method proposed by (Mazeran et al., 2012). Experiments were performed on different species of bones for different conditions.

Wistar rat femoral cortical bone was used to assess the evolution of the mechanical properties in a life span model (from growth to senescence). The variation of the mechanical properties with age was evidenced and their correlation with physico-chemical properties was established. Then, prediction equations were proposed to describe these behaviours. From these equations, it is possible to estimate an apparent maturation age for each mechanical property. *Our findings suggest maturation age is earlier and growth rate are higher for elastic properties than for time-dependent mechanical properties*.

Time-dependent mechanical behaviour of Human femoral cortical bones were assessed considering its heterogeneity. Haversian systems with different apparent mineral content were identified by means of their apparent grey levels obtained from ESEM images. Results prove the mechanical heterogeneity of the Haversian systems and highlight the influence of the *time-dependent mechanical properties in the anisotropic behaviour of bone.*

Bovine femoral cortical bone was used to quantify the mechanical and morphological effects of the demineralization process. *Bone seems to have a quasi-isotropic mechanical behaviour after mineral loss*. AFM images of the remaining organic components show that collagen fibrils are oriented in a possible privileged direction.

According to our knowledge, few investigations have been performed simultaneously on mechanical, morphological and physico-chemical properties of bone. All these results provide a better understanding of the interactions of the collagen-mineral matrix, bone remodelling and their influence especially in the time-dependent mechanical response. Data reported in this work could be useful to develop and to improve multi-scale bone models and multi-scale constitutive laws for cortical bone.

Acknowledgements

I wish to thank Dr. Pierre-Emmanuel Mazeran, Dr. Karim El-Kirat and Pr. Marie-Christine Ho Ba Tho for their scientific and technical support. Thank you so much for those very interesting scientific talks; for your guidance, patience and trust you have always demonstrated in me. Without your advices and skills this work would not have ever been possible. I could not have imagined having a better advisor and mentors for my thesis work.

To Pr. Jean-Marie Crolet and Pr. Elisa Budyn for accepting to be the referees of my dissertation. Their detailed reports and advices helped me to improve my work. To Pr. Jean-Luc Loubet for accepting to be the president of the jury and for sharing his wonderful experience. To Pr. Miguel Cerrolaza and Dr. Sabine Bensamoun for accepting to examine my work, for their encouragement and insightful comments.

I would like to express my sincere gratitude to my fellow labmates: Gwladys Leclerc, Clint Hansen, Quentin Dermigny, Jeremy Laforet, Jean-Sebastien Affagard for your friendship, support and sympathy. I will never forget all the people at BMBI (BioMécanique et BioIngénierie) laboratory especially the C3M team. It was a real pleasure to be part of it.

Special thanks to the people I love: my mom and dad for your sacrifice and dedication to raise our family within strong principles: perseverance, humility and respect. My siblings, nephews and nieces and all my family for being my motivation and inspiration during all this time. To Juana and Mari my two angels who always take care of me. Particular thanks to Marcela Múnera for always supporting me and to push me to give my best.

“What the result of these investigations will be the future will tell; but whatever they may be, and to whatever this principle may lead, I shall be sufficiently recompensed if later it will be admitted that I have contributed a share, however small, to the advancement of science.”

Nikola Tesla

“The Tesla Alternate Current Motor” (The Electrical Engineer, June 22, 1888)

Summary

ABSTRACT **3**
ACKNOWLEDGEMENTS **4**
GENERAL INTRODUCTION **10**

CHAPTER 1: BIBLIOGRAPHIC BACKGROUND **14**
A. BONE TISSUE 15
  I. Generalities *15*
  II. Types of bone *15*
    1. Organ level 15
    2. Tissue level 17
    3. Cellular level 21
    4. Molecular level 23
  III. Bone remodeling *27*
  IV. Differences between species *28*
    1. Human bone 29
    2. Rat bone 29
    3. Bovine bone 30
  V. Mechanical characterization of bone at the macro scale *31*
B. NANOINDENTATION TECHNIQUE 36
  I. Generalities *36*
    1. Contact theory 37
    2. Elastoplastic contact 40
    3. Experimental curve and contact area 41
  II. Instrumental aspects *43*
    1. Tip geometry 43
    2. Calibration materials 45
    3. Strain rate 45
  III. Data analyses models *46*
    1. Oliver and Pharr Method 46
    2. Continuous Stiffness Measurement (CSM) 49
    3. Time-dependent mechanical models 53
  IV. Nanoindentation of bone samples *58*

C. ATOMIC FORCE MICROSCOPY 67
I. Generalities........ 67
II. Imaging modes........ 68
1 Contact mode 68
2 Tapping mode 69
3 Non-contact mode 70
4. Dilation phenomenon in AFM imaging 71
III. Mechanical characterization by AFM 72
1 Measurement of the spring constant 73
2 Tip radius of curvature 76
3 Cantilever deflection 76
4 Force-displacement curves 77
5 Data analysis 78
IV. AFM for bone characterization 79

BIBLIOGRAPHIC SYNTHESIS........ 82

CHAPTER 2: MATERIALS AND METHODS 85
A. MATERIALS 86
I. Samples preparation 86
1. Cutting 86
2. Grounding and Polishing 87
3. Cleaning 87
II. Bone types 88
1 Rat bone model (growth to senescence) 88
2 Human bone 88
3 Bovine bone (Effects of demineralization) 90
B. METHODS 90
I. Identification of osteons with different mineral degrees 90
II. Nanoindentation tests 91
1 Accuracy and repeatability 91
2 Bone samples 91
3 Elastic-Viscoelastic-Plastic-Viscoplastic (EVEPVP) Model 92
4 Nanoindentation protocol 93

5 Data analysis and assessment of the mechanical properties 93
6 Correlations, multiple regression analyses and Statistical tests 97
III. Morphological characterization by AFM 98
C. RECAPITULATION OF THE DIFFERENT STUDIES 99

CHAPTER 3: STUDY OF A BONE MODEL FROM GROWTH TO SENESCENCE 101
A. TIME-DEPENDENT MECHANICAL RESPONSE 102
B. CORRELATIONS BETWEEN MECHANICAL AND PHYSICO-CHEMICAL PROPERTIES 109
C. MULTIPLE REGRESSION ANALYSES 112
D. MORPHOLOGICAL CHARACTERIZATION BY AFM 118
CHAPTER SYNTHESIS 124

CHAPTER 4: TIME-DEPENDENT AND MORPHOLOGICAL PROPERTIES OF HUMAN FEMORAL CORTICAL BONE 125
A. ESEM IMAGING 126
B. NANOINDENTATION TESTS 127
C. MORPHOLOGICAL CHARACTERIZATION BY AFM 138
CHAPTER SYNTHESIS 146

CHAPTER 5: ANISOTROPY OF THE TIME-DEPENDENT MECHANICAL PROPERTIES OF HUMAN FEMORAL CORTICAL BONE 148
A. SAMPLE GEOMETRY 149
B. NANOINDENTATION TESTS 150
C. ANISOTROPY RATIO 167
CHAPTER SYNTHESIS 170

CHAPTER 6: MECHANICAL PROPERTIES OF DEMINERALIZED CORTICAL BONE 171
A. DEMINERALIZATION PROTOCOLS 172
B. STRUCTURAL EFFECTS OF THE DEMINERALIZATION PROCESS 173
C. MECHANICAL PROPERTIES 175
D. MORPHOLOGICAL CHARACTERIZATION BY AFM 186
CHAPTER SYNTHESIS 190

CONCLUSIONS AND OUTLOOK 191

REFERENCES 196

COMMUNICATIONS 210

A. ARTICLE 210

B. INTERNATIONAL COMMUNICATIONS 210

C. NATIONAL COMMUNICATIONS 210

D. AD-JOINT RESEARCH PROJECTS 211

E. VALORIZATION PROJECT FOR THE CNRS 211

General Introduction

Bone, like most of the biological materials, has a very complex hierarchical structure, which even in our days is not completely described and understood. Bone strength is determined by its material composition and structure. That is why understanding the mechanical properties of bone material requires a detailed knowledge of their interactions and structural organizations at different scale levels (Ho Ba Tho et al., 2012).

Bone tissue is responsible for the protection, structure, movement and sound transduction of humans and vertebrate body. Bone tissue has a high biological activity that make possible to rebuild its structure constantly throughout life. During growth, the body adds new bone faster than it removes old bone. During adulthood, bone is constantly rebuilt and repaired in case of fracture. Finally, during senescence bone mass decrease (osteoporosis) and bone becomes less stiff.

Bone diseases are a global public health problem currently affecting more than 250 million persons around the world. While they may not get as much attention as heart disease, cancer, and other major diseases, bone diseases are common in Europe, especially among the elderly people and they take a large toll on the Nation’s overall health status.

Fractures are the biggest problem associated with bone disease. They are common, costly, and become a chronic burden on both individuals and society. For example, according to the French Society of Rheumatology, every year in France, around 145000 individuals suffer a fracture due to bone diseases. Most of these fractures are treated by prosthesis replacements that are very expensive and sometimes only a temporary solution.

The quality of bone tissue is significantly influenced by its mechanical properties. Research into the aetiology and enhanced detection of bone diseases may require the assessment of bone’s mechanical properties at the level of the tissue. Preventions of bone diseases and their consequences have thus important socio-economic impact. It needs a better understanding of the knowledge of bone and their diseases in order to find new preventive and curative solutions to them.

Since the 90's, the structure and the mechanical properties of bone tissue has been investigated at different scales. Actually, previous works have been performed in our laboratory at the macro and micro scales. At the macro scale, it was showed that variations of bone mechanical properties were correlated with their morphological and structural characteristics for the cancellous bone (Destresse, 1998) and cortical bones (Bensamoun, 2003). At the micro scale, the assessments of the microstructural mechanical heterogeneity and their correlations with their physico-chemical properties (Vanleene, 2006) and finally, bone anisotropic behaviour was assessed experimentally and simulated numerically (Brockaert, 2010).

Nevertheless, the mechanical properties of bone are far to be enough known. The aim of this thesis is then to pursue the previous works mentioned above by investigating the time dependent mechanical properties at the microscopic scale and to correlate them to structural interactions at the nanometre scale thanks to the improvement realized by nanoindentation and atomic force microscopy.

This work is co-financed by the European Union engaged in Picardie Region with the European Regional Development Fund and CNRS (Grant Collegium UTC-CNRS-INSIS). This grant makes possible the collaboration between two research units of the University of Technology of Compiègne: BMBI laboratory (**B**io**M**écanique **B**io**I**ngénierie) and ROBERVAL laboratory of mechanics. This thesis deals will an original problematic associated to the multi-scale mechanical description of biological tissues, its modelling and simulation.

In this manuscript, the following chapters will be addressed:

In chapter 1, a complete bibliography is presented. Bone characteristics are introduced, hierarchical structure and some values of its mechanical properties assessed at the macro, micro and nano scales. Thus, nanoindentation technique is introduced and the characterization of the mechanical properties of bone by nanoindentation is reviewed. Finally, the Atomic Force Microscopy is described as well as the works accomplished on bone tissues.

In chapter 2, the protocols developed for samples preparation (surface, geometry, size and demineralization process) are described. In addition, the nanoindentation protocol for the experimental tests, the mechanical model used to assess the time-dependent mechanical properties and the AFM imaging modes are detailed.

In chapter 3, the evolution of the time-dependent, elastic and plastic mechanical properties with age are assessed using a Wistar rat cortical bone growth model. Fitting equations for the variation of each mechanical property with age are computed. The correlations between those mechanical properties and the physico-chemical properties (obtained in a previous study performed in our laboratory over a similar set of samples) are established using multivariable linear regressions. Finally, morphological characterization of bone nanostructure at different ages is provided using AFM method.

In chapter 4, the time-dependent, elastic and plastic mechanical properties for human femoral bone samples with different apparent densities are computed. ESEM images were obtained over the samples surface in order to identify osteons with different mineral contents from their different grey levels. Then, osteons were classified according to their grey levels in white osteons for an apparent high mineral content and in black osteons for an apparent low mineral content. Nanoindentation tests were carried out into the interstitial lamellae and the different osteons in order to highlight bone mechanical heterogeneity at the micro scale. Finally, the chapter presents the results of a morphological nano-characterization performed using AFM method into the nanoindentation imprints.

In Chapter 5, the anisotropic behaviour of the mechanical properties including the time-dependent mechanical properties of human femoral cortical bone is characterized. This behaviour was evaluated in samples obtained from three different anatomical quadrants of the cortical shell (posterior, lateral and medial). As performed in chapter 4, osteons with different mineral content were identified from ESEM images. Mechanical assessments were computed using nanoindentation technique over the three principal directions (longitudinal, transverse and radial). Then, an average anisotropy ratio is computed for each typology of the cortical structure (interstitial lamellae and Haversian systems).

In Chapter 6, bovine cortical bone is used to assess the effects of demineralization process in their mechanical properties. Two different chemical attacks are used to perform the demineralization process. The structural and morphological effects were measured quantitative and qualitatively by computing changes in bone apparent density, mechanical response and by performing AFM characterization of the sample surface. Nanoindentation technique will be used to quantify the time-dependent mechanical properties of the remained “organic” phase of bone. Mechanical properties of bone before and after demineralization were compared for the principal directions in order to identify possible quasi-isotropic behaviour.

Finally, a conclusion chapter summarizes the most relevant results. The outlook of this work will be addressed to potential applications such as new models of bone remodelling, development of new biomimetic materials; proposing new indentation protocols for mechanical assessments of bone nanostructure using AFM.

Chapter 1: Bibliographic background

The first part of this chapter contains an overview on bone tissue: Its hierarchical structure and its architecture, as well as its composition, remodelling and mechanical behaviour is presented. The values reported for the elastic properties of bone determined by different techniques are summarized.

Later, the mechanical basics of the nanoindentation technique are described. Some nanoindentation methods are briefly presented. Applications of nanoindentation on human bone are reviewed. Some values reported in the literature related to the elastic, plastic and time-dependent mechanical properties of bone assessed by nanoindentation are summarized.

Finally, a review about the Atomic Force Microscopy framework is provided. The background of this technique is presented. The steps for the morphological and mechanical characterization are briefly described. Some values of the elastic properties of the organic components of bone are also presented.

A. Bone tissue

I. Generalities

Bone is a dynamic, complex and specialized biological material that provides structural framework (rigidity, movement) and metabolic functions. The structural properties are responsible for the protection of the soft tissues and vital internal organs. The metabolic functions guarantee the mineral and fat storage, the haematopoiesis process and regulate of the acid-base balance.

The most fantastic characteristic of bone is its ability to adapt its functions effectively under imposed loads. This characteristic depends mostly on two factors: 1) the properties of bone material and arrangement of this material in space, 2) the size and shape of bone (Currey, 2003).

All bone mechanical characteristics are the results of a long-term improvement and optimization of the interactions between the organic matrix and the mineral components driven by the evolutionary processes.

In this section, an overview of bone structural characteristics, composition and mechanical properties is presented.

II. Types of bone

Bone gives the structural support to the muscular-skeletal system. However, bone can vary its structural geometry because of the mechanical function; the anatomical localization and biological needs (Currey, 1984). Bone biological and chemical function arises from the complex arrangement of its structure. In order to completely understand the mechanical properties of bone material; it is important to understand not only the mechanical properties of its component phases; but also the structural relationship between them at various levels of hierarchical structural organization (Rho et al., 1998). Human bone can be classified according to the physiological level at the organ, tissue, cellular and molecular levels.

1. Organ level

At this scale, bone is classified in Cancellous and cortical bone. In global terms, the adult human skeleton mass is composed of ~80% cortical bone and ~20% trabecular bone (Dempster, 2006). However, the proportional ratios of each type vary considerably among to the different bones (vertebra, femur) and some pathological conditions. Typically, at this level bone can be classified in:

1.1 Long bones

These bones typically have an elongated shaft and two expanded ends one on either side of the shaft. The shaft is known as diaphysis and the ends are called epiphyses. Normally the epiphyses are smooth and articular. The shaft has a central medullary cavity where lies the bone marrow. The diaphysis is composed mostly of cortical bone that provides important mechanical stiffness. The epiphyses are composed of trabecular bone surrounded by an outer shell of thick compact bone.

1.2 Short bones

These bones are short in posture and can be of any shape. Most of them are named according to their shape. Examples of this class of bones include cuboid, cuneiform, scaphoid, trapezoid etc. In fact, all the carpal and tarsal bones are included in this category.

1.3 Flat bones

These bones are flat in appearance and have two prominent surfaces. They resemble shallow plates and form boundaries of certain body cavities. Examples include scapula, ribs, sternum etc.

1.4 Irregular bones

The shape of these bones is completely irregular and they do not fit into any category of shape. Examples of this type of bones are vertebrae, hip bone and bones in the base of skull. Inside this kind of bones, there is a very particular type call pneumatic bones. The particularity of this kind of bone is the presence of large air spaces that make them light in mass. They form the major portion of skull in the form of sphenoid, ethmoid and maxilla. Besides making the skull light in weight, they also help in resonance of sound and as air conditioning chambers for the inspired air.

An example of each category of bones is presented in figure 1.1.

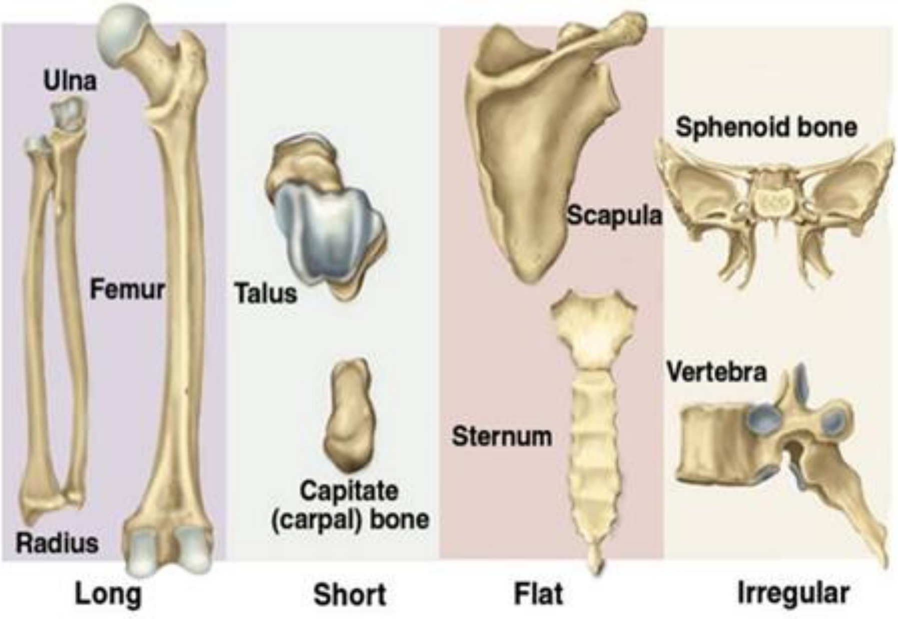

Figure 1.1 Classification of bone according to their geometrical characteristics (Saladin, 2002)

2. Tissue level

At this level, bone can be classified as a function of the porosity and density degrees in compact or cancellous bone, (Gibson, 1985; Goldstein, 1987; Rho et al., 1998) or according to the arrangement of the collagen fibrils in woven or parallel-fibered type (Smith, 1960). A briefly description of each type of bone is presented hereafter.

2.1 Compact Bone (osteonal Bone):

It forms the bone cortex. The outer shell of the skeletal segments consists of compact bone. Cortical bone has important mechanical functions. It is responsible for mechanical resistance and the structural rigidity. In cortical bone, several complex cylindrical structure called osteons (or Haversian systems) are mixed with interstitial bone. Osteons look like cylinders of about 200–250 μm in diameter running roughly parallel to the long axis of the bone. Two kinds of osteons can be recognized: primary and secondary (Smith, 1960). Primary osteons are structures formed around blood vessels in the initial growing phase of bone. Secondary osteons form after remodelling. During this process, bone cells first excavate a tubular path through the hard tissue, and then deposit the osteon layer by layer.

Using microradiography and the polarizing light microscope (Evans and Vincentelli, 1974) classified osteons according to their radiolucency on the basis of their appearance in the microradiographs in light, intermediate or dark osteons. Later, using Circularly Polarized Light (CPL) (Bromage et al., 2003) identified the collagen fibres orientation (figure 1.2) and (Bensamoun et al., 2008) used BackScattered Electron imaging (BSE) to detect the differences in the mineral content of the osteons. These results make possible to classify osteons in three types as follows:

- **Type I:** CPL shows that collagen fibres are oriented transversally to the osteon axis. BSE images show high degree of mineralization. CPL and BSE images show lightest grey levels.
- **Type II:** CPL shows that collagen fibres present an alternate between transverse and longitudinal orientation to the osteons axis. BSE suggest that osteons presents an intermediate degree of mineral. Images obtained from both methods prove that osteons are bright and dark (grey) contrast levels.
- **Type III:** CPL show that collagen fibres are oriented longitudinally (parallel) to the osteons axis. The mineral content is the lowest according to the BSE images. CPL and BSE images show blackest grey levels.

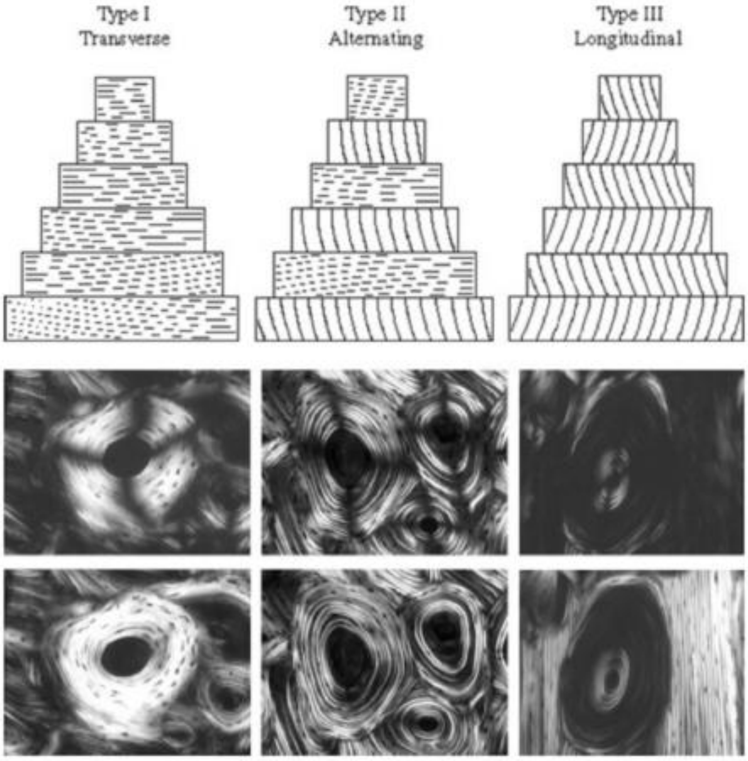

Figure 1.2 Scheme of the collagen fibres arrangement inside the lamellae and imaged by circularly polarized light (Bromage et al., 2003)

Interstitial tissue is found between osteons. Depending on the amount of remodelling that has occurred, the interstitial tissue may be a mixture of primary bone or the remnants of primary and secondary osteons; Normally this tissue is stiffer and harder that the lamella present in the osteons (Rho et al., 2001, 1999)

Other components of the compact bone are the Volkmann canals which are large but smaller that osteons, they connect the Haversian canals to each other and to the outside surface of bone. These canals also contain blood vessels and nerves. Resorption cavities are also found. They are temporal spaces created by bone-removing cell (osteoclast) in the initial stage of bone remodelling.

2.2 Cancellous bone :

Cancellous bone is a cellular material made up of a connected network of rods or plates. A network of rods produces open cells while one of plates gives closed cells. Cancellous bone generally exists only within the confines of the cortical bone coverings. Cancellous bone is also called trabecular and spongy bone, because it is composed of short interconnected struts of bone called trabeculae responsible for its spongy appearance. Due to its high porosity, it is lighter and less dense than compact bone, has vast surface area and allows a higher concentration of blood vessels and bone marrow. The pores are interconnected and their diameter range from few micrometres to millimetres). The millimetre-sized spaces in between trabeculae house bone marrow are much more metabolically active than cortical bone due to their high surface-to-volume ratio. Trabeculae are organized to provide maximum strength, they follow the lines of principal stress and can realign if the direction of stress changes (Ascenzi et al., 1982; Evans, 1973; Gibson, 1985; Hodgskinson and Currey, 1992; Rho et al., 1998; Rice et al., 1988)

A diagram of the structure of cortical and cancellous bone is represented in figure 1.3.

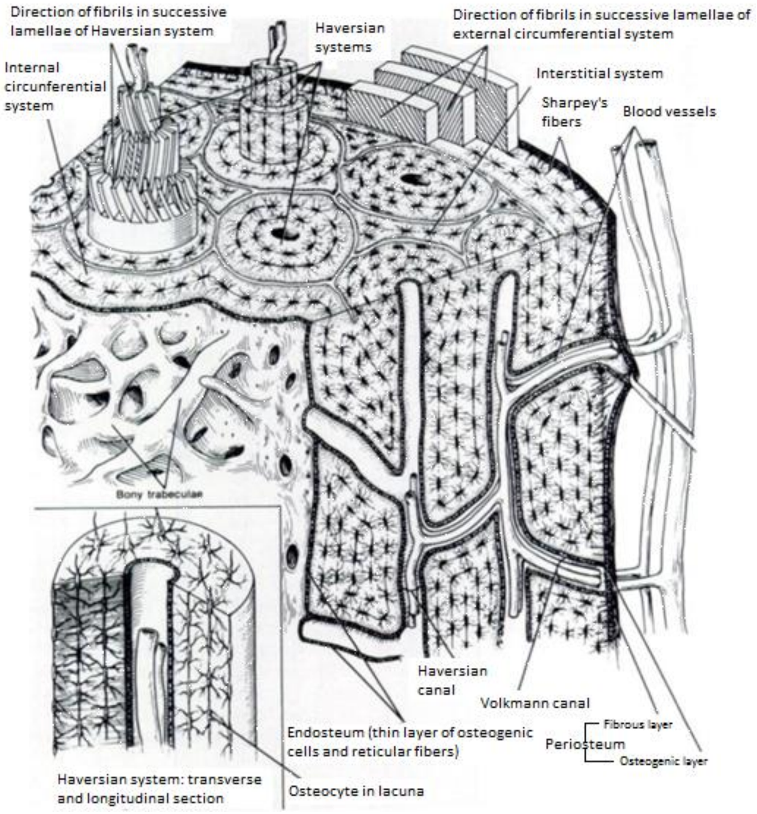

Figure 1.3 Representation of the compact and cancellous bone, showing the types of bone: the internal circumferential system, interstitial system, osteonal lamellae, the Haversian canal and the Volkmann canals. It should be noted the cement lines, which separate each osteon from the surrounding, bone. (Buckwalter et al., 1995)

2.3 Woven bone

Also called coarse-fibre bone, woven bone is the bone formed first during skeletal embryogenesis. After birth, it is gradually removed by the process of bone remodelling and is substituted by lamellar bone (Bonucci, 1999). It can, however, be formed again in pathological conditions, such as callus formation, bone tumours and ectopic ossification. This kind of bone is characterized by the presence in the matrix of, irregularly oriented collagen fibrils that, under the polarization microscope, appear as uneven anisotropic structures. They encircle osteocyte lacunae of globular shape that are irregularly distributed in the matrix. Moreover, they surround relatively large canal-like structures, which are penetrated by capillary vessels. When these canals are small, they correspond to primary osteons and the appearance of the bone is compact; when they are conspicuous, their appearance is that of spongy bone and the intertrabecular spaces contain bone marrow elements. The matrix of woven bone is characterized by the presence of wide interfibrillary spaces which contain abundant interfibrillar non-collagenous material and relatively abundant proteoglycans (Bonucci, 2013).

Woven bone contains relatively more cells per unit area than mature bone. Although woven bone is the major bone type in the developing foetus and it is often found in young growing skeletons, and lamellar (mature) bone is the major bone type in the adult, areas of immature bone are also present in adults, especially where bone is being remodelled, around bone fracture sites in cases of trauma and disease. Early formation of woven bone enhances early restoration of skeletal mechanical integrity before its replacement by lamellar bone.

2.4 Parallel-fibered bone:

Parallel-fibered bone consist of relatively thin, parallel-oriented collagen fibrils (Ziv et al., 1996). In reality, their orientation is only prevalently parallel, because many of them interlace their course, moreover, they may be regularly organized into unit layers called lamellae. Because collagen fibrils in parallel-fibered bone are rather uniformly oriented, they appear anisotropic when their axis is perpendicular to the optical axis of the polarization microscope. In this type of bone, as well as in lamellar bone, osteocytes have an elongated ovoidal shape; however, they do not show the regular distribution they have in lamellar bone.

3. Cellular level

Bone metabolism is regulated by multiple environmental signals (chemical, mechanical, electrical and magnetic signals). The response of bone to these signals is to modulate the balance between new bone formation and the local resorption of older bone (figure 1.4). To understand how bone modulates this balance is necessary to go to the molecular level to the bone cells that participate in bone homeostasis. Normally, they are divided in four types of cells:

3.1 Osteoblast:

They are known as the bone-forming cells. They are connective tissue cells found at the surface of bone. These cells can be stimulated to proliferate and differentiate as osteocytes. Normally, these types of cells are the major cellular component of bone. The functional part of bone, the bone matrix, is entirely extracellular (outside of the cells). The bone matrix consists of protein and mineral. The protein is called the organic matrix; it is synthesized first, and then the mineral is added. The vast majority of the organic matrix is collagen, which provides tensile strength. Then the matrix is mineralized by deposition of a calcium-phosphate-hydroxide salt called hydroxyapatite. This mineral is very hard, and provides compressive strength. Thus, the collagen and mineral together are a composite material with excellent tensile and compressive strength, which can bend under a strain and recover its shape without damage. This is called elastic deformation. Forces that exceed the capacity of bone to behave elastically may cause failure, typically bone fractures.

3.2 Osteocytes:

They are the most commonly found cells in mature bone**.** Osteocytes manufacture type I collagen and other substances that make up the bone extracellular matrix. Osteocytes will be found enclosed in bone inside spaces called lacunae. Osteocytes are thought to be mechanic-sensor cells that control the activity of osteoblasts and osteoclasts within a Basic Multicellular Unit (BMU), a temporary anatomic structure where bone remodelling occurs. Osteocytes generate an inhibitory signal that is passed through their cell processes to osteoblasts for recruitment to enable bone formation.

3.3 Osteoclasts:

These cells are responsible for bone resorption. They are characterized by their big size (diameter of 10-100µm) and for be the multicore structure. Their cytoplasm looks like a brush in the zone that is on contact with bone surface. Their function consists to reabsorb bone. To do that, these cells are fixed to the bone surface; this situation generates a sub-osteoplastic resorption compartment where the pH level decreases locally. This fact decreases the mineral component of the bone matrix and creates the entourage necessary for the collagen component being degraded by catalytic enzymes. The compartment created during this process is also called “Howship lacunae”.

3.4 Bone lining cells:

Bone lining cells come from osteoblasts which have become flattened. Bone lining cells have flat organelles so they can easily cover the bone without interfering with other cells functions. They are found mainly in adults, some however are in the bones of children. Bone lining cells are connected to other bone lining cells through gap junctions and they have the capability to mediate cell processes through bone. The lining cells are relatively inactive forms of osteoblasts that cover all available surfaces of the bone. Bone lining cells take action in metabolic activities as the immediate release of calcium in the bone if calcium in the blood is too low. This kind of cells is also responsible for the protection of the bone from harmful chemicals that would degrade away the bone.

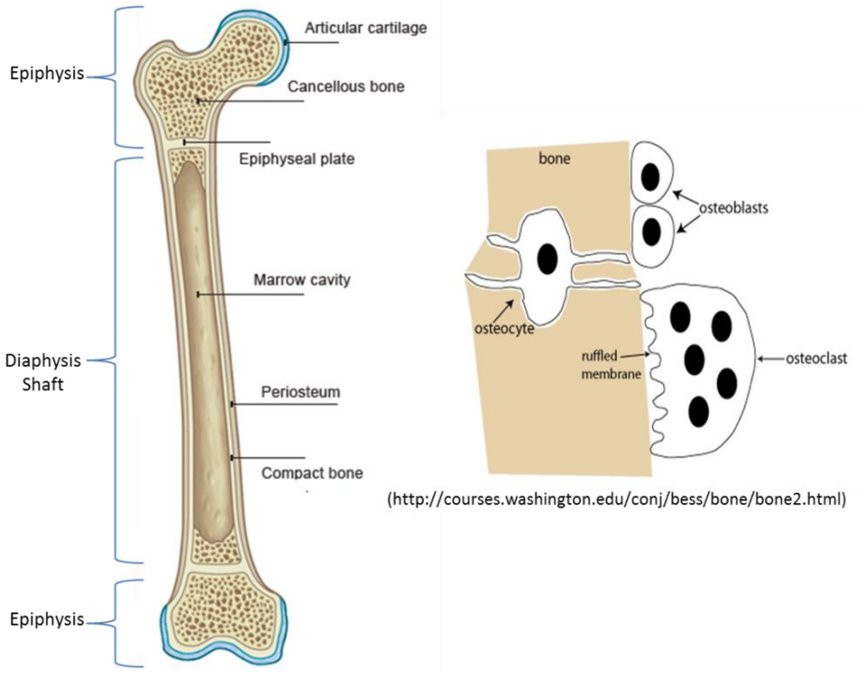

(http://courses.washington.edu/conj/bess/bone/bone2.html)

Figure 1.4 Scheme of the bone cells involved in metabolic process for bone remodelling. Osteoblasts are bone-forming cells. Osteocytes are bone cells that will be found enclosed in bone. Osteoclasts are bone resorbing cells ("-clast" means to break; osteoclasts break down bone).

4. Molecular level

At this level, bone material is composed by an organic framework of collagen, a mineral substance composed by crystals of carbonate apatite and water. Bone structure and mechanical properties are normally considered as the results of the interactions and distribution of these three elements. The attachment sites of macromolecules onto the collagen framework are not distinctly known, although several immune histological studies have shown preferential labelling of some macromolecules in a periodic fashion along the collagen molecules and fibres. However, water in also present at this scale. A briefly description of the different components found at this level is presented hereafter.

4.1 Organic Matrix

The organic matrix of bone is composed of type I collagen fibrils and non-collagenous proteins.

Collagen fibrils type I: Type I collagen is an ubiquitous protein of extremely low solubility that represent between 90 to 95% of the organic bone matrix. These fibrils are formed by the assemblage of filamentous molecules that are themselves made up of three polypeptide chains arranged in a helical configuration. These chains may include a variety of amino acid sequences, so that the molecules may show diversity. These chains take the form of a triple helix of two identical α_1 chains and one unique α_2 chain cross-linked by hydrogen bonding between hydroxyproline and other charged residues. This produces a very rigid linear molecule that is approximately 300 nm in length. Each molecule is aligned with the next in a parallel fashion and in a quarter-staggered array producing a collagen fibril. The collagen fibrils are then grouped in bundles to form the collagen fibre. A diagram of the collagen fibrils assembly is presented in figure 1.5.

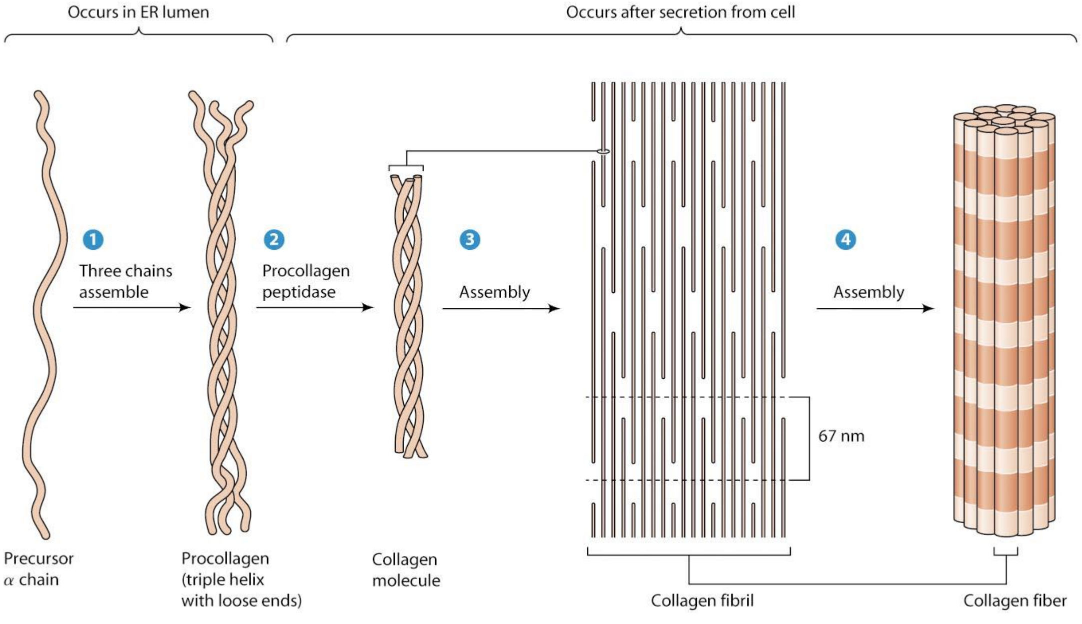

Copyright © 2009 Pearson Education, Inc.

Figure 1.5 Collagen assembly process is described: Collagen precursor chains are assembled to form triple–helical procollagen molecules. The fibrils assemble laterally into collagen fibres. In striated collagen, the 67–nm repeat distance is created by packing together rows of collagen molecules in which each row is displaced by one–fourth the length of a single molecule (Hardin et al., 2010).

Noncollagenous components: The noncollagenous components of bone include noncollagenous proteins as osteocalcin, proteoglycans, phospholipids, glycoproteins and phosproteins. The distributions and amounts of noncollagenous proteins are variable according to the type of bone and zones of bone matrix where they are located. They principal functions are related to regulatory effects, inhibitors or promoters of the calcification process, bone cell differentiation, recruitment, and some osteo-inductive properties.

4.2 Inorganic components

The mineral substance of bone is a calcium phosphate hydroxyapatite [$Ca_{10}(PO_4)_6(OH)_2$] (Jiang et al., 2008). However, this hydroxyapatite is not pure. This substance contains apatite crystals with a small crystal size (20-80 nm long and 2-5 nm of thick) and several impurities, most notably carbonate in place of phosphate groups. These impurities increase their solubility and change other physical properties. This fact creates biological effects, which can be fundamental for some functions like the mineral homeostasis and bone adaptation. The concentration of the inorganic components of bone changes with age. Normally the phosphate concentration decreases and crystallinity increases. The crystal size and crystallinity, which is the degree of structural order, of bone mineral can be altered with certain diseases and therapies as the Paget's disease, the diabetes and bisphosphonate treatment. Others inorganic components are potassium, magnesium, sodium, chloride and fluoride. A diagram of the apatite molecular composition is displayed in figure 1.6.

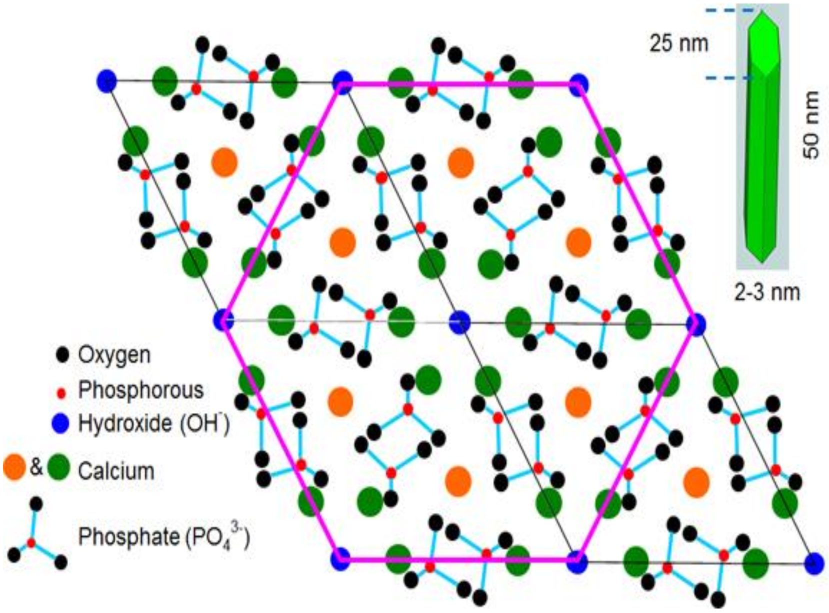

Figure 1.6 Scheme of the atoms orientation, structural assembly and morphology of the apatite crystals ("Bone Biology and Mechanics Lab," 2012).

4.3 Water

The function of water component in bone is not clear yet however it could contribute to the biological process inside the bone marrow. In addition, water layers presents in bone cavities could play an important role in the mechanical response of bone. It has been reported that layered water in crystals interfaces play a crucial role in bone viscoelasticity (Eberhardsteiner et al., 2014). In addition, according to (Timmins and Wall, 1977) there is a critical hydration degree in bone structures, form 37 to 49 mg H_2O/g bone, water pass to be fixed to the bone structure to a “freedom” state.

Bone composition is summarized in the scheme presented in figure 1.7. Each component has an estimated percentage of their contribution to the bone matrix.

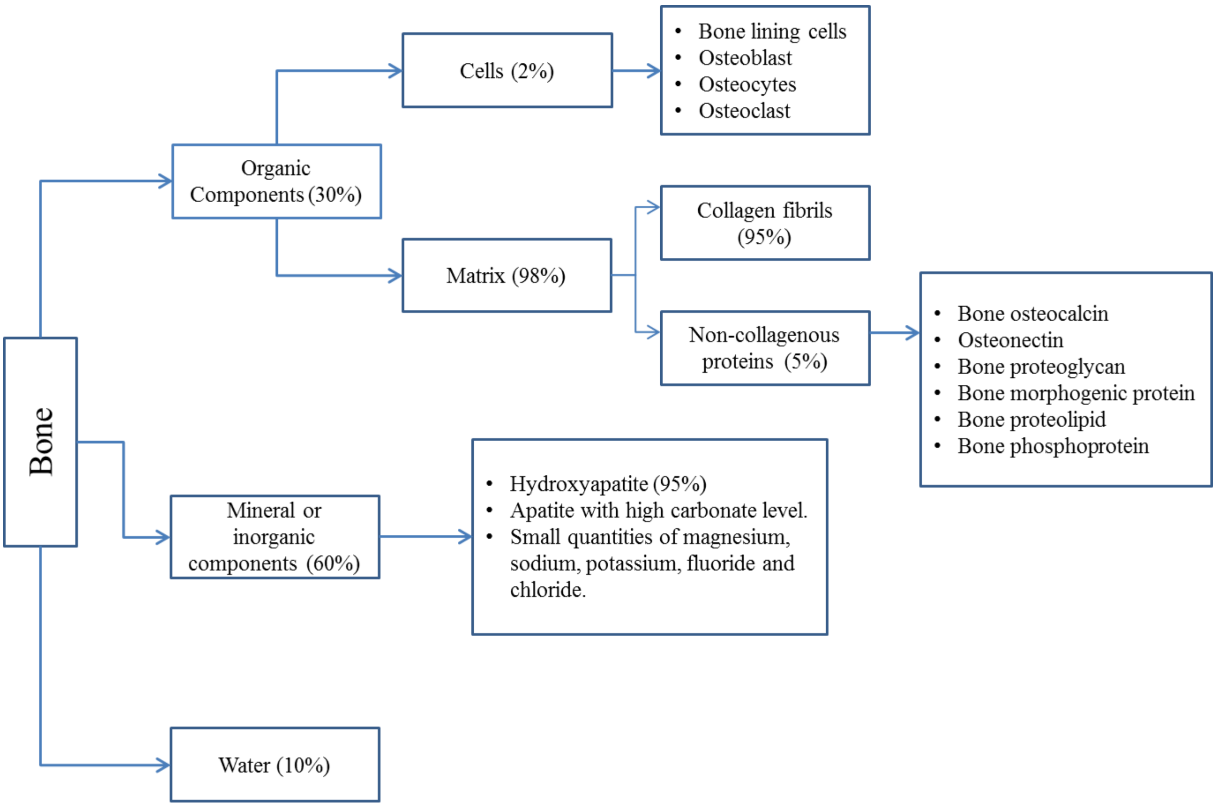

Figure 1.7. Scheme presents the bone tissue organic and inorganic composition at the molecular scale. The values reported for the estimated percentage of contribution of each component are approximated values. These values can increase or decrease according to several factors as bone type, age, diseases, species or samples state (dry or fresh).

III. Bone remodelling

The skeleton is a metabolically active organ that undergoes continuous remodelling throughout life. Bone remodelling involves the removal of mineralized bone by osteoclasts followed by the formation of bone matrix through the osteoblasts that subsequently become mineralized. The remodelling cycle consists of three consecutive phases:

- Resorption, during this phase osteoclasts digest old bone.
- Reversal, when mononuclear cells appear on the bone surface.
- Formation, when osteoblasts lay down new bone until the resorbed bone is completely replaced.

Bone remodelling serves to adjust bone architecture to meet changing mechanical needs and it helps to repair micro damages in bone matrix preventing the accumulation of old bone (figure 1.8). It also plays an important role in maintaining plasma calcium homeostasis. (Hadjidakis and Androulakis, 2006).

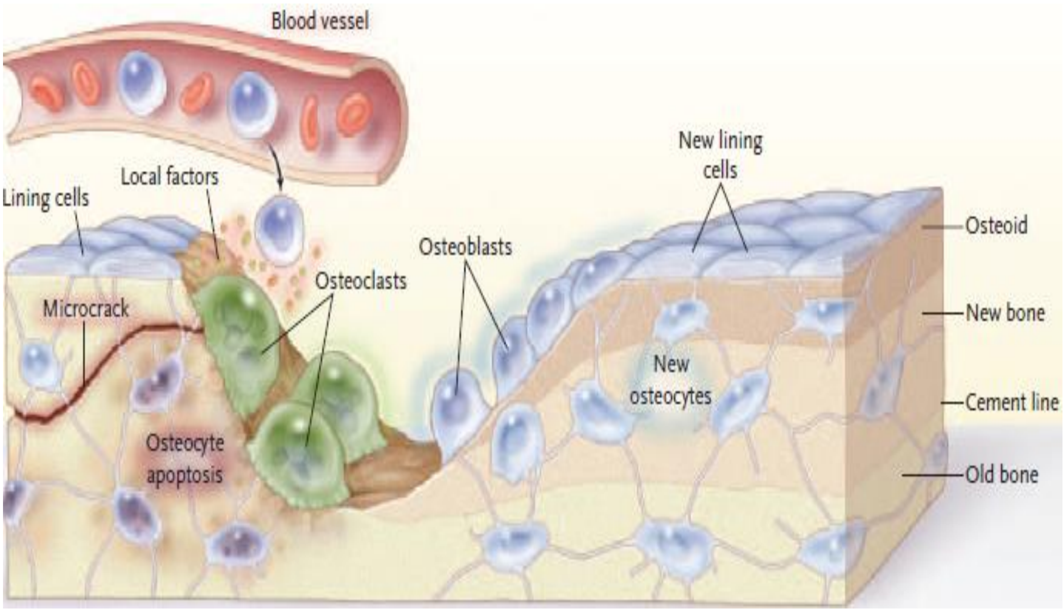

Figure 1.8 Scheme of bone remodelling cycle. Micro crack severs canaliculi, which causes osteocytes' apoptosis, with the location and extent of the damage defined by signals to lining cells. Lining cells and osteocytes release local factors that attract cells from blood and marrow into the remodelling compartment in which osteoclastogenesis occurs. Osteoclasts resorb matrix and the micro crack, and then successive teams of osteoblasts deposit new lamellar bone. Osteoblasts that are trapped in the matrix become osteocytes; others die or form new, flattened osteoblast lining cells (Seeman and Delmas, 2006).

Remodelling is continuous and coordinated cycle of removal of old bone by osteoclasts followed by the deposition of new bone by osteoblasts in response to micro damage and variable mechanical loadings. Bone remodelling is a continuous process throughout life. In the first three decades of life, bone turnover is coupled tightly to maintain a steady state between bone resorption and bone formation. Although there are variances in turnover rates, peak bone mass and size is achieved around the age of 15–20 years in women and later in men (Raisz and Seeman, 2001). After reaching the peak of bone mass, bone turnover continues at a slower rate as suggested by a rapid decline in biochemical measures of bone remodelling with the predominance of bone resorption over bone formation (Raisz and Seeman, 2001).

At the bone surface level, age-related bone loss is the consequence of two simultaneous but opposing processes: sub periosteal apposition, which takes place on the outside of the bone, and endosteal bone resorption, which takes place on the inside of the bone. With increasing age, bone remodelling is reduced leading to a negative bone balance at individual basic multicellular unit (BMU) sites. After the fourth decade of life, there is a reduction in the formation of periosteal bone and at the same time, there is increasing number of remodelling units within endosteal bone resulting in a linear increase in endosteal bone resorption in both sexes. The overall consequences of these age-related changes are cortical thinning, increased cortical porosity, thinning of the trabeculae and loss of trabecular connectivity, all of which reduce bone quality and consequently bone strength (Rosen et al., 1994; Seeman, 2003, 2002).

IV. Differences between species

Structural differences between species are not evident at the macro scale. However when we descend in the scale to the micro scale, the structural and morphological differences are evident (Hillier and Bell, 2007). These differences between species are the most important factors that need to be considered when choosing an animal model. The most often used animal models in bone studies include the rat, mouse, dog, cow, pig, sheep, rabbit etc. (Hillier and Bell, 2007; Liebschner, 2004; Potes et al., 2008). An ideal model that can be perfectly mimic human body does not exist. However, the animal is selected according to a series of criteria such as availability, biological homogeneity of individual specimen, ease of handling and experimentation on, purchase price, cost for maintenance and cultural sensitivity, which may exclude the use of a given species in some countries. Using histological methods, the main differences between the human, rat and bovine bone are presented hereafter.

1. Human bone

The typical appearance of a cross-section of an adult human long bone consists of circumferential lamellae bone at the endosteal and periosteal surfaces and a middle component of dense Haversian bone (Hillier and Bell, 2007). Approximately 50% of this dense Haversian bone consists of Haversian systems while the other 50% consists of interstitial lamellae, occurring at irregular angular spaces between Haversian systems. The Haversian systems appear as both complete and active systems. The complete systems are comprised of a central Haversian canal, often off-centred in position, surrounded by 16–20 cylindrical lamellae with an outer border consisting of a cement line. These systems are commonly oval or round in shape. The active Haversian systems, or remodelling units, differ in appearance to that of complete Haversian systems. Depending on where the cross-section intercepts the active Haversian system on its course of formation; three different appearances may be seen: (1) a resorptive bay (also referred to as a cutting cone) bordered by Howship's lacunae; (2) a forming site, with osteoblasts bordering a varied amount of freshly deposited, unmineralized bone that is contained within a cement line; or (3) a complete Haversian system. The circumferential lamellae appearing at the periosteal and endosteal surfaces are often times fragmentary, with the number of periosteal lamellae generally exceeding that of endosteal lamellae. Volkmann's canals may also be seen on a thin section of bone and run perpendicular to the Haversian canals. While the cortical bone tissue of other shaped bones, such as flat (cranial) and short (vertebra), contain the same histological structures as long bones, their histological appearance may differ.

2. Rat bone

The histological appearance of rat long bone cortical bone is comprised mainly of primary longitudinal bone tissue. Haversian systems do appear; however, these systems are rare and scattered near the endosteal surface. Endosteal and periosteal circumferential lamellae are also present, but are poorly developed at the endosteal surface due to the presence of Haversian systems here. Additionally, there may be small areas of avascular and a cellular bone located throughout (Hillier and Bell, 2007).

3. Bovine bone

Bovine bone structure has a laminar structure, which consists of an alternating layering of parallel-fibered bone and lamellae. Sandwiched between lamellae is two-dimensional network of blood vessels and vascular spaces. Bovine bone's primary osteons lack any cement lines, hence in most cases it shows higher strength than the secondary osteonal structures. Haversian bone is located near the endosteal surface, and osteonal banding at the interface between both. Haversian canals are medium in size and irregular in shape. Foetal calf femora also exhibit the same pattern: plexiform bone tissue near the endosteal surface, a middle portion of laminar bone with an irregular arrangement, and a periosteal area of Haversian bone. According to (Hillier and Bell, 2007), no information exists for adult cow bone and this is thought to be an outcome of modern butchering practices, where sub-adult (13–24 months) cows are preferentially slaughtered.

Data reported in the literature for the structural and biochemical composition of human, adult rat and bovine cortical bone is summarized in Table 1.1.

Table 1.1 Structural properties of human, rat and bovine bone

Species (mature specimens)	Bone	Density of cortical bone (kg.m^{-3})	% H_2O	%Apatite Crystal	%Dry weight collagen
Human (Bensamoun, 2003; Espinoza Orías et al., 2009; Herring, 1977; Ho Ba Tho et al., 1991a)	Femur	1545 – 2118* 1468 – 2127** 1800 ± 0.07 1960 ± 0.05	7.3	67.2	21.2
Rat (Vanleene et al., 2008)	Femur	1659 ± 0.85 2083 ± 0.13	N/A	69 to 71	21.4 to 17.4
Bovine (Herring, 1977; Katz et al., 1984)	Femur	2032 ± 0.15 2093 ± 0.12	9.1	68.8	22.1

*, ** Range of densities reported in Ho Ba Tho et al. 1991 and Bensamoun 2003 respectively.

V. Mechanical characterization of bone at the macro scale

Mechanical properties of bone have been always a topic of huge interest. Bone being the biomechanical part of the skeleton, it is of vital importance to know the bone mechanical properties for its analysis to study the failure aspects, early detection and monitoring of bone diseases. Due to the important structural function, almost 3/4 of the studies reported in the literature have been performed in the cortical zone of the long bones. Therefore, because of its hierarchical structure, the mechanical responses have been widely characterized at different scales. The values reported are constantly improved thanks to the growing accuracy of the new mechanical methods.

At the macro scale, the mechanical properties most frequently reported are the elastic modulus (E), shear modulus (G) and Poisson' ratio (ν). The most common mechanical methods used to quantify the mechanical properties of bone are the tensile, bending and compression tests (Ascenzi et al., 1990, 1982; Burstein et al., 1972; Cowin, 1983; Reilly and Burstein, 1975; Reilly et al., 1974). The main problem with these methods is that bone sample is destroyed during the mechanical assessment. This fact make necessary to use many bone samples in order to obtained significant results.

An alternative method to assess the mechanical properties of bone without destroying the sample is based on ultrasound technique. This technique can be carried out under different experimental conditions such as contact or immersion modes. The differences between the ultrasounds modes are the wave frequency (low frequency KHz or high frequency MHz) and the propagation media. Some author who are used this method are Advantages of this technique are first, that it can be used to build up maps of the spatial distribution of material impedance across the bone surface. Second, that the mechanical assessment can be performed in different directions over the same sample (Ashman et al., 1984; Bensamoun et al., 2004b; Ho Ba Tho et al., 1991a, 1991b; Katz et al., 1984; Pithioux et al., 2002).

Other important details about the mechanical response of bone at the macro scale were reported by (Ho Ba Tho et al., 1991b). They concluded that mechanical properties vary according to the type of bone (cortical or cancellous bone) and according to the anatomical origin of the sample (femur, tibia; vertebrae) and those mechanical properties are not completely equivalent between subjects and specimens even for the same organs.

A summary of the values reported in some studies for the elastic mechanical properties for long bones assessed at the macro scale are presented in Tables 1.2 to 1.4.

Table 1.2 Values of the mechanical properties of HUMAN bone assessed by tensile, compression and bending mechanical tests and ultrasounds

Reference	Bone specie	Anatomical origin	Test	Load direction	Elastic Modulus (GPa)
(Reilly et al., 1974)	Human	Femur	Tension and compression	Longitudinal	$E_{LONG\ \_femur} = 17.1 \pm 3.15$
(Reilly and Burstein, 1975)	Human	Femur	Tension and compression	Longitudinal, transverse and radial	$E_{RAD} = 11.5$ $E_{TRANSV} = 11.5$ $E_{LONG} = 17.0$
(Ascenzi et al., 1990)	Human	Femur	Bending	Longitudinal and radial	Radial $E_{load1} = 2.31 \pm 1.28$ to 2.69 ± 0.93 $E_{load2} = 1.22 \pm 0.59$ to 1.53 ± 0.79 Longitudinal $E_{load1} = 2.31 \pm 1.23$ to 2.32 ± 1.20 $E_{load2} = 0.60 \pm 0.44$ to 0.81 ± 0.49
(Zioupos and Currey, 1998)	Human	Femur	Flexion	Transverse	$E_{TRANSV\ =}$ 15.2 Decreasing ratio = 2.3%/year
(Evans and Vincentelli, 1974)	Human	Tibia	Compression	longitudinal	$E_{26years} = 23.3 \pm 7.3$ $E_{31years} = 20.0 \pm 6.0$ $E_{54years} = 17.4 \pm 2.2$ $E_{61years} = 19.0 \pm 8.9$ $E_{75years} = 18.4 \pm 5.6$
(Ho Ba Tho et al., 1991b)	Human	Femur and tibia	Contact ultrasounds	Longitudinal, transverse and radial	$E_{RAD\_F} = 11.7 \pm 1.9\ _{\_Tb} = 11.7 \pm 1.3$ $E_{TRANSV\_F} = 12.3 \pm 2.0\ _{\_Tb} = 12.2 \pm 1.4$ $E_{LONG\_F} = 19.9 \pm 2.7\ _{\_Tb} = 20.7 \pm 1.9$

LONG= Longitudinal; TRANSV= Transverse; RAD= Radial

Table 1.3 Values of the mechanical properties of BOVINE bone assessed by tensile, compression and bending mechanical tests and ultrasounds

Reference	Bone specie	Anatomical origin	Test	Load direction	Elastic Modulus (GPa)
(Burstein et al., 1972)	Bovine	Femur	Tension	Longitudinal	E_{LONG} = 24.5 ± 5.1
(Reilly et al., 1974)	Bovine	Femur	Tension and compression	Longitudinal	Laminar femur E_{LONG_T} = 27.4 ± 6.3 E_{LONG_C} = 30.3 ± 6.0 Haversian system femur E_{LONG_T} = 24.4 ± 5.5 E_{LONG_C} = 23.3 ± 4.0
(Katz, 1980)	Bovine	Femur	Ultrasounds	Longitudinal, transverse and radial	E_{TRANSV} = 8.7 to 10.3 E_{LONG} = 17.3 to 19.7
(Van Buskirk et al., 1981)	Bovine	Femur	Ultrasounds	Longitudinal, transverse and radial	E_{RAD} = 11.6 E_{TRANSV} = 14.6 E_{LONG} = 21.9
(Lipson and Katz, 1984)	Bovine	Femur	Ultrasounds	Longitudinal, transverse and radial	E_{RAD} = 15.4 ± 0.5 to 17.3 ± 0.9 E_{TRANSV} = 16.4 ± 0.5 to 21.4 ± 0.6 E_{LONG} = 24.7 ± 1.0 to 29.8 ± 1.2

LONG= Longitudinal; TRANSV= Transverse; RAD= Radial; T=Tension; C=Compression; F=Femur; Tb=Tibia

Table 1.4 Values of the mechanical properties of RAT bone assessed by tensile, compression and bending mechanical tests and ultrasounds

Reference	Bone specie	Anatomical origin	Test	Load direction	Elastic Modulus (GPa)
(Jørgensen et al., 1991)	Rat	Femur and tibia	Tension	Transverse	Femur E_{TRANSV} = 5.9 ± 0.2 to 7.7 ± 0.5 Tibia E_{TRANSV} = 10.8 ± 0.8 to 12.1 ± 0.1
(Kohles et al., 1996)	Rat	Femur	Ultrasounds	Longitudinal, transverse and radial	E_{RAD}= 15.3 ± 1.1 to19.2 ± 0.7 E_{TRANSV}= 20.3 ± 0.6 to 24.0 ± 1.2 E_{LONG}= 22.1 ± 1.7 to 25.8 ± 0.9
(Akkus et al., 2004)	Rat	Femur	Bending	Longitudinal	E_{LONG} = 3.3 to 6.5
(Vanleene et al., 2008)	Rat	Femur	Ultrasounds	Longitudinal	E_{LONG} = 8.0 ± 0.8 to 19.8 ± 1.3

LONG= Longitudinal; TRANSV= Transverse; RAD= Radial

Independently of the mechanical technique used for the quantification of the mechanical properties, the variation of the macroscopic mechanical response of the bone is continuously correlated to structural factors such as porosity, density and mineral composition. Whatever the species of bone, the mechanical response presents a dependency in the load direction. Values computed in the longitudinal direction tend to be higher than in the transverse and radial directions. Values of the mechanical properties assessed by bending tests are lower than those obtained from tensile, compression and ultrasounds tests. The range of values for the elastic modulus of long bones for human femoral and tibia bones are between 17 and 23.3 GPa in the longitudinal direction; between 11.5 and 15.2 GPa and between 11.5 and 11.7 GPa for the radial direction. For bovine femoral bone, the elastic properties vary between 21.9 and 30.3 GPa in the longitudinal direction; between 8.7 and 21.4 GPa in the transverse direction and between 11.6 and 17.3 GPa in the radial direction. Finally, for rat femoral and tibia cortical bone the values vary between 8.0 and 25.8 GPa in the longitudinal direction; between 5.9 and 24.0 GPa in the transverse direction and between 15.3 and 19.2 GPa in the radial direction.

Time-dependent mechanical properties are rarely assessed at the macro scale. Nevertheless, some studies reported values for viscoelasticity of cortical bone. (McElhaney, 1966) obtained stress, strain and strain-rate representations of bone samples under different test velocities. He used a kind of air-gun testing machine capable of performing constant velocity compression tests with strain rate up to $4000 s^{-1}$. He showed that the mechanical properties of bone in compression are significantly dependent of the rate of deformation. In addition, he reported that a critical velocity for bone corresponds to a strain rate of $1 s^{-1}$. At this strain rate value, he found important increasing strain at break. He reported that elastic modulus increase from 15.1 to 29.5 GPa when the strain rate increases from $0.001 s^{-1}$ to $300 s^{-1}$. (Crowninshield and Pope, 1974) examined the behaviour of anisotropic compact bone in tension at a range of strain rates. The tests were performed under strain rate in a range between 0.01 and $200 s^{-1}$. There is a maximum energy absorption capability at a strain rate of $0.1 s^{-1}$. They determined that modulus of elasticity of bone in tension is significantly sensitive to the strain rate in the longitudinal direction but not so much in the transverse. (Katsamanis and Raftopoulos, 1990) used the Hopkinson bar stress technique to investigate the dynamic and static mechanical properties of human femoral cortical bone. Young's modulus value in dynamic ($\dot{\varepsilon} = 100 s^{-1}$) conditions ($E_d$ = 19.9 GPa) is 23% higher than the average static ($\dot{\varepsilon} = 2\times10^{-5} s^{-1}$) Young's modulus ($E_s$= 16.2 GPa).

B. Nanoindentation technique

I. Generalities

Nanoindentation is a very powerful technique used for assessing mechanical properties of classical and biological materials at the micro/nano scale. The principle consists to apply a prescribed load to an indenter in contact with the specimen. Then, from the experimental data, load vs. indentation depth (displacement) curves are plotted.

The central assumptions of nanoindentation are the absence of adhesion and frictional stresses acting between the surfaces. The main limitations of the nanoindentation technique are the assessment of the contact area and the absence of theories dealing accurately with elastoplastic contacts.

Mechanical models are used to estimate different materials properties like the elastic modulus, hardness, toughness, viscoelastic modulus. Forces involved are usually in the milli or micro newton range and depth can go from some nanometres to several micrometres. Different kind of tips can be used for making an imprint into the material surface; however, the tip geometry must be considered when the mechanical response is assessed. The principal advantage of this technique is that a very small material volume is used and some mechanical properties can be assessed from the same indentation test.

At the international level, this technique has been regulating by a standard ISO 14577. This standard defines the test method, as well as the procedures for the verification and calibration of this kind of machines. This standard contains the following parts (Lucca et al., 2010)

- ISO 14577-1 Part 1: Defines three application ranges of instrumented indentation testing:
    Nano range: $h_{max} \leq 200$ nm.
    Micro range: $h_{max} > 200$ nm and $F_{max} < 2$N.
    Macro range: $2\text{ N} \leq F_{max} \leq 30$ kN.

Where h_{max} is the maximum indentation depth and F_{max} is the maximum test force.

- ISO 14577-2 Part 2: Verification and calibration of testing machines.
- ISO 14577-3 Part 3: Calibration of reference blocks.
- ISO 14577-4 Part 4: Test method for coatings

A summary of some of the most relevant concepts necessary to understand nanoindentation technique is provided hereafter.

1. Contact theory

Contact mechanics is the study of the deformation of solids bodies caused by the load generated when they touch each other at one or more points. Under the action of the load the solids deforms and a contact area is formed. Earliest theories about contact mechanics started at the end of the 19th century with the studies of Hertz (Hertz, 1882), Boussinesq (Boussinesq, 1885) and later by Sneddon (Sneddon, 1965). Hertz studied the contact of a rigid spherical indenter onto a flat isotropic half-space, Boussinesq the contact between a rigid cylindrical flat indenter and an elastic half-space and Sneddon did the same for a conical indenter (figure 1.9).

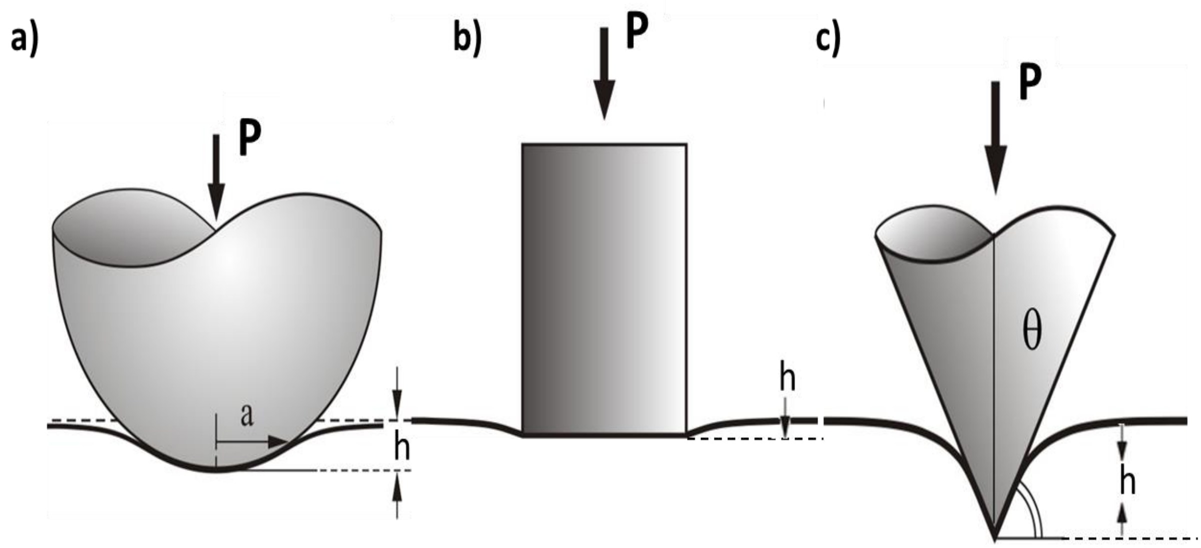

Figure 1.9 Scheme of contact models a) Hertz for contact between a rigid sphere and an elastic half-space and b) Boussinesq for a contact between a rigid cylindrical indenter and an elastic half-space; c) Sneddon for contact between a rigid conical indenter and an elastic half-space.

1.1 Hertz contact

Hertz theory describes the contact between a sphere and an elastic half-space. This theory allows the quantification of the resulting contact area, contact pressure, compression of the bodies, and the induced stress in the bodies. Hertz determined that the radius "**a**" of the circular contact area could be computed as:

$$a^3 = \frac{3}{4}\frac{PR}{E^*} \qquad (1.1)$$

Where P is the load, R is the radius of the indenter and E* is called reduced modulus which is a combination of the indentation moduli E_i of indenter and samples. The reduced modulus can be represented by:

$$\frac{1}{E^*} = \frac{1-v_s^2}{E_s} + \frac{1-v_i^2}{E_i} \tag{1.2}$$

Where E and v are the Elastic moduli and Poisson's ratio of the sample (s) and indenter (i) respectively. Usually the indenter tip is made of diamond were E = 1141 GPa and v= 0.07 (Oliver and Pharr, 1992) .

The indentation depth δ on the axis is described by:

$$\delta^3 = \left(\frac{3}{4E^*}\right)^2 \frac{P^2}{R} \tag{1.3}$$

In addition, the load P can be described as a function of the penetration depth by:

$$P = \frac{4}{3} E^* \sqrt{R} \delta^{\frac{3}{2}} \tag{1.4}$$

However, Hertz theory needs some simplifying assumptions such as:

- Surface are continuous
- Surface are frictionless
- Solids are purely elastic
- Strains are small

The problem appears for the Hertz model when the contact load is high enough to generate plastic stain.

1.2 Boussinesq contact

Boussinesq developed a method based on potential theory for computing the stresses and displacements in an elastic half space elastic body loaded by a rigid-axisymmetric indenter. Boussinesq proposed that penetration h of an elastic solid caused by a rigid cylindrical flat indenter could be described by the follow relationship

$$P = \frac{2E\mathrm{a}}{(1-\nu^2)} h \tag{1.5}$$

Where the term P is the applied load, the contact radius is “a”, the Poisson’s ratio ν and the elastic modulus E.

The derivative of P with respect to h gives us the contact elastic stiffness S.

$$\frac{dP}{dh} = S = \frac{2E}{(1-\nu^2)}\mathrm{a} \tag{1.6}$$

1.3 Sneddon contact

A solution to the indentation with conical indenters was provided by (Sneddon, 1965). His method proposed a new relation to describe the case of frictionless indentation of an isotropic elastic half-space but with a rigid conical indenter. Sneddon proposed that indentation of a semi-infinite elastic solid by a conical indenter could be described as a function of the applied force and the displacement of the indenter of angle2θ. However, this relation is only exactly satisfied by a perfect cone infinitely rigid.

From this, the total load can be expressed by:

$$P = \frac{\pi \mathrm{a}}{2} E^{*} \mathrm{a} cot\theta \tag{1.7}$$

Where “a” is the contact radius and θ is the cone half angle.

The displacement on the axis is:

$$h_{max} = \frac{\pi}{2} \mathrm{a} cot\theta \tag{1.8}$$

Then, the load can be rewritten as:

$$P = \frac{2}{\pi} E^{*} h_{max}^{2} tan\theta \tag{1.9}$$

The projected contact area A is assumed as:

$$A = \pi \mathrm{a}^2 \tag{1.10}$$

In addition, the contact stiffness S is defined by:

$$S = \frac{dP}{dh}|_{h=hmax} = 2E^{*}\sqrt{\frac{A}{\pi}} \tag{1.11}$$

In addition, the reduced modulus is rewritten as:

$$E^{*} = \frac{S}{2}\sqrt{\frac{\pi}{A}} \tag{1.12}$$

This expression will be improved and adapted for nanoindentation analysis for the Oliver and Pharr model.

1.4 Sneddon’s equation

The equation 1.12 linking the contact stiffness to the reduced elastic modulus is known as the Sneddon’s equation. It is particularly robust because it is valid for Hertz, Boussinesq and Sneddon contacts for which the strain field are very different. Thus, the Sneddon equation is supposed to be valid for any elastic or plastic axisymmetric isotropic contact.

2. Elastoplastic contact

One on the most debated topics in contact mechanics is the elastoplastic contact. This is due to the lack of theories that could estimate accurately the indentation depth and thus the contact area during the plastic deformation. Misunderstanding this behaviour could generate miscalculations in the modulus and hardness values reported during a nanoindentation tests. This phenomenon occurs when the load applied for the indenter is high enough to initiate a zone of plastic deformation in the material increasing with the load. But the size of the deformed zone (under the indenter) remains unknown until it arrives to the fully developed contact. The size and behaviour of the plastic zone could change as a function of the indenters’ geometries (spherical, Vickers or Berkovich) and material properties.

The figure 1.10 illustrates the elastoplastic process during an indentation tests with a spherical indenter in an elastic-plastic solid.

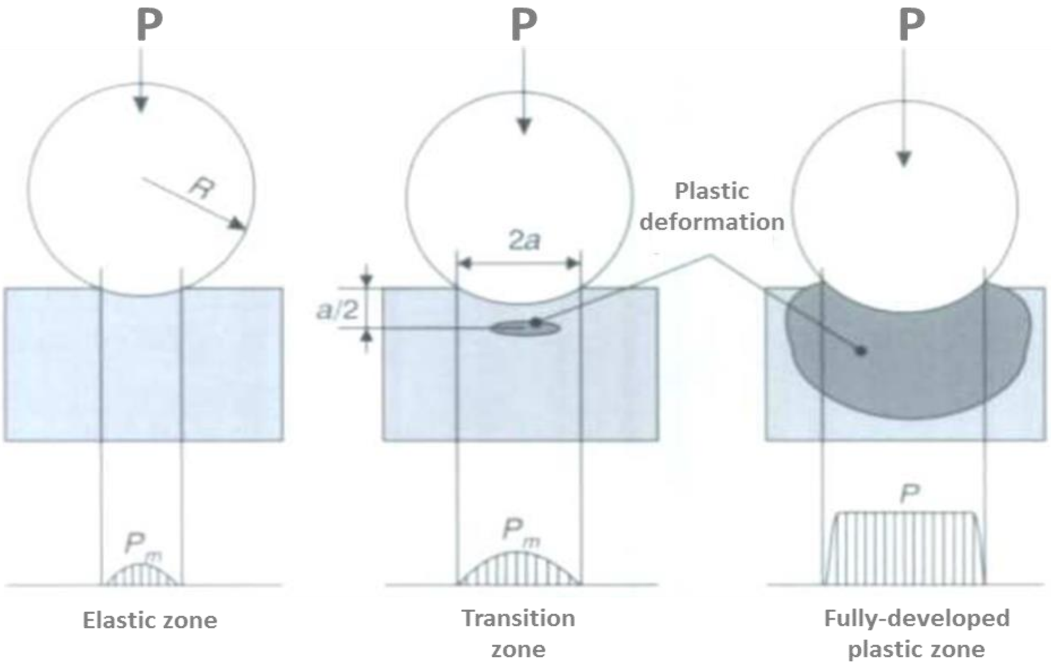

Figure 1.10 Evolution of the elastoplastic contact under a spherical indenter. Where P is the load applied, P_m is the mean contact pressure (the indentation stress) which is linearly proportional to the ratio a/R which is called the indentation strain. (Beyaoui, 2009; Fischer-Cripps, 2009; Tabor, 1970)

Understanding the significance of the developing elastoplastic contact is critical for the use and interpretation of nanoindentation test data (Fischer-Cripps, 2009).

3. Experimental curve and contact area

The experimental data is represented graphically for curves representing the interaction between the indenter load P and indentation depth *h* (figure 1.11). In a typical test, force and indentation depth are recorded as load is applied from zero to some maximum and then from maximum force back to zero. This experimental curve allows one to compute the elastic and plastic mechanical properties. To achieve this goal, analysis of the load-displacement curves are required.

The indentation depth together with the know geometry of the indenter provides and indirect measure of the area of contact at full load, from which the mean contact pressure may be computed. When load is removed from the indenter, the material attempts to regain its original shape, but it prevented from doing so because of plastic deformation. However, there is some degree of recovery due to the relaxation of elastic strain within the material.

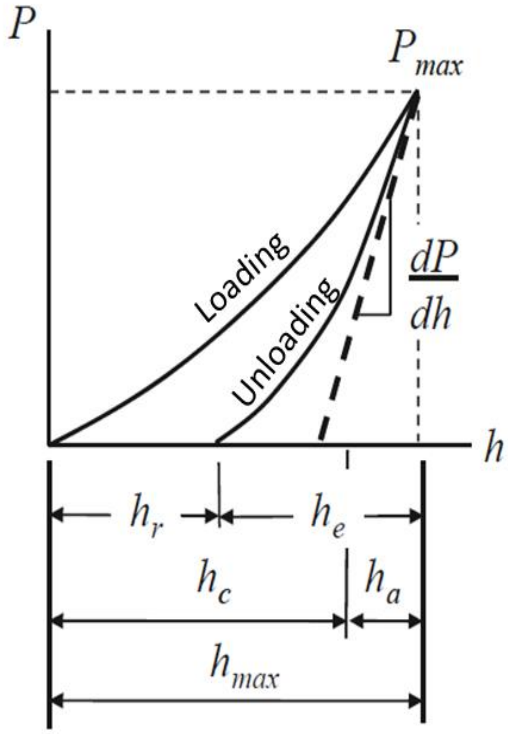

Figure 1.11 Typical Load vs. Displacement curve. Here, the term P is the load; the displacement is h; P_{max} is the peak load; h_r is the final depth of the contact impression after unloading; he is the surface displacement at the contact perimeter, h_c is the contact depth; h_{max} is the indenter displacement at the peak load, and dP/dh is the initial unloading stiffness (Fischer-Cripps, 2009; Oliver and Pharr, 1992).

Because of contact area changes continuously during unloading it is necessary to identify the indenter geometries that best describes the experimental data. (Oliver and Pharr, 1992) tested different indenter geometry and computed different power law exponents (m), which best describe the unloading behaviour. They reported that the unloading behaviour is best described by the paraboloids geometry (m=1.5) with a geometrical constant $\epsilon = 0.75$. This allows them to compute the indentation depth and by consequence, the contact area could be described by the equation:

$$A(h_c) = 24.5h_c^2 \tag{1.13}$$

Sneddon’s equation 1.12 gives the relationship among the contact stiffness S, the reduced elastic modulus of the material E* and the contact area A. This Sneddon’s theory was studied and improved by Oliver and Pharr. In the data analysis section, the Oliver and Pharr analysis method will be described. This method uses an analysis of the initial portion of this elastic unloading response which corresponds to the elastic contact stiffness (S= dP/dh). This stiffness is then used to estimate the elastic modulus of the indented material.

II. Instrumental aspects

Nanoindentation testing requires a judicial choice of indenter geometry, indentation protocol and load as well as many other test variables such as number of data points, percentage of unloading, indentation depth or maximum load and the way in which the load is applied (constant load rate, constant depth rate, and constant strain rate). Here a briefly list of some factors that could affect the nanoindentation experiments is listed:

- The tip initialization: it is necessary to verify if the tip is parked and functional. It is recommended indenting a well knowing referent material (most of time is a fused silica sample) in order to check if the elastic moduli and hardness are correct otherwise, it is necessary to check if the tip has been correctly installed.
- The thermal drift: nanoindentation is a trade-off between the displacement due to penetration and the displacement due to thermal drift. If maximum penetration depth is 50nm and thermal drift is 1 nm per second, then if the test takes one minute, error due to thermal drift will completely swamp the true penetration reading.
- The thickness of the sample could affect the mechanical response. If the sample holder is compliant (low E); then elastic deformation may occur in the sample holder affecting the value of the elastic modulus.
- The surface roughness is too high relative to the maximum penetration, thus the assumption of a semi-infinite specimen embodied in the contact equation is invalid.
- If the tested material exhibits creep, then the displacements recorded will contain creep and penetration. It may be possible to wait at maximum load for creep to subside before unloading. If creep continues, then it is generally not possible to consider a static indentation test.

1. Tip geometry

Indenters for nanoindentation testing are usually made from diamond. The Berkovich indenter is the tip most commonly used for nanoindentation testing because it is more readily fashioned to a sharper point than the four-sided Vickers geometry, thus ensuring a more precise control over the indentation process. The mean contact pressure is usually determined from a measure of the contact depth of penetration h_c. Table 1.5 is a compilation of geometrical parameters of typical nanoindenters, especially the project area of the contact.

Table 1.5 Parameters for common indenter shapes

Indenter Shape	Indenter	Projected area (A)	Correction factor β	Indenter Shape	Indenter	Projected area (A)	Correction factor β
Berkovich	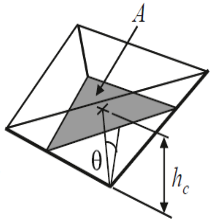 θ= 65.3°	$24.56h_c^2$	1.05	**Spherical**	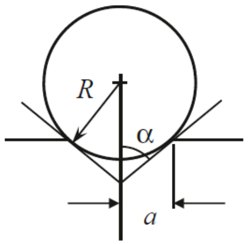	$\pi(2Rh_c - h_c^2)$	1
Vickers	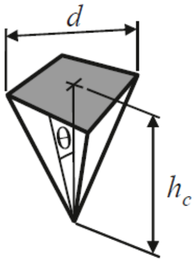 θ= 68°	$24.504h_c^2$	1.012	**Cube corner**	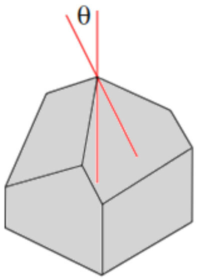 θ= 35.26°	$2.60h_c^2$	1.034
Conical	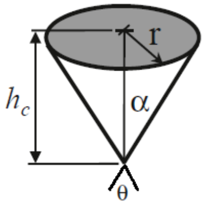 α=70.3° 20° > θ > 140°	$2\pi h_c \tan^2 \theta$	1	**Knopp**	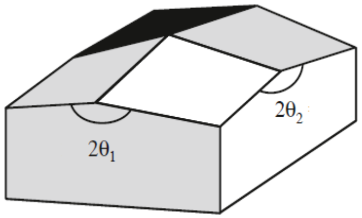 θ_1= 86.25° θ_2= 65°	$65.438h_c^2$	1.012

2. Calibration materials

In order to guarantee the accuracy and repeatability of the nanoindentation results, the nanoindentation systems require calibration and calibration standards. Three calibration measurements are required for all nanoindentation systems (Wheeler, 2006):

Some mechanical properties of the most commons calibration materials are summarized in Table 1.6 These values are used to assess the accuracy of the nanoindentation tip.

Table 1.6 Materials properties of most commonly used calibration standard materials (Wheeler, 2006)

Material	Elastic modulus E (GPa)	Poisson's ratio v	Hardness H (GPa)
Fused silica	72	0.17	8.8
Aluminium	70.8	0.36	0.25
Tungsten	412	0.28	~6.6
Sapphire	370	0.25	30
Tool steel	220	0.28	8.8

3. Strain rate

In nanoindentation tests, the experimental protocol is very important in order to quantify accurately the values of the mechanical properties. Since measurements from nanoindentation, experiments were initially developed for ceramic and metallic materials. These materials are not sensitive to strain- rate effects at room temperature (Hochstetter et al., 1999; Loubet et al., 1993; Oliver and Pharr, 1992). However, in the case of time-dependent materials the strain rate is the key to assure the measurements reproducibility. The theory consists in keeping the strain rate constant during the entire nanoindentation test. The principle of geometrical similarity impose that strain rate must be proportional to $\dot{h}/h$. According to Lucas et al., 1996a this can be done by keeping the loading rate/load ratio and the unloading rate/load ratio constant ($\dot{P}/P = cte$) during the loading. Experimentally, if H=cte and $\dot{P}/P = cte$ thus $\dot{h}/h = cte$) (Beyaoui et al., 2009; Beyaoui, 2009; Lucas et al., 1996b).

III. Data analyses models

Nowadays, there are several models to analyse nanoindentation data and extract the mechanical properties of the material. The methods most commonly used are briefly described below.

1. Oliver and Pharr Method

This method allow us to compute the elastic modulus and the hardness of isotropic materials (Oliver and Pharr, 1992). In this method, the depth of penetration of a diamond indenter is measured along with the prescribed load. The resulting load-displacement response typically shows an elastic-plastic loading followed by an elastic unloading (figure 1.12). The elastic equations of contact are then used in conjunction with the unloading data to determine the elastic modulus and hardness of the specimen material.

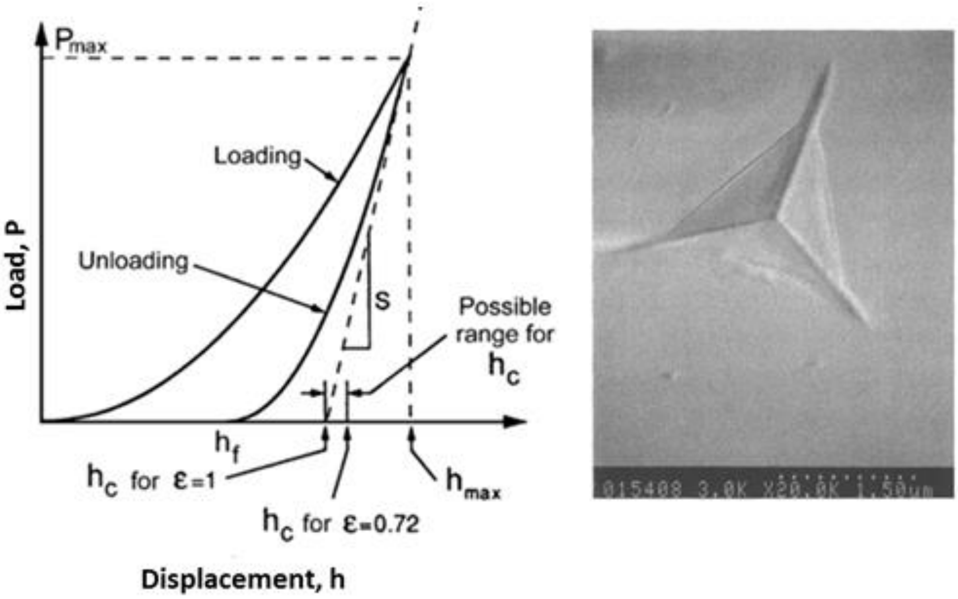

Figure 1.12 A schematic representation of the quantities used in Oliver and Pharr analysis method and the SEM image of the indentation trace performed in fused silica (Oliver and Pharr, 1992)

The procedure adopted is based on the observation that unloading data are well described by a simple power law relation defined by

$$P = B\left(h - h_f\right)^m \tag{1.14}$$

Where the P is the indenter load, h is the elastic displacement of the indenter and the constants B, m and h_f are all determined by a least square fitting procedure. For the theoretical case of indentation in elastic solids, values of the exponent m for some punch geometries varies between 1 for flat cylinders, 2 for cones and 1.5 for paraboloids of revolution and spheres in the limit of smalls displacements. Experimentally, Oliver and Pharr observe that the unloading curve on elastoplastic materials was close to 1.5. Then they deduce that the unloading curve, and thus the elastic return of a Berkovich indenter on elastoplastic material was similar to the unloading curve of a paraboloid indenter on an elastic half space.

The total displacement h showed in figure 8 is written as:

$$h = h_c + h_s \tag{1.15}$$

Where, the term h_c is the vertical distance along contact is made and the term h_s is the displacement of the surface at the perimeter of the contact. A scheme of the different displacement is displayed in figure 1.13.

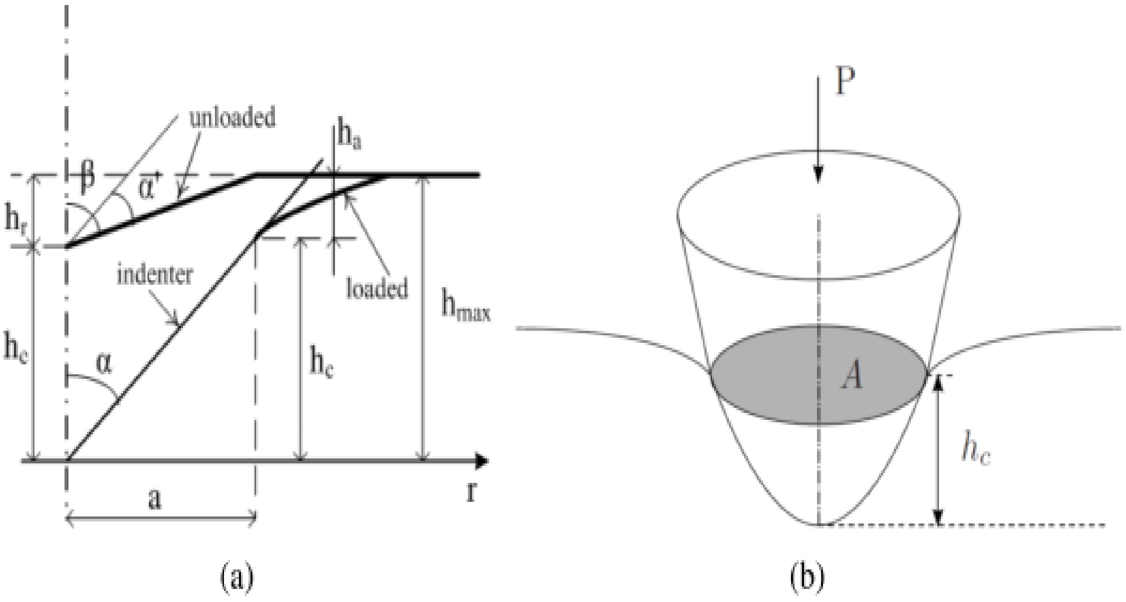

Figure 1.13 A schematic representation of a section through an indentation showing various quantities used in the analysis (Oliver and Pharr, 1992)

To determine the contact depth h_c from the experimental data the follow equation is used

$$h_c = h_{max} - h_s \tag{1.16}$$

Where, h_{max} is the displacement at the peak load. To determine h_c the follow relation is used:

$$h_S = h_{max} - \epsilon \frac{P_{max}}{S} \tag{1.17}$$

Where P_{max} is the peak load value, S is the stiffness and ϵ is a geometrical constant, which values vary according to the indenter geometry to 0.72 for conical indenters, 0.75 for the paraboloids of revolution and 1 for the flat punch in the case of an elastic contact. According to the previous remark, they choose a value of 0.75 in the case of an elastoplastic contact with a Berkovich indenter.

Then, the contact area A for a Berkovich indenter can be computed by using the following relation:

$$A(h_c) = 3\sqrt{3}tan^2\theta = 24.5h_c^2 \tag{1.18}$$

Where, the term θ is the angle formed between the faces of the indenter and the normal to the base.

Then deriving equation (1.14) the experimental measured stiffness S can be assessed

$$\frac{dP}{dh} = S = mB(h - h_f)^{m-1} \tag{1.19}$$

The reduced modulus E_r can be adapted to different shaped tips by adding a correction factor β that depends on the indenter geometry. According to the Oliver and Pharr model, the stiffness can be described by

$$S = 2\beta E^* \sqrt{\frac{A}{\pi}} \tag{1.20}$$

In addition, the reduced modulus E^* is defined as:

$$E^* = \frac{S}{2\beta}\sqrt{\frac{\pi}{A}} \tag{1.21}$$

However, the reduced modulus E_r can be also expressed by

$$\frac{1}{E_r} = \frac{(1-v_s^2)}{E_s} + \frac{(1-v_i^2)}{E_i} \tag{1.22}$$

Where, the E and v are the Young's modulus and Poisson's ratio for the specimen (s) and for the indenter (i).

Finally, with the contact area the hardness can be computed by:

$$H = \frac{P_{max}}{A} \tag{1.23}$$

Where, P_{max} is the maximum indentation load and A is the projected area of the hardness impression.

However, this method is based on a combination of experimental and empirical assumptions. This is why the method proposed by Oliver and Pharr needs to be assumed with precaution especially in the case of low hardness samples.

2. Continuous Stiffness Measurement (CSM)

This method makes possible to measure continuously the contact force and the penetration of the indenter during the nanoindentation test. The principle consists in imposing a small harmonic oscillation on the semistatic force and then a frequency-specific amplifier is used to measure the amplitude and phase of the corresponding displacement of force signal generated by the indenter (Li and Bhushan, 2002; Odegard et al., 2005; Oliver and Pharr, 2004, 1992). A representation of this method is showed in figure 1.14.

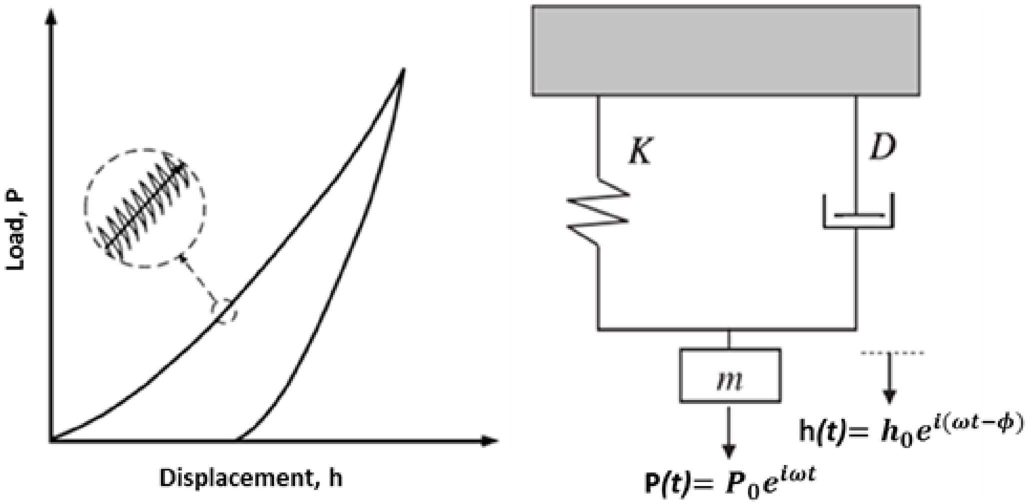

Figure 1.14 CSM method : Imposed signal during the load stage and simple-harmonic oscillator model to represent only the indenter (Hay et al., 2010; Li and Bhushan, 2002).

The main benefits of this method are:

- The ability to measure mechanical properties as a continuous function of distance into the surface (depth profiles of properties).
- The time required for calibration and testing procedures is reduced because there is no need for multiple indentations or unloadings.
- The ability to measure mechanical storage and loss modulus as a function of frequency.
- Improved in situ surface detection and allow avoiding some of the effects of time-dependent plasticity and thermal drift.

The differential equation for harmonic oscillation is given by

$$P(t) = m\ddot{h} + C\dot{h} + Kh(t) \tag{1.24}$$

The imposed force is:

$$P(t) = P_{os}e^{(i\omega t)} \tag{1.25}$$

Where, the term P_{os} is the excitation force amplitude. The response to the indenter displacement is described by

$$h(t) = h_o e^{i(\omega t-\varphi)} \tag{1.26}$$

Where, h_0 is the displacement amplitude and the contact stiffness could be computed from the signal displacement.

From the equation (1.26), the first and second derived respects to *h(t)* are:

$$\dot{h}(t) = h_0 iwe^{i(\omega t-\emptyset)} \tag{1.27}$$

$$\ddot{h}(t) = -h_0\omega^2 iwe^{i(\omega t-\emptyset)} \tag{1.28}$$

Replacing $\ddot{h}(t), \dot{h}(t)$ and $h(t)$ in (1.24) the expression becomes:

$$P_{os}e^{i\omega t} = -mh_0\omega^2 e^{i(\omega t-\emptyset)} + Ch_0 i\omega e^{i(\omega t-\emptyset)} + Kh_0 e^{i(\omega t-\emptyset)} \tag{1.29}$$

When the last expression is multiplied by $e^{i\emptyset}/\left(h_0 e^{i\omega t}\right)$ and the Euler’s law ($e^{i\emptyset} = (cos\emptyset + isin\emptyset)$) is used; then the equation is:

$$\frac{P_{os}}{h_0}(cos\emptyset + isin\emptyset) = -m\omega^2 + iC\omega + K \tag{1.30}$$

Then, dividing the real and the imaginary part of the equation, the following equations are computed:

$$\frac{K-m\omega^2}{cos\emptyset} = \frac{P_{os}}{h_0} \tag{1.31}$$

$$\frac{C\omega}{sin\emptyset} = \frac{P_{os}}{h_0} \tag{1.32}$$

In order to obtain the phase angle $\emptyset$ the equations (1.28) and (1.29) are equalized and the follow equation is acquired:

$$tan\emptyset = \frac{C\omega}{K-m\omega^2} \tag{1.33}$$

Using a simple trigonometric law, the P_{os}/h_0 can be computed by the following expression:

$$\left|\frac{P_{os}}{h_0}\right| = \sqrt{\{K - m\omega^2\}^2 + \omega^2 C^2} \tag{1.34}$$

Where, the term P_{os} is the magnitude of the oscillation force, $h_0(t)$ is the magnitude of the oscillation displacement, ω is the excitation frequency, K is the spring constant and C is the damping coefficient. The figure 1.15 represents the mechanical model of the contact between the indenter and the sample. From this model, the contact stiffness of the system can be computed.

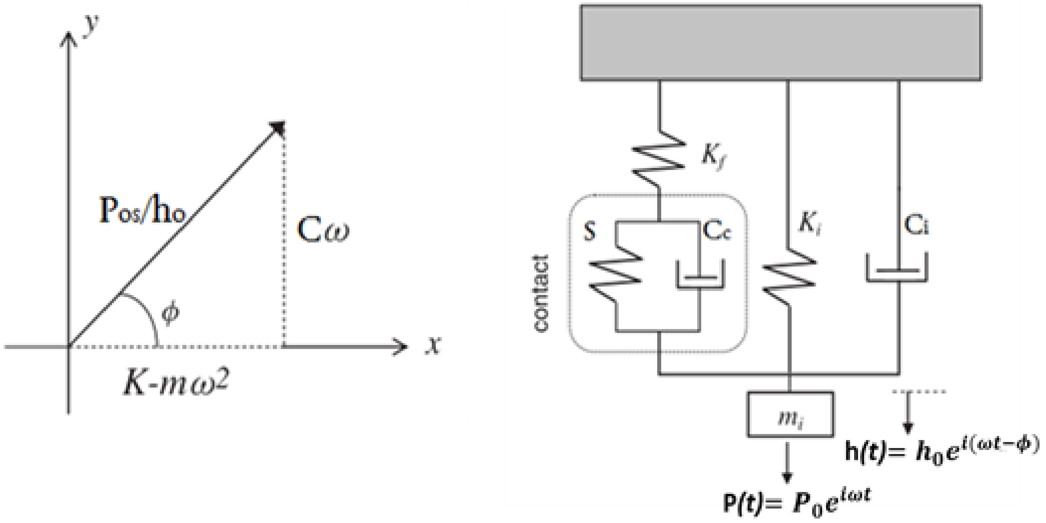

Figure 1.158 Scheme of the CSM model accommodating both instrument and contact (Hay et al., 2010; Li and Bhushan, 2002).

In this mechanical model, the spring constant is described by the expression:

$$K = \left[\frac{1}{S} + \frac{1}{k_f}\right]^{-1} + k_i \tag{1.35}$$

In addition, the damping constant is

$$C = C_i + C_C \tag{1.36}$$

Where, the terms C_i and C_c are the damping constant of the indenter and the sample respectively.

Then the following expression is computed:

$$\left|\frac{P_{os}}{h_0}\right| = \sqrt{\left\{\left(S^{-1} - K_f^{-1}\right)^{-1} + K_i - m\omega^2\right\}^2 + \omega^2 C^2} \tag{1.37}$$

Where, K_f is the stiffness of the indenter frame, K_i is the spring constant of the leaf springs that supports the indenter and S is the contact stiffness. The values of the constants K_f and K_i are characteristic of each nanoindenter and normally are given by the manufacturer.

The phase difference between the signals generated by the force and displacement allows one to compute the new phase angle φ of the system:

$$\tan(\phi) = \frac{\omega C}{\left(S^{-1} - K_f^{-1}\right)^{-1} + K_i - m\omega^2} \tag{1.38}$$

To compute the contact stiffness, the following equation is used:

$$S = \left[\frac{1}{\frac{P_{os}}{h_0}\cos\phi - (K_i - m\omega^2)} - \frac{1}{K_f}\right]^{-1} \tag{1.39}$$

And,

$$\omega C_s = \frac{P_{os}}{h(\omega)}\sin\phi - \omega C_i \tag{1.40}$$

For linear viscoelastic materials, it is convenient to express the overall constitutive behaviour in terms of the complex modulus (Odegard et al., 2005; Sakamoto and Kobayashi, 2009).

$$E^* = E' + iE'' \tag{1.41}$$

The storage modulus E' of the material is determined by:

$$E' = \frac{\sqrt{\pi}}{2\beta}\frac{S}{\sqrt{A}} \tag{1.42}$$

Where A is the projected contact area of the indenter (A=24.56h_c^2), β is the indenter shape factor (Berkovich indenter β = 1.034). Moreover, the loss modulus E'' is characteristic of the internal damping and can be computed as:

$$E'' = \frac{\sqrt{\pi}}{2\beta}\,\frac{\omega C_S}{\sqrt{A}} \tag{1.43}$$

3. Time-dependent mechanical models

Most of the classical nanoindentation analysis methods presented here above, do not consider the effects of the strain rate in the mechanical response of the material. In this order, new mechanical models have been developed in order to reflect the consequences of the strain rate in the mechanical response.

Hereafter, two different methods used to analyse and to quantify the viscoelastic properties of viscous materials are presented. Both of them have been tested and validated in viscous materials and then extended and reported in biological material as bone.

3.1 Visco-Elastic-Plastic (VEP) model

The VEP model combines, in series, three extensive quadratic elements, viscous, elastic, and plastic, to create a time-dependent indentation model which uses a general trapezoidal function (figure 1.16) during the indentation experiments (Oyen, 2005).

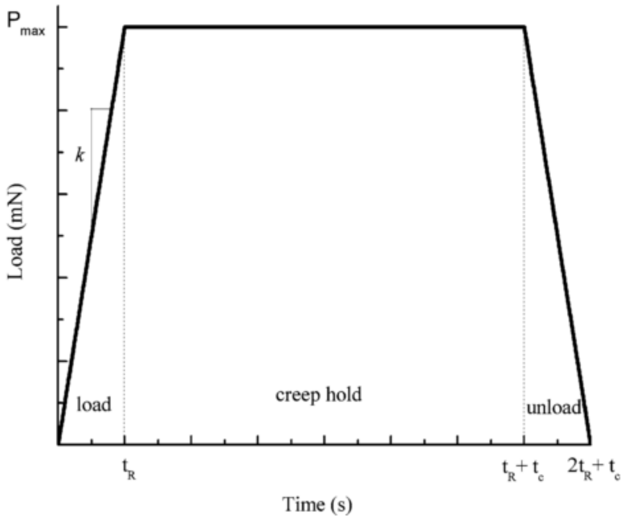

Figure 1.16 Representation of the general trapezoidal function using during indentation experiments (Olesiak et al., 2009)

The VEP model uses a general trapezoidal loading function represented in the figure and the load is proportional to the square of the displacement in conical-pyramidal indentation testing. Equal loads (P) are distributed in the three elements leading to a total displacement that is equivalent to the sum of the displacement of the individual elements (Oyen & Cook, 2003).

$$h = h_e + h_p + h_v \tag{1.44}$$

As the displacement responses are independent under load control and can therefore be separated into elastic, plastic and viscous contributions (Ferguson, 2009). Where each of the deformations can be defined as:

$$h_e = \sqrt{\frac{P_{max}}{\alpha_2 E\prime}} \tag{1.45}$$

$$h_p = \sqrt{\frac{P_{max}}{\alpha_1 H}} \tag{1.46}$$

$$h_v = \sqrt{\frac{P_{max}}{\alpha_3 \eta_Q}}\ (2/3\, t_R + t_c) \tag{1.47}$$

Where P_{max} is the peak load, E' is the plane strain modulus, H is the resistance to plastic deformation, η_Q is the indentation viscosity, t_R and tc stand for the rising time and holding time and $\alpha_{1,2\ and\ 3}$are the dimensionless geometric constant which change according to the tip geometry (for a Berkovich indenter $\alpha_1 = 24.5,\ \alpha_2 = \alpha_3 = 4.4$ (Olesiak et al., 2009; Oyen and Cook, 2003)

Then, by replacing the equations (1.45, 1.46 and 1.47) in equation (1.44) and deriving respect to the time, we obtain the displacement rates of each element. This displacement is described by the follow expression:

$$\frac{dh}{dt} = \frac{dh_e}{dt} + \frac{dh_p}{dt} + \frac{dh_v}{dt} \tag{1.48}$$

This can be rewritten as follow:

$$\frac{dh}{dt} = \frac{1}{P^{1/2}}\frac{dP}{dt}\frac{1}{2(\alpha_2 E^{\prime})^{1/2}} + \frac{1}{P^{1/2}}\frac{dP}{dt}\frac{1}{2(\alpha_1 H)^{1/2}} + \frac{P^{1/2}}{(\alpha_3 \eta_Q)^{1/2}} \tag{1.49}$$

The plane strain modulus (E’) can be related to elastic modulus (E) with a known Poisson’s ratio by:

$$E^{\prime} = \frac{E}{1-v^2} \tag{1.50}$$

Where, E and v are the Young’s modulus and the Poisson’s ratio respectively of the tested sample.

Hardness is the resistance of a material to localized deformation and it can be expressed by:

$$H_c = \frac{P_{max}}{\alpha_1(h_e+h_p+h_v)^2} = \frac{1}{\alpha_1(2t_R/3(\alpha_3\eta_Q)^{-1/2}+(\alpha_2 E^{\prime})^{-1/2}+(\alpha_1 H)^{-1/2})^2} \tag{1.51}$$

Finally, the viscosity term (η_Q) can be assessed by assuming a linear creep rate for the entire hold period and by using only the steady-state creep:

$$h^{CREEP}(t) = \frac{(kt_R)^{1/2}}{(\alpha_3\eta_Q)^{1/2}}(t - t_1) + h(t_1) \tag{1.52}$$

Where k is the constant load and unload rate, t is the total time of the test, t_1 is defined as $t_1 = t_R + t_C/6$ (t_R and t_C were defined above) to only consider the last 5/6 of the holding period and obtain a better fit of the curve (Rodriguez-Florez et al., 2013).

3.2 Creep analysis

Many materials such as metals and plastics exhibit creep under steady load conditions. In an indentation test, creep often manifests itself as a bowing out or “nose” in the unloading portion of the load-displacement curve. This fact makes impossible to obtain a measurement of hardness and modulus of the material since the slope of the unloading response, which is ultimately used to determine the contact area; is affected by creep in the material.

The most common method of measuring creep is to apply a constant load to the indenter and measure the change in depth of the indenter as a function of time. The resulting “creep curve” can then be analysed using conventional spring and dashpot mechanical models.

The term creep is often used to describe a delayed response to an applied stress or strain that may be a result of visco-elastic or visco-plastic deformation. In a nanoindentation test, the depth recorded at each load increment will be, in general, the addition of the elastic-plastic properties of the material and what is occurring during creep, either visco-elastic or visco-plastic (Fischer-Cripps, 2004). Different rheological models could be used to describe this behaviour (figure 1.17).

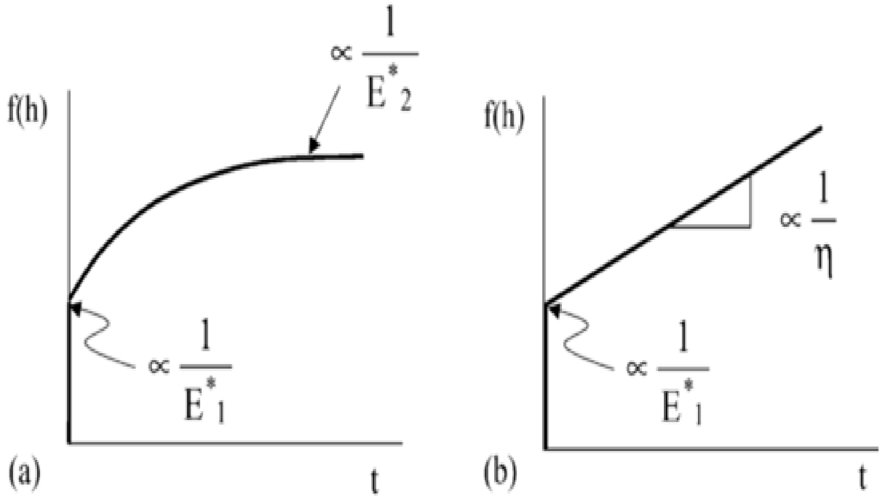

Figure 1.17 Diagram of displacement response according to the creep analysis for a step increase in load for (a) Voigt model (b) Maxwell model. (Fischer-Cripps, 2004)

In Creep analysis, mechanical models as (Maxwell, Voigt) are used to simplify and to represent the stress (hydrostatic compression, tension and shear) present during an indentation test.

To represent these behaviours, the Hertz equation that represents the depth penetration is modified according to the tip geometry with the addition of a time-dependent exponential.

On one hand, by using the three elements Voigt model, the Hertz equation becomes:

For a spherical indenter

$$h^{32}(t) = \frac{3}{4}\frac{P_0}{\sqrt{R}}\left[\frac{1}{E_1^*} + \frac{1}{E_2^*}(1 - e^{-tE_2^*/\eta})\right] \tag{1.53}$$

For a conical indenter

$$h^2(t) = \frac{\pi}{2}P_0 cot\alpha\left[\frac{1}{E_1^*} + \frac{1}{E_2^*}(1 - e^{-tE_2^*/\eta})\right] \tag{1.54}$$

On the other hand, by using the Maxwell model the Hertz equation become

For a spherical indenter

$$h^{32}(t) = \frac{3}{4}\frac{P_0}{\sqrt{R}}\left[\frac{1}{E_1^*} + \frac{1}{\eta}t\right] \tag{1.55}$$

In addition, for a conical indenter:

$$h^2(t) = \frac{\pi}{2}P_0 cot\alpha\left[\frac{1}{E_1^*} + \frac{1}{\eta}t\right] \tag{1.56}$$

In all these equations P_0 is the peak force, α is the equivalent cone semi-angle (70.3° for the Berkovich indenter, see values for other indenters in table….), E1 and E2 are moduli (GPa), η is the long term creep viscosities (GPa.s).

From the above information, it is possible to construct equations and new mechanical models by adding components in series or parallel. For example, for a four elements Burger model, using a conical indenter the initial equation becomes:

$$h^2(t) = \frac{\pi}{2}P_0 cot\alpha\left[\frac{1}{E_1} + \frac{1}{E_2}\left(1 - e^{-tE_2/\eta_1}\right) + \frac{1}{\eta_2}t\right] \tag{1.57}$$

IV. Nanoindentation of bone samples

At the end of the 90's, new mechanical methods as the nanoindentation technique were used to test biological tissues as bone. This technique allowed the quantification of the local mechanical properties of bone at the micro scale. These studies used different experimental conditions and samples preparation to characterize the mechanical response of bone microstructure.

The most common method used to analyse the nanoindentation data is the Oliver and Pharr mechanical method (Oliver and Pharr, 1992). This method is adapted to isotropic elasto-plastic material. It allows one to compute a modulus of elasticity and the hardness of bone material with the assumption that it is a quasi-isotropic non-viscous material.

Using this method, authors such as (Bensamoun et al., 2004b) showed the variation of the mechanical response of bone is caused by the intrinsic heterogeneity of bone. Later, (Bensamoun et al., 2008; Hoc et al., 2006) proved the differences in the mechanical response of osteons with different mineral degrees and highlight the importance of the remodelling process in the mechanical response of bone.

(Fan et al., 2002; Hengsberger et al., 2002; Rho and Pharr, 1999; Rho et al., 2001, 2000, 1997) suggested that mechanical response of bone could vary according to the hydration state of the sample: values of the elastic modulus and hardness could increase between 10% and 17.6% from wet to dry conditions. In addition, they demonstrated the variation of bone mechanical response depending on the test direction (longitudinal, transverse or radial). This bone anisotropic mechanical response reflects the ultrastructural organization of collagen fibrils and mineral crystals within the osteons as well as the lamellar microstructure. The anisotropy ratio for the elastic properties for cortical zone of long bones was found to be within a rank between 1.61 and 1.79 at the macro scale (Ho Ba Tho et al., 1991b; Turner et al., 1995) and between 1.41 and 2.7 at the micro scale (Franzoso and Zysset, 2009; Turner et al., 1999, Vanleene 2006).

Studies demonstrate the viscoelastic and viscoplastic mechanical behaviour of bone at the micro scale (Fan and Rho, 2003; Vanleene et al., 2006). Because of the nature of viscoelasticity and time-dependent plasticity of bone material, it is believed that the load-time sequence affects nanoindentation measurements, however most previous studies did not take into account viscoelasticity and time-dependent plasticity. They showed that mechanical properties of bone increase or decrease according to the hold time and strain rate used through the nanoindentation tests. This time-dependent mechanical behaviour of bone could be due to the collagen fibres and fluid layers presents within the bone matrix. These results stress the need for developing new methods to assess mechanical properties from nanoindentation experiments taking into account the time-dependent behaviour.

These results demonstrate that new methods were needed to describe the viscous properties of bone. As far as we know, (Oyen and Cook, 2003) were one of the first to use a rheological method to investigate the time-dependent mechanical response of polymers during nanoindentation experiments. This method was used to assess the time-dependent behaviour of biological materials such as healing bone (Oyen and Ko, 2007) and cortical bone (Olesiak et al., 2009; Michelle L Oyen, 2006; Rodriguez-Florez et al., 2013). Another studies investigated the viscoelastic responses on cortical and trabecular bones (Isaksson et al., 2010a, 2010b). Nevertheless, all these studies demonstrated that different time-dependent methods could be developed and adapted depending on one’s research interests.

At the micro scale, nanoindentation technique has been used for different authors to compute the anisotropy ratio of each microstructural component of the cortical bone.

A briefly review of the values reported for the anisotropy ratio, elastic modulus, hardness, and some time-dependent mechanical properties for human, bovine and rat bones assessed by nanoindentation are summarized in the Tables 1.7 to 1.11.

Table 1.7 Anisotropy ratios for human cortical bone at the micro scale.

Author	Anatomical origin	Microstructural zone	Anisotropy ratio
(Turner et al. 1999)	Human Femur	Lamellar bone	E_{LONG}/E_{TRANS}= 1.41
(Franzoso and Zysset. 2009)	Human Femur	Secondary osteons	E_{LONG}/E_{RAD} = 2.69 E_{LONG}/E_{TRANS} = 1.43 E_{TRANS}/E_{RAD} = 1.89
(Fan et al., 2002)	Human Tibia	*Lamellar bone	E_{LONG}/E_{RAD}=1.38 E_{LONG}/E_{TRANS} = 1.47 E_{TRANS}/E_{RAD} = 0.94
		*Osteons	E_{LONG}/E_{RAD} =1.51, E_{LONG}/E_{TRANS} = 1.48 E_{TRANS}/E_{RAD} = 1.02
(Vanleene, 2006)	Human Femur	Lamellar bone	E_{LONG}/E_{RAD}=1.50 E_{LONG}/E_{TRANS} = 1.36 E_{TRANS}/E_{RAD} = 1.10
		Osteons	E_{LONG}/E_{RAD} =0.98 E_{LONG}/E_{TRANS} = 1.18 E_{TRANS}/E_{RAD} = 1.19

LONG= Longitudinal, TRANS= Transverse, RAD= Radial.
The * signals the values reported before algorithm of structural fusion between lamellar bone and osteons.

Table 1.8 Mechanical properties of human cortical bone assessed by nanoindentation by using the Oliver-Pharr model

Reference	Specie	Anatomical origin	Test direction	Test condition	Elastic Modulus (GPa)	Hardness (GPa)
(Rho et al., 1997)	Human	Tibia	Longitudinal	Dry + epoxy resin	$E_{LONG\_OST} = 22.5 \pm 1.3$ $E_{LONG\_INTL} = 25.8 \pm 0.7$	$H_{LONG\_OST} = 0.614 \pm 0.04$ $H_{LONG\_INTL} = 0.736 \pm 0.03$
(Rho et al., 1999)	Human	Tibia	Longitudinal	Dry + epoxy resin	$E_{LONG\_OST} = 22.4 \pm 1.2$ $E_{LONG\_INTL} = 25.7 \pm 1.0$	$H_{LONG\_OST} = 0.617 \pm 0.04$ $H_{LONG\_INTL} = 0.736 \pm 0.03$
*****(Fan and Rho, 2003)	Human	Tibia	Longitudinal	Dry + epoxy resin	$E_{LONG\_OST\_fc} = 23.4 \pm 1.3$ 26.8 ± 2.6	N/A
(Goodwin and Sharkey, 2002)	Human	Tibia and first metatarsal	Longitudinal	Dry	$E_{LONG\_OST\_tib} = 17.8 \pm 1.7$ $E_{LONG\_INTL\_tib} = 20.1 \pm 1.7$ $E_{LONG\_OST\_met} = 16.9 \pm 1.0$ $E_{LONG\_INTL\_met} = 19.8 \pm 1.2$	N/A
(Roy et al., 1999)	Human	Vertebra	Longitudinal and transverse	Dry + epoxy resin	$E_{LONG} = 18.1 \pm 2.7$ $E_{TRANSV} = 16.9 \pm 3.2$	$H_{LONG} = 0.549 \pm 0.07$ $H_{TRANSV} = 0.542 \pm 0.10$
(Dall'Ara et al., 2012)	Human	Vertebra	Longitudinal	Wet + epoxy resin	$E_{INTL} = 13.2 \pm 4.4$ $E_{OST} = 10.9 \pm 3.8$	$H_{LONG} = 0.447 \pm 0.20$ $H_{TRANSV} = 0.378 \pm 0.17$

LONG= Longitudinal, TRANS= Transverse, INTL= Interstitial lamellae and OST= Osteons, ANT= Anterior, POST= Posterior, LAT= Lateral.
The *= in this study due to its experimental conditions (different max loads), the elasticity or hardness values were reported as a range and not as mean

Table 1.8 (continue) Mechanical properties of human cortical bone assessed by nanoindentation by using the Oliver-Pharr model

Reference	Specie	Anatomical origin	Test direction	Test condition	Elastic Modulus (GPa)	Hardness (GPa)
(Turner et al., 1999)	Human	Femur	Longitudinal and transverse	Dry + epoxy resin	E_{LONG} = 23.5 ± 0.2 E_{TRANSV} = 16.6 ± 0.3	N/A
(Rho et al., 2000)	Human	Femur	Longitudinal	Dry + epoxy resin	$E_{LONG\_OST\_inner}$= 20.8 ± 1.3 $E_{LONG\_OST\_outer}$= 18.8 ± 1.0 E_{LONG_INTL}= 26.1 ± 1.8	$H_{LONG\_OST\_inner}$ = 0.65 ± 0.06 $H_{LONG\_OST\_outer}$ = 0.55 ± 0.05 H_{LONG_INTL}= 0.80 ± 0.09
(Hengsberger et al., 2001)	Human	Femur	Longitudinal	Dry + epoxy resin	E_{LONG_OST} = 18.0 ± 1.7	H_{LONG_OST} = 0.6 ± 0.1
*****(Hengsberger et al., 2002)	Human	Femur	Longitudinal	Dry + epoxy resin and Wet	$E_{LONG\_OST\_dry}$= 11.1 to 31.6 $E_{LONG\_OST\_wet}$= 7.4 ± 0.5 18.5 ± 4.9	$H_{LONG\_OST\_dry}$= 0.48 ± 0.1 1.25 ± 0.26 $H_{LONG\_OST\_wet}$= 0.29 ± 0.13 0.95 ± 0.44
(Bensamoun et al., 2008)	Human	Femur	Longitudinal	Dry	$E_{LONG\_OST\_W}$ = 21.3 ± 3.0 $E_{LONG\_OST\_G}$ = 19.3 ± 1.8 $E_{LONG\_OST\_B}$ = 13.0 ± 2.7	$H_{LONG\_OST\_W}$ = 0.55 ± 0.15 $H_{LONG\_OST\_G}$ = 0.41 ± 0.09 $H_{LONG\_OST\_B}$ = 0.30 ± 0.10

LONG= Longitudinal; INTL= Interstitial lamellae; OST= Osteons; ANT= Anterior; LAT= Lateral; W=White; G=Grey; B= Black; fc= function C
The * in this study is because of its experimental conditions (different max loads); the elasticity or hardness values were reported as a range and not as mean values.

Table 1.9 Mechanical properties of bovine and rat cortical bone assessed by nanoindentation by using the Oliver-Pharr model

Reference	**Specie**	**Anatomical origin**	**Test direction**	**Test condition**	**Elastic Modulus (GPa)**	**Hardness (GPa)**
(Tai et al., 2005)	Bovine	Tibia	Transversal	Dry	$E_{TRAN\_58\%miner} = 12.9 \pm 2.9$ $E_{TRANS\_0\%\ miner} = 1.9 \pm 0.1$	N/A
(Wang et al., 2006)	Bovine	Tibia	Longitudinal and transverse	Dry + epoxy resin	$E_{LONG\_OST} = 24.7 \pm 2.5$ $E_{LONG\_INTL} = 30.1 \pm 2.4$ $E_{TRANSV} = 19.8 \pm 2.4$	$H_{LONG\_OST} = 0.811 \pm 0.155$ $H_{LONG\_INTL} = 0.892 \pm 0.113$ $H_{TRANSV} = 0.647 \pm 0.06$
(Rho and Pharr, 1999)	Bovine	Femur	Longitudinal	Wet / dry	$E_{LONG\_OST\_wet} = 21.1 \pm 2.0$ $E_{LONG\_INTL\_wet} = 24.4 \pm 2.2$ $E_{LONG\_OST\_dry} = 24.2 \pm 2.2$ $E_{LONG\_INTL\_dry} = 27.5 \pm 1.2$	$H_{LONG\_OST\_wet} = 0.578 \pm 0.05$ $H_{LONG\_INTL\_wet} = 0.730 \pm 0.05$ $H_{LONG\_OST\_dry} = 0.680 \pm 0.1$ $H_{LONG\_INTL\_dry} = 0.818 \pm 0.05$
(Hoc et al., 2006)	Bovine	Femur	Longitudinal	Dry	$E_{LONG\_OST} = 19.3$	N/A
(Jämsä et al., 2002)	Rat	Femur and tibia	Longitudinal	Dry	$E_{LONG\_femur} = 19.9 \pm 2.1$ $E_{LONG\_tibia} = 22.39 \pm 0.8$	$H_{LONG\_femur} = 0.795 \pm 0.02$ $H_{LONG\_tibia} = 0.823 \pm 0.05$
(Hengsberger et al., 2005)	Rat	Vertebrae	Longitudinal	Dry	$E_{LONG\_POST} = 19.0 \pm 1.3$ $E_{LONG\_LAT} = 19.5 \pm 1.8$ $E_{LONG\_ANT} = 15.2 \pm 1.9$	$H_{LONG\_POST} = 0.89 \pm 0.07$ $H_{LONG\_LAT} = 0.87 \pm 0.08$ $H_{LONG\_ANT} = 0.67 \pm 0.09$
(Vanleene, 2006)	Rat	Femur	Longitudinal	Dry + fixed by resin	$E_{LONG\_1month} = 20.7 \pm 2.1$ $E_{LONG\_9months} = 28.8 \pm 2.4$	N/A

LONG= Longitudinal, TRANS= Transverse, INTL= Interstitial lamellae and OST= Osteons, ANT= Anterior, POST= Posterior, LAT= Lateral.

Table 1.10 Mechanical properties of cancellous bone assessed by nanoindentation

Reference	Specie	Anatomical origin	Test direction	Test condition	Elastic Modulus (GPa)	Hardness (GPa)
(Rho et al., 1997)	Human	Vertebrae	Transverse	Dry + epoxy resin	$E_{TRANSV} = 13.4 \pm 2.0$	$H_{TRANSV} = 0.468 \pm 0.08$
(Rho et al., 1999)	Human	Vertebrae	Longitudinal Transverse 1 Transverse 2	Dry + epoxy resin	$E_{LONG} = 19.4 \pm 2.3$ $E_{TRANSV1} = 16.6 \pm 1.1$ $E_{TRANSV2} = 15.0 \pm 2.5$	$H_{LONG} = 0.618 \pm 0.06$ $H_{TRANSV1} = 0.564 \pm 0.03$ $H_{TRANSV2} = 0.515 \pm 0.08$
(Roy et al., 1999)	Human	Vertebrae	Longitudinal Transverse	Dry + epoxy resin	$E_{LONG\_axial} = 18.0 \pm 2.2$ $E_{TRANSV\_axial} = 22.7 \pm 3.1$ $E_{LONG\_radial} = 16.3 \pm 2.4$ $E_{LONG\_circumf} = 15.7 \pm 1.5$	$H_{LONG\_axial} = 0.572 \pm 0.107$ $H_{TRANSV\_axial} = 0.664 \pm 0.098$ $H_{LONG\_radial} = 0.553 \pm 0.088$ $H_{LONG\_circumf} = 0.553 \pm 0.063$
(Hengsberger et al., 2005)	Rat	Vertebrae (SHAM method)	Longitudinal	Dry	$E_{LONG\_posterior} = 21.8 \pm 1.6$ $E_{LONG\_lateral} = 20.5 \pm 1.2$ $E_{LONG\_anterior} = 15.41 \pm 2.2$	$H_{LONG\_posterior} = 1.02 \pm 0.06$ $H_{LONG\_lateral} = 0.92 \pm 0.04$ $H_{LONG\_anterior} = 0.60 \pm 0.07$
(Wang et al., 2006)	Bovine	Vertebrae	Longitudinal Transverse	Dry + epoxy resin	$E_{LONG} = 20.0 \pm 2.0$ $E_{TRANSV} = 14.7 \pm 1.9$	$H_{LONG} = 0.53 \pm 0.09$ $H_{TRANSV} = 0.41 \pm 0.06$

LONG= Longitudinal, TRANS= Transverse

Table 1.11 Values of the time-dependent mechanical properties of cortical bone by nanoindentation using (*Different strain rates), (ViscousElasticPlastic model) and (*** Creep analysis)**

Reference	Specie and Anatomical origin	Test direction	Test condition	Elastic Modulus (GPa)	Hardness (GPa)	Viscoelasticity ($x10^{15}$) ($Pa.s^2$)
*****(Fan and Rho, 2003)	Human tibia	Longitudinal	Dry + epoxy resin	$\dot{\varepsilon} = 0.0003s^{-1}$ $E_{OST=}$ 18.6 to 22.7 $\dot{\varepsilon} = 0.03s^{-1}$ $E_{OST=}$ 30.4 to 32.2	N/A	N/A
*****(Vanleene et al., 2006)	Human femur, lateral and medial	Longitudinal	Dry	$\dot{\varepsilon} = 0.005s^{-1}$ $E_{MD\_INTL=}$ 21.1 ± 2.0 $E_{LT\_INTL=}$ 22.2 ± 2.1 $\dot{\varepsilon} = 0.05s^{-1}$ $E_{MD\_INTL=}$ 22.3 ± 2.2 $E_{LT\_INTL=}$ 24.3 ± 1.6 $\dot{\varepsilon} = 0.5s^{-1}$ $E_{MD\_INTL=}$ 24.4 ± 1.9 $E_{LT\_INTL=}$ 25.0 ± 3.1	$\dot{\varepsilon} = 0.005s^{-1}$ $H_{MD\_INTL=}$ 0.5 ± 0.1 $H_{BF\_INTL\,=}$ 0.7 ±0.1 $\dot{\varepsilon} = 0.05s^{-1}$ $H_{MD\_INTL=}$ 0.7 ± 0.1 $H_{BF\_INTL\,=}$ 0.9 ±0.1 $\dot{\varepsilon} = 0.5s^{-1}$ $H_{MD\_INTL=}$ 0.9 ± 0.1 $H_{BF\_INTL\,=}$ 1.0 ±0.1	N/A
******(Oyen and Ko, 2007)	Miniswine Jaw	Longitudinal	Dry + epoxy resin	E_{VEP} = 21.6	H_{VEP} = 0.43	η_{QVEP} = 0.1 to 1

INTL= Interstitial lamellae and OST= Osteons

Table 1.11 (Continue) Values of the time-dependent mechanical properties of cortical bone by nanoindentation using (*Different strain rates), (ViscousElasticPlastic model) and (*** Creep analysis)**

Reference	Specie and Anatomical origin	Test direction	Test condition	Elastic Modulus (GPa)	Hardness (GPa)	Viscoelasticity($x10^{15}$) (Pa.s²)
**(Olesiak et al., 2009)	Porcine Jaw (PJ) Bovine Femur (BF) Porcine Tibia (PT)	Longitudinal	N/A	$E_{PJ} =$ 17.8 ± 2.7 $E_{BF\_INTL}=$ 24.8 ± 3.1 $E_{BF\_OST} =$ 22.6 ± 2.8 $E_{PT\_INTL} =$ 23.0 ± 1.8 $E_{PT\_OST} =$ 22.8 ± 2.6	$H_{PJ} =$ 0.51 ± 0.08 $H_{BF\_INTL} =$ 0.79 ±0.06 $H_{BF\_OST} =$ 0.80 ±0.06 $H_{PT\_INTL} =$ 0.61 ±0.1 $H_{PT\_OST} =$ 0.72 ±0.1	$\eta_{QPJ} =$ 6.29±3.01 $\eta_{QBF\_INTL} =$ 9.45±1.01 $\eta_{QBF\_OST} =$ 9.24±1.08 $\eta_{QPT\_INTL} =$ 4.90±0.98 $\eta_{QPT\_OST} =$ 5.53±1.24
***(Isaksson et al., 2010a)	Rabbit femur	Longitudinal	N/A	$E_{reduced} =$ 24 to 36 $E_{ve1} =$ 14 to 25 $E_{ve2} =$ 90 to 160	H = 0.95 to 1.3	$\eta_{ve1} =$ 400 to 800 ‡ $\eta_{ve2} =$ 10 to 28 ‡
**(Rodriguez-Florez et al., 2013)	Mice femur	Longitudinal	Dry epoxy + wet epoxy	$E_{dry} =$ 33.7 ± 6.4 $E_{wet} =$ 27.5 ± 6.5	$H_{dry} =$ 0.75 ± 0.16 $H_{wet} =$ 0.26 ± 0.04	$\eta_{Qdry} =$ 2.53 ± 1.62 $\eta_{Qwet} =$ 0.50 ± 0.28

‡ Viscous units reported by (Isaksson et al., 2010a) are (GPa.s) for η_{ve1} and ($x10^3$ GPa.s) for $\eta_{ve2,}$ INTL= Interstitial lamellae and OST= Osteons

From the data reported in these tables, one could identify that as occurred at the macro scale, the mechanical response of bone has a strong dependency on the load direction. Variations in the mechanical response are mostly due to the indentation zone (osteons or interstitial lamellae) or to the hydration state (wet or dry). In contrast, the difference in the mechanical response between cortical and cancellous bone is less manifested at the micro scale and due to possible to decrease in the local porosity. Moreover, even if the analysis method used to compute the mechanical properties is different, most of the studies reported using nanoindentation tests have been carried out in the longitudinal direction of bone axis under dry conditions. In addition, the anisotropy ratio at the micro scale has been reported for the $E_{LONG}/E_{TRANS\_OR\_RAD}$ relationship to be in a range between 1.38 and 1.50 for lamellar bone and between 0.98 and 2.69 for osteons.

Whatever the anatomical origin of the cortical bone (long bone or vertebra), the elastic properties and hardness computed in the longitudinal or transverse direction, stay in a very close range. Nevertheless, it is necessary to precise that results of the indentation tests performed at any direction do not reflect the mechanical properties at the tested direction. On the contrary, the results allow us to assess the apparent mechanical properties that are a combination of the mechanical properties of the three directions.

In the longitudinal direction under dry conditions the values for the elastic properties for human cortical bone vary between 16.1 and 25.8 GPa in the osteonal zone and between 15.1 and 26.1 GPa in the lamellar bone. Hardness values vary between 0.30 and 0.65 GPa for the osteonal zone and between 0.51 and 0.80 GPa for the lamellar bone.

In the case of bovine cortical bone, the elastic values vary between 19.3 and 24.7 GPa in the osteonal zone and between 27.5 and 30.1 GPa in the lamellar bone; meanwhile hardness values vary between 0.68 and 0.81 GPa in the osteonal zone and between 0.82 and 0.89 for the lamellar bone.

For rat cortical bone, results reported were computed in the lamellar zone of the cortical shell. Thus, the elastic values vary between 15.2 and 28.8 GPa meanwhile the hardness values vary between 0.67 and 0.89 GPa.

The number of studies performed to characterize the time-dependent mechanical properties is less significant than those carried out with the classical methods. From the data reviewed in the Table 1.11, it should be noted that the mechanical methods used to assess the time-dependent mechanical properties, compute only the viscous-elastic-plastic response of the material. They are not able to discriminate the viscoelastic and the viscoplastic responses of the material.

C. Atomic Force Microscopy

I. Generalities

The Atomic Force Microscope AFM or Scanning Force Microscopy SFM is one of the families of scanning probe microscopes and is widely used in biological applications. It was developed by Binnig, Quate and Gerber in 1986. The general principle consists in using the weak interaction forces (van der Waals forces, capillary forces, steric repulsion, electrostatic, magnetic, etc.) created between the specimen surface and the probe mounted at the end of a cantilever in order to obtain topographic images. The basic idea behind AFM is to scan a sharp tip over the surface of a sample, while sensing the interaction force between the tip and the sample. This allows three-dimensional images to be generated directly in aqueous solution or environmental conditions. The sample is mounted on a piezoelectric scanner that ensures three-dimensional positioning with high accuracy. While the tip (or sample) is being scanned in the (x, y) directions, the force interacting between the tip and the specimen is monitored with piconewton sensitivity. This force is measured by the deflection of a soft cantilever which is detected by a laser beam focused on the free end of the cantilever and reflected into a photodiode (El Kirat et al., 2010). Depending on the cantilever deflection, the position of the reflected beam changes. The photodetector converts this change in an electrical signal (figure 1.18). AFM can be also used to perform indentation tests and to manipulate atoms and structures on a variety of surfaces.

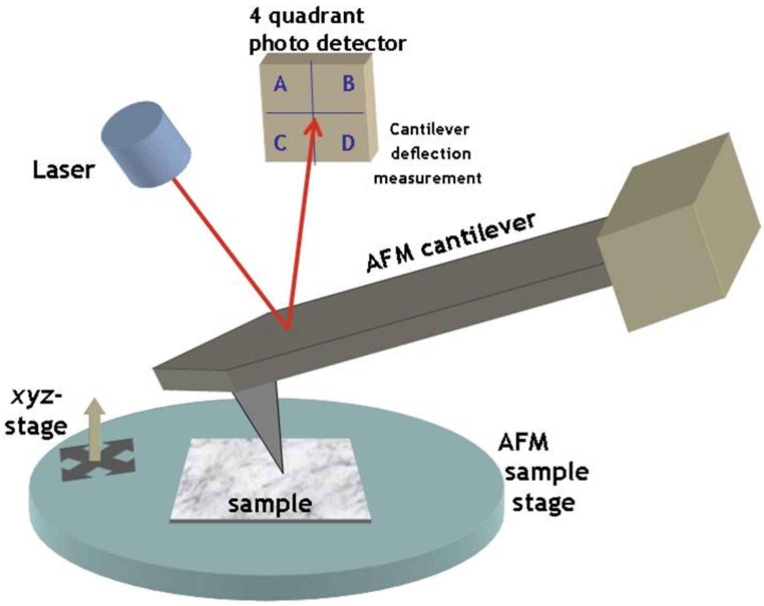

Figure 1.18 Typical atomic force microscope (AFM) setup: The deflection of a micro fabricated cantilever with a sharp tip is measured by reflecting a laser beam off the backside of the cantilever while it is scanning over the surface of the sample. (Open source Handbook of Nanoscience and Nanotechnology)

The principal advantages are that AFM scans very small areas of the material, it can characterize non-conductive electrical surfaces, AFM provides three-dimensional surface profile and the image resolution is more than 1000 times better than the optical diffraction limit.

II. Imaging modes

Different AFM imaging modes are available, which differ mainly in the way the tip is moving over the sample (El Kirat et al., 2010). They can be selected according to the specimen characteristic, imaging conditions (ambient or liquid environment) and the nature of the tip motion. The commons operation modes are briefly summarized hereafter:

1 Contact mode

In contact mode, the tip is pulled across the surface of the sample and the contours of the surface are measured either using the deflection of the cantilever directly or using the feedback signal required to keep the cantilever at a constant z-position or at constant force. Close to the surface of the sample, attractive forces can be quite strong, causing the tip to "snap-in" contact with the surface. Thus, contact mode AFM is usually done at a depth where the overall force is repulsive, that is, in firm "contact" with the solid surface below any adsorbed layers (figure 1.19). The detection system measures the cantilever response as the tip is moved over the surface by the scanning system.

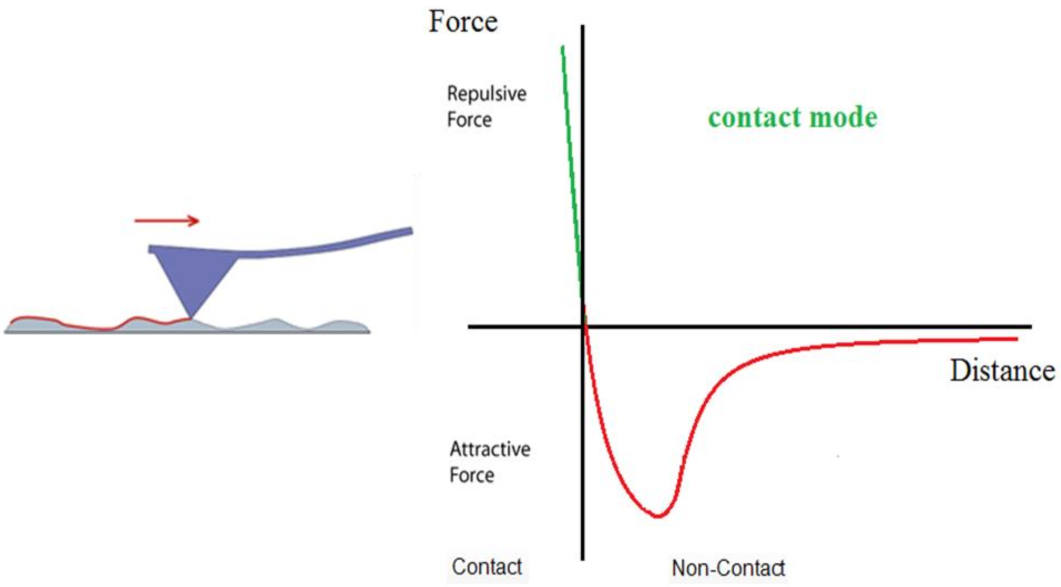

Figure 1.19 Scheme of the contact AFM mode and the typical force-distance curve

2 Tapping mode

This method is widely used and can give a combination of the benefits of the other modes. This method of "tapping" lessens the damage done to the surface and the tip compared to the contact mode. The cantilever oscillates and the tip makes repulsive contact with the surface of the sample at the lowest point of the oscillation. The lateral forces can be much lower than contact mode, since the proportion of the time where the tip and sample are in contact is quite low (Geisse, 2009).

In tapping mode, the cantilever is driven to oscillate up and down at near its resonance frequency by a small piezoelectric element mounted in the AFM tip holder. The interaction of forces acting on the cantilever when the tip comes close to the surface cause the amplitude of this oscillation to decrease as the tip gets closer to the sample. An electronic device uses the piezoelectric actuator to regulate the height of the cantilever above the sample. Then this device adjusts the height to maintain constant cantilever oscillation amplitude while the cantilever is scanned over the sample. A tapping AFM image is therefore produced by the corresponding z-position of the tip or the piezoelectric in relation to the sample (figure 1.20). In multimode AFM is the sample that moves in the z-axis meanwhile in dimension AFM is the tip, which change their position in the z-axis.

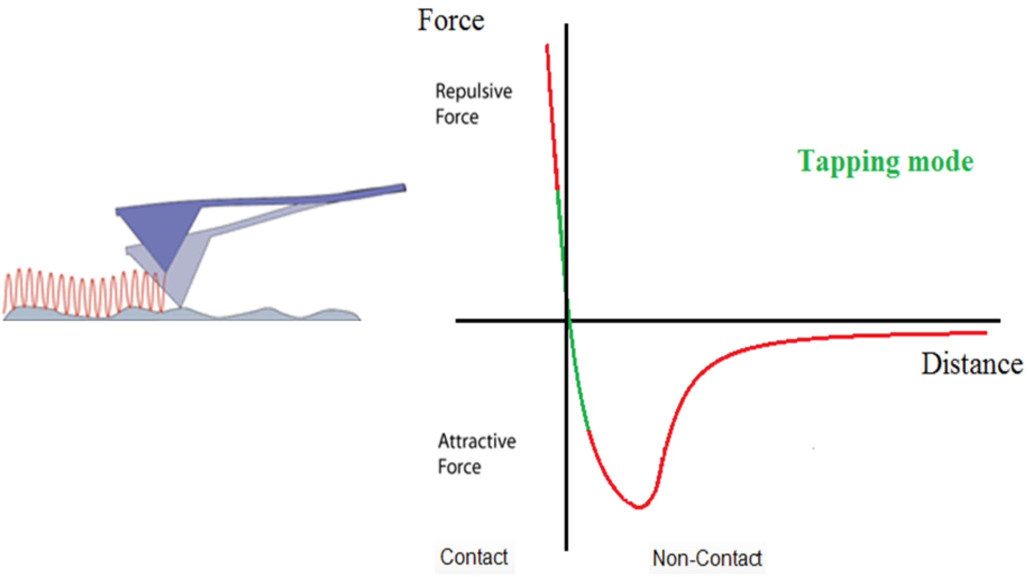

Figure 1.20 Scheme of the tapping AFM mode and the typical force-distance curve

3 Non-contact mode

In non-contact mode, the cantilever oscillates close to the sample surface, but without making contact with the surface. The cantilever is instead oscillated at either its resonant frequency (frequency modulation) or just above (amplitude modulation) where the amplitude of oscillation is typically a few nanometres (figure 1.21) (Gross et al., 2009).

This mode is not so widely used, since the attractive force means that there is a possibility of the tip jumping into contact with the surface. The capillary force makes this particularly difficult to control in ambient conditions. Very stiff cantilevers are needed so that the attraction does not overcome the spring constant of the cantilever, but the lack of contact with the sample means that this mode should cause the least disruption.

Non-contact mode AFM does not suffer from tip or sample degradation effects that are sometimes observed after taking numerous scans with contact AFM. This makes non-contact AFM preferable to contact AFM for measuring soft samples, e.g., biology sample and organic thin film. In the case of rigid samples, contact and non-contact images may look the same. However, if a few monolayers of adsorbed fluid are lying on the surface of a rigid sample, the images may look quite different.

.

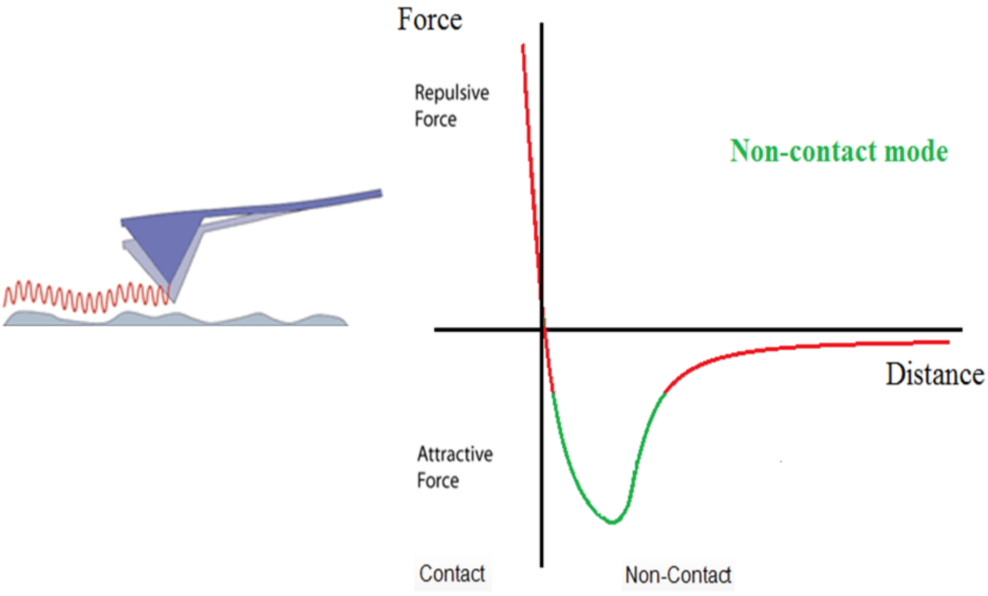

Figure 1.21 Scheme of the Non-contact AFM mode and the typical force-distance curve

4. Dilation phenomenon in AFM imaging

A dilation loosely called tip "convolution" is a spurious phenomenon in AFM imaging. This phenomenon affects the AFM images' accuracy and it could induce miscalculations in the information obtained from the particle analyses. The dilation manifests itself in a broadening of the lateral dimensions of the surface topography. Tip-induced distortions are significant whenever the specimen contains features with aspect ratios comparable to the tips. Imaging very sharp vertical surfaces (those with high relief) is influenced by the sharpness of the tip. Only a tip with sufficient sharpness and aspect ratio can property image a given vertical or horizontal profile (Villarrubia, 1997; Wong et al., 2007).

An example of tip dilation is represented in figure 1.22. This figure show how AFM images information could be affected by the condition of the tip and the dilation of the tip-surface interaction.

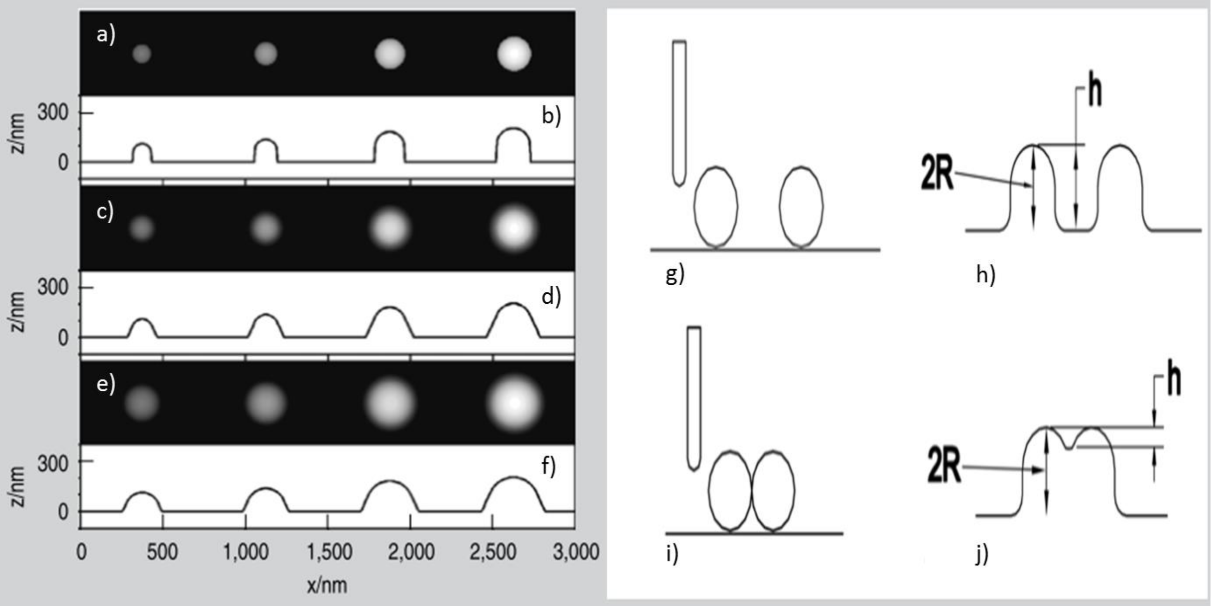

Figure 1.22 Scheme of Line profiles—b), d), and f) and simulated topographical images a, c, and e for four different diameter spheres scanned with three different types of probes (ideal tip (a), conical tip with 6-nm apex radius (c) and tip with 50-nm apex radius (e). Images (g) and (i) show probe gliding over two spheres. The size of probe is smaller than the diameter of particles. In (g) and (h) the particles are far apart. In (i) and (j) the particles are touching. (Wong et al., 2007)

To avoid the "deconvolution" issue, it is necessary the treatment of the tip-surface interaction by a geometrical exclusion known as tip erosion. To perform this task, several algorithms could be used for these geometrical simplifications. These algorithms make possible to calculate an image given a specimen and the tip dilation or tip erosion; the reconstruction of the specimen surface or the tip shape (Markiewicz and Goh, 1995;

Villarrubia, 1997). A sketch of AFM images topography change before and after tip "deconvolution" is presented in figure 1.23.

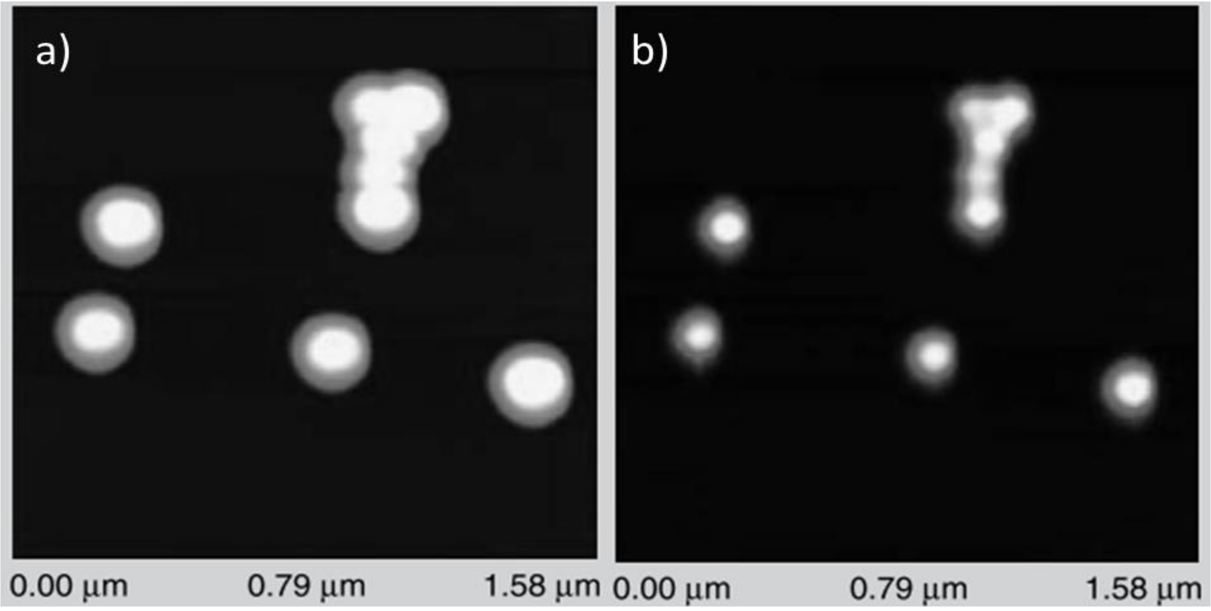

Figure 1.23 Comparison of the AFM topography data a) before and b) after tip deconvolution. (Wong et al., 2007)

III. Mechanical characterization by AFM

In the recent years, Atomic Force Microscope (AFM) for nanoindentation has arisen as a new option to quantify the mechanical properties like the elastic modulus and hardness for thin layers and biological samples (cells, tissues) (Monclus et al., 2010; Strasser et al., 2007; Wenger et al., 2007). To calculate the parameter of interest various models are used, but the most of them are based on the Hertz model assuming only a purely elastic contact. These models are extended to match the experimental conditions concerning the indenters' shape or the thickness of the sample. Normally, the measured force in an AFM indentation test follow the Hooke's law and it could be obtained by multiplying the known spring constant of the cantilever k_c and its deflection d.

$$F = k_c d \tag{1.58}$$

However, this operation is far to be simple because spring constant values provided by manufactures are not accurate. This is due to the difficulty in controlling all cantilevers' thickness with a narrow tolerance during the manufacturing process. In the following section, the parameters to determine the material mechanical properties will be briefly described.

1 Measurement of the spring constant

Over the last 20 years several calibration methods have been proposed to measure the cantilevers spring constants (Hutter and Bechhoefer, 1993; Sader et al., 1999). Here, the most commons methods used to achieve it are presented.

1.1 Dimensional method (Euler's Formula)

This method requires the knowledge of the cantilevers' material Young's modulus and physical dimensions. If the cantilever beams look like a diving board, the spring constant can be analytically obtained using relatively simple mechanics. The cantilever beam is of uniform cross section and carries a load, F, at its free end. By assuming a small vertical deflection, the deflection z, at the end of the cantilever could be calculated to be

$$z = \frac{FL^3}{3EI} \tag{1.59}$$

Where, the term L is the length of the cantilever, E is Young's modulus and I is the moment of inertia. For a rectangular cross section cantilever of width, w and thickness, t, I is given by

$$I = \frac{1}{12} wt^3 \tag{1.60}$$

The spring constant for the rectangular beam is defined by k = F/z and hence is expressed as a simple closed form as follows:

$$k = \frac{Ew}{4}\left(\frac{t}{L}\right)^3 \tag{1.61}$$

According to the literature, this equation is only applicable to cantilevers where w<<L since the bowing of the cantilever across the width is ignored (Kim et al., 2010). In case of cantilevers with more complex geometries, the spring constant can be estimated by using the Parallel Beam Approximation (PBA) or finite element analysis.

1.2 Cantilever On Cantilever (COC) Method

This method needs a reference cantilever for which the spring constant is known. In practice the reference cantilever is used to calibrate all other cantilevers by pressing them against the reference cantilever (Butt et al., 2005). This method is composed by two steps. In the first one, the “unknown” cantilevers are mounted on a piezoelectric translator and it is pushed against a flat and hard surface. The slope, S_h, stands for the cantilever deflection when the “unknown” cantilever is in contact with the hard surface. On the second one, the end of the unknown cantilever is landed to the end of the reference cantilever as show in figure 1.24.

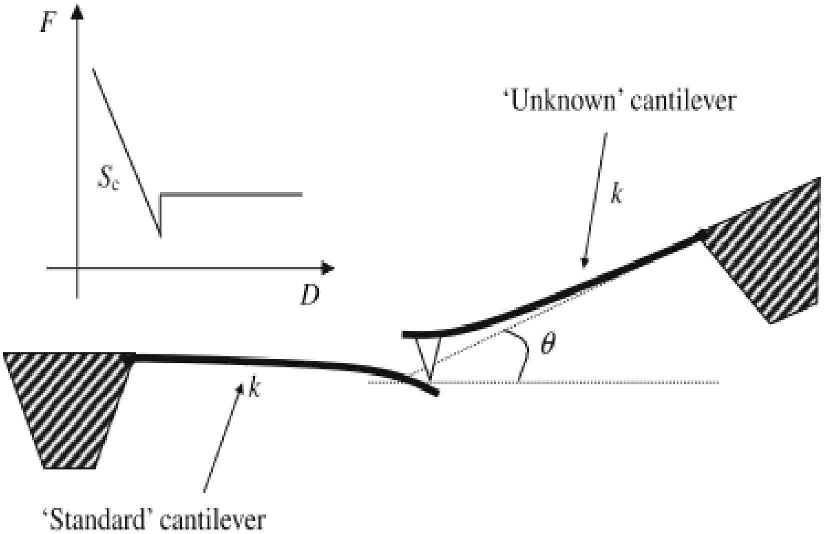

Figure 1.24 Scheme of the COC calibration method. Setup for force-distance measurement of an “unknown” cantilever relative to a “standard” cantilever according to (Kim et al., 2010)

The slope S_c in contact region will be a measure of the combined spring constants of the two-cantilever system. Since the spring constant k_s of the reference cantilever is known, that of the unknown k can be computed from the follow equation

$$k = k_s \left(\frac{S_h}{S_c} - 1\right) cos^2\alpha \tag{1.62}$$

Where, the term α is the angle of the unknown cantilever from the horizontal.

1.3 Thermal noise (or tune) method

This method requires the cantilever’s resonance frequency (usually provided by the manufacturer). This method is probably the most widely used due to its applicability to most type of cantilevers and to the little potential damage to the tip, and to the possibility to be used in air and fluid conditions. The thermal noise method is based on the equipartition theorem from fundamental thermodynamic theory (Hutter and Bechhoefer, 1993)(Cook et al., 2006)(Ohler, 2007). Modelling the cantilever as a harmonic oscillator, the Hamiltonian of such system is:

$$H = \frac{p^2}{2m} + \frac{1}{2} m\omega_0^2 z^2 \tag{1.63}$$

Where, the term q is the displacement of the oscillator, p is its momentum, m is the oscillating mass, and ω_0 is the resonant angular frequency of the system. By applying the equipartition theorem to the quadratic term of the Hamiltonian expression to relate it to its thermal energy

$$\frac{1}{2} m\omega_0^2 z^2 = \frac{1}{2} k_B T \tag{1.64}$$

Where, the term k_B is Boltzmann's constant (1.38 x 10^{-23} J/K) and T is the temperature. Knowing that $\omega_0^2 = k/m$, the force constant may be obtained from a measurement of the mean-square spring displacement as:

$$k = \frac{k_B T}{z^2} \tag{1.65}$$

Where, z^2 is the mean square displacement of the cantilever. This quantity is usually obtained by performing a power spectral density analysis of cantilever oscillations and integrating the area under the peak of the first oscillation mode (Kim et al., 2010). Nevertheless, equation 1.62 has been corrected for higher modes of oscillation of the cantilever (Ohler, 2007). The expression to calculate the spring constant by the thermal noise method is:

$$k = \beta \frac{k_B T}{z_c^{*2}} cos^2\alpha \tag{1.66}$$

Where, the term β is a correction factor equal to 0.817; z_c^{*2} is the "virtual" cantilever displacement as is measured by the optical lever and α is the angle off horizontal when the cantilever is mounted as is usual in an AFM.

2 Tip radius of curvature

The tip radius of curvature is an important parameter that affects the AFM indentation procedure. Tip radius can affect i) the nature of the penetration process, ii) deforms the specimen with a different geometry, iii) became a source of artefacts (Calabri et al., 2008; Passeri et al., 2005). Nevertheless, most of AFM probes exhibit a small rate of change during indentation test (Monclus et al., 2010). There are numerical, imaging and theoretical models to measure the tip radius of curvature. However, SEM and AFM images are the most common methods because tip geometry can be obtained directly from the image (figure 1.25). Images of the AFM probes are obtained before and after the indentation tests. Then, the difference between tip radius will be considered in the mechanical model (Wenger et al., 2007).

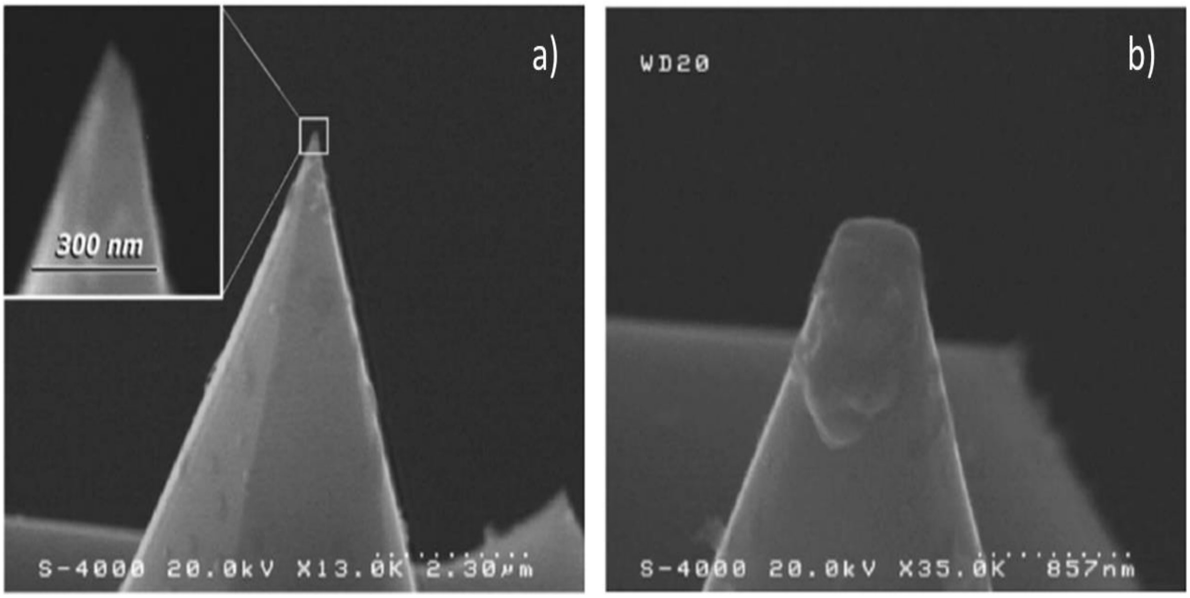

Figure 1.25 SEM images of AFM probes a) View of a brand new tip, b) view of the AFM tip after some indentation sessions. (Passeri et al., 2005)

3 Cantilever deflection

The most common methods to detect cantilever deflections are the optical lever method, the interferometric method, and the electronic tunnelling method (Cappella and Dietler, 1999). Usually the deflection of the cantilever (*d*) depends on the indentation of the tip into the elastic half space or rather the sample (figure 1.26) (Strasser et al., 2007).

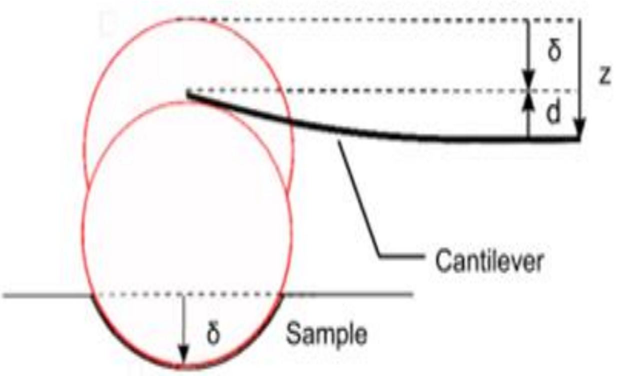

Figure 1.26 Sketch of the cantilever deflection, where, *d* is the cantilever deflection, the distance *z* is the height (measured) and *δ* is the indentation depth (JPK Instruments AG, n.d.)

The measurement of *d* is accomplished by taking a 'force curve' that measures the change in the photodetector voltage as a function of the separation between the scanner and the base of the cantilever (Cook et al., 2006). To calculate a given deflection *d*, it is required to know the detector voltage V at that deflection and the specific sensitivity S, then:

$$d = \frac{\Delta V}{S} \equiv \frac{V}{S} \tag{1.67}$$

4 Force-displacement curves

As in the nanoindentation technique, in mechanical characterization by AFM the force-displacement curves are used to represent the interaction between tip-sample interaction forces vs. tip-sample distance (figure 1.27). Commonly, force-displacement curves are computed during the approach and retracting cycles of the AFM tip into the sample. However, approaching and retracting parts of force curves are often non identical (Butt et al., 2005; Wallace, 2012).

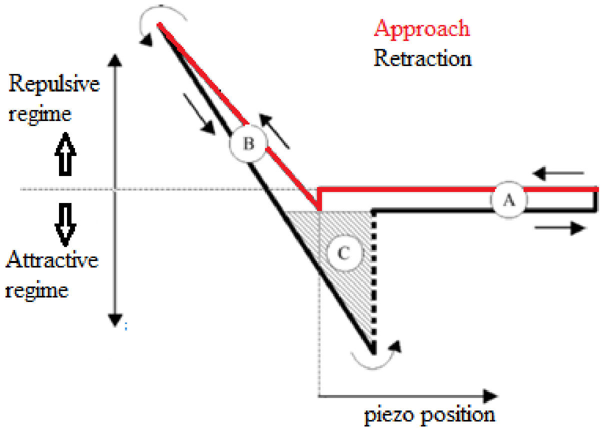

Figure 1.27 Schematic of the tip position during AFM indentation test. Three zones can be distinguish: (A) the zero force line, (B) the contact part when force is positive (repulsive) atoms are in contact and (C) adhesion where id due to the contribution of weak force (van der Waals, capillarity etc.).

Force-displacement curves can roughly be divided in three regions: i) the contact line, ii) the non-contact region and iii) the zero line (Cappella and Dietler, 1999). The direct result of a force measurement is a measurement of the photodiode current I_{PSD} versus height position of the piezoelectric translator Z_p. To obtain a force-versus-distance curve, I_{PSD} and Z_p have to be converted into force and distance (Senden, 2001) by using two parameters: the sensitivity and the zero distance. In AFM, both parameters must be inferred from the force curve itself and non- through an independent method. Practically, the beginning of the increasing linear part of the ‘‘contact regime’’ is assumed to be zero distance and its slope is the sensitivity.

5 Data analysis

In order to determine the material elastic response, the linear zone during the repulsive regime of the extended or the retracted curve of the force-displacement curve is fitted by Hertz or Sneddon mechanical model. This fitting can be accomplished by AFM data analyses software (Nanoscope Analysis®, JPK IP® or AFM Analysis Gwyddion®) or by Matlab® or LabView® routines.

To fit the modulus for force-displacement curves some equations are needed, the mechanical parameters used for this fitting are summarized in table 1.11.

Table 1.11 Parameters for the Hertz mechanical model according to the tip geometry (Lin et al., 2007)

Tip geometry	**Contact radius a**	**Sample indentation depth δ**	**Force**
Parabolic	$a = \sqrt{R\delta}$	$\delta = (z - z_0) - (d - d_0)$	$F = \frac{4\sqrt{R}}{3}\frac{E}{1-v^2}\delta^{3/2}$
Spherical	$a = \sqrt[3]{\frac{RF}{E_{tot}}}$	$\delta = \frac{a}{2} ln \frac{R+a}{R-a}$	$F = \frac{E}{1-v^2}\left[\frac{a^2+R^2}{2} ln \frac{R+a}{R-a} a\mathrm{R}\right]$
Conical	$a = \frac{2\tan\alpha}{\pi}\delta$	$\delta = (z - z_0) - (d - d_0)$	$F = \frac{E}{1-v^2}\frac{2\tan\alpha}{\pi}\delta^2$
Four-sided pyramid	$a = \frac{\tan\alpha}{\sqrt{2}}\delta$	$\delta = (z - z_0) - (d - d_0)$	$F = \frac{E}{1-v^2}\frac{\tan\alpha}{\sqrt{2}}\delta^2$

IV. AFM for bone characterization

The mechanical assessments are achieved using tensile, bending and indentation tests. These techniques have been adapted to the AFM and they allow the quantification of the elastic properties of the nanostructurale components of bone.

The mechanical and morphological characterization of the nano components of bone have been mostly oriented to the collagen fibres than to the hydroxyapatite crystals (Thurner, 2009).

For the mineral components, (Saber-Samandari and Gross, 2009) reported an elastic modulus for a single hydroxyapatite crystal of 150.4 GPa in the longitudinal direction and 143.6 GPa in the transverse direction.

For the organic components, many authors have performed mechanical characterization of isolated collagen fibrils using AFM (Andriotis et al., 2014; Balooch et al., 2008; Eppell et al., 2006; Gautieri et al., 2013; Grant et al., 2009, 2012; Minary-Jolandan and Yu, 2009; Shen et al., 2011, 2008; Svensson et al., 2010; Wenger et al., 2008, 2007; Yang et al., 2008). The samples of collagen fibres are frequently obtained from sea cucumber or animal sources such as rat or bovine tendons and to this author’s knowledge, only one study has been reported in human collagen from bronchial origin (Andriotis et al., 2014). Moreover, for this author’s knowledge, the mechanical assessment of the collagen fibrils of bone has never been performed in native state. That could due to the difficult to find healthy bones exposing collagen abundantly.

However, the mechanical characterization at the nanoscale must be handled carefully. It is noted that indentation tests performed in AFM have some limitations especially due to the experimental conditions. This in part because the AFM microscopes are used idiosyncratically without controlling all the variables involved in the contacts mechanics. When the mechanical assessments are doing using the Hertz model, the experimental conditions must keep the indentation in the elastic regimen. This is because Hertz theory is not valid in the elastoplastic domain. Meanwhile, indentations performed using the Oliver and Pharr model could have some miscalculation due to the estimation of the real contact area and control of a constant strain rate. In addition, most of the values reported in the literature applied some adjustments to the values in order to reduce the influence of the thermal drift, tip-sample plastic deformation and tip stiffness constant. Despite all these assumptions, the values reported in the literature for the elastic modulus of isolated collagen fibrils type I and the experimental conditions are summarized in Table 1.12.

Table 1.12 Studies reported elastic modulus of collagen fibres assessed by indentation in atomic force microscopy

Reference	Origin of the collagen fibre	Experimental conditions	Tip geometry and Mechanical approach	Elastic Modulus (GPa)
(Strasser et al., 2007)	Calfskin	Isolated and micro-dissected fibres, drying on freshly cleaved mica.	Parabolic and Hertzian contact mechanics	E_{core} = 1.2 E_{shell} = 1.2
(Wenger et al., 2008)	Rat tail tendons	Isolated, drying and scraped fibres. Diameter diminution after scraping : 10, 15, 20 and 35%	Spherical and Oliver and Phar mechanical model	E_{Shell}= 3.7 ± 1.2 6.4 ± 3.1 E_{Core}= 3.7 ± 1.0 8.7 ± 3.1
(Minary-Jolandan and Yu, 2009)	Bovine Achilles tendon	Isolated fibres drying on Si surface.	Spherical and classical Hertzian contact theory.	$E_{overlap}$ = 2.2 E_{gap} = 1.2
(Grant et al., 2012)	Rat tail tendons	Isolated fibrils transferred to a silicon wafer glued to glass microscope slide, the drying in air in a covered petri dish.	Spherical and classical Hertzian contact theory.	E_{peak} = 4.96 ± 0.57 E_{trough} = 3.07 ± 0.23
(Andriotis et al., 2014)	Rat tail tendon Human bronchial biopsies	Dry fibrils stored in desiccating box with silica gels until testing.	Oliver and Pharr	E_{rat} =3.27±1.1 E_{human} =6.67 ± 0.7

From the results reported in the literature on should note that mechanical characterization has not been performed in native bone yet. The Hertzian and the Oliver and Pharr methods are commonly used for the quantification of the elastic modulus. Without considering the origin of the fibrils, the values of the modulus could vary in a range between 1.2 to 8.7 GPa.

In the case of the morphological characterization of nano structural components of bone, they have been rarely observed in native state. Some authors who have reported their results in this field are (Bozec et al., 2005; Hansma et al., 2005; Hassenkam et al., 2005, 2004; Minary-Jolandan and Yu, 2009; Thurner et al., 2007; Wallace et al., 2010). They used to measure the D-band periodicity of the collagen fibrils from the AFM images (67nm) and shape of mineral particles. Some examples of these AFM images are presented in figure 1.28.

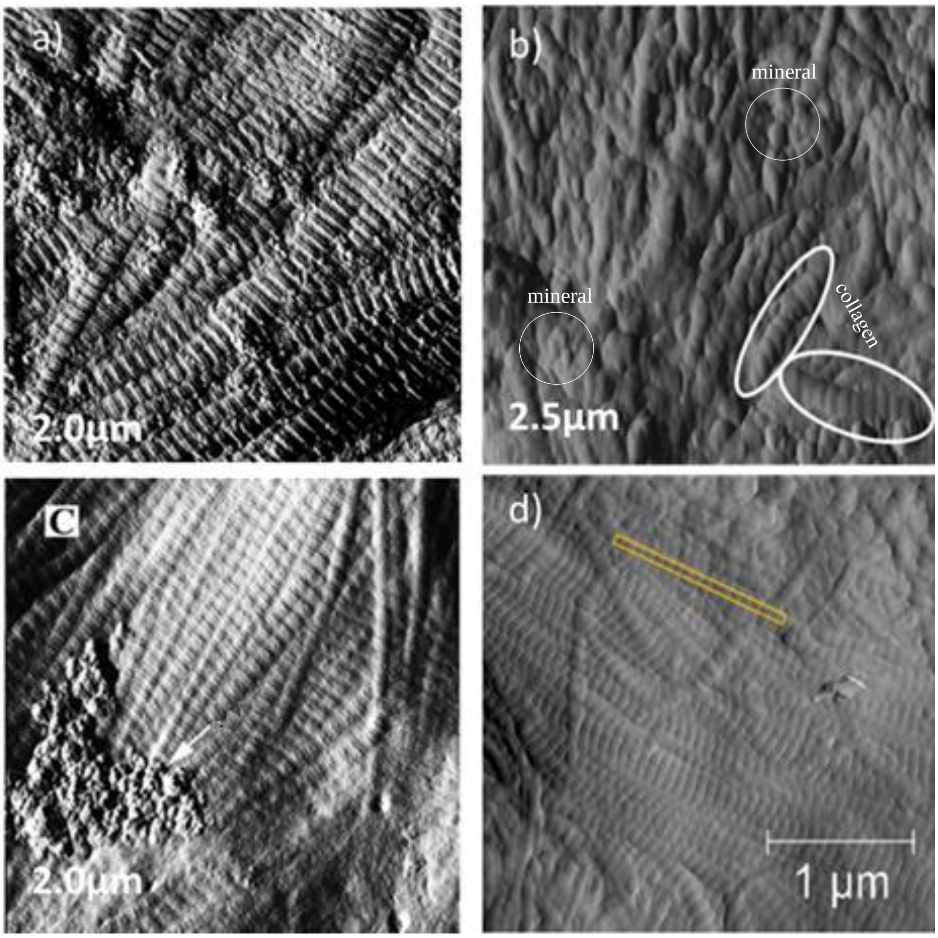

Figure 1.28 AFM images of the nano components of bone obtained in native state. a) from fresh bovine vertebrae (Hassenkam et al., 2004); b) from rabbit bone (Bozec et al., 2005); c) from human trabecular bone (Hassenkam et al., 2005) and d) from femoral mice bone (Wallace et al., 2010).

From these images it should be noted that collagen fibrils have a privileged orientation (figure 1.29 a, c and d), but no quantitative assessment was provided, they seem to be immersed in mineral matrix (figure 1.29b). The arrow in figure 1.29c, indicates the position of a group of possible mineral particles on the surface (Hassenkam et al., 2005).

Bibliographic synthesis

Bone is a dynamic, inhomogeneous, hierarchical and anisotropic biological material that presents viscoelastic and viscoplastic mechanical properties. Structurally, bone is a two-phase porous composite material compounded of collagen fibres type I, mineral crystallites, non-organic particles and water. Most of its mechanical properties are strongly linked to the interactions, quantity, distributions, orientations and shape of its mineral and organic components.

At the macro scale, mechanical properties of cortical bone of different species have been widely characterized using classical tensile, compression, bending and ultrasounds tests. This mechanical characterization has been mostly oriented to the long bones. This is due to its structural functions and their tendency to suffer diseases that affect their mechanical response. According to the values reported, the elastic properties of human cortical bone vary in a range between 17 and 23.3 GPa in the longitudinal direction; between 11.5 and 15.2 GPa in the transverse direction and between 11.5 and 11.7 GPa for the radial direction.

At the micro scale, nanoindentation technique is mostly used to characterize the local micromechanical properties of the different typologies of bone. The mechanical properties are frequently computed by the elastic-plastic Oliver and Pharr (OP) mechanical method. In fact, according to the literature, the values of the elastic modulus measured using OP in the longitudinal direction under dry conditions for human femoral bone vary between 16.1 and 25.8 GPa in the osteonal zone and between 15.1 and 26.1 GPa in the lamellar bone; meanwhile hardness values vary between 0.30 and 0.65 GPa for the osteonal zone and between 0.51 and 0.80 GPa for the lamellar bone. Nevertheless, few studies performed on human bone are dealing with time-dependent mechanical properties and recent studies revealed that the time-dependent mechanical properties of viscoelastic materials assessed by the OP mechanical method exhibit significant miscalculations. This fact gives an opening for new nanoindentation analysis methods for the specific case of viscous materials as bone. Less has been the studies performed in growth models using human bone. They are rarely reported particularly due to the difficulties to build up samples that cover all the life span (from growth to senescence).

At the nano scale, the morphological characterization of bone is performed by Atomic Force Microscopy (AFM). This technique allows one to display images of the nano structural components of bone (collagen fibrils and hydroxyapatite crystallites) and to assess different morphological characteristics as periodicity of the collagen fibrils and mineral shape. Nevertheless, the collagen fibrils are rarely observed in native state and even more those obtained from non-pathologic bones. Mechanical characterization of isolated collagen fibrils type I has been performed using nanoindentation adapted to the AFM microscope. However, only values of the elastic properties have been reported in the literature. These values vary in a range between 1.2 and 8.7 GPa. Meanwhile for hydroxyapatite crystals the elastic properties reported are 143.6 GPa in the transverse direction and 150.4 GPa in the longitudinal direction.

Always dealing the extrapolation to human being with extreme precaution, all these experimental data could be used to improve or/and to validate numerical models of bone remodelling, bone fracture, multi-scale constitutive laws or bone evolutional process (Aoubiza et al., 1996; Budyn et al., 2012, 2008; Crolet et al., 1993; Sansalone et al., 2010).

The next chapter deals with the details of the protocols developed for the preparation of the different bones samples. In addition, the experimental condition for nanoindentation tests and AFM imaging are presented. The method to compute the time-dependent, elastic and plastic mechanical properties is described as well.

Chapter 2: Materials and Methods

In the present chapter, the first part presents the different types of bones used during this work and the protocols developed for the samples' preparation are described.

After the second part describes the indentation protocol and the mechanical model used to assess the time-dependent, elastic and plastic mechanical properties. The AFM modes utilized to perform the morphological characterization are also introduced. The statistical and mathematical analyses carried out in the results and the description of the model used to describe and to correlate the experimental data.

Finally, a recapitulative section is presented in order to summarize precisely all the experimental tests performed during this work.

A. Materials

I. Samples preparation

In this work, bone is considered as a heterogeneous, hierarchical and anisotropic biological material. In order to perform a complete mechanical and morphological characterization, different bone characteristics have been investigated using different species (human, rat and bovine). Before starting the nanoindentation tests and the morphological characterization by AFM, the samples' surface of all specimens of bone were prepared following the above protocol.

1. Cutting

Samples were cut using a diamond saw (Microcut Hergon, BROT Technologies, Argenteuil, France) using low disc velocity (150 RPM) under abundant deionized water irrigation in order to avoid surface modifications due to increase of temperature. Samples were cut in different geometries according to the test interest: thin samples (~5×5×1.5 mm^3 size) for 1-direction nanoindentation tests or AFM characterization and parallelepiped samples (~5×5×5 mm^3 size) for the assessment of the anisotropic behaviour of the mechanical properties and demineralization effects. (figure2.1)

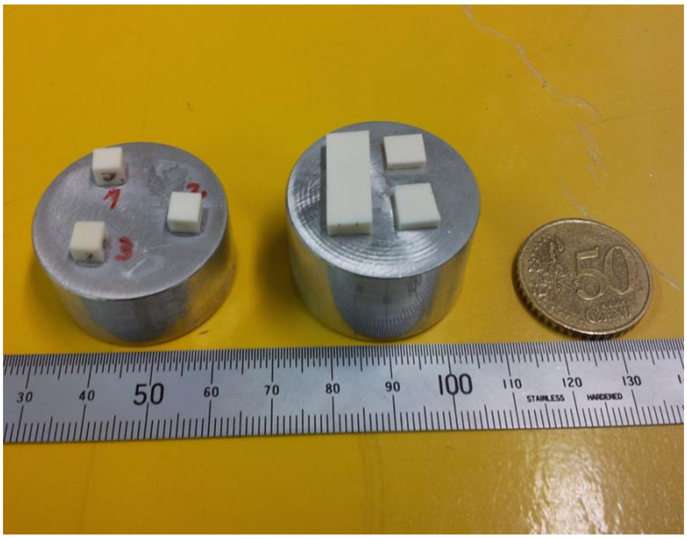

Figure 2.1 Bone samples with different geometries obtained after cutting process

2. Grounding and Polishing

Samples were ground and polished using a semi-automatic polishing machine Mecatech®234 (PRESI, Brié-et-Angonnes, France). A samples holder (see figure 2.2) was designed with a double purpose: 1) to polish the maximal number of samples at the same time and 2) to be used also during the nanoindentation tests. Both faces of the holder were using to fix the samples. On one hand, the cubic samples were fixed by small screws without additional resins; on the other hand, the thin samples were fixed to the holder by a cyanoacrylate resin.

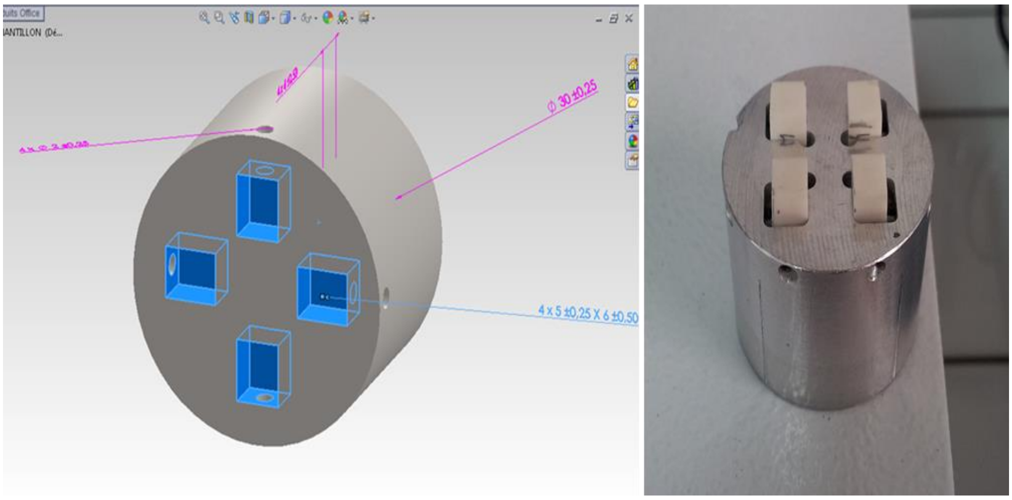

Figure 2.2 Diagram of the sample holder designed and used for polishing and nanoindentation test

After fixing the sample to the holder, the exposed surfaces were ground with successive grades of abrasive papers (P800, P1200, P2400, P4000) under abundant deionized water irrigation. The surfaces were then polished with successive decreasing grades of alumina suspensions with a particle size of 1, 0.3 and 0.04 µm to ensure that surface roughness is well lower than the final indentation depth (> 3000 nm).

3. Cleaning

Finally, after the polishing stage the samples were ultrasonically cleaned in ultrapure water (Ultrasonic cleaner Bransonic®200, 19W, Branson Ultrasonics Corp.). Three cycles of five minutes each were performed changing the water at each cycle in order to remove all alumina particles and other wear debris. After this, samples were stored and preserved in dry conditions until tests.

II. Bone types

The experimental tests were performed over different types of cortical bones. Specifically rat, human and bovine cortical bones were used. This allows us to test bone material under different experimental conditions.

1 Rat bone model (growth to senescence)

The evolution of time-dependent mechanical properties will be quantified using a life span model from growth to senescence. To achieve this task, male rats type Wistar RJHan has been used. The ages of the specimens used for the nanoindentation tests are: 1, 4, 9, 12, 18 and 24 months old. The diaphysis zone of the right and left femurs were cut using a diamond saw. Thus, around 50% of the effective zone of the femur was embedded in an epoxy resin. A diagram of the sample used is presented in figure 2.3.

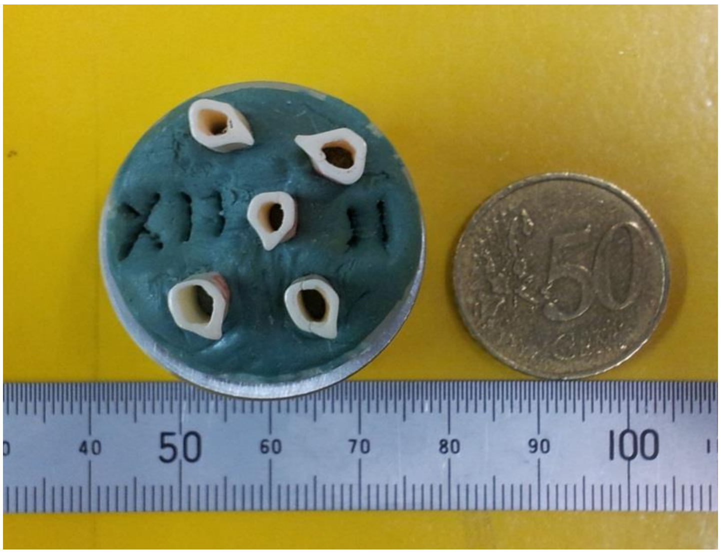

Figure 2.3 Rat femoral bone samples classed by age and embedded in epoxy resin

2 Human bone

Time-dependent mechanical properties and its anisotropic ratio were determined in Human cortical bone samples. All bone samples used during this study come from unembalmed male cadavers who donned their bodies for scientific purposes. All bones were recovered from University Hospital of Amiens and were classed according to their bone density as: F1 (high density), F2 (intermediate density) and F3 (low density). Densities values are presented in Table 2.1.

Table 2.1 Apparent density of samples used in nanoindentation tests (Ho Ba Tho et al., 2012)

Nomenclature	Density (kg/m^3)
F1 (high density)	1892 ± 29
F2	1650 ± 275
F3 (low density)	1221 ± 161

Mean values ± standard deviation

Femurs owning different densities were sectioned transversally to the bone axis. Diaphysis zone corresponding to the 40 – 70% of the total femur length were obtained with the low-speed diamond saw. This zone corresponds to the region where only cortical bone is present. Then, parallelepipeds with plane symmetry were built from each zone of the cortical shell (anterior, posterior, lateral and medial) and stored in physiological fluid at 4°C (Bensamoun, 2003).

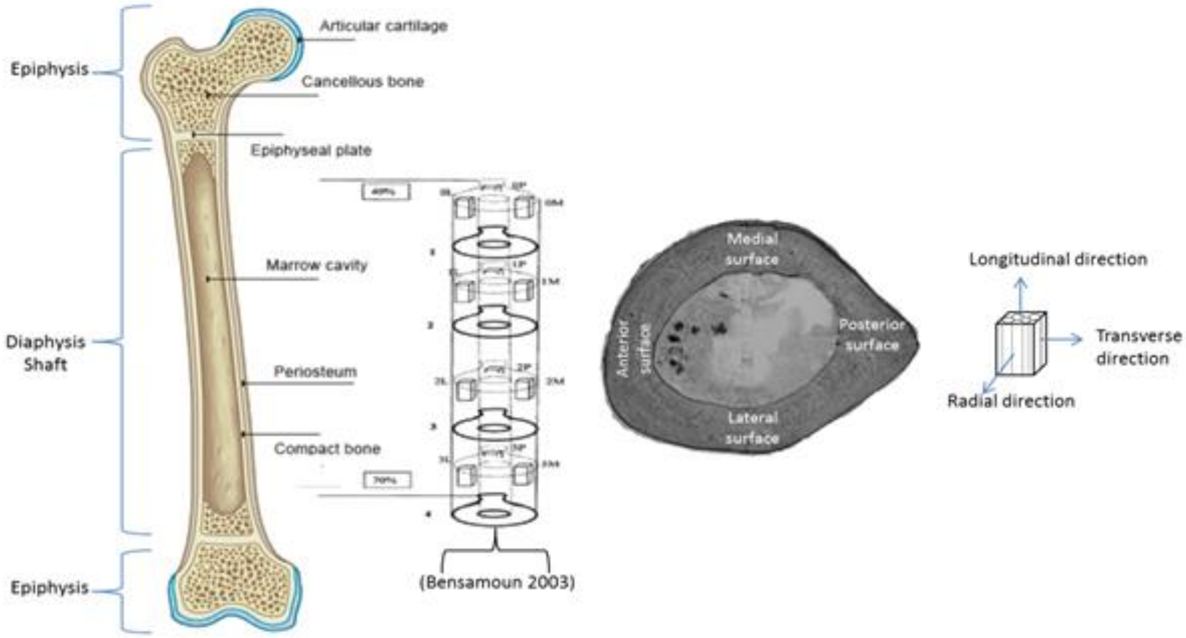

Figure 2.4 Human bone samples obtained from the diaphysis zone of a femoral bone. Different anatomical quadrants of the femoral shell (Posterior, Anterior, Medial, Lateral) and test directions (longitudinal, transverse and radial).

The faces of the parallelepiped sample were classified as:

- Face 1 (f1): Orthogonal face to the radial axis
- Face 2 (f2): Orthogonal face to the transversal axis
- Face 3 (f3): Orthogonal face to the longitudinal axis.

Finally, parallelepiped and sheets of human bone were obtained from each quadrant of the cortical shell. These samples will be used in nanoindentation tests to determine the anisotropic ratio of the time-dependent mechanical properties.

3 Bovine bone (Effects of demineralization)

Two different bovine femoral bones were used. Samples were bought from a local butchery. The purposes of these tests are to quantify the effects of mineral loss in the mechanical response of bone and to verify if there is a possible privileged orientation of the remaining collagen fibrils. Two different protocols (I and II) were used to induce a softly demineralization process and to perform the mechanical assessment by nanoindentation. Nevertheless, protocol I requires more time for samples preparation (at least 3 weeks) opposite to protocol II (1.2 weeks).

It must be informed that protocol II was not tested for this author and the results are part of a M.Sc. research project in which the author was a co-advisor (more details in the ad-joint research section). In that M.Sc. project, the demineralization protocol (protocol II) was developed and only the values of the elastic modulus and hardness were reported. However, in our consideration, the results obtained for the time-dependent mechanical properties complement the aims of this thesis and justified their use in this work.

B. Methods

I. Identification of osteons with different mineral degrees

Based in the results reported by (Bensamoun et al., 2008), ESEM (Philips XL30 ESEM-FEG) was used to identify the mineral degrees of osteons by means of grey level imaging. This technique allows working with bone samples without desiccation metal coatings and coated with gold-palladium and thus their original characteristics may be preserved for the nanoindentation and AFM testing. The images were carried out in three directions of the bone axis (longitudinal, transversal and radial). Images of the dry sample were recorded under lower-pressure gaseous environment (1.4 Torr) using an acceleration of 20 kV and a magnification of 600×. Osteons exhibiting relative different grey levels can be distinguished in the images. These differences are commonly associated to variations in the material composition of the osteons and it could be extrapolated to a difference in the mineral content.

II. Nanoindentation tests

All the Nanoindentation tests were performed with a Nano Indenter G200 (Agilent Technologies), under dry conditions, using a Berkovich tip (Micro Star Technologies) and the measurement of the contact stiffness via the Continuous Stiffness Measurement (CSM) method and the protocol developed by (Mazeran et al., 2012) to assess the time-dependent mechanical properties.

1 Accuracy and repeatability

Tests accuracy was verified by performing indentation tests in a reference material in this case silica. Values were found to be in agreement with those reported in the literature for silica material by nanoindentation: elastic modulus between 70 to 72 GPa and hardness equal to 8 GPa (see chapter 1, Table 1.6). Repeatability was verified by comparing the values of the mechanical properties of the reference material at different times.

2 Bone samples

For each bone model, different indentations protocols were used. The number of indentations and the indentation zones are described hereafter:

2.1 Rat bone tests

A total of 300 indentations (6 ages, 5 samples per age coming from five different specimens and 10 tests per sample) were performed in the longitudinal direction of the lamellar bone of the femoral section.

2.2 Human bone tests

Different densities: A total of 450 indentations (5 white osteons, 5 black osteons and 5 zones of interstitial lamellae and 10 tests per zone performed onto 3 human femoral cortical bone samples exhibiting different apparent density F1, F2 and F3 (see chapter 2, Table 2.1 for densities values). Tests were carried out in the longitudinal direction of the femoral sections.

Assessment of the anisotropic ratio: A total of 1050 indentations were carried out in the longitudinal, transverse and radial direction of the femoral sample. Each sample comes from a different anatomical quadrant of the cortical shell: posterior, median and lateral.

2.3 Bovine bone tests

Effects of total demineralization process (Protocol I): A total of 60 indentations performed in osteons and interstitial lamellae of 2 bovine femoral cortical bone samples (normal and demineralized). Nanoindentation tests were carried out in the longitudinal direction of the femoral section.

Effects of total demineralization process (Protocol II): A total of 60 indentations (30 indentations after and 30 indentations before demineralization) were performed over osteons and interstitial lamellae from 4 samples of femoral cortical bone. The experimental tests were carried out in the three principal directions (longitudinal, transverse and radial).

3 Elastic-Viscoelastic-Plastic-Viscoplastic (EVEPVP) Model

In classical nanoindentation experiments conducted on ideal elastoplastic materials, the two mechanical properties, elastic modulus and hardness, necessary to describe the elastoplastic behaviour, are computed via a two stages protocol: 1) a loading stage generating an elastoplastic response of the sample and 2) an unloading stage reflecting the elastic return of the sample. In the case of viscous materials like bone, the mechanical behaviour is composed of elastic, viscoelastic, plastic and viscoplastic components. To discriminate them correctly four stages are required. (Mazeran et al., 2012) have recently proposed a four stages protocol composed of a loading stage, a first hold load plateau, an unloading stage and a second hold load plateau. The two hold load plateaus are needed to discriminate the reversible and irreversible time-dependent elastic-plastic response, i.e. the viscoelasticity and viscoplasticity. A diagram of the mechanical model used in this work is showed in figure 2.5.

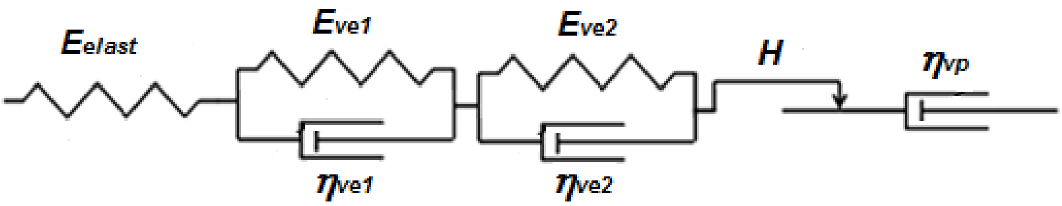

Figure 2.5 Mechanical model used to describe the mechanical behaviour of the rat femoral cortical bone. This model is composed of an elastic modulus, two viscoelasticities with different time-constants, plasticity and viscoplasticity

4 Nanoindentation protocol

Concretely, the experimental protocol is composed of four steps (see figure 2.6). The first step is the loading stage at constant loading rate/load ($\dot{\varepsilon}$ = 0.05 s^{-1}) leading to an exponential loading (F=F$_0$.exp(α.t)) in order to obtain a constant strain rate (Lucas et al., 1996b), until an indentation depth of 3 µm. This stage is performed after checking that the thermal drift is inferior to a value of 0.05 nm/s in order to limit it influence on the value of the indentation depth. The second step consists in maintaining a hold load plateau after loading. The hold time (300 s) has been chosen long enough to highlight the relaxation time of the material and to avoid the “nose” phenomenon of the unloading curve (Oyen and Cook, 2003); and short enough to prevent the effect of the thermal drift. The third step is the unloading stage until 50% of the maximum load at constant unloading rate/load˙ = -0.05 s^{-1} in order to obtain a quasi-constant strain rate. The value of the unloading ratio (F/F$_{max}$) has been chosen to be 50% because it is a good compromise between the generations of a measurable visco-elastic return and to maintain a quasi-constant contact area during unloading. Results show that beyond an unloading ratio of 25%, the experimental curves cannot be fitted correctly. The last step is to provide a constant load plateau after unloading (300 s).

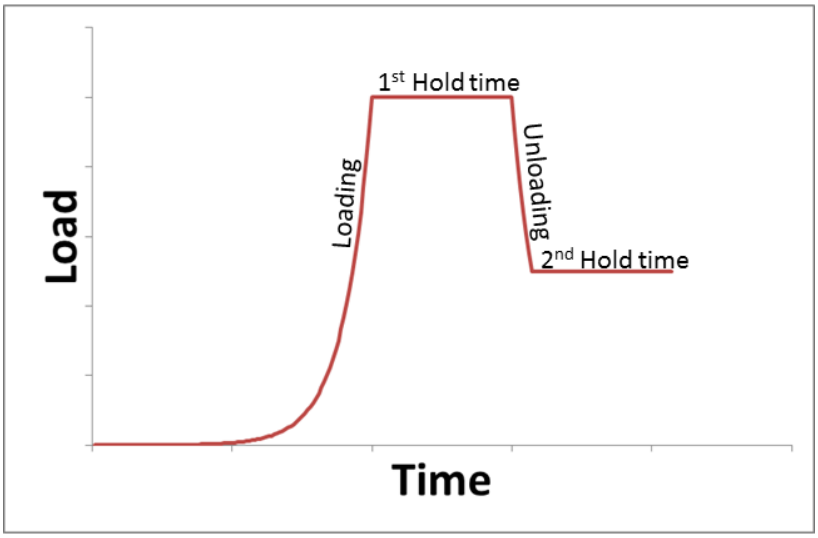

Figure 2.6 Protocol for nanoindentation tests to determinate the time-dependent mechanical properties. The representative steps of the nanoindentation protocol chosen to measure the time-dependent mechanical properties are: the loading, two hold-times and unloading stages.

5 Data analysis and assessment of the mechanical properties

The experimental curves obtained with this protocol are analysed via a specific method. In a first step, the experimental curves are fitted by an indentation mechanical model based on a set of mechanical elements in series to simulate the different behaviour of the materials. A spring that models elasticity, two Kelvin-Voigt elements for two viscoelasticities characterized by two time-constants, a slider for plasticity and a dashpot for viscoplasticity (figure 2.5). Two Kelvin-Voigt elements are enough to describe correctly the viscoelastic response of the samples in our specific conditions. This description leads to a good fit of the indentation depth versus time, in opposite to a one Kelvin-Voigt element model. The displacement d of each element has a quadratic response to load P

$$\sqrt{P} = k_e . d_e \tag{2.1}$$

For the spring (elastic response). Where k_e and d_e are the mechanical parameter of the spring and the displacement respectively.

$$\sqrt{P} = k_{ve1} . d_{ve1} + \eta_{ve1} . \dot{d}_{ve1} \tag{2.2}$$

$$\sqrt{P} = k_{ve2} . d_{ve2} + \eta_{ve2} . \dot{d}_{ve2} \tag{2.3}$$

For the two Kelvin-Voigt elements (viscoelastic responses) where d_{ve}, k_{ve} and η_{ve}, are the displacement and the mechanical parameters of the Kelvin-Voigt elements respectively

$$\sqrt{P} = p . d_P \tag{2.4}$$

$$d_P(t + \Delta t) \geq d_P(t) \tag{2.5}$$

For the slider (plastic response) where d_p et p are the displacement and the mechanical parameter of the slider respectively.

$$\sqrt{P} = \eta_{vp} . \dot{d}_{vp} \tag{2.6}$$

$$d_{vp}(t + \Delta t) \geq d_{vp}(t) \tag{2.7}$$

For the dashpot (viscoplastic response), d_{vp} and n_{vp} are the displacement and the mechanical parameter of the dashpot respectively. The two displacements of the plastic slider and viscoplastic dashpot follow a monotonic law (equations 2.5 and 2.7) in order to realize an irreversibility of the response.

Then, the sum of the displacement of all the elements d_t is summed and compare to the indentation depth h_t.

$$d_t = d_e + d_p + d_{ve1} + d_{ve2} + d_{vp} \tag{2.8}$$

The set of parameters values that gives the best fit of the indentation depth versus time is established. An excellent agreement is generally observed between the experimental curve and the indentation mechanical model fit. To limit the error on the determination of the indentation depth due to the tip defect (missing end of the tip compared to a perfect Berkovich geometry) and roughness, the zero point is determined using the method proposed by (Hochstetter et al., 1999). With this method the uncertainties on the zero point is estimated to less than 10 nm.

In a second step, the contact area is calculated from the beginning of the unloading curve using the Oliver and Pharr method. The indentation mechanical model used to fit the experimental curve in the first step is transformed into a corresponding material mechanical model composed of one elastic modulus E_{elas}, two viscoelastic moduli composed of an elastic component E_{ve} and viscous component η_{ve}, one hardness H and one viscoplasticity η_{vp}. These mechanical properties could be related to the parameter values of the spring, Kelvin-Voigt elements, slider and dashpot respectively of the indentation mechanical model. The experimental curve and the fitting performed by model are presented in figure 2.7.

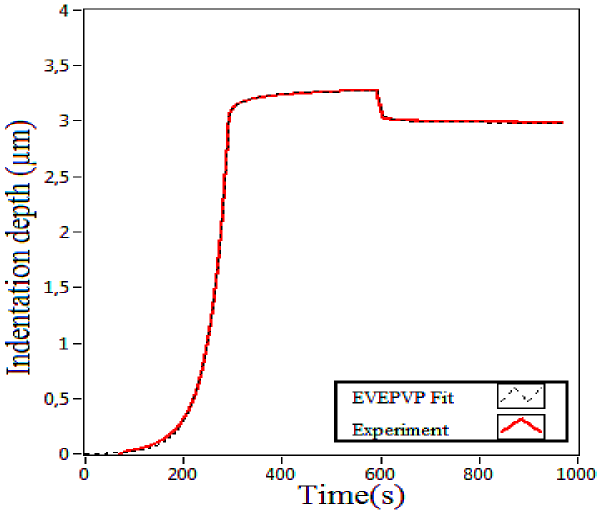

Figure 2.7 Indentation depth h_t (red curve) and sum of the displacement of the mechanical model elements d_p (black dashed line) versus time during the nanoindentation experiment. An excellent agreement was found between experimental data and the fit proposed by the mechanical model. In this example, the results for one indentation performed on rat cortical bone

Then, the mechanical properties can be computed from the equations summarized in Table 2.2 by using the parameters of the different elements and the contact area. For more details about this method please see (Mazeran et al., 2012).

Table 2.2 Equations used to assess the mechanical properties from the nanoindentation model. The values of the displacement of the different elements are taken at the beginning of the unloading curve, point of the curve from which the contact area is computed

Mechanical behaviour	Rheological element	Mechanical property
Elasticity	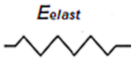	$E_{elast} = k_e^2 . d_e . \sqrt{\pi / A}$
Viscoelasticity	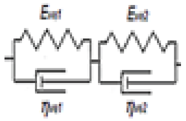	$E_{ve1} = k_{ve1}^2 . d_{ve1} . \sqrt{\pi / A}$ $\eta_{ve1} = 2. k_{ve1} . \eta_{ve1} . d_{ve1} . \sqrt{\pi / A}$ $E_{ve2} = k_{ve2}^2 . d_{ve2} . \sqrt{\pi / A}$ $\eta_{ve2} = 2. k_{ve2} . \eta_{ve2} . d_{ve2} . \sqrt{\pi / A}$
Hardness	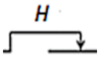	$H = p^2 . d_p^2 / A$
Viscoplasticity	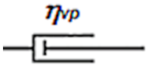	$\eta_{vp} = \eta_{vp}^2 . d_{vp} . \dot{d}_{vp} / A$

The method gives excellent fits of the experimental curves on polymers (Mazeran et al., 2012) and bones. Nevertheless, for different load-time history the method gives different values of mechanical properties. This is due to the difficulties 1) to compute the material mechanical properties from the values of the parameter of the indentation mechanical model, 2) to differentiate the visco-plastic behaviour from the visco-elastic behaviours with long time constant in a short time experiments and to obtain a unique solution of parameters for a given experimental curve. This phenomenon is a general problem in mechanical characterization and especially in nanoindentation for viscous materials. Thus the values of the mechanical properties determined by this method and generally by nanoindentation in the case of viscous materials cannot be considered as accurate but as semi-quantitative. They could be used for comparison between different materials if the experimental conditions are similar. In the present study, the method is used to highlight the evolution of the different mechanical behaviours with age of rat cortical bone and determine maturation ages.

From this experimental data, the apparent elastic modulus of the samples for a given strain rate $\dot{\varepsilon}$ is computed using the following equations:

First, a reduced apparent elastic modulus E^*_{app}, is computed i.e. the apparent value of the elastic modulus when the sample is strained at a given strain rate $\dot{\varepsilon}$.

$$\frac{1}{E_{app}^*} = \frac{1}{E_{elast}} + \frac{1}{E_{ve1} + \dot{\varepsilon}.\eta_{ve1}} + \frac{1}{E_{ve2} + \dot{\varepsilon}.\eta_{ve2}} \tag{2.9}$$

The values of the reduced apparent elastic modulus has been calculated for 3 values of $\dot{\varepsilon}$ equal to 1) 0 s^{-1} in order to assess the quasi-static elastic modulus, 2) 0.05 s^{-1} corresponding to the typical strain rate used in the nanoindentation tests and 3) an infinity strain rate to highlight the highest value that can reached by the apparent elastic modulus.

Then, the equivalent elastic modulus is computed with the bulk nominal value of the Poisson's ratio:

$$\frac{1}{E^*_{app}} = \frac{1\text{-}\nu_s^2}{E_{app}} \tag{2.10}$$

Where E_{app} corresponds to the apparent elastic modulus as a function of the reduced elastic modulus E^*_{app} and the average Poisson's ratio commonly used for cortical bone ν_s= 0.3.

6 Correlations, multiple regression analyses and Statistical tests

6.1 Growth model

An exponential growth model for male rats Wistar (equation 2.11) and their coefficient of determination R^2 were computed for each mechanical property. This equation could be used in growing models to predict the evolution of the mechanical properties related to ageing.

$$X = k_0 * \left(1 - exp^{(-k_1 - k_2 . Age)}\right) \tag{2.11}$$

Where, the term X corresponds to each mechanical property of the model, k_0 is the estimated asymptote value when age approaches infinity. The term k_1 is the coefficient to adjust the equation for the initial conditions and the term k_2 is the growth rate. The asymptote value k_0 represents the end of growth; maturation age is computed as 95% of the estimated asymptote (k_0). Our proposed model is similar to most of growth models derived from Gompertz growth curve and reported by (Winsor, 1932). The growth model used in this work is frequently used to describe monotone mechanical behaviours but sometimes this situation do not corresponds to the experimental results. In that case, it must be informed that others growth models could be used to fit mathematically the experimental data but most of the time they do not have any physiological sense.

6.2 Correlations and Multiple regression analyses

Samples correlations were determined between the mechanical properties of rat cortical bone and the physico-chemical results reported by Vanleene et al. performed over the same set of samples (Vanleene, 2006; Vanleene et al., 2008). The correlation coefficient and the determination coefficient were computed for all mechanical and physico-chemical properties using the statistical analysis and graphics software SYSTAT version 2012 (SYSTAT Software Inc.).

Then multiple regression analyses were performed on each mechanical property to obtain regression models as a function of the high-correlated physico-chemical properties. These models allow one to identify the most relevant physico-chemical characteristics, which could alter the mechanical response of bone.

6.4 Non-parametric statistical tests

Shapiro-Wilk normality tests were primary performed in the experimental results to check it they fulfil the hypothesis of the normal distribution. Because in this work experimental data frequently does not have a normal distribution, non-parametric statistical tests Kruskal and Wallis test and Dwass-Steel-Chritchlow-Fligner (DSCF) were performed to highlight statistical significant differences. The significant p-value selected is $p < 0.05$. Just in the case of the life span model another significance p-value<0.001 was used. All statistical tests were performed in the statistical analysis and graphics software SYSTAT version 2012 (SYSTAT Software Inc.).

III. Morphological characterization by AFM

After the first AFM images of biological structures were obtained, it was soon realized that a crucial factor for successful imaging is the specimen preparation (El Kirat et al., 2005). Atomic force microscopy images were carried out with a *Multimode AFM Nanoscope® IIIa* (Bruker Inc.). Images were captured in both environmental tapping and contact AFM mode. In this study, in order to analyse the structural characteristics, the samples were polished as described (in section A) and imaging without further treatment as vacuum coat or biological markers. The individual imaging parameters are given in the corresponding figure captions. Generally, all images were processed using two softwares: *Nanoscope® software* (Version 5.31r1, Veeco Inc.) and *Nanoscope® analysis software* (Version 1.5, Bruker Inc).

Morphological characterization was performed in rat, bovine and human bone samples. Usually, these samples were the same used for nanoindentation tests. The samples were dried and glued to steel disks with double-face adhesive tape. Images were recorded in contact and tapping AFM mode in air in room conditions (~21° C) (figure 2.8).

The AFM probes used were MLCT and NP-S10 with silicon nitride cantilevers for contact mode and RTESP MPP-11100-10 with phosphorus (n) doped Si cantilevers for tapping mode. All probes from *(Bruker Inc.®)*. Generally, the scan rate used was 2.5 Hz for contact mode and 1.8 Hz in tapping mode and a maximum sampling size of 512 × 512 pixels.

Morphological analyses: height, diameter, length, width and shape for the mineral crystals and D-band periodicity and orientation for the collagen fibrils were carried out using section analysis option in the AFM images. These analyses were performed using two different software *Nanoscope® 5.31r1* and *Nanoscope Analysis 1.5* both from *(Bruker Inc.®)*. Fibre collagen orientations were quantified by measuring the angle of the fibres in reference to the transverse plane of the bone. The origin axis is the vertical axis and IMAGE J (National Institute of Health, USA) software was used.

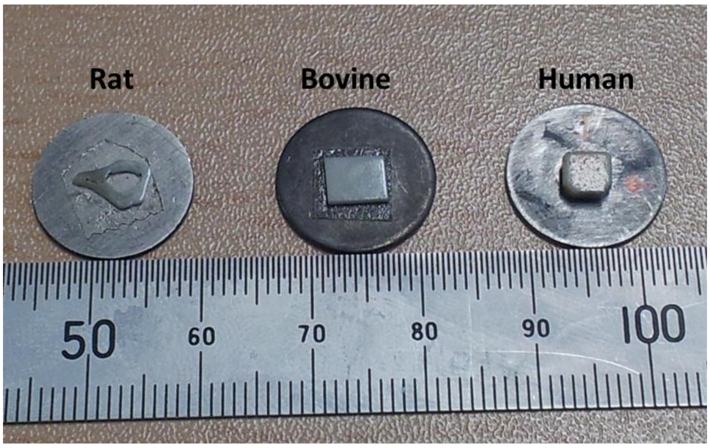

Figure 2.8 AFM samples of rat, bovine and human bone glued to the AFM steel disk and ready to be used for morphological characterization.

The AFM characterization was not performed in bone samples with a cubic geometry. This is due to the Multimode AFM restriction related to the high of samples, which is not allowed to be higher than 2.5 mm. beyond this high the cantilevers' holder cannot be placed in the optical head.

C. Recapitulation of the different studies

In order to provide a study guide, Table 2.3 presents a summary of all the most relevant information about the experiments that were performed during this work.

Table 2.3 Recapitulation of the nanoindentation tests performed in this work

Samples' characteristics	Species	Bone type	Number of subjects	Number of samples	Indentation direction	Indentation zone	Number of indentation tests n	Morphological characterization by AFM
Life span model (1,4,9,12,18,24 months old)	Wistar rat	Femur	5* bones per group	1 sample one bone (N=29)	Longitudinal	Lamellar bone	290	Yes
Different apparent densities (F1, F2, F3)	Human	Femur	3	1 sample one bone (N=3)	Longitudinal	Lamellae and osteons	450	Yes
Anisotropy behaviour (F2)	Human	Femur	1	3 samples (N=3)	Longitudinal, transverse and radial	Lamellae and osteons	1050	Non
Demineralization (Protocol I)	Bovine	Femur	1	2 samples (N=2)	Longitudinal	Lamellae and osteons	60	Yes
Demineralization (Protocol II)	Bovine	Femur	1	4 samples (N=4)	Longitudinal, transverse and radial	Lamellae and osteons	60	Non

* For the sample of 4 months old only 4 femurs and 4 samples were used

Chapter 3: Study of a bone model from growth to senescence

In this chapter, the mechanical properties of cortical bone were assessed in a growth model. The aims are to quantify the evolution of the mechanical properties with age; to correlate the results to physico-chemical characteristics, to propose prediction equations of the mechanical properties as a function of age and their physico-chemical properties.

AFM images were displayed on the samples surface in order to perform a morphological and structural characterization of the bone surface and its nano components (mineral crystal and mineralized collagen fibrils type I). The purposes of this morphological characterization is to assess the possible size evolution of the mineral crystal with age and to examine it the collagen fibrils have a privileged orientation in the bone matrix.

A. Time-dependent mechanical response

To compute the values of the time-dependent mechanical properties using nanoindentation technique, it is necessary to use specific protocols (Isaksson et al., 2010b; Mazeran et al., 2012; Olesiak et al., 2009; M. L. Oyen, 2006). In this section, time-dependent mechanical properties were assessed in a growth bone model from growth to senescence. All bone sample come from different femurs. A total of 290 indentations (10 indentations per sample) were performed in the longitudinal direction.

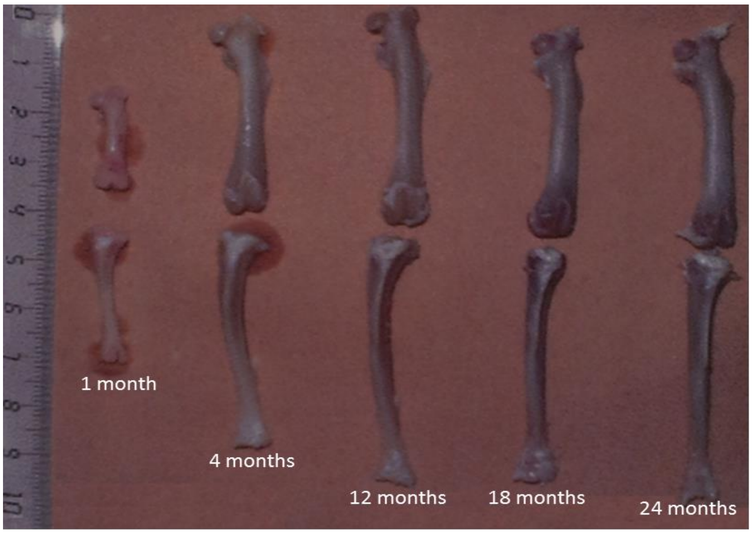

Figure 3.1 Femurs and tibias from Wistar rat classed according to their age: 1, 4, 12, 18, 24 months old (Vanleene, 2006)

A summary of all mechanical properties computed from the nanoindentation data using the mechanical method proposed by Mazeran et al. are presented in Table 3.1. The results have been expressed as the mean ± standard deviation (SD).

Table 3.1 Values of the mechanical properties computed from the nanoindentation experiments in the longitudinal direction of the rat femoral cortical bone.

Age (Months)	E_{elast} **(GPa)**	E_{ve1} **(GPa)**	$\eta_{ve1}\times10^2$ **(GPa.s)**	E_{ve2} **(GPa)**	$\eta_{ve2}\times10^3$ **(GPa.s)**	**H (GPa)**	η_{vp} **(GPa.s)**
1	26.4 ± 3.4	43.2 ± 6.1	17.6 ± 3.3	79.0 ± 12.3	48.0 ± 9.9	0.70 ± 0.09	250.9±28.8
4	40.7 ± 6.7	57.6 ± 16.9	19.3 ± 4.6	114.8 ± 15.8	64.0 ± 13.6	0.93 ± 0.06	334.6±27.9
9	35.9 ± 3.8	75.6 ± 17.7	28.3 ± 8.2	140.1 ± 23.0	73.6 ± 12.1	0.97 ± 0.10	364.3±43.0
12	39.8 ± 6.3	78.2 ± 18.4	23.6 ± 9.6	150.1 ± 25.9	57.4 ± 13.5	1.04 ± 0.12	357.6±45.5
18	38.4 ± 6.8	75.1 ± 19.1	28.2 ± 8.4	150.4 ± 25.9	71,5 ± 15.1	1.06 ± 0.10	381.6±35.8
24	34.6 ± 4.6	71.4 ± 15.4	22.6 ± 9.6	146.0 ± 18.6	68.6 ± 18.2	1.13 ± 0.09	408.5±43.1

Mean ± standard deviation

These values are represented graphically by box plot charts. This type of graphs represents clearly the variation of the mechanical response (Fig. 3.2 to 3.4). In addition, the curve of the function generated by the growth model (see chapter II section B) was fitted to the experimental data. These prediction equations allow one to identify a possible maturation age for each mechanical property. This maturation age is considered as the age when the mechanical property reaches the 95% of its maximum value. Non-parametric statistical tests were performed in order to highlight the main statistical significant differences between the mechanical response and the age of the samples.

The values computed for the elastic response E_{elast} are represented in Figure 3.2.

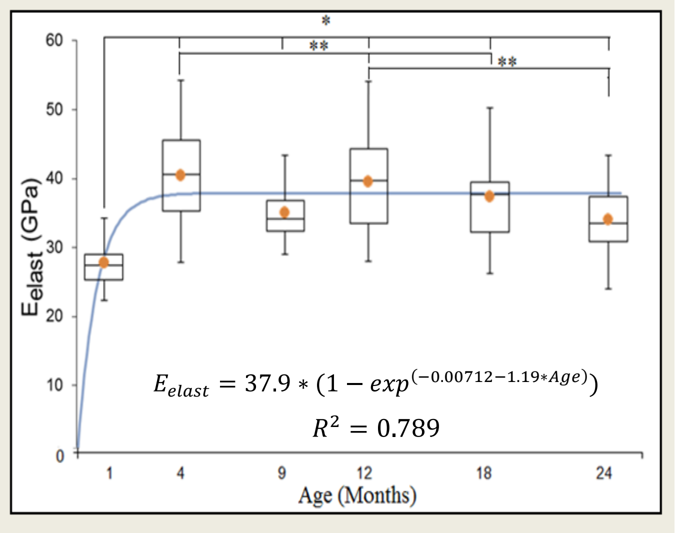

Figure 3.2 Variation of Elastic modulus Eelast of the rat femoral cortical bone with age. Symbol “•” represents the mean value. (Significant differences from the DSCF test *p< 0.001 and **p<0.05). The prediction equation computed from the growth model is presented. The determination coefficient for the curve generated by this equation is R^2= 0.789

The E_{elast} is very statistically significantly different ($p<0.001$) between 1 to 4 months, the values increase about 50% in a period of 3 months. Group of samples of 4 months old shows statistical significant differences ($p<0.05$) compared to the group of 12 and 18 months old. The values have a light decrease between 12 to 24 months old but it remains statistically non-significant. The curve obtained for the elastic response from the growth model was found to start at 0.4 GPa. This value is well lower than expected for a hard biological material as bone. In rats’ bone, this mechanical response could be assigned to earliest stages of bone material with mechanical characteristics similar to cartilage. Nevertheless, this value should be taken with precaution because the prediction equation is clearly not adapted to the real evolution of the elastic modulus. Significant differences between 1 and 18 month and between 12 and 24 months clearly suggest that the elastic modulus decreases at older ages.

Previous studies ((Hodgskinson and Currey, 1992; Vanleene et al., 2008) suggest that variation of the elastic response at the macro scale are strongly correlated to structural characteristics as the micro-porosity and density. In the case of Wistar rat cortical bone, (Vanleene et al., 2008) found that cross sectional area passes from a structure with a high porosity during 1 to 4 months old to a more mature lamellar shell during 4 to 12 months old. Then, micro-porosity increases between 12 to 24 months old but variation was not statistically significant. This behaviour is similar to our results. It fact confirms that microporosity affects the elastic response of bone both at the macro and micro scale.

The viscoelastic response of bone samples was assessed by two Kelvin-Voigt components. The values obtained for each component are represented in Figure 3.3.

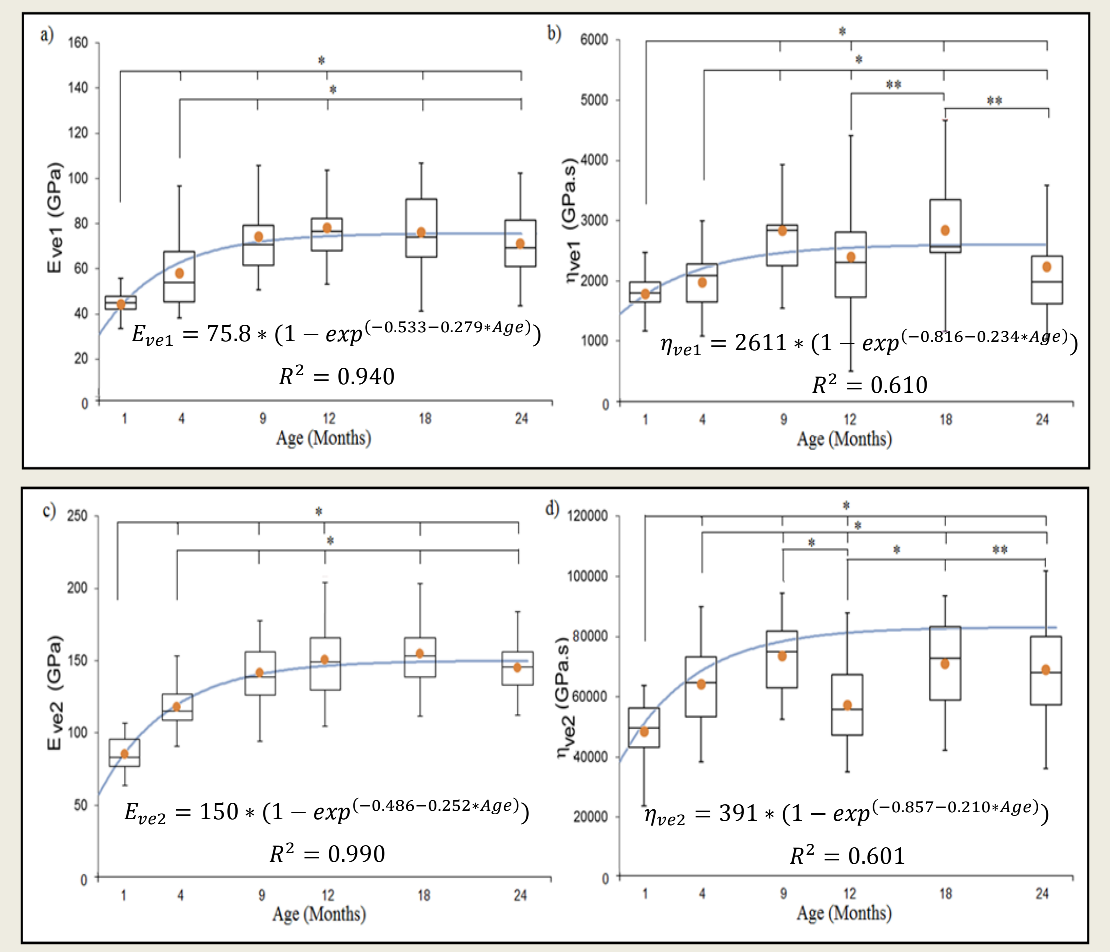

Figure 3.3 Variation of Viscoelastic moduli of the rat femoral cortical bone with age : Elastic components ((a) for the first elastic component described by a prediction equation with a R^2= 0.940 and (c) for the second elastic component described by a prediction equation with a R^2= 0.990) and the Viscous component ((b) for the first viscous component described by a prediction equation with a R^2= 0.610and (d) for the second viscous component described by a prediction equation with a R^2= 0.601). Symbol "•" represents the mean value. (Significant differences from the DSCF test *p< 0.001 and **p<0.05).

On one hand, values of the elastic component of the viscoelastic behaviour E_{ve1} and E_{ve2} (figure 3.3(a) and (c)) increase with statistical significantly differences ($p<0.001$) between 1 to 9 months of the lifespan. After this age, the mechanical values have not statistically significant differences until senescence. Additionally, the viscous component η_{ve1} and η_{ve2} (Figure 3.3(b) and (d)) have a similar evolution in their mechanical behaviour. Values increase between 1 to 9 months with statistically significant differences ($p<0.001$). However, after this period important dispersions were noted. For η_{ve2} at 12 months old, the values decrease and the statistical tests show significant differences ($p<0.001$) between age groups. Statistical significant differences $p<0.05$ were obtained as well for both viscous components between the groups of 18 and 24 months old.

Globally, the viscoelastic properties E_{ve} and η_{ve} increase from 1 to 9 months old. During this period, the values increase 80% for the elastic components and 60% for the viscous components. Then, the values remain constant until senescence. This variation could be explained by an increase of the density and the percentage of the carbonate weight ($CO_3W\%$) and a diminution of protein weight between 1 to 9 months old as reported by (Vanleene et al., 2008). The viscoelastic response of bone may be related to layered water located between the crystal interfaces of the extrafibrillar mineral of bone as suggested by (Eberhardsteiner et al., 2014). Other authors computed the viscoelastic properties of life span model of bone (Isaksson et al., 2010a). However, the ranges of values reported in these studies are lightly lower than those obtained in this study. These differences could be explained by the different bone species (rabbit and rat) and the mechanical model used to assess the viscoelastic response. In fact, (Isaksson et al., 2010a, 2010b) used a Burger model to describe the time-dependent viscoelasticity meanwhile the present study uses two Kelvin-Voigt elements coupled with a dashpot to describe the time-dependent response.

The results for Hardness (H) and Viscoplasticity (η_{vp}) are presented in Figure 3.4(a) and 3.4(b) respectively.

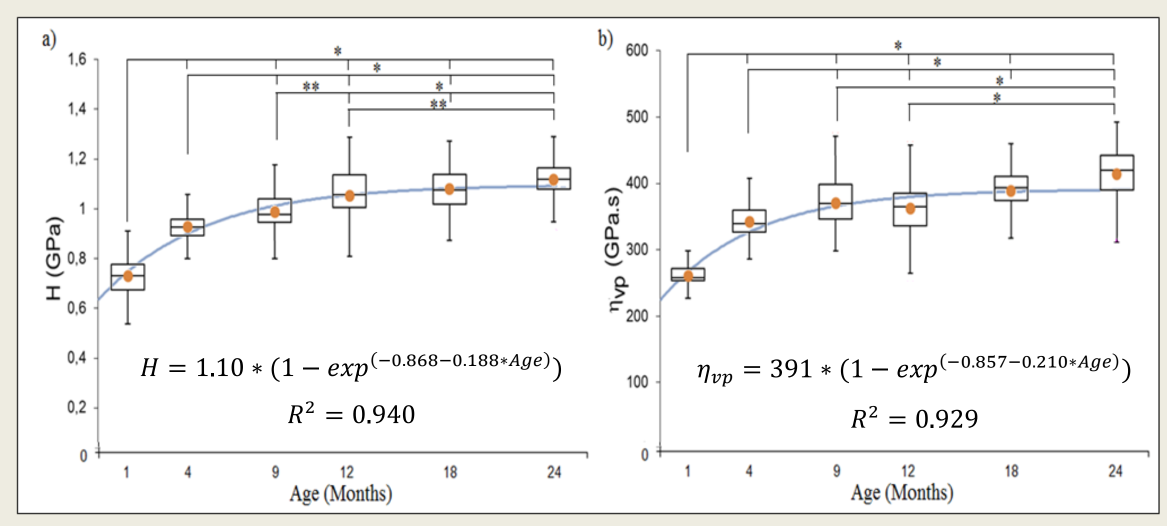

Figure 3.4. Evolution of the mechanical properties of the rat femoral cortical bone with age. (a) Variation of Hardness described by a prediction equation with a R^2=0.940 and (b) Viscoplasticity described by a prediction equation with a R^2=0.929. Symbol "•" represents the mean value. (Significant differences from the DSCF test *p< 0.001 and **p<0.05).

Both, hardness and the viscoplasticity increase during all lifespan. These properties increase 33% during the period between 1 to 4 months old and by about 20% until senescence ($p<0.001$). This increase can be quantified by the prediction equations. The maturation age computed for H and η_{vp} are almost identical and the ratio of η_{vp}/H is constant (360 ± 10 s). This behaviour suggests that plasticity and viscoplasticity are intrinsically linked. Because the value of the viscoplasticity is well higher than the hardness, it is possible to suggest that the apparent hardness is only slightly affected by the strain rate.

It must be noted that during senescence the values of H and η_{vp} continue to increase. This suggests a process of hardening in the cortical shell of bone during all life span. This behaviour is similar to some results reported in older human bone (Currey et al., 1996) and mature rat cortical bone (Akkus et al., 2004). Normally, hardness decrease during aging because of the increase of porosity, low density and the increase of bone resorption with age.

Using the adaptation of the Gompertz growth model, the prediction equations were computed for each mechanical property as a function of age. From these equations is possible to compute the apparent maturation ages (see chapter 2 section B) for each mechanical property. In addition, from the values obtained for the growth rate (factor k_2 of the growth model) could highlight some clues about. The values computed for the maturation age and the growth rate are summarized in Table 3.2.

Table 3.2 Maturation age and growth rate of the different mechanical properties for male rats RJHan:WI Wistar. Maturation age was computed at the 95% of the maximal values of the function.

Mechanical property	Maturation Age (Months)	Growth rate
E_{elast} (GPa)	2.7	1.19
E_{ve1} (GPa)	8.7	0.28
η_{ve1} (GPa.s)	9.2	0.23
E_{ve2} (GPa)	9.8	0.25
η_{ve2} (GPa.s)	9.3	0.25
H (GPa)	10.9	0.19
η_{vp} (GPa.s)	10.1	0.21

One should note that maturation age and growth rate is different for elastic response and the others mechanical properties. The elastic response was found to have a maturation age at 2.7 months old and a growth rate of 1.19. This fact could explain the high slope of the elastic response during growth age. It could be also linked to the high reduction of bone porosity during the first four months of the life due to bone structural development. For viscoelasticity, hardness and viscoplasticity the maturation age and the growth rate were found to be about 9 and 10 months old with a growth rate between 0.19 and 0.28. This different maturation ages and growth rate could be linked to different phenomenon as the evolution of the bone organic-inorganic matrix, decrease of porosity, picks of metabolic activities, bone remodelling process and maturation of the apatite crystals.

Finally, using the mechanical elastic and viscoelastic values in equation (2.9) (see chapter II section B), an apparent elastic modulus as a function of age and the given strain rate can be represented. The strain rate values 0, $0.05s^{-1}$ and ∞ were selected to highlight the minimum and maximal values of the apparent elastic modulus. The results are represented in figure 3.5.

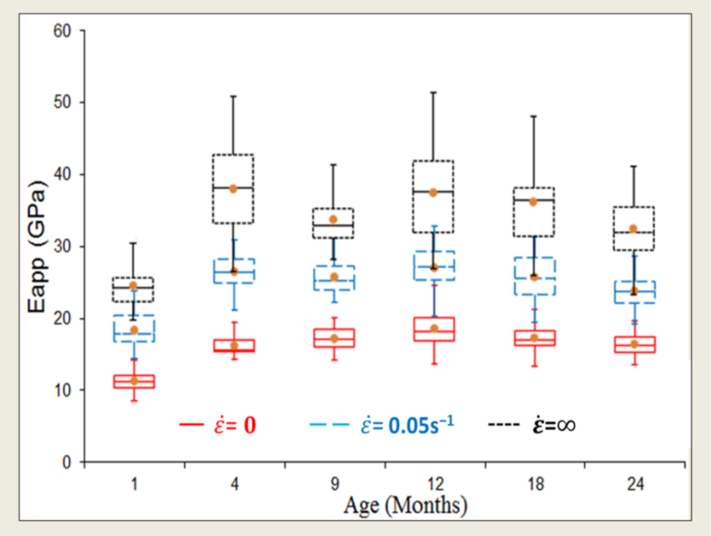

Figure 3.5 Apparent elastic modulus as a function of age and strain rate: from top to bottom strain rate $\dot{\varepsilon}$= 0.05 s-1 and 0. DSCF test show that variation is statistically significant from 1 to 4 months old (*p*<0.001).

The values increase by a factor of two when the strain rate rises from 0 to infinity. This behaviour is similar to that reported by (McElhaney, 1966) who reported the increase of the elastic modulus from 15.1 to 29.5 GPa when the strain rate increase from 0.001s^{-1} to 300s^{-1} and also similar to (Abdel-Wahab et al., 2011) who reported the increase of the elastic modulus from 11.9 to 21.2 GPa while the strain rate increase from 10^{-5} s^{-1} to 1 s^{-1}. Additionally, it could be noted that nanoindentation experiments used classical strain rate of 0.05s^{-1}. The apparent elastic modulus obtained with this strain rate is around the average between the extreme values. These facts suggest that apparent elastic modulus increases with the strain rate

The results obtained in this work while the strain rate is take into account are in good agreement with previous studies reported by (Fan and Rho, 2003; Vanleene et al., 2006). They showed that the increase of the strain rate affects the mechanical response of bone. Our results suggest that this parameter should be considered in the analyses of nanoindentation data as mentioned in previous study (Mazeran et al., 2012). Consequently, our protocol allowed us to highlight the different maturation ages for the different mechanical properties for male Wistar rats.

It should be noted that after 4 months old, the apparent elastic modulus remains constant until the 12 months then a lightly decrease is noted until the senescence. Similar behaviour was found in human bone samples by (Rho et al., 2002). This behaviour could be attributed to structural and histological features than alterations in bone matrix itself.

B. Correlations between mechanical and physico-chemical properties

The mechanical properties obtained from this study were correlated with the macro structural and physico-chemical properties obtained from a same set of samples by Vanleene et al. (Vanleene, 2006; Vanleene et al., 2008)..

Porosity were analysed from complete images of proximal cross sections of femurs which were first reconstructed from about 10 partial images (pixel resolution: 2µm) using an ESEM (Environmental Scanning Electron Microscope) (PhilipsXL30ESEM-FEG, Royal Philips Electronics, the Netherlands).Then, ESEM images were analysed using QWinStandard image analysis software V2.7 (Leica Microsystems Imaging Solution Ltd., UK). Percentage of porosity (porosity %) was calculated from the total pore area, including canals and lacunae, divided by the total cross sectional area.

On the other hand, physic-chemical values were obtained with three different characterization methods:

First, Fourier Transformed Infra-Red (FTIR) spectroscopy analyses were performed on six samples per age group (1760- X FTIR Spectrometer, PerkinElmer Inc., MA, USA). The spectra were curve-fitted in the ν_4 PO_4, ν_2 CO_3 and collagen amide band domains (GalacticGRAMSsoftware,NH,USA).

Second, two chemical analyses were performed on samples. Carbonate weight percentage (CO_3W%) was measured on six samples per age group using a CO_2 Coulometer (Coulometrics Inc., Co, USA). Protein nitrogen-weight content was analysed on three samples per age group using an Elemental Analyser EA 1110 CHNS (Thermo Fisher Scientific Inc., MA, USA).

Third, as previous analyses consumed most of sample powder, specimens were pooled in each age group. X-ray diffraction was recorded with a X-ray diffract-meter (Inel CPS 120, Enraf Nonius SA, France) using Co radiation (X- ray wave length=1789 A).Two peaks at 30° and 45°(2θ) were identified respectively to 002 (c-axis of apatite lattice) and 310 diffraction planes of the apatite crystals.

The mean values of each physico-chemical property are summarized in Table 3.3.

Table 3.3 Variation of the physico-chemical properties of Wistar rat femoral cortical bone with age according to (Vanleene, 2006; Vanleene et al., 2008)

Age (Months)	Porosity%	CO_3W%	PO_4%	Ca%	N%	Collagen%
1	8.1	4.1	20.7	42.2	4	21.4
4	3.1	4.9	18.2	39.2	3.6	19
9	3.3	6.1	17.9	39.4	3.3	17.6
12	2.6	6.1	18	39.7	3.3	18.3
18	3.6	6	18	39.3	3.3	17.8
24	4	6	18	39.3	3.3	17.4

According to these values, most of the physicochemical properties of Wistar rat femoral cortical bone tend to decrease with age. Only the values of CO_3W% increase with aging. This fact could be due to the remodelling process and the apposition of remaining carbonate.

Using the physico-chemical properties, single correlations were performed in order to identify those that could be linked to the mechanical response of bone. Thus, the correlation coefficient R that denotes the strength and direction of the linear relationship between the variables and the determination coefficient R^2 are reported for each mechanical and physicochemical property (Tables 3.4 to 3.6). Correlation between the physical chemical properties is useful to identify independent and dependent variables. Even if this coefficient is high, as an assumption for this work, all physico-chemical properties are considered as independent variables. The highest values of the correlation coefficients for each mechanical property were underline.

Table 3.4 Simple Correlation coefficient R for the mechanical and physicochemical properties of rat cortical bone

Mechanical property	Porosity%	CO_3W%	PO_4%	Ca%	N%	Collagen%
E_{elast}	-0.949	0.608	-0.867	-0.878	-0.703	-0.673
E_{ve1}	-0.828	0.992	-0.885	-0.780	-0.981	-0.919
η_{ve1}	-0.576	0.842	-0.682	-0.597	-0.810	-0.778
E_{ve2}	-0.842	0.981	-0.914	-0.837	-0.991	-0.948
η_{ve2}	-0.679	0.744	-0.822	-0.844	-0.794	-0.884
H	-0.799	0.900	-0.899	-0.864	-0.937	-0.940
η_{vp}	-0.781	0.903	-0.908	-0.886	-0.942	-0.974

Table 3.5 Determination coefficient R^2 for the mechanical and physicochemical properties of rat cortical bone

Mechanical property	Porosity%	CO_3W%	PO_4%	Ca%	N%	Collagen%
E_{elast}	0.901	0,370	0,752	0,771	0,494	0,453
E_{ve1}	0.686	0,983	0,782	0,609	0,963	0,845
η_{ve1}	0.332	0,708	0,466	0,357	0,656	0,605
E_{ve2}	0.71	0,963	0,836	0,7	0,982	0,899
η_{ve2}	0.461	0,553	0,676	0,713	0,63	0,781
H	0.639	0,809	0,806	0,750	0,879	0,884
η_{vp}	0.609	0,815	0,824	0,785	0,887	0,949

Table 3.6 Simple correlation coefficients between the physico-chemical properties

	Porosity%	CO_3W%	PO_4%	Ca%	N%	Collagen%
%Porosity	1,000					
% CO_3W	-0,792	1,000				
% PO_4	0,964	-0,878	1,000			
% Ca	0,939	-0,779	0,979	1,000		
% N	0,861	-0,987	0,939	0,866	1,000	
% Collagen	0,838	-0,945	0,949	0,910	0,976	1,000

From these tables it should be noted that the most of the mechanical properties were negatively correlated with the compositional properties.

The Pearson's correlation show that all the high correlated physicochemical properties have significant statistical level ($p<0.05$). According to the correlation coefficients, the elastic response E_{elast} has a strong relationship with porosity, phosphate and calcium and a weak relationship with carbonate and collagen content.

Elastic components E_{ve} of viscoelasticity are strongly correlated to the nitrogen content of bone meanwhile they are less correlated to calcium content and porosity. The viscous component η_{ve} of viscoelasticity are affected by different physicochemical properties but they are poorly correlated to values reported in this study. Particularity, the first viscous component is mostly correlated to carbonate and nitrogen content while the second viscous component is more correlated to phosphate, calcium and collagen content.

Hardness H and viscoplasticity are correlated to the same properties (CO_3W%, PO_4%, Nitrogen% and collagen %) and they are poorly correlated to porosity.

Globally, porosity affects the elastic response of bone but not those properties linked to permanent deformation and viscosity. This fact is in good agreement to previous studies which have reported a strong relationship between this structural characteristic and the elastic response of bone (Currey, 1969a; Ho Ba Tho et al., 2012; Vanleene et al., 2008). Nitrogen content seems to play an important role in the mechanical response of bone. It was found that this element is very linked to almost all the mechanical properties. This fact could be explained by (Dominguez et al., 2011) who proposed that nitrogen is very linked to enzymes and proteins responsible of the increase of resorption and reduction of bone formation with aging.

C. Multiple regression analyses

Multivariable regressions were computed in the non-normalized experimental data. These regressions were carried out using the physicochemical properties that are in a good correlation and could fit better the mechanical response. It must be mentioned that in this work we consider that all physico-chemical variables are independent even if they are strongly correlated (see table 3.6). They will be considered different just when multicollinearity is detected.

These regressions were performed to obtain the best fit of the experimental data and to assess the relevance of each physicochemical property to increase or decrease the mean value of the mechanical response.

The model used for these regressions is represented by the equation:

$$M_{property} = Constant + A * X_{Property} + \ B * Y_{property} \dots ..$$

Where, M is the mechanical property and X, Y… are the stronger correlated physicochemical properties and the sign positive or negative indicate their effect in the mechanical response. In addition, square multiple coefficients (R^2) are provided to prove the explanatory power of the model with the selected physicochemical properties.

For each mechanical property, the follow equations were found;

Elastic response

The equation obtained from the multivariable regression is:

$$E_{elast} = 73.7 + 8.03 * PO_4\% - 4.42 * Porosity - 4.21 * Ca\%$$

$$R^2 = 0.971$$

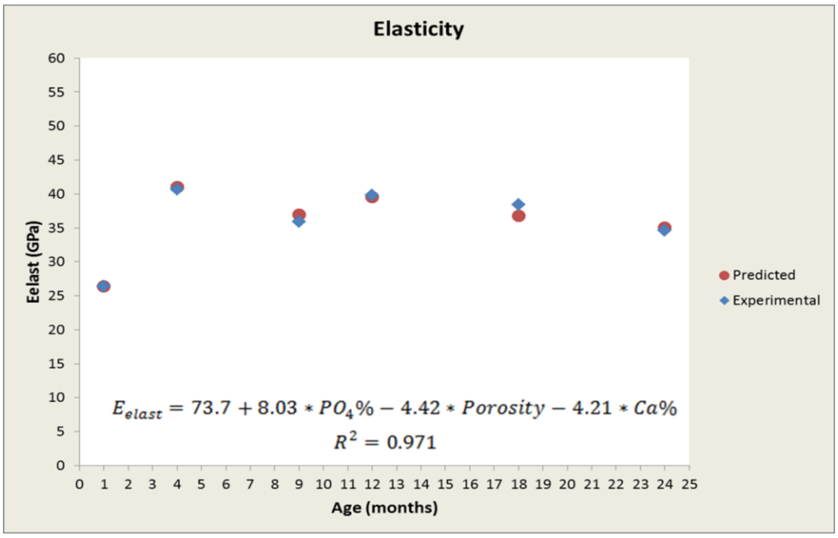

Figure 3.6 Values of the elastic response obtained from: ♦ the experimental data obtained from the nanoindentation tests and • from the prediction equation computed by multivariable regression analyses as a function of bone porosity, phosphate and calcium content with R^2= 0.971.

According to the prediction equation, the elastic response reacts positively to the increase of phosphate (elastic response varies by about 30%) but negatively to the increase of porosity (values vary by about 33%), and calcium (variation of about 17%). According to (Vanleene et al., 2008) porosity decrease with age and affects the elastic response of bone. In addition excess of calcium is associated with bone pathologies (Dent et al., 1965) and could decrease the stiffness of bone material.

Viscoelasticity

For the first elastic components of viscoelasticity, the following equations were computed:

$$E_{ve1} = 110 - 55.0 * N\% + 7.27 * CO_3W\% + 5.76 * Collagen\%$$

$$R^2 = 0.997$$

$$E_{ve2} = 1278 - 396 * N\% - 60.2 * CO_3W\% + 18.9 * PO_4\ \% + 11.2 * Collagen\%$$

$$R^2 = 0.999$$

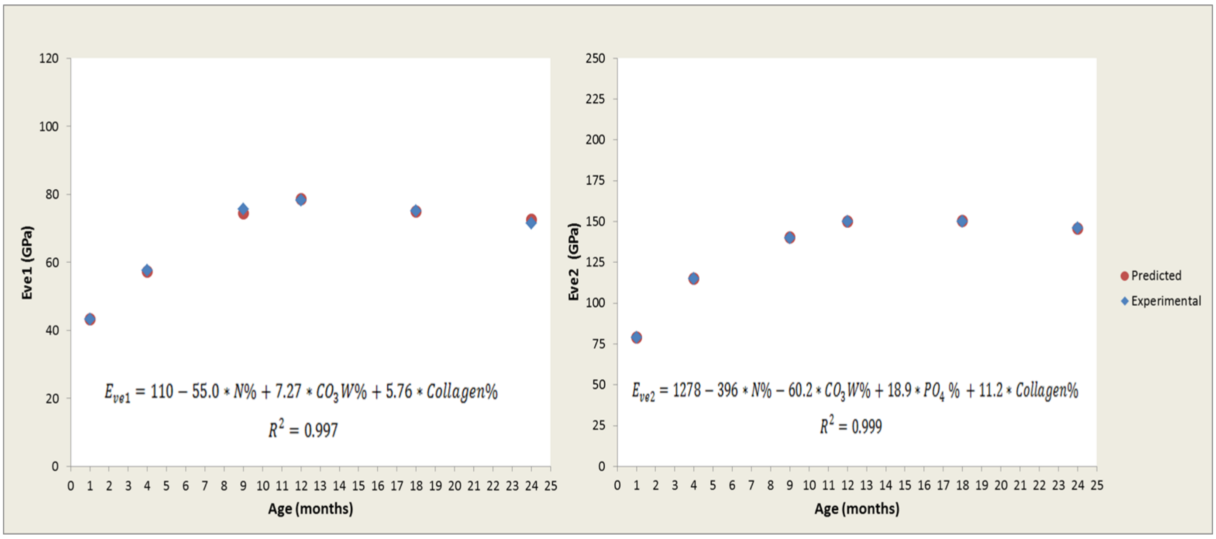

Figure 3.7 Values of the elastic components of viscoelasticity obtained from: ♦ the experimental data and • from the prediction equation computed by multivariable regression analyses as a function of: For the elastic component E_{ve1} bone carbonate, nitrogen, collagen and phosphate with $R^2 = 0.997$. For the viscous component E_{ve2} bone nitrogen, carbonate and collagen with $R^2 = 0.999$

According to the prediction equation, the elastic component E_{ve1} reacts positively to the increase of carbonate (variation about 13%) and collagen (21%) but negatively to the increase of nitrogen (35%). Meanwhile the second elastic component reacts positively to the increase phosphate (variation close to 4%) and collagen (about 4%) but it is affected by the increase of nitrogen (22%) and carbonate (10%). Taking in account the information proposed by the prediction equations, nitrogen content is a critical parameter that affects the elastic response of viscoelasticity. According to (Jarvis, 1997), nitrogen content present in human bone decrease with burial age and acts as an inhibitor of decomposition during the initial period of interment.

For the viscous components of viscoelasticity, the correlation coefficients were low for all the physical chemical properties. Nevertheless, the following equations were computed with those that are lightly correlated and are able to reproduce the chaotic aspect of the curve:

$$\eta_{ve1} = -10236 + 2733 * N\% + 1097 * CO_3W\% - 160 * Collagen\%$$

$$R^2 = 0.740$$

$$\eta_{ve2} = 420 + 17.3 * P0_4\% - 12.9 * Ca\% - 8.60 * Collagen\%$$

$$R^2 = 0.874$$

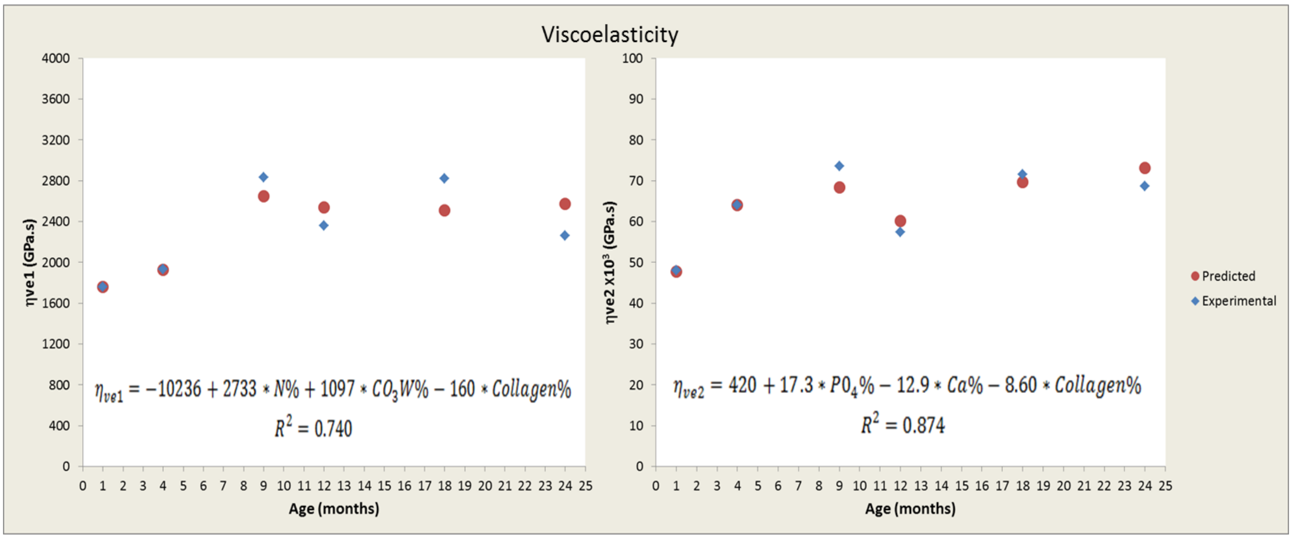

Figure 3.8 Values of the viscous component of viscoelasticity obtained from: ♦ the experimental data and • from the prediction equation computed by multivariable regression analyses as a function of: For the elastic component η_{ve1} bone nitrogen, carbonate and collagen with R^2= 0.740. For the second viscous component η_{ve2} bone phosphate, calcium and collagen with R^2=0.874

According to these results for the first viscous component, η_{ve1} of viscoelasticity reacts positively to the increase of nitrogen (19%) and carbonate (21%) and negatively to collagen (6%). Meanwhile the second viscous component η_{ve2} reacts positively to the increase of phosphate (12%) and negatively to the increase of calcium (9%) and collagen (8%).

In summary, the predicted variables which affect the viscoelastic behaviour of bone take part in bone capacity to accumulate and to release kinetic energy during and after a mechanical stress. One should note that R^2 of the viscous components are lower than the elastic components of viscoelasticity. This fact denotes that other parameters are necessary to better fitting the viscous elements of viscoelasticity. Others factors could be the hydration state of the sample. It is known that viscoelastic response could be also affected by layered particles of water and other fluids (Eberhardsteiner et al., 2014). These particles may play an important role as damping elements of the viscoelastic response.

Hardness

For bone hardness, the following equation was computed:

$$H = 18.3 - 6.16 * N\% - 1.65 * CO_3W\% + 0.368 * Ca\% - 0.0780 * Collagen\%$$

$$R^2 = 0.991$$

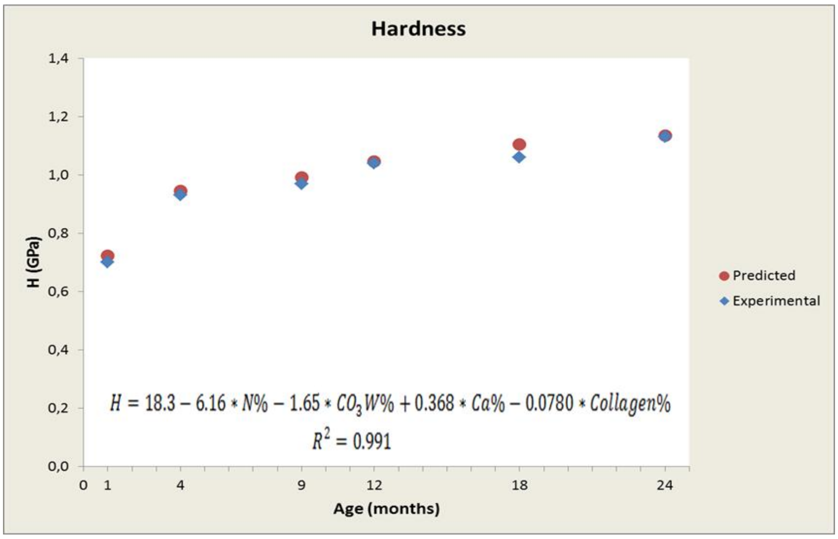

Figure 3.9 Values of the bone hardness obtained from: ♦ the experimental data obtained from the nanoindentation tests and • from the prediction equation computed by multivariable regression analyses as a function of bone carbonate, nitrogen, calcium and collagen with R^2= 0.991.

Hardness is related to bone strength. According to our results, this property reacts positively to the increase of calcium (6%). This calcium is an essential mineral involved in bone mass and structure. Meanwhile the increase of nitrogen (24%), carbonate (18%) and collagen (2%) seem to have a negative effect in bone toughness.

Viscoplasticity

The viscoplastic response of bone could be described the following equation as:

$$\eta_{vp} = 4810 - 1457 * N\% - 418 * CO_3W\% + 97.8 * Ca\% - 53.5 * Collagen\%$$

$$R^2 = 0.999$$

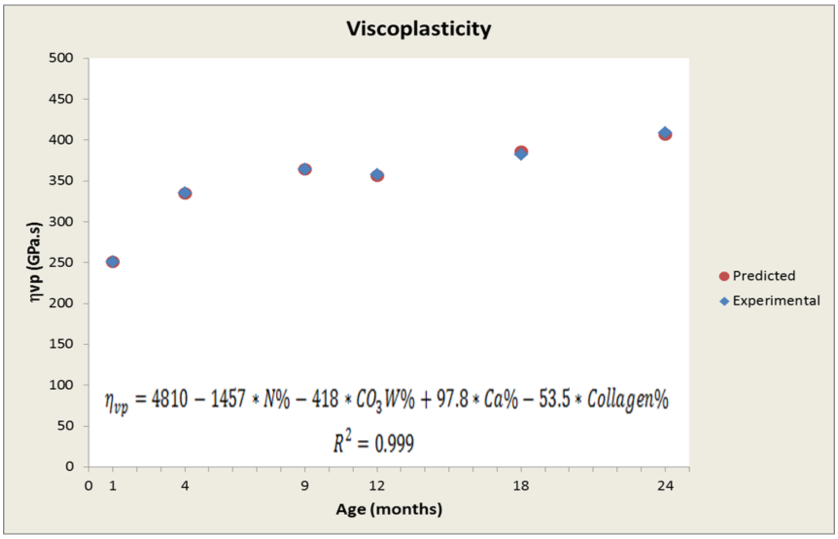

Figure 3.10 Values of the bone hardness obtained from: ♦ the experimental data obtained from the nanoindentation tests and • from the prediction equation computed by multivariable regression analyses as a function of bone carbonate, nitrogen, calcium and collagen with R^2= 0.999.

Viscoplasticity is related to the permanent deformation of the bone structure when a constant stress is hold during a considerable amount of time. According to our results, this property reacts positively to the increase of calcium (6%); meanwhile it is affected negatively by the increase of nitrogen (21%), carbonate (17%) and collagen (4%). The organic components of bone as collagen fibrils take part in the elastic recovery of bone. This could justify why the increase of collagen can affect negatively the viscoplastic response of bone.

R^2 coefficients vary from 74 and 99% and are able to correlate the variation in the mechanical properties to the variation of the physicochemical properties. Nevertheless, the prediction variables were selected because they provide a good R^2 coefficient. This does not mean that others physico-chemical variables cannot affect the mechanical properties of bone. Nevertheless, this information could be useful to understand which mechanical properties of bone are affected by the variation of some physico-chemical properties. In the particular case of viscous components of viscoelasticity, the remaining ~25% can be associated to the derived parameter not included in the regression.

D. Morphological characterization by AFM

Understanding the mechanics of living bone and the structural relationships that make possible its mechanical behaviour continues to be a major scientific challenge. One of the most important aspects of this challenge is to understand the nanoscopic interplay between the basic building blocks of bone. It is known that bone is primarily composed of mineralized collagen fibrils (Revenko et al., 1994) and hydroxyapatite crystals. In this case, we are interested in characterizing the micro morphology of rat cortical bone and then, we will show some mineralized collagen fibrils found across the endosteal region of the cortical shell.

Images of the cortical shell were performed using the contact and tapping AFM mode. Particles analyses for all ages were carried out in the mineral crystallites exposed in the AFM images. However, mineralized collagen fibrils were observed only in bone sample of 9 months old. Within this sample, collagen fibrils were frequently observed close to the endosteal zone of the posterior zone (figure 3.11). Because of these images, we have been able to carry out section analysis to measure the D-band periodicity and to verify the alignment direction of the mineralized collagen fibrils.

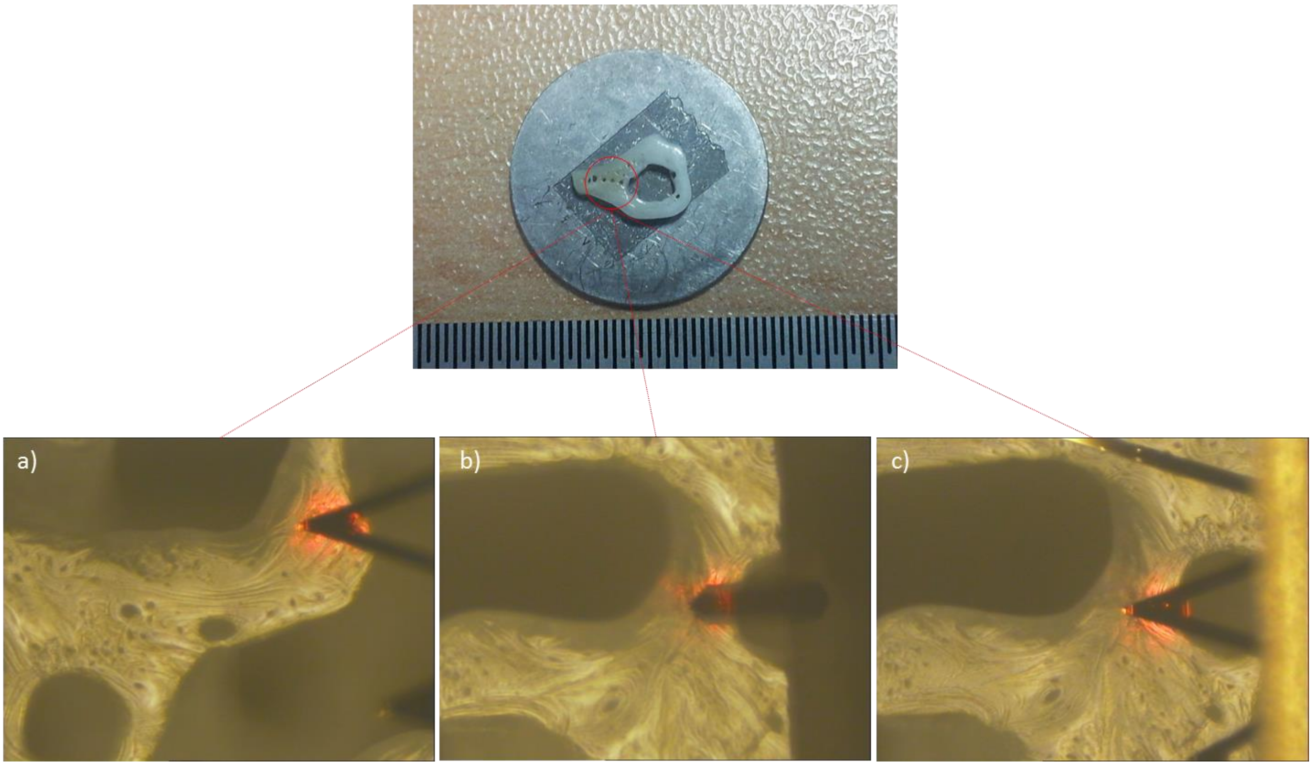

Figure 3.11 Zone of the rat cortical shell where collagen fibril can be imaged. These zones are near to the porous of the posterior zone and they were particularly identified due their brown colour that suggests a possible depletion in mineral content.

Morphological organization of the lamellar shell of the rat bone is showed in figure 3.12.

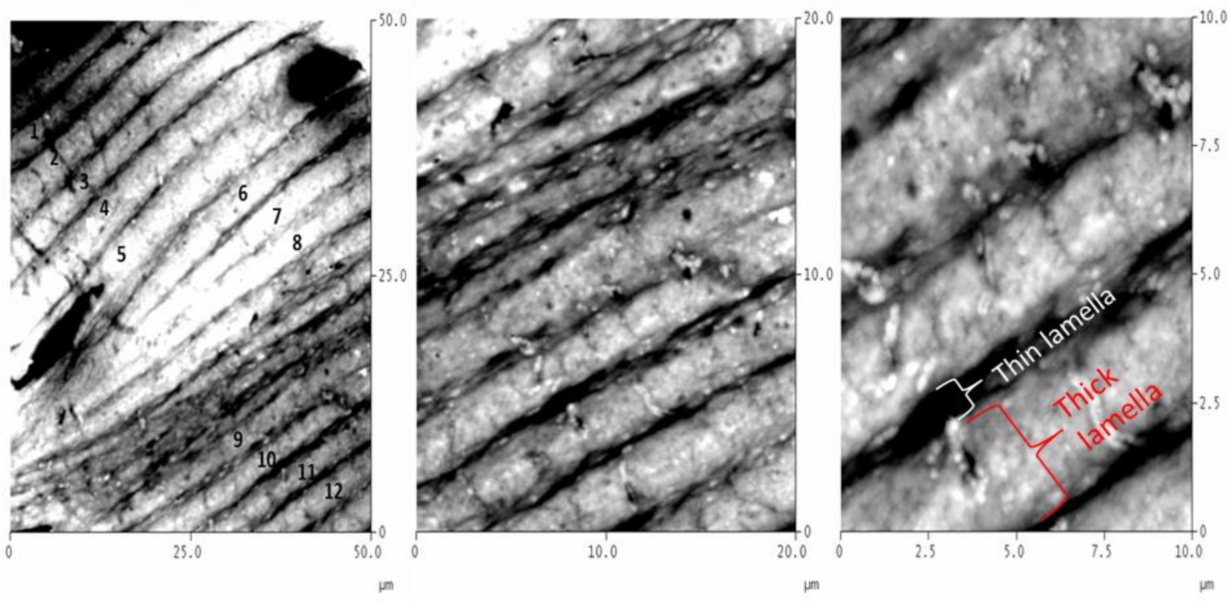

Figure 3.12 Contact mode height AFM images of the interstitial lamellae of the rat cortical shell. The scan rate was ~3.0 Hz and the z-scale=150 nm.

Osteons with their representative inner lamellae were rarely observed. This fact could be due to the evolution of the tissue morphology with age. Bone surface passes from a very porous structure (1 month old) to a very lamellar in the periosteal zone (4 to 9 months old) (Vanleene et al., 2008).

Before the surface roughness analysis, the AFM images must be processed adequately. To achieve this task, all AFM the images were subjected to the same order of noise and artefacts reduction by flattening and plane fitting process. The flatten allows us to subtract a number of line of data from each line of data meanwhile the planefit order allow to remove other flattening artefacts (streaks). After this, values of the surface roughness Ra were found to vary between 49.5 and 57.3 nm for an area of 50×50 µm^2. This value confirms the efficacy of the protocol for the preparation of samples surface.

Then the thickness of each lamella was measured by section analyses. The section analyses allow us to quantify the distance between two points chosen from the AFM image. The points were placed to compute the width of the thick lamella and the thin lamella. The mean values were 2.8 ± 0.4 µm for the thick lamellae and 1.1 ± 0.2 µm for the thin lamella.

Thickness values for the combined lamellar bone (thin and thick lamellae) were found to vary in a range between 3 and 6 µm. These values are in agreement with previous values reported by (Katz et al., 1984).

Mineral crystallites mostly platelet-shape were observed for all ages. Results of the mineral organization inside bone structure are presented in figure 3.13.

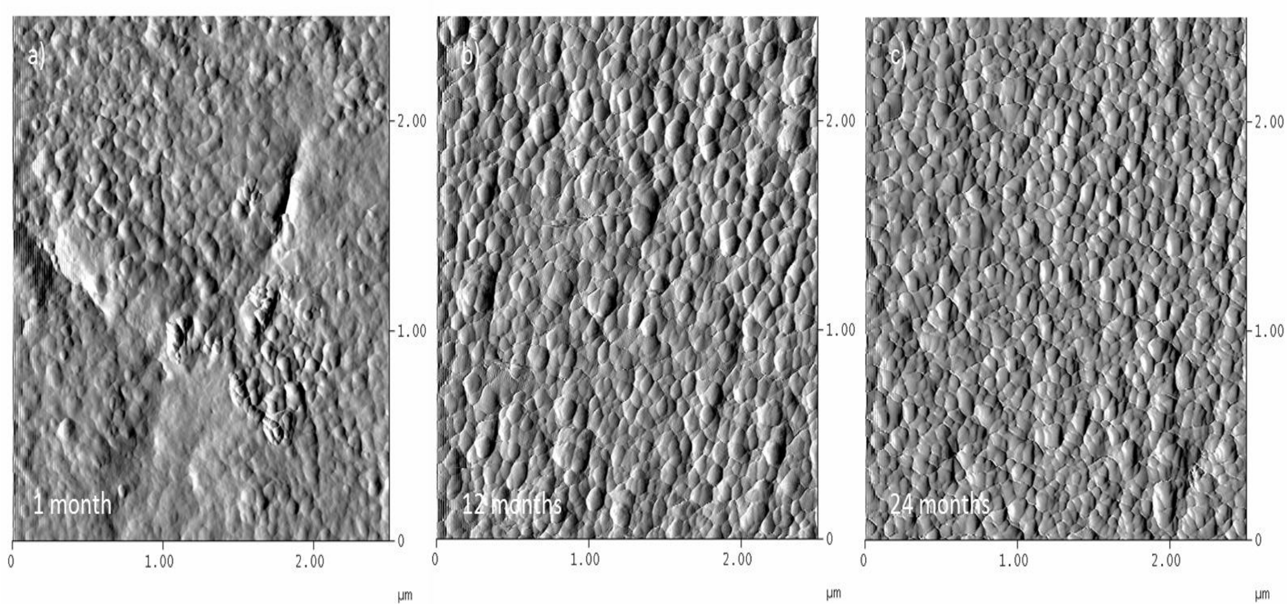

Figure 3.13 Contact mode deflection AFM images of the mineral crystallites, scan rate ~3 Hz and data scale 45 mV obtained from a) sample of 12 months old and b) sample of 24 months old.

For all the bone ages was found that mineral crystallites trend to have mostly a platelet-like shape than a needle-shape. Some images were selected to measure their apparent crystals size. The results of the particles analyses are presented in Table 3.7.

Table 3.7 Morphological characterization of mineral crystallites through the rat life span computed by particle analyses in NanoScope®II version 5.31R1

	Age (months)					
	1	**4**	**9**	**12**	**18**	**24**
Height (nm)	1.4 – 48.7 3.8	1.8– 20.4 3.9	2.0 – 38.0 4.8	1.5 – 62.7 4.3	1.6 – 62.7 4.8	1.3 – 29.4 4.6
Diameter (nm)	11.1 – 929 54.1	2.2 – 126.8 55.2	11.0 – 657 67.5	22.0 – 552 63.6	11.0 – 641 43.7	22.0 – 943 51.5
Length (nm)	13.8 - 580 45.0	2.8 - 240.7 59.4	13.8 – 870 79.2	27.6 – 610 74.6	13.8 – 809 62.3	27.6 – 706 73.4
Width (nm)	13.8 – 356 31.2	2.8 – 106.9 34.2	13.8 – 352.2 48.5	27.6 – 449 42.5	27.6 – 549 31.6	27.6 – 403 37.8

min – max values and mean value

Values reported must be analysed with precaution due to the dilation phenomena present in the AFM images and the software limitation to differentiate the real size of the grains. This phenomenon could affect the curvature of the objects present in the image. Nevertheless, from these values it should be noted that crystals increase slightly their size with age and decrease during senescence. This fact suggests that the increase of the mechanical properties with age could be also linked to the maturation of the mineral crystallites and could explain the small decrease noted in the values during the senescence.

Imaging these mineralized fibrils and their structural relations inside bone is a daunting task since both the fibrils and the mineral plates are very small. The AFM images obtained in native state are presented in figure 3.14.

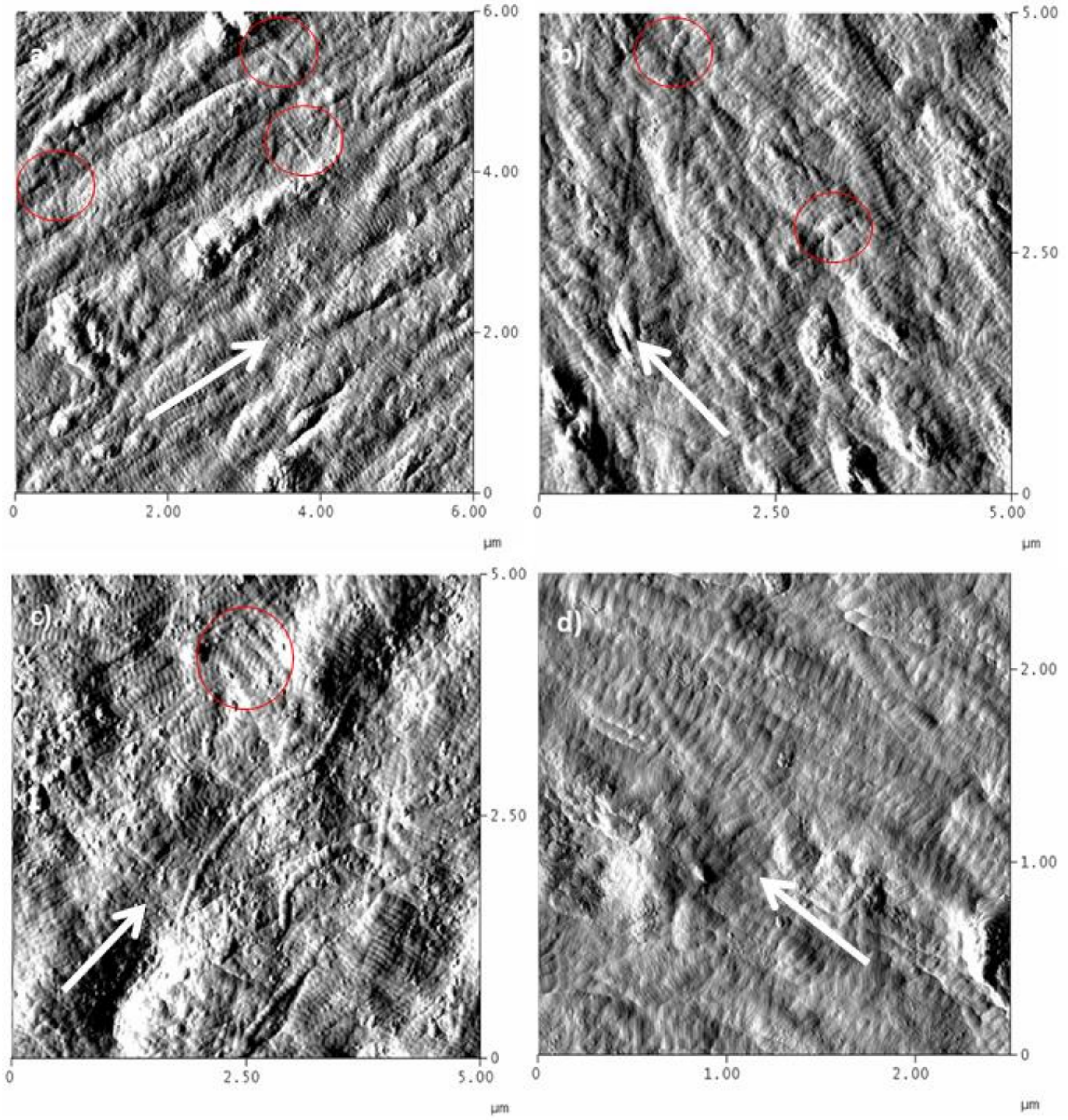

Figure 3.14 Mineralized collagen fibrils obtained by a), b) and d) Contact mode deflection AFM image scan rate ~1.8 Hz and data scale 18 mV c) Tapping mode amplitude AFM image, scan rate ~1.8 Hz and data scale 650 mV. The arrows suggest a possible privileged direction for fibrils orientation and the circles signal isolated collagen fibrils that cross the privileged orientation.

After magnification of the scale to 1 × 1 µm² section analyses were performed and the D-band patron was quantified. At this scale, the markers used to measure the D-band periodicity could be placed more accurately.

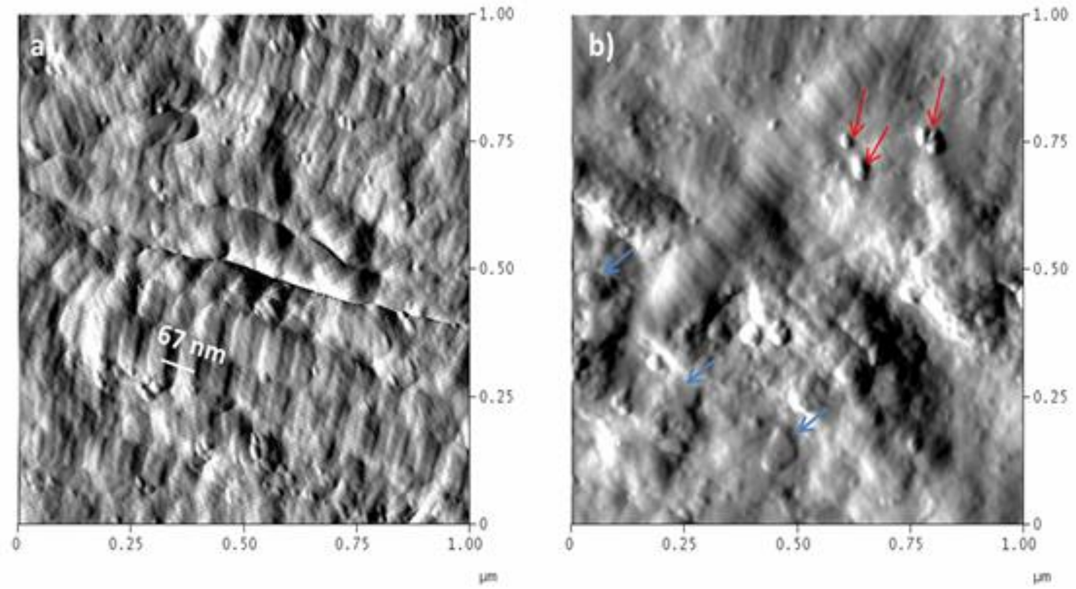

Figure 3.15 Mineralized collagen fibrils obtained by a) Contact mode deflection AFM image scan rate 1.8 Hz and data scale 18 mV, b) Tapping mode amplitude AFM image, scan rate ~2.0 Hz and data scale 600 mV. The white bar in (a) shows D-band periodicity of the collagen fibrils. In this study, this patron was found to be 68.5 ± 1.4 nm. The blue arrows marked in (b) indicate the position of a group of possible platelet-like shape of mineral particles on the surface and the red arrows show some possible artefacts due to room conditions such as dust/contaminants and alumina debris.

Bone nano structure consisting of mineralized collagen fibrils seem to be assembled in a rotated plywood-like fashion. A great variety of structures results from the assembly of mineralized collagen fibrils, thus allowing the adaptation of bones to their actual mechanical function.

Collagen fibrils with a privileged fibrils network orientation are displayed in native conditions in normal bone samples. Measurements of collagen fibrils orientation are found to be between 45° and 60° in the transverse plane of the bone. Nevertheless, the exposition of these collagen fibrils in bone surface and their privileged direction could be due to the polishing stage during samples preparation. Collagen fibrils in native state are not commonly observed in samples with normal surface preparation. This is due to in native state a dense mineral phase recovers all the collagen-network masking the fibrils to the surfaces imaging analysis. The collagen fibrils are commonly detected in cancellous bone or in osteoporotic bones, near to fracture zones or in the interface bone-ligament (Hassenkam et al., 2005, 2004)

Presence of collagen fibrils increases close to the endosteum. This could be due to the porosity of the endosteal region. In addition, endosteal region is composed by small pores and some osteons while periosteal region is composed mostly by lamellar bone (Vanleene, 2006; Vanleene et al., 2008). These characteristics of the endosteal zone could be responsible of its higher biological activity.

The most representative features in the images were the fibrils loosely confined into bundles with varying orientations. However, AFM images such as the figure 3.15 are useful to quantify the D-band periodicity of the collagen fibrils. The band pattern is well known to be an element representative of the collagen present in the organic matrix of bone. According to (Eyden and Tzaphlidou, 2001; Revenko et al., 1994) the banding pattern of collagen fibrils is about 67-68 nm. Nevertheless, this value can vary by some nanometres because of the non-linearity of the piezo scanner. The value computed in this work for the D-band patron periodicity computed across 6 different collagen fibrils was 68.5 ± 1.4 nm. The fibrils extended for several nm, were about 100–140 nm thick and the cross section thus being oval in shape. These values is within the range of previous values reported in the literature (Hassenkam et al., 2005, 2004; Thalhammer et al., 2001).

The second representative feature is collagen fibrils that seem to have a privileged orientation. This fact could match with the simple plywood model with parallel fibrils spanning several micrometres. This plywood structure is believed to be a general structural motif for bone structure (Weiner et al., 1999, 1997). As it should be noted in figure 3.12b and d, the collagen fibrils look to be superimposed one over the other but with a privileged fibrils orientation. It is possible however; that this could be due to the imaged zone, which is near to the endosteum, and the orientation could change for zones placed in the periosteum of the cortical shell. Nevertheless this fact complements the results of (Hassenkam et al., 2004) who found a similar behaviour of the collagen fibrils orientation placed near to the periosteum zone.

As it could be noted in figure 3.15b, in a few spots the mineral crystals appeared to show a structural relationship to the underlying collagen fibrils. AFM images did not show the presence of any needle-shaped minerals. Most of the possible mineral crystallites are similar to those displayed in figure 3.13 with a well-defined platelet-shape. Diameters of the mineral particles were found to vary in a range from 40 nm to about 80 nm. Nevertheless, more zones of the cortical shell must be explored in order to perform more extended particle analyses of the mineral components.

Chapter synthesis

This chapter demonstrates that an elastic viscoelastic plastic viscoplastic model could describe the time-dependent mechanical behaviour of bone. This model can differentiates efficiently the viscoelastic and the viscoplastic response of bone. The results show that mechanical properties assessed by nanoindentation vary with age. These variations are due to the change in the tissue composition, i.e. ratio between mineral and collagen content as evidenced in previous studies (Burket et al., 2011; Busa et al., 2005; Donnelly et al., 2010; Iida and Fukuda, 2002; Isaksson et al., 2010a; Vanleene et al., 2008).

Using the growth model, it is possible to predict the evolution of the mechanical properties with age. Particularly, the elastic response was found to have a maturation age faster (2.7 months) and growth rate higher (1.19) than the other mechanical properties (maturation age 8.7 to 11 months old and growth rate between 0.19 and 0.28). Mechanical properties are correlated to different physico-chemical properties. In addition, each mechanical property could be predicted as a function of different physico-chemical properties. Porosity was found to be strongly linked to the elastic response meanwhile nitrogen content affects all the others mechanical properties.

The AFM images suggest possible evolution of mineral crystal size until 9 months with a slightly decrease during senescence. This fact could be linked and justify the maturation age of the viscoelasticity, hardness and viscoplasticity found to be between 9 and 11 months old. Collagen fibrils showed a privileged orientation (between 45° and 60° in the transverse plane of the bone). D-band periodicity of mineralized collagen fibrils and thickness of the interstitial lamellae are within the range of the values reported in the literature. Unfortunately, the comparison to human life span models is not possible especially due to the absence of experimental data during human bone growth and to the simplicity of the rat bone microstructure (mostly lamellar bone and non-Haversian systems). Nevertheless, life span models of rat cortical bone are useful to quantify the evolution of the mechanical properties mainly for new properties such as the time dependency or to test the influence of dietary or metabolic factors. Next chapter is oriented to assess the µm mechanical properties of human cortical bone, the impact of different densities in the time-dependent mechanical properties and its mechanical heterogeneity at the micro scale.

Chapter 4: Time-dependent and morphological properties of human femoral cortical bone

In this chapter, the time-dependent, elastic and plastic mechanical properties and morphological characteristics of human femoral bones exhibiting different apparent densities were computed and compared. From ESEM images, Haversian systems exhibiting different mineral content were identified and classified by means of their grey levels. The aims of these mechanical assessments are to demonstrate the mechanical heterogeneity of bone at the micro scale and to evaluate the influence of density in the time-dependent mechanical properties.

AFM images were obtained from the bone surface and near to the nanoindentation imprints. These images were used to perform the morphological identification of the nano structural components of bone. AFM images allow one to quantify the approximate size and shape of the hydroxyapatite crystals and D-band periodicity of some isolated collagen fibrils. The purpose of the morphological assessments is to identify possible links between densities and mineral crystals size.

A. ESEM imaging

Cortical bone can be modelled as a complex hierarchical composite interrelating both structure and material properties on five levels of structural organization: molecular, cellular, ultrastructural, microscopic, and macroscopic. For young mammals, the microstructural systems are long parallel lamellar units, plexiform bone, which in older or more mature mammals converts by internal remodelling into multiple concentric lamellar units, young osteons, forming haversian bone (Katz et al., 1984; Rho et al., 1997). Then, by the same remodelling process young osteons become secondary osteons and finally by resorption process in interstitial lamellae.

In order to identify osteons with different apparent mineral contents, ESEM images were performed on each sample. These samples vary in apparent density and they were selected to simulate different aging process (F1-high density-, F2 normal density and F3-low density). These images allow us to select different Haversian systems varying in mineral content (figure 4.1) to be tested by nanoindentation (Bensamoun et al., 2008). According to our knowledge, osteons with low apparent mineral content tend to absorb light and appear darker than others osteons; whereas osteons with high mineral content tend to reflect the light beams and be white. A diagram of this difference is illustrated in figure 4.1.

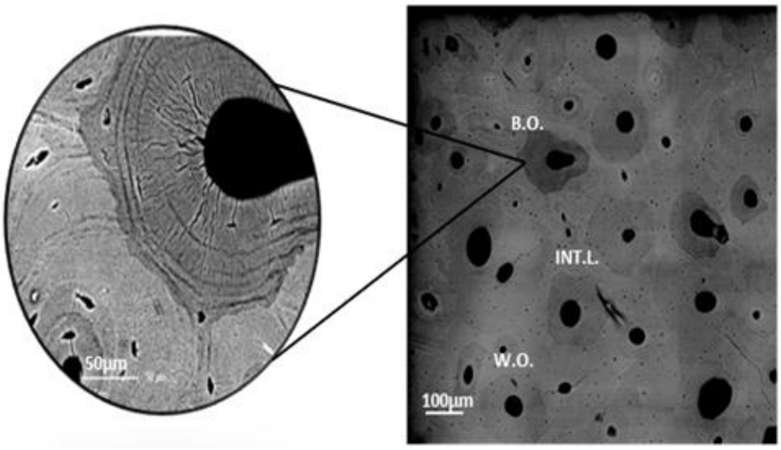

Figure 4.1 ESEM image of the longitudinal axis reflecting different structural composition. In this image, we can recognize Black osteons (B.O), white osteons (W.O.) and interstitial lamella (INT.L.)

ESEM images of each sample show important results (figure 4.2). The presence of Haversian systems with different apparent mineral contents is clearly identified. They highlight on the surface of the low density and normal samples but they are rarely observed in the high-density sample. From ESEM images, it was noted that the increase of porosity is proportional to the decrease of density.

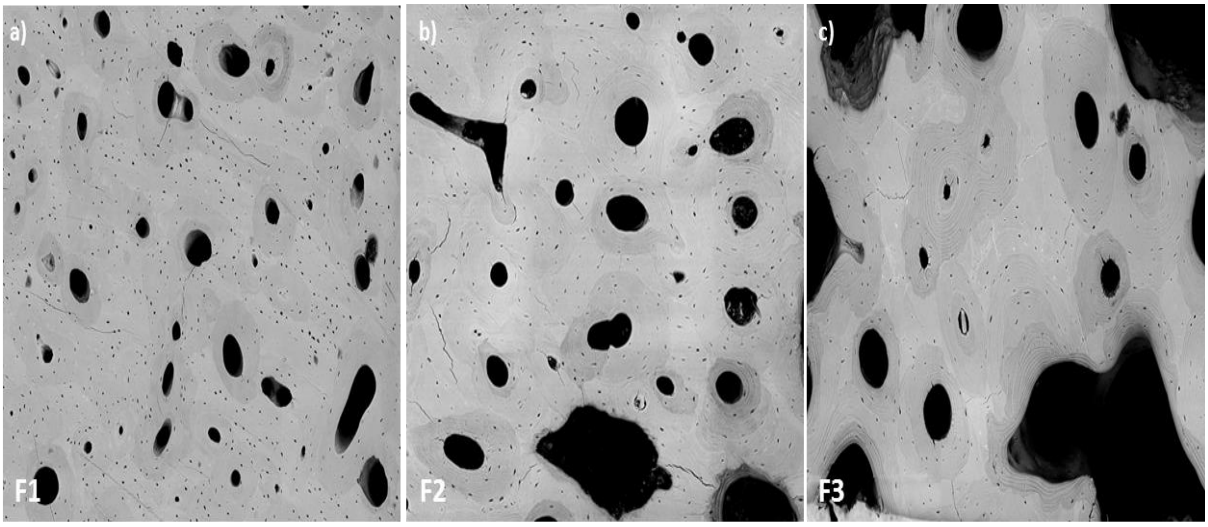

Figure 4.2 ESEM images of the each sample a) high density bone F1, b) normal bone F2 and c) low density bone F3

Nevertheless, the identification of Haversian systems with different mineral content before the nanoindentation tests is not common. In this work, this task is extremely important to expand the concept of bone microstructural heterogeneity. The difference between an ESEM image and a normal microscopy image can be noted in figure 4.3.

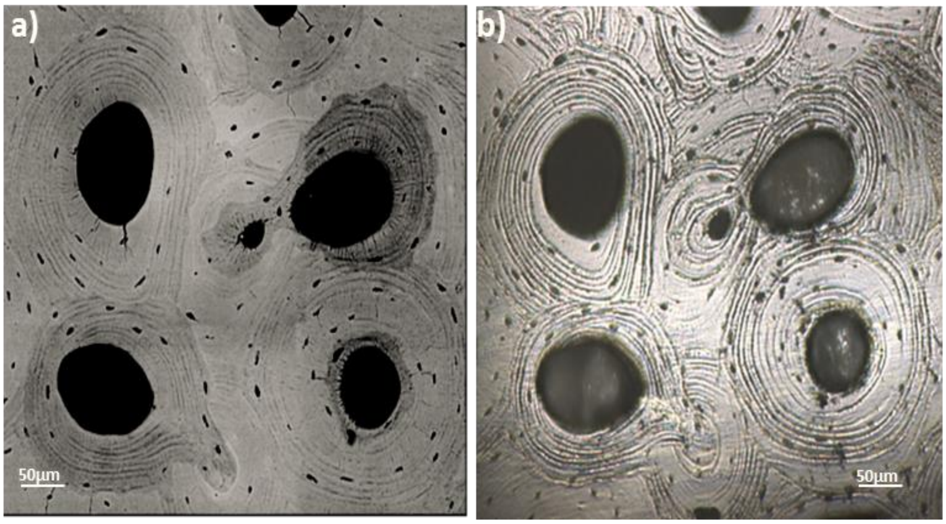

Figure 4.3 Images obtained for the same area from different imaging techniques a) ESEM image and b) Nanoindenter optical microscope of Human cortical bone.

B. Nanoindentation tests

Nanoindentation tests were performed using the protocol and data analysis method proposed by Mazeran et al (see chapter 2 section B). A total of 450 indentations were performed in the longitudinal direction under dry conditions. The mean values ± standard deviations (SD) of the nanoindentation tests for each sample are summarized in Table 4.1.

Table 4.1 Mean values and SD of the nanoindentation results performed on the high-density sample F1, normal density F2 and low density F3

Mechanical properties	**High density sample F1**		
	Interstitial lamellae	**White Osteons**	**Black Osteons**
E_{elast} (GPa)	31.8 ± 3.4	31.3 ± 5.2	28.0 ± 3.8
E_{ve1} (GPa)	75.3 ± 9.0	65.0 ± 9.4	57.7 ± 10.8
$\eta_{ve1} \times 10^2$ (GPa.s)	32.9 ± 5.0	28.5 ± 8.4	27.5 ± 6.2
E_{ve2} (GPa)	141.5 ± 18.3	132.1 ± 20.1	96.9 ± 17.5
$\eta_{ve2} \times 10^3$(GPa.s)	66.5 ± 12.5	62.2 ± 14.2	71.1 ± 12.9
H (GPa)	0.83 ± 0.07	0.78 ± 0.05	0.69 ± 0.08
η_{vp} (GPa.s)	292.0 ± 32.6	273.7 ± 35.0	260.7 ± 32.3

Mechanical properties	**Normal density sample F2**		
	Interstitial lamellae	**White Osteons**	**Black Osteons**
E_{elast} (GPa)	31.5 ± 2.8	32.0 ± 3.8	25.5 ± 5.3
E_{ve1} (GPa)	83.4 ± 15.2	70.8 ± 14.5	50.8 ± 17.2
$\eta_{ve1} \times 10^2$ (GPa.s)	39.8 ± 9.8	29.8 ± 9.6	19.9 ± 9.8
E_{ve2} (GPa)	122.3 ± 17.8	96.8 ± 11.8	87.2 ± 15.6
$\eta_{ve2} \times 10^3$(GPa.s)	72.1 ± 10.9	54.0 ± 6.8	45.9 ± 9.1
H (GPa)	0.80 ± 0.06	0.72 ± 0.06	0.64 ± 0.07
η_{vp} (GPa.s)	282.2 ± 35.2	271.9 ± 30.4	238.2 ± 27.9

Mechanical properties	**Low density sample F3**		
	Interstitial lamellae	**White Osteons**	**Black Osteons**
E_{elast} (GPa)	24.5 ± 4.9	24.1 ± 2.2	19.7 ± 2.9
E_{ve1} (GPa)	70.9 ± 19.1	52.4 ± 10.1	52.7 ± 9.2
$\eta_{ve1} \times 10^2$ (GPa.s)	31.2 ± 14.4	24.8 ± 6.0	23.5 ± 5.8
E_{ve2} (GPa)	100.4 ± 28.3	75.8 ± 17.5	84.8 ± 19.2
$\eta_{ve2} \times 10^3$(GPa.s)	64.4 ± 12.3	54.2 ± 10.0	43.9 ± 7.0
H (GPa)	0.76 ± 0.08	0.63 ± 0.06	0.61 ± 0.1
η_{vp} (GPa.s)	275.2 ± 37.0	230.0 ± 29.0	237.1 ± 35.3

Mean values ± standard deviation.

Results of the nanoindentation tests have been represented by boxplot graphs in order to highlights bone heterogeneity and data variability. Box plots are also used to compare the mechanical response among the different microstructural components.

The elastic response E_{elast} is represented in figure 4.4. E_{elast} shows statistically significant difference ($p < 0.05$) for interstitial lamellae (INTL) and white osteons (WO) of all samples. Black osteons (BO) of the low-density sample F3 are statistically significant different from the high-density sample F1 and the normal sample F2.

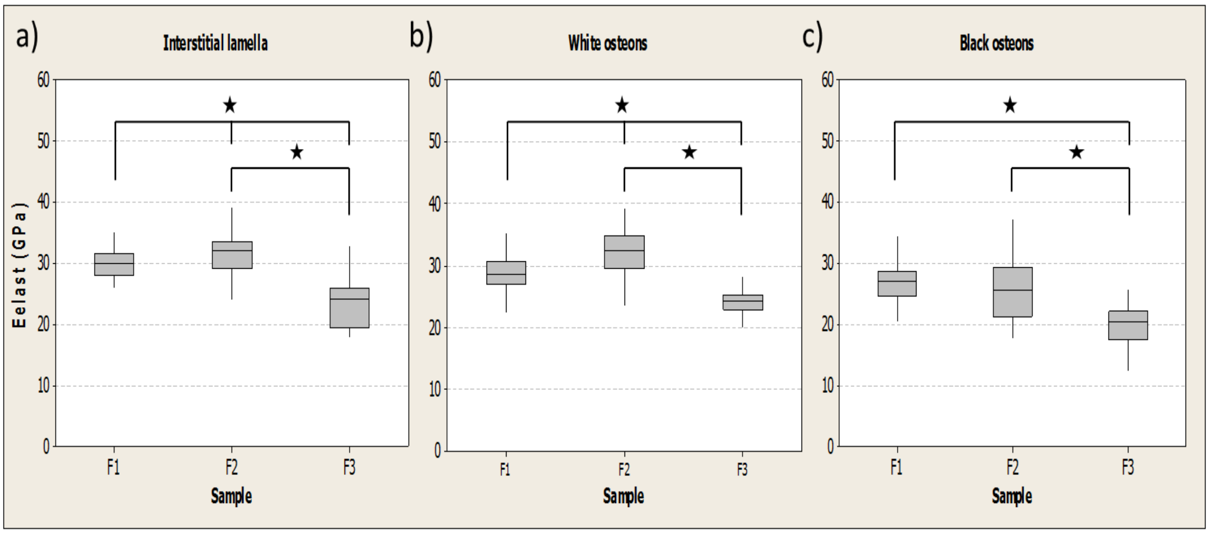

Figure 4.4 Elastic response of human femoral cortical bone of each microstructural component of bone shell for each pathologic and normal bone samples. The stars represent statistically significant differences between the results with a significant value (p<0.05)

In this work, the values of the elastic response E_{elast} for the interstitial lamellae and white osteons were found to be very similar for all samples. (Hoffler et al., 2000) found a similar behaviour between concentric lamellae of the Haversian systems and the interstitial lamellae. They explained their results because of the distal origin of the femoral samples and the mineralization process. This theory was completely different to the classical mechanical differences between osteons and interstitial lamellae proposed by (Rho et al., 2000, 1999). Hoffler et al. highlight for the first time a difference in the mechanical response of proximal or distal samples at the micro scale. In our case, this behaviour could be also due to the maturation state of the tested osteons. This means that those osteons had suffer many remodelling cycles causing that mineral content increases within the structure of those osteons (Katz et al., 1984). By contrast, values of E_{elast} for black osteons were found to be lower than values for white osteons and interstitial lamellae. This behaviour evidences particularly structural difference between mature (white) and newer (black) osteons. However, the values are higher than those reported by (Bensamoun et al., 2008) for osteons with the same classification. Nevertheless, this fact could be due to the indentation protocol, indentation depth, and the hydration state of the sample.

The viscoelastic behaviour is described by two Kelvin-Voigt elements. The values computed for the elastic component E_{ve1} and for the viscous component η_{ve1} are represented in figure 4.5.

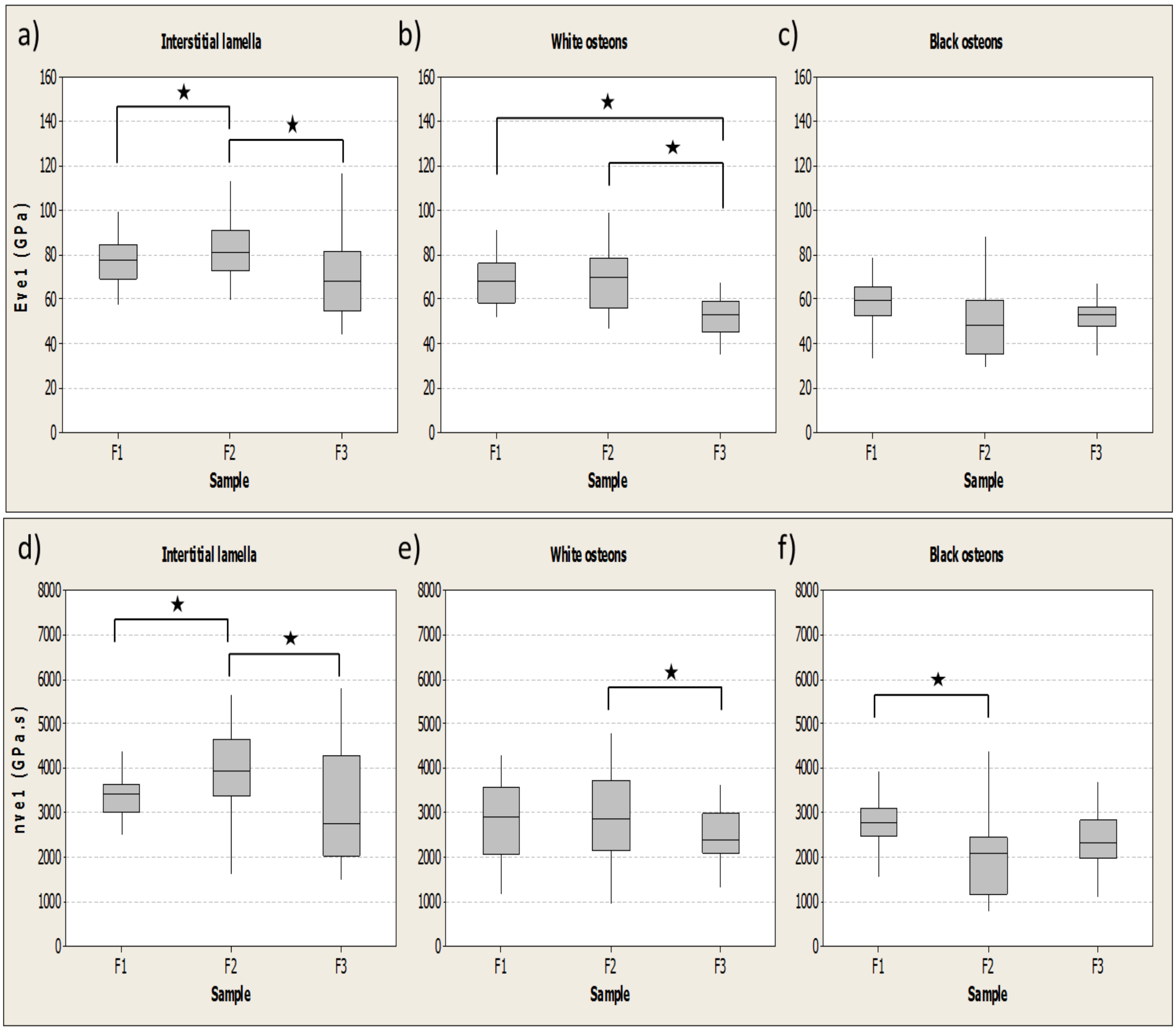

Figure 4.5 First Kelvin-Voigt component of viscoelasticity of human femoral cortical bone of each microstructural component of bone shell for each pathologic and normal bone samples. The stars represent statistically significant differences between the results with a significant value ($p<0.05$)

The values computed for the elastic component E_{ve2} and for the viscous component η_{ve2} are represented in figure 4.6.

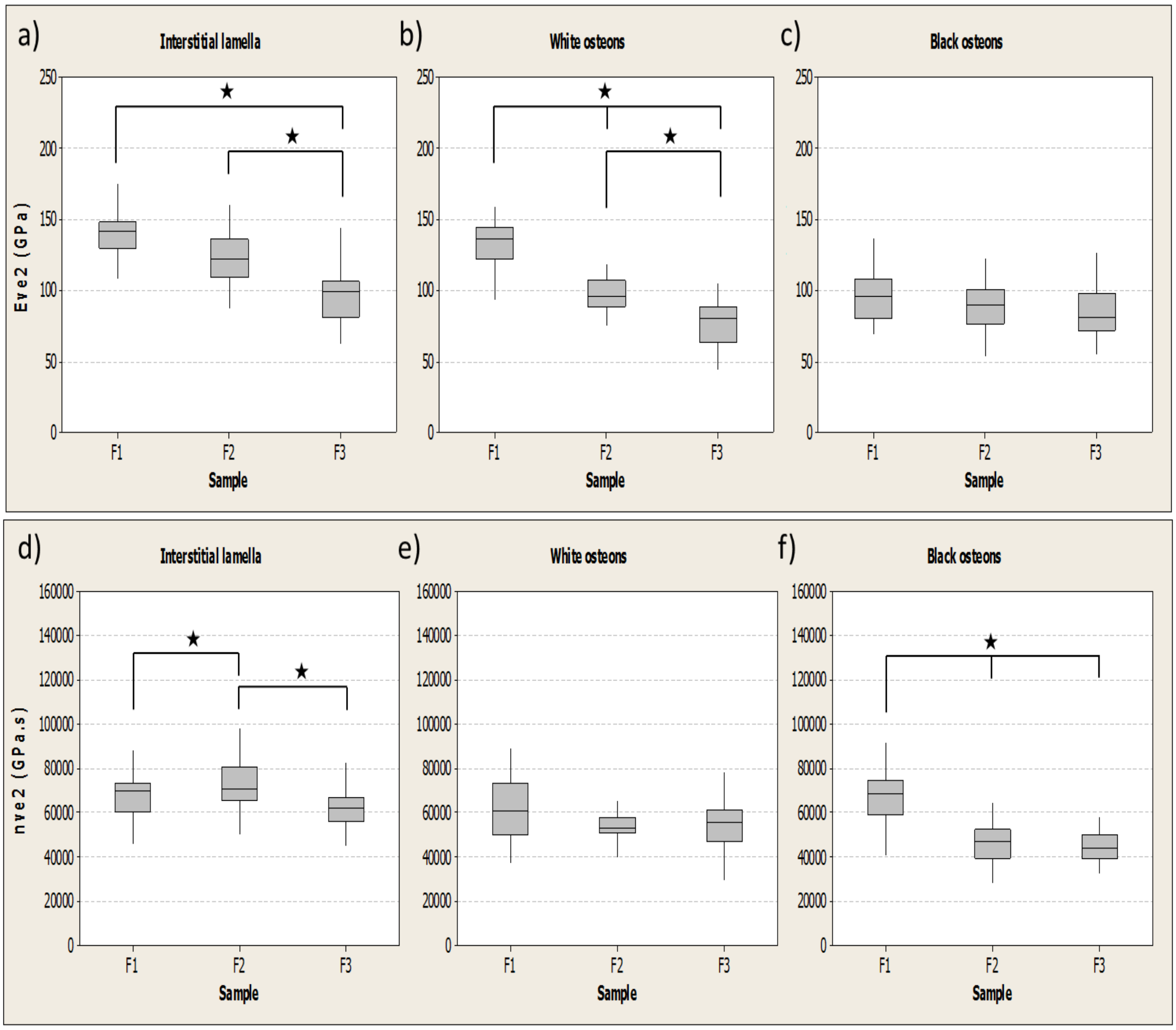

Figure 4.6 Second Kelvin-Voigt component of viscoelasticity of human femoral cortical bone of each microstructural component of bone shell for each pathologic and normal bone samples. The stars represent statistically significant differences between the results with a significant value (p<0.05)

For the first elastic element E_{ve1} (figure 4.5a, b and c), interstitial lamella of normal bone sample F2 is statistically and significantly different ($p < 0.05$) compared to the pathologic samples F1 and F3. White osteons of the low-density sample F3 are statistically significant different ($p < 0.05$) compared to the F1 and F2 bone samples. Nevertheless, black osteons do not show statistically significant differences ($p > 0.05$) for any sample.

For the viscous element η_{ve1} (figure 4.5d, e and f), interstitial lamella of normal bone sample F2 is statistically and significantly different ($p < 0.05$) compared to the pathologic samples F1 and F3. White osteons of the low-density sample F3 are statistically and significantly different ($p < 0.05$) compared to the F2 bone sample. Finally, black osteons of the high-density sample are statistically significantly different ($p > 0.05$) from the normal sample F2.

For the second elastic element E_{ve2} (figure 4.6a, b and c), interstitial lamella is statistical significant different ($p < 0.05$) between the low-density sample the high density and the normal sample. White Osteons (WO) presents significant statistical differences for all samples. Meanwhile non-significant statistical differences were found for black osteons.

Finally, for the second the viscous element η_{ve2} (figure 4.6d, e and f), interstitial lamella of normal bone is statistically and significantly different ($p < 0.05$) from both pathologic bone samples. White osteons do not present significant statistical differences among samples. Black osteons of the high-density sample are statistically significant different ($p<0.05$) from F2 and F3 bone samples.

The viscoelastic response has been assessed by two Kelvin-Voigt models in series. The elastic component E_{ve1} and E_{ve2}, have different mechanical response between all the microstructural components for sample F1 and F2. Whereas sample F3 differences are present between interstitial lamellae and both type of osteons but not between osteons. For the viscous component of viscoelasticity η_{ve1} and $\eta_{ve2,}$ values were found to be different between all the microstructural components only for sample F2. According to the behaviour reported in figures 4.5 and 4.6 density affects more the elastic response than the viscous response of bone viscoelasticity. Normally, viscoelastic response of bone is associated to the collagen network present in bone structure (Currey, 2008; Fratzl et al., 2004; Tzaphlidou, 2005). In normal collagen; the fibril component has a high elasticity (storage modulus) and low viscosity (loss modulus) (Gupta, 2008). Therefore, variation of osteons viscoelastic response could be explained in two factors: the collagen fibrils orientation and the amount of collagen present in the zone. It has been reported that collagen can be oriented longitudinally, transversally or alternating. The study of (Burr, 2002) proposed that changes in the structure of collagen affects the mechanical properties of bone independent to bone mineral density. In addition, viscoelastic response of bone could be affected by the hydration state of the sample. In our case, the nanoindentation tests were performed on wet specimens under dry conditions. As suggested by (Eberhardsteiner et al., 2014), in this state the viscoelastic response of bone could be affected by layers of water located between the crystal interfaces of the extrafibrillar mineral of bone.

Hardness results for each sample are represented in figure 4.7. Interstitial lamella of normal sample F2 is statistically significant different ($p < 0.05$) compared to the low-density sample F3. White osteons of the low-density sample are statistically and significantly different in relation to the F1 and F2 bone samples. Black osteons present statistically significant differences only between the high and low-density samples.

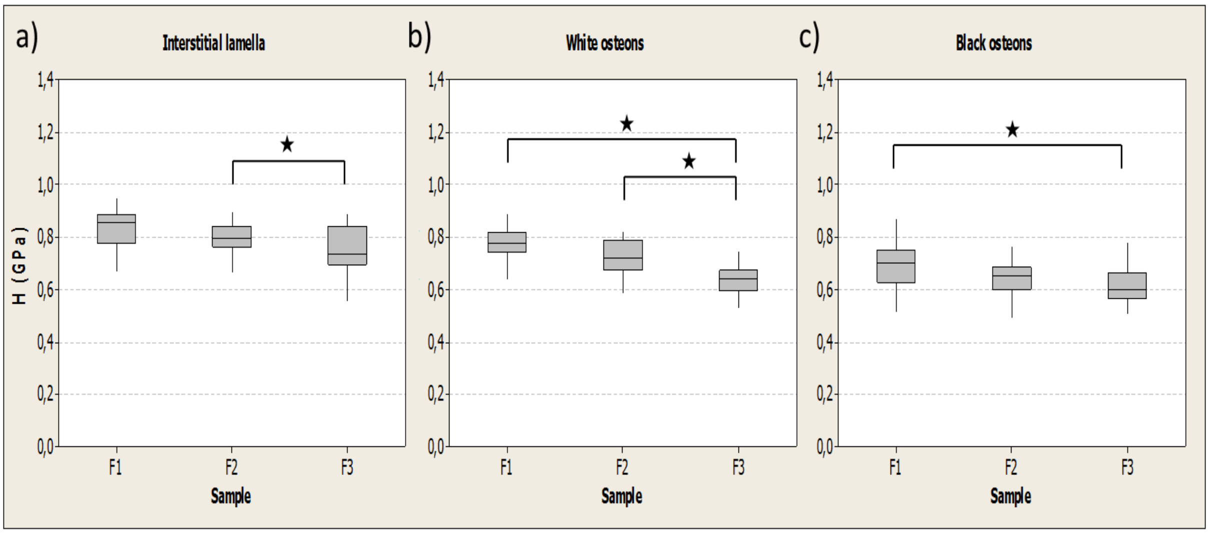

Figure 4.7 Hardness of human femoral cortical bone of each microstructural component of bone shell for each pathologic and normal bone samples. The stars represent statistically significant differences between the results with a significant value ($p<0.05$)

Hardness values were found to be different among all elements of the microstructure for samples F1 and F2. While the sample F3 does not show differences between white and black osteons. Previous studies reported that hardness variation at the micro scale is strongly related to the mineral content, mineralized collagen and tissue hydration state (Hoffler et al., 2000; Michelle L Oyen, 2006; Tjhia et al., 2011). Nevertheless, individual physico-chemical characterization of black and white osteons is needed in order to highlight better interpretations. In comparison with similar studies, in this work hardness values were found to be higher than those reported by (Bensamoun et al., 2008). This fact could be due to the indentation depth of the nanoindentation imprint. The study by (Chen et al., 2007) reported that superficial penetration of the nanoindentation tip creates lower values of hardness.

Viscoplasticity η_{vp} results for each sample are presented in figure 4.8. Only white osteons of the low-density sample F3 are statistically significant different ($p < 0.05$) from the other samples.

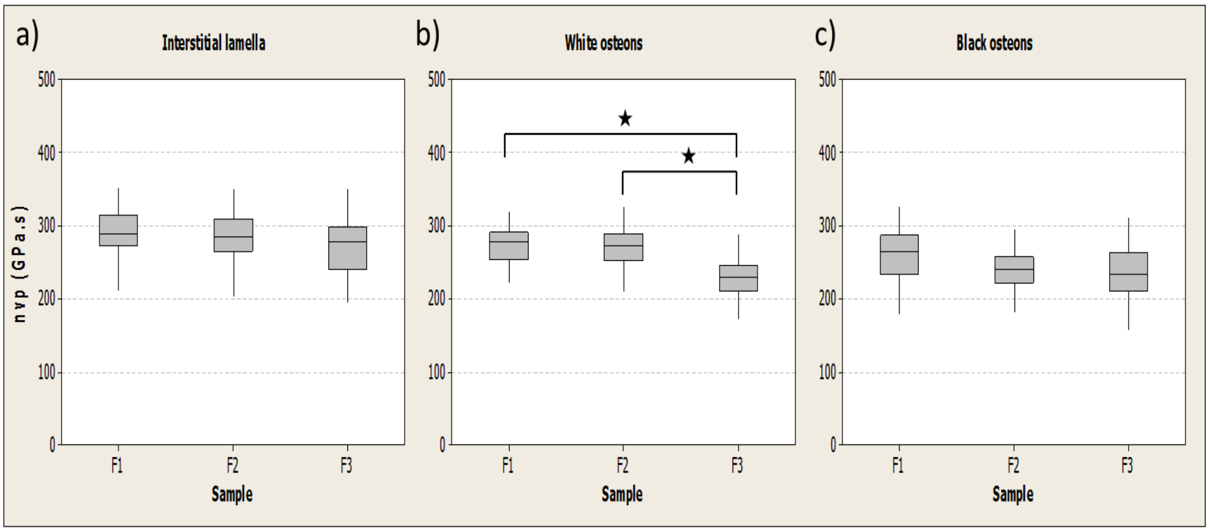

Figure 4.8 Viscoplasticity of human femoral cortical bone of each microstructural component of bone shell for each pathologic and normal bone samples. The ・ represents a significant statistically difference between the results with a significant value ($p<0.05$)

Using the elastic and viscoelastic mechanical properties computed for F1, F2 and F3, the apparent elastic modulus was computed for different strain rates. These strain rates are 0 s^{-1} : to highlight the quasi-static elastic modulus; 0.05s^{-1} to compute the elastic modulus at the strain rate used in the nanoindentation tests and infinite strain rate to highlight the maximum value of the apparent elastic modulus. The values obtained for each sample at each strain rate are summarized in Table 4.2.

The values for the viscoplasticity η_{vp} highlight the different mechanical response between white and black osteons for all the samples. This suggests that osteons structure keep deforming during hold times of the nanoindentation protocol but they do it at different ratio. They confirm the hypothesis of structural differences between osteons. In addition; the study of (Vanleene et al., 2006) suggests that hardness of cortical bone change according to the strain rate of the test highlighting a viscoplastic behaviour.

Table 4.2 Apparent elastic modulus in GPa as a function of a given strain rate for all samples

Strain rate ($\dot{\varepsilon}$)	**High density sample F1**		
(s^{-1})	**Interstitial lamellae**	**White osteons**	**Black osteons**
0	16.8 ± 1.1	15.8 ± 1.4	13.8 ± 1.5
0.05	23.9 ± 1.6	22.5 ± 2.3	21.1 ± 2.3
∞	27.1 ± 2.0	26.3 ± 3.9	24.3 ± 2.9

Strain rate ($\dot{\varepsilon}$)	**Normal density sample F2**		
(s^{-1})	**Interstitial lamellae**	**White osteons**	**Black osteons**
0	17.4 ± 1.6	16.0 ± 1.3	12.3 ± 1.3
0.05	25.5 ± 2.0	24.8 ± 2.1	18.9 ± 2.7
∞	28.7 ± 2.5	29.2 ± 3.5	22.2 ± 4.7

Strain rate ($\dot{\varepsilon}$)	**Low density sample F3**		
(s^{-1})	**Interstitial lamellae**	**White osteons**	**Black osteons**
0	13.6 ± 1.6	12.1 ± 1.2	11.0 ± 1.5
0.05	19.5 ± 2.9	19.1 ± 1.7	15.8 ± 2.1
∞	22.3 ± 4.5	21.9 ± 2.0	17.9 ± 2.7

The box-plot graphs show how apparent modulus values increase with the strain rate. It was found that values of apparent elastic modulus of the microstructural components increase from 60% to 76% for F1, from 65% to 82% for F2 and from 62% to 81% for F3 while the strain rate passes from 0 s^{-1} to infinite. Results are represented in figure 4.9.

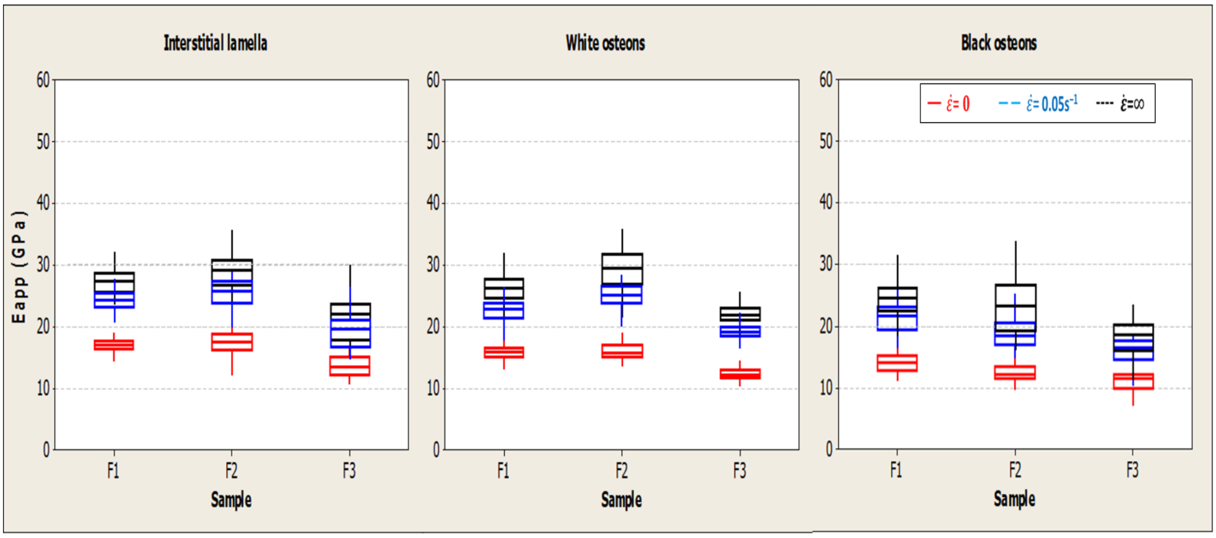

Figure 4.9 Values of the apparent elastic modulus of a) F1, b) F2 and c) F3 represented as a function of the given strain rate 0 s^{-1}, 0.05s^{-1} and ∞.

As for the previous results, in order to establish statistical differences between the values obtained for different strain rates, non-parametric statistical tests were performed over all the output data. The statistical results are presented in Table 4.3.

Table 4.3 Statistical significant differences ($p<0.05$) of the apparent elastic modulus

For a given strain rate 0

Indentation zone	**Interstitial lamella**		**White osteons**		**Black osteons**	
	F2	**F3**	**F2**	**F3**	**F2**	**F3**
F1	≠	≠	ND	≠	≠	≠
F2		≠		≠		≠

For a given strain rate $0.05s^{-1}$

Indentation zone	**Interstitial lamella**		**White osteons**		**Black osteons**	
	F2	**F3**	**F2**	**F3**	**F2**	**F3**
F1	≠	≠	≠	≠	ND	≠
F2		≠		≠		≠

For a given strain rate ∞

Indentation zone	**Interstitial lamella**		**White osteons**		**Black osteons**	
	F2	**F3**	**F2**	**F3**	**F2**	**F3**
F1	≠	≠	≠	≠	ND	≠
F2		≠		≠		≠

The apparent elastic modulus of the cortical bone was found to vary with the strain rate. These values increase by a factor 1.61 to 1.83 between lower and higher values. Elastic modulus obtained for samples F1 and F2 are very similar to those reported by (Abdel-Wahab et al., 2011; McElhaney, 1966) and similar to the studies by (Fan and Rho, 2003; Vanleene et al., 2006) the results of this work suggest that elastic modulus has a strong dependency in the strain rate. This fact highlights the need to consider the effects of the strain rate in the assessment of the mechanical response from the nanoindentation data. Similar to (Cowin, 1983), the results of this work reflects bone adaptability under different stress conditions.

According to the nanoindentation results, the mechanical properties of black osteons are weaker than those ones found for lamellar bone and white osteons. This fact suggests probably that the structural organization is almost finished for lamellar bone and white osteons compared to the black osteons which are in more activate modelling, remodelling process

According to our results, bone density affects the mechanical response of bone at the micro scale. Values of the low-density sample F3 were found to be until 23% lower than the high density F1 and normal F2 bone samples. Nevertheless, these density effects are lower than at the macroscopic level. This could be due to a higher influence of local characteristics as bone composition and roughness at the micro scale. Similar experiments were performed on osteopetrotic (very high bone density) and osteoporotic bone (low density as a consequence of high porosity) using different macroscopic experimental methods showing important differences between samples (Katz et al., 1984; Schaffler and Burr, 1988). At the micro scale, while the results for low-density (F3) bone are understandable in terms of the increased porosity, the results for the high-density (F1) bone are anomalous with respect to its density. The values were lower than expected and sometimes similar to the normal F2 bone sample. Nevertheless, this behaviour is in agreement with previous works (Jämsä et al., 2002; Tjhia et al., 2011) which do not show mechanical differences between bones with high density and normal samples at the micro scale. From the experimental results obtained during this work, it is possible to affirm that at the micro scale density have important effects in the elastic and hardness mechanical properties of bone meanwhile the effects are less apparent for the time-dependent mechanical properties.

At the micro scale, the study of bone mechanical heterogeneity has been underestimated during the last 20 years. A reflect of this is the few publications about that topic found in the literature. For this work, bone mechanical heterogeneity is extremely important to understand bone adaptability and the structural effects of remodelling cycles. Since Wolff 1884, the remodelling process of bone has been understood as a way of modifying the mechanical properties of the bone structure. For us, the Haversian remodelling from interstitial bone, the argument that adaptation occurs to optimize properties requires additional clarification since Haversian bone appears to have inferior mechanical properties to interstitial bone. The different values obtained for the Haversian system confirm bone heterogeneity at the micro-scale. This heterogeneity of the mechanical properties is found to reflect the tissue symmetry; moreover, interstitial bone is stiffer, viscous and more rigid than is Haversian bone.

C. Morphological characterization by AFM

Images of the cortical shell were performed using contact and tapping AFM modes. The images were obtained from the concentric lamellae of the Haversian systems and from the nanoindentation imprints performed on the F2 sample. A diagram of the imaging zones is displayed in figure 4.10.

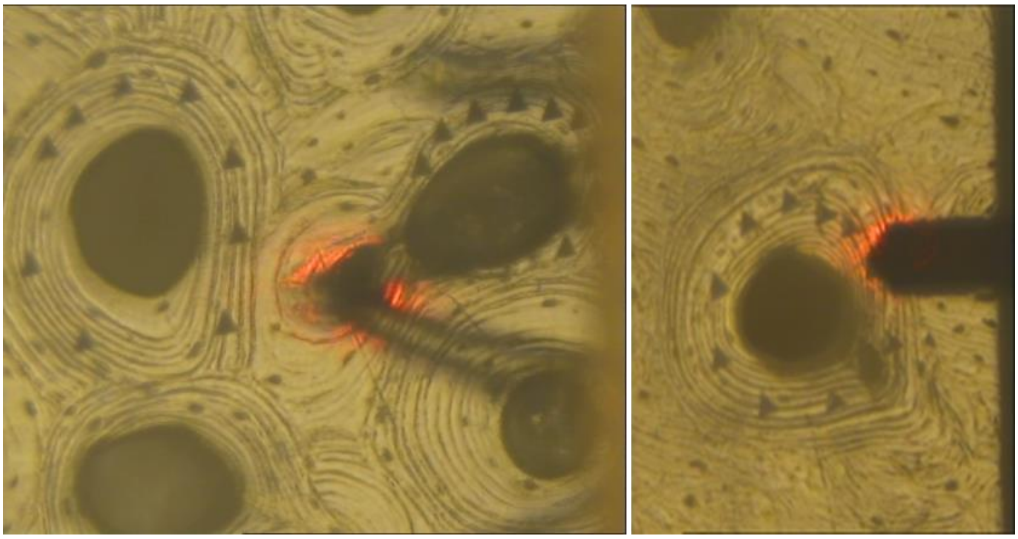

Figure 4.10 Haversian systems with nanoindentation imprints ready to be imaged by AFM technique

The purposes of this morphological characterization are on one hand, to inspect the structural effects of the nanoindentation tests within the bone surface by analysing the zone inside the indentation imprints. On the other hand, to identify the nano structural components of human cortical bone (mineralized collagen fibrils and hydroxyapatite crystals). In addition, AFM images can be used to carry out section analysis to measure the D-band periodicity and to check the alignment of the mineralized collagen fibrils. Moreover, these images are useful to perform particles size analysis over the hydroxyapatite crystals to quantify the crystals size and shape.

White osteons of each sample were imaged in order to measure the thickness of the concentric lamellae. Images were obtained in contact AFM mode and they are presented in figure 4.11. Local surface roughness and thickness were measured by section analyses.

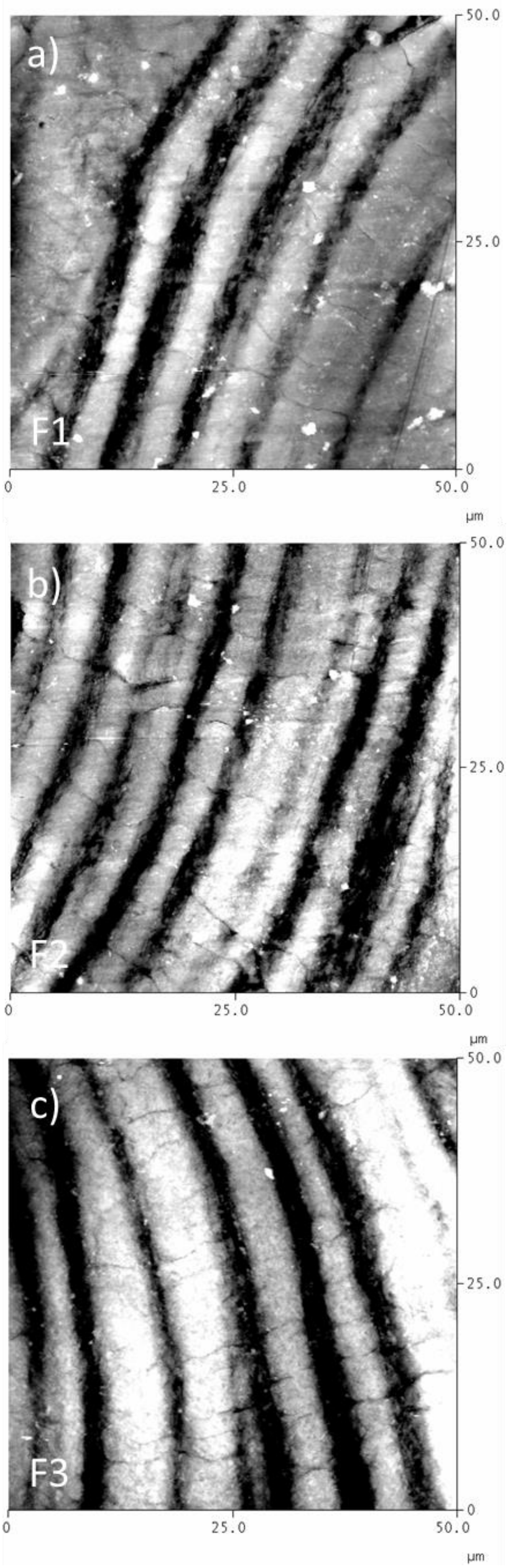

Figure 4.11 Image is showing the concentric lamellae (thick and thin) of the Haversian systems for samples a) high density bone F1, b) normal bone F2 and c) low density bone F3. Height images acquired in contact AFM mode, data scale 250nm.

Images presented in figure 4.11 show the structural organization of the concentric lamellar shell of the human Haversian system. Local surface roughness Ra was found to be higher in the zone of the Haversian systems than in the interstitial lamella zone. In osteons zone, Ra values were found to vary between 43.7 and 76.5 nm for an area of 50 × 50 µm. Meanwhile in the interstitial lamellae zone, Ra was found to vary between 36.7 nm to 51.5nm for an area of 50 × 50 µm.

The distance between consecutive groups of thick and thin concentric osteon's lamellae were measured by section analyses. Thickness mean values and standard deviation for each sample are summarized in table 4.4.

Table 4.4 Mean values and standard deviation of thickness (µm) for the concentric thick and thin lamellae of the bone Haversian systems

	Concentric Haversian system lamellae		
	F1	**F2**	**F3**
Thick	6.0 ± 1.3	5.0 ± 0.9	5.4 ± 1.3
Thin	2.9 ± 0.5	1.9 ± 0.5	2.4 ± 0.6

Section analyses show that thickness of the concentric thick lamellae varies between 4.1 µm and 7.3 µm and for the thin lamellae between 1.4 µm and 3.5 µm. Nevertheless, one should notice that lamellar thickness is quite similar for all the samples. Moreover, the values of lamellar thickness are in agreement with those reported earlier by (Katz et al., 1984; Rho et al., 1998) for human cortical bone. This fact suggests that variation of bone density does not modify the microstructural morphology of cortical bone.

AFM images of the nanoindentation imprints are presented in figures 4.12 and 4.13. Imaging task was difficult because of the imprint depth. If must be highlighted that AFM technique requires very low slope surfaces in order to ensure optimized tip-surface contact.

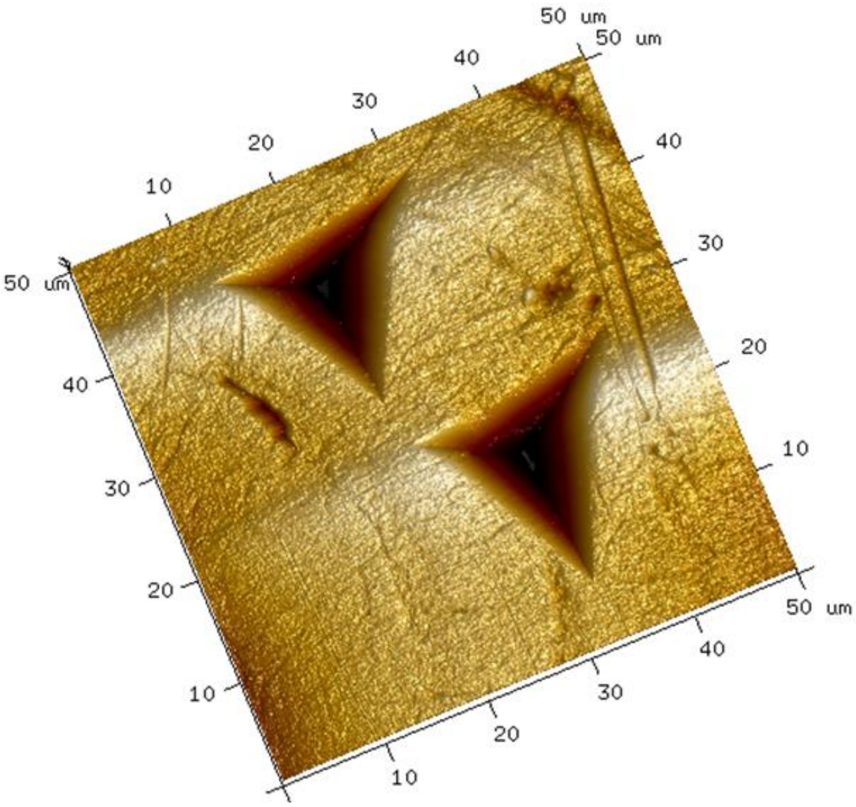

Figure 4.12 Reconstruction of a 3D nanoindentation imprint performed on bone surface. The image was build up from a height AFM image, scan rate ~3.5 Hz and data scale 150nm obtained in contact AFM mode.

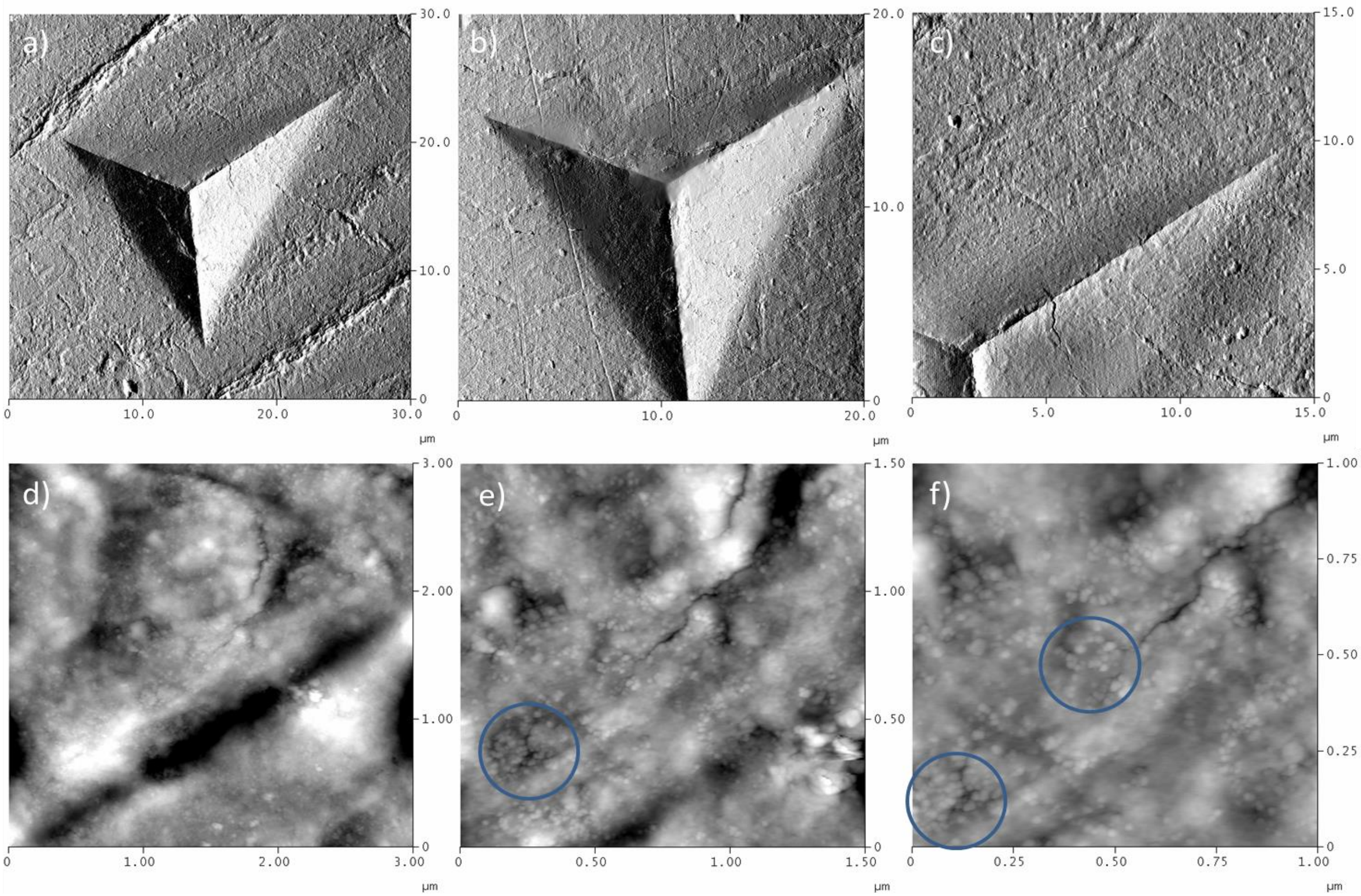

Figure 4.13 Contact mode deflection (a-c) and height (d-f) AFM images of the nanoindentation imprints. Blue circles show mineral particles near to the edges of the nanoindentation imprints.

Moving to the nano scale, zones with typical mineral particles were found (figure 4.14a and 4.14c). Using the Bruker Inc. Nanoscope® analysis software 1.5 and the NanoScope® version 5.31R1, these images were used to carry out particles size analyses in order to determine some geometrical properties (see Table 4.5). Normally, these softwares have deconvolution algorithms to reduce the effects of the tip dilation.

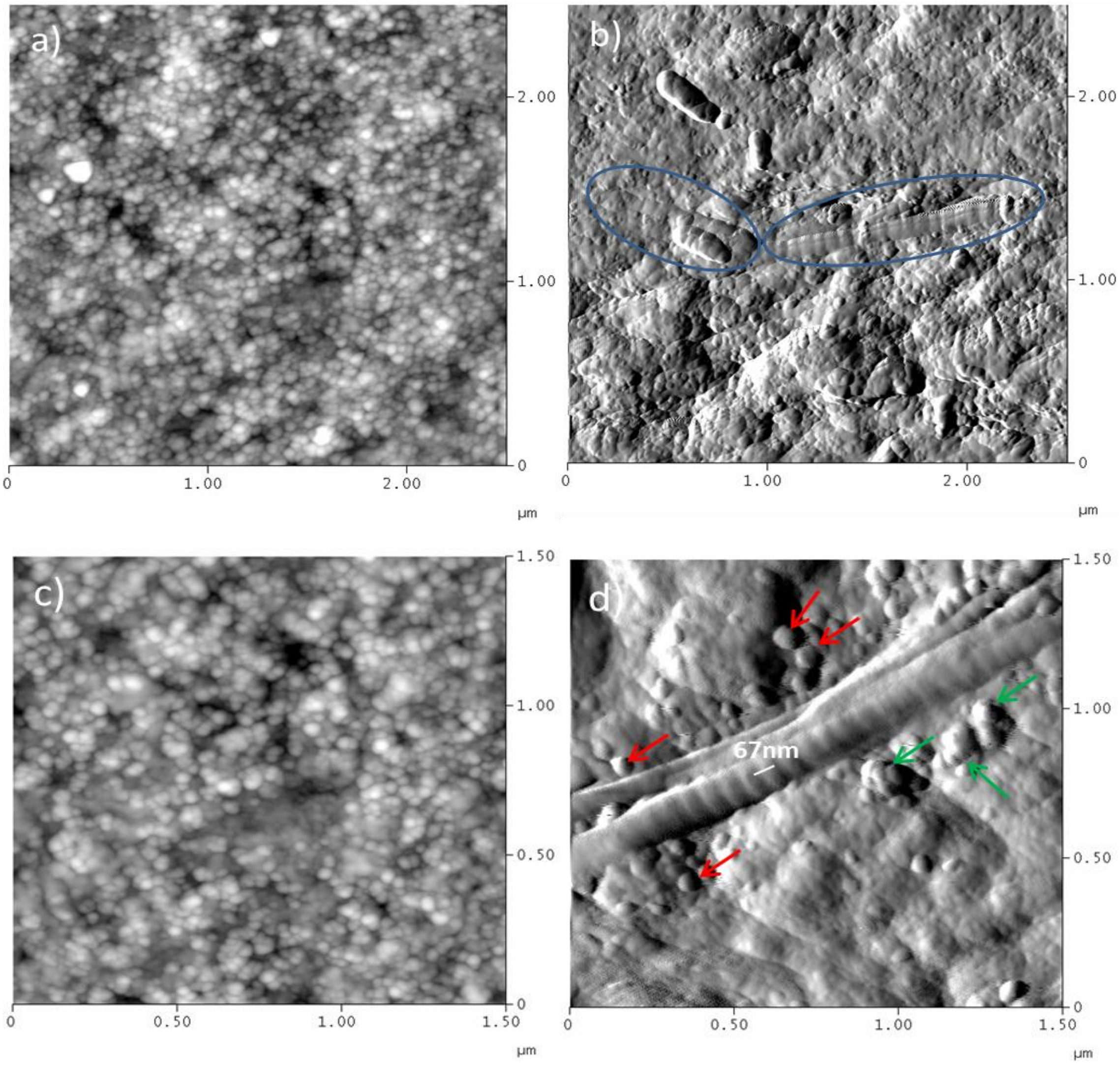

Figure 4.14 Mineral crystals and collagen fibrils of sample F2 imaged by AFM obtained in a) and c) tapping mode height image scan rate ~3.2 and data scale 50nm; b) Contact mode deflection image, scan rate ~1.8 mode of collagen fibrils with a data scale 45mV and d) tapping mode amplitude image, scan rate ~1.8 and data scale 75mV.

Among the parameters that distinguish hard tissue crystals, size is one of the hardest to measure, not only because it is intrinsically variable, especially with crystal maturation, but also because the apparent values for crystals dimensions typically shift with orientation and can vary according to the measure technique ("The Size of Inorganic Particles," 2007) . Other issue is the dilation phenomena present in the AFM images. Since here none others deconvolution algorithms were used to increase the accuracy of the particle analysis. This fact can hold a decrease in the accuracy of the values reported for the particle size. Nevertheless, mean values still being a good indicator of crystals size. Besides, few collagen fibrils were observed. In this work, only two collagen fibrils in native state were clearly identified inside the nanoindentation imprints (figure 4.14b and 4.14d).

Values for the mineral particles size (diameter, width and length) for sample F1, F2 and F3 were summarized in Table 4.7. The letter N represents the number of mineral particles that was clearly identified from the AFM images. Their size values are in good agreement with those reported by (Fratzl et al., 2004; Rho et al., 1998; Rosen et al., 2002). The AFM images show that crystals shape are mostly platelet-like (figure 4.14c and 4.14d) than needle-like shape.

Table 4.5 Values of particle size acquired by AFM particle analysis for all bone samples

N= 75	**High density sample F1**		
	Minimum (nm)	**Maximum (nm)**	**Mean (nm)**
Height	3.6	23.7	7.0
Diameter	5.5	233.3	47.4
Length	6.9	295.0	64.4
Width	6.9	223.7	32.8
N= 150	**Normal density sample F2**		
	Minimum (nm)	**Maximum (nm)**	**Mean (nm)**
Height	0.9	18.6	4.5
Diameter	3.3	398.3	38.2
Length	4.1	729.0	55.3
Width	4.1	293.2	28.4
N= 115	**Low density sample F3**		
	Minimum (nm)	**Maximum (nm)**	**Mean (nm)**
Height	1.2	17.6	5.1
Diameter	5.5	241.39	43.4
Length	6.9	395.0	60.7
Width	6.9	182.2	32.0

The section analysis performed in isolated collagen fibrils confirms the value of D-band periodicity. The measurements were performed over 4 different collagen fibrils. The average value was found to be 67.9 ± 0.8 nm. In addition, collagen fibrils orientation measured were found to be around 45° in the transverse plane of the bone. This value is within the range of D-band periodicity found for collagen fibrils of rat cortical bone (See chapter 3section C)

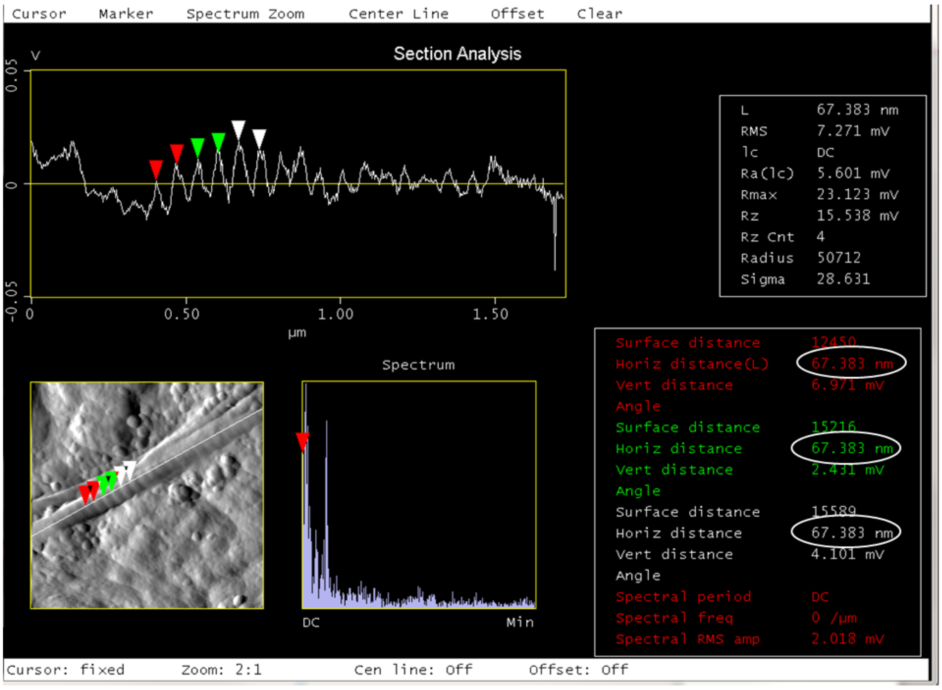

```
L         67.383 nm
RMS       7.271 mV
lc        DC
Ra(lc)    5.601 mV
Rmax      23.123 mV
Rz        15.538 mV
Rz Cnt    4
Radius    50712
Sigma     28.631
```

```
Surface distance        12450
Horiz distance(L)       67.383 nm
Vert distance           6.971 mV
Angle
Surface distance        15216
Horiz distance          67.383 nm
Vert distance           2.431 mV
Angle
Surface distance        15589
Horiz distance          67.383 nm
Vert distance           4.101 mV
Angle
Spectral period         DC
Spectral freq           0 /µm
Spectral RMS amp        2.018 mV
```

```
Cursor: fixed      Zoom: 2:1          Cen line: Off        Offset: Off
```

Figure 4.15 Sketch of the AFM image section analysis test to measure D-band periodicity over an isolated mineralized collagen fibril type I.

Bone sub-nanostructure is composed of four main materials: crystals, collagens, non-collagenous organic proteins and layered water particles. Many of the physiological functions and mechanical characteristics of bone tissue are highly dependent of the volume fraction of mineral particles as well as the size, shape and alignment of the particles.

AFM images as reported in figure 4.14 suggest that mature mineral crystals are mostly platelet-like shaped than needle-shaped. According to (Gupta and Zioupos, 2008; Rho et al., 1998) platelet-like apatite crystals of bone occur within the discrete spaces within the collagen fibrils, thereby limiting the possible primary growth of the mineral crystals, and forcing the crystals to be discrete and discontinuous. However, the exact distribution, relationships, amounts and changes with time of the nano structural component are still not clear.

The mineral crystals grow with a variable crystalline orientation. In this study, the lengths and widths of the platelet vary between 55-64 × 28-32 nm². It must be told that crystal size could be affected by the small but significant amounts of impurities present in bone nano structure such as HPO_4, Na, Mg, carbonate, K, and others for which positions and configurations are not completely known. In addition, most of the reference values for apatite crystals size available in the literature were obtained from isolated crystals and non-in native state. According to Rho et al., 1998 non-collagenous organic proteins, including phosphoproteins, such as osteopontin, sialoprotein, osteonectin, and osteocalcin, could play an important role to regulate the size, orientation, and crystal habit of the mineral deposits.

According to the literature ("The Shape of Inorganic Particles," 2007), crystals shape can be classified as needle-, rod-, ribbon-, filament- or platelet-like. This is contrary to the accepted belief that if they are crystals, they must be rigid structures. However, this classification comprises the question of how crystals are formed, as give some clues about geometrical changes of the crystals structure and the role of the crystals maturity degree.

Type I collagen is the primary organic component of the bone matrix. Normally, collagen molecules secreted by osteoblasts self-assemble into fibrils with a specific quaternary structure having a 67 nm periodicity (as the one presented in Figure 4.14). These values are very close to those reported in chapter 3 for rat cortical bone. This fact suggests that mineralized collagen fibrils type I could be inner structural material that do not change among species.

Even if additional studies are needed to conclusively defining the actions, mechanisms and relationship between organic and mineral component of bone; these data are a necessary first step in modelling and theoretically predicting the underlying basis for the mechanical characteristics of bone tissue at the micro and nano scales. They provide a starting place for predicting mechanical function utilizing the structural aspects of mineral content and collagen fibrils arrangement and it provides a source to compare these predictions with experimental measurements.

Chapter synthesis

The mechanical heterogeneity of bone at the microstructural level has been confirmed. Mechanical properties are different between the different components of bone microstructure.

Time-dependency of the mechanical response of bone has been proved for all the micro structural components.

Mineral content affects the mechanical response of osteons, thus black osteons have weaker mechanical properties compared to the other micro structural typologies of bone. Globally, the values of the mechanical response for black osteons are around 20% lower than white osteons.

Values of the mechanical response quantified for the lamellar bone and white osteons are similar. This could be due to the cycle of bone remodelling and their consequence mineral build-up.

Differences in bone densities decrease the elastic response of bone (low-density sample F3 has values 25% lower than the other samples) meanwhile the time-dependent and hardness are apparently not affected.

Globally, the apparent elastic modulus increases by a factor between 1.61 and 1.83 independent of bone density and according to the typology while the strain rate increases from quasi-static to infinite.

There are not apparent morphological differences at the micro and nano scale due to difference in bone densities. Lamellae and minerals crystals size were found to be similar for all samples. Mineral crystallites have mostly a platelet-like shape and a diameter in a range between 38 to 49 nm.

Collagen fibrils found in sample F2 have D-band patron of 67.9 ± 0.8 nm with an apparent privileged orientation of 45° in the transverse plane of bone.

Next chapter is focused in the anisotropy behaviour of the mechanical properties of bone especially the time-dependent. Inside, it is explored if the mechanical response could change according to the anatomical quadrant suggesting a possible direction of the remodelling processes.

Chapter 5: Anisotropy of the time-dependent mechanical properties of human femoral cortical bone

This chapter presents the assessment of the anisotropy behaviour of the mechanical properties including time-dependent of human femoral cortical bone. It inspects also the variation of the mechanical response as a function of three different anatomical quadrants (posterior, medial and lateral) of the femoral shell and the mineral content of different Haversian systems. Nanoindentation tests were performed in three directions (longitudinal, transverse and radial directions). The aim of this mechanical characterization is to assess the influence of the time-dependent mechanical properties in the anisotropic ratio of cortical bone.

A. Sample geometry

Human femoral diaphysis was sectioned into four 7.5% length segments from 40% to 70% of the total femur length. A segment from the distal zone (See figure 5.1 zone between segments 3 and 4) of the diaphysis was subsequently sectioned in a parallelepiped specimen (nominally ~4.5×5×5 mm^3 in size). Each sample was obtained from three different anatomical quadrants (M= Medial, L = Lateral, P = Posterior). Samples from the anterior anatomical quadrant were not used because they ran out in a previous study. Samples orientation was defined by the axes of an anatomically based orthogonal curvilinear coordinate system (R= radial, T= transverse, L= longitudinal).

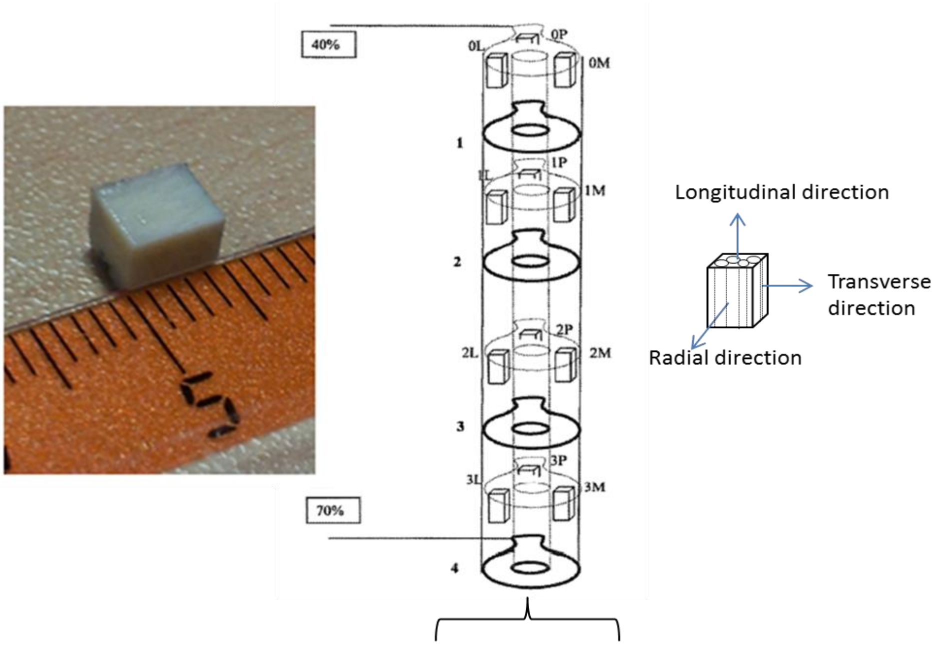

Bensamoun 2003

Figure 5.1. Diagram shows specimen preparation. Human femoral diaphysis was sectioned in different segments. Samples were obtained from different anatomical quadrants (P=posterior, L=lateral and M=medial). Lateral and medial zone are located approximately at 90° respectively from the posterior zone.

As performed in chapter 4, ESEM images were displayed for each sample over the three faces to identify osteons with different apparent mineral content. ESEM images were displayed without additional sample treatments other than polishing. This is because some coatings used in electronic microscopy could affect the bone surface i.e. their mechanical response.

One must be inform that black osteons were not identified in the images of samples from the medial and posterior anatomical quadrants.

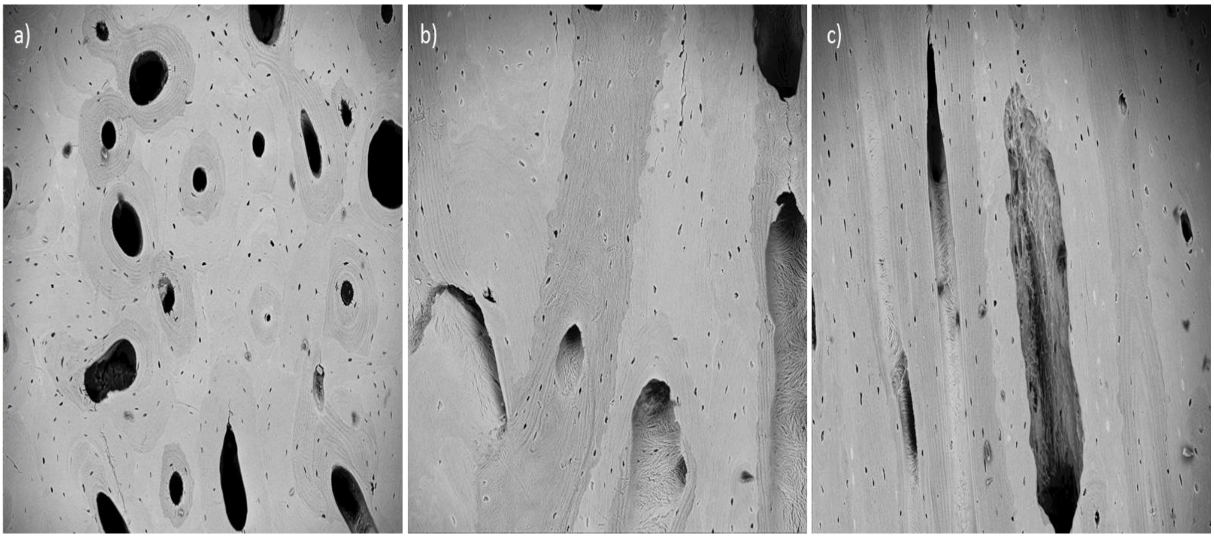

Figure 5.2 ESEM images of the posterior bone sample show different typological organizations according to the watched direction. Images displayed come from a) longitudinal axis, b) transverse axis and c) radial axis.

B. Nanoindentation tests

Anisotropy is defined as the material's directional dependence of a physical property (Wenk and Houtte, 2004). In biological materials as bone, the anisotropy mechanical response reflects the ultra-structural organization of collagen fibrils and mineral crystals within the osteons as well as the lamellar microstructure (Turner et al., 1995).

A total 1035 indentations were achieved in each sample on the three principal directions (longitudinal, transverse and radial). Tests were carried out in the lamellar bone and in the white and black osteons under dry conditions. Values for each sample at each typological position are summarized in Tables 5.1 to 5.3 and they were represented by box plot graphs in figures 5.3 to 5.9. Bow plot graphs highlight the values variability and the anisotropy response of the mechanical response. Results for black osteons of the medial and posterior samples in the radial direction were not reported. This is because ESEM images performed in radial direction did not display the presence of this kind of osteons. Besides, non-parametric statistical tests were performed to compare the results between the different samples and at each tested direction. The significance level for the *p*-value for statistical significant differences is ($p< 0.05$). These results are summarized in Tables 5.4 to 5.6. The symbol ≠ indicates a statistically significant difference while ND points out the absence of statistical differences.

Table 5.1 Mean values ± standard deviation (SD) of the nanoindentation results performed on the LATERAL zone of the cortical shell

Mechanical properties	**Longitudinal direction**			**Transverse direction**			**Radial Direction**		
	INTL$_{LL}$ **n = 46**	**WO$_{LL}$** **n = 47**	**BO$_{LL}$** **n = 47**	**INTL$_{LT}$** **n = 45**	**WO$_{LT}$** **n = 47**	**BO$_{LT}$** **n = 26**	**INTL$_{LR}$** **n = 37**	**WO$_{LR}$** **n = 37**	**BO$_{LR}$** **n = 21**
E_{elast} (GPa)	31,7 ± 3.1	32.0 ± 3.8	25.5 ± 5.3	20.2 ± 2.2	17.3 ± 1.7	14.9 ± 3.1	21.8 ± 2.7	21.7 ± 3.8	18.3 ± 3.1
E_{ve1} (GPa)	81,1 ± 14.4	69.9 ± 15.5	52.1 ± 18.1	45.6 ± 6.6	47.0 ± 6.9	31.1 ± 5.2	47.7 ± 6.6	50.1 ± 9.7	36.9 ± 6.9
$\eta_{ve1} \times 10^{2}$(GPa.s)	40.2 ± 10.1	30.0 ± 11.0	20.6 ± 11.7	20.3 ± 4.9	23.1 ± 4.1	13.3 ± 4.2	19.3 ± 4.7	24.3 ± 5.5	16.3 ± 4.4
E_{ve2} (GPa)	121.7 ± 17.3	96.8 ± 11.8	87.8 ± 17.3	76.1 ± 8.2	69.2 ± 7.7	48.8 ± 5.6	83.7 ± 12.6	85.4 ± 10.4	50.1 ± 9.1
$\eta_{ve2} \times 10^{3}$(GPa.s)	71.5 ± 11.6	54.0 ± 6.8	47.1 ± 10.6	38.7 ± 7.5	32.9 ± 4.4	24.0 ± 2.6	38.9 ± 6.0	44.9 ± 9.2	32.9 ± 9.6
H (GPa)	0.80 ± 0.06	0.72 ± 0.06	0.63 ± 0.06	0.59 ± 0.04	0.53 ± 0.04	0.45 ± 0.05	0.61 ± 0.04	0.58 ± 0.07	0.49 ± 0.08
η_{vp} (GPa.s)	284.5 ± 31.6	271.3± 34.6	239.7± 27.5	207.0 ± 26.6	188.0 ± 24.8	163.2 ± 26.0	209.1 ± 25.1	211.7 ± 35.2	174.0 ± 28.9

LL: lateral longitudinal, LT: lateral transverse, LR: Lateral radial, n= number of successful indentation

Table 5.2 Mean values ± standard deviation (SD) of the nanoindentation results performed on the MEDIAL zone of the cortical shell

Mechanical properties	**Longitudinal direction**			**Transverse direction**			**Radial Direction**	
	$INTL_{ML}$ n = 41	**WO_{ML} n = 48**	**BO_{ML} n = 48**	**$INTL_{MT}$ n = 48**	**WO_{MT} n = 34**	**BO_{MT} n = 39**	**$INTL_{MR}$ n = 46**	**WO_{MR} n = 37**
E_{elast} (GPa)	33.3 ± 3.4	31.7 ± 3.2	26.0 ± 3.4	19.7 ± 2.9	20.4 ± 2.3	19.6 ± 2.0	20.0 ± 1.8	19.5 ± 1.7
E_{ve1} (GPa)	84.7 ± 13.2	93.6 ± 24.8	55.0 ± 10.7	58.1 ± 11.0	57.7 ± 10.8	51.9 ± 9.9	49.1 ± 8.3	54.7 ± 13.3
$\eta_{ve1} \times 10^2$ (GPa.s)	36.4 ± 8.7	45.4 ± 14.4	25.6 ± 8.6	26.9 ± 5.3	23.2 ± 5.7	24.9 ± 4.4	21.2 ± 4.8	25.1 ± 7.2
E_{ve2} (GPa)	148.3 ± 21.0	154.6 ± 21.6	80.9 ± 11.7	96.6 ± 14.3	91.5 ± 14.3	77.4 ± 14.6	84.5 ± 8.1	87.9 ± 13.6
$\eta_{ve2} \times 10^3$(GPa.s)	76.7 ± 18.9	89.1 ± 19.3	50.1 ± 15.1	49.9 ± 12.0	44.2 ± 7.7	44.2 ± 7.3	48.2 ± 6.3	41.5 ± 7.2
H (GPa)	0.87 ± 0.07	0.81 ± 0.05	0.61 ± 0.06	0.66 ± 0.09	0.66 ± 0.05	0.58 ± 0.07	0.63 ± 0.06	0.57 ± 0.05
η_{vp} (GPa.s)	333.8 ± 40.3	297.7 ± 33.0	234.5 ± 26.1	224.7 ± 32.2	234.3 ± 22.4	203.1 ± 31.4	234.1± 25.6	210.5 ± 30.4

ML: medial longitudinal, MT: medial transverse, MR: medial radial, n= number of successful indentation

Table 5.3 Mean values ± standard deviation (SD) of the nanoindentation results performed on POSTERIOR zone of the cortical shell

Mechanical properties	**Longitudinal direction**			**Transverse direction**			**Radial Direction**	
	INTL$_{PL}$ **n = 50**	**W O$_{PL}$** **n = 48**	**BO$_{PL}$** **n = 42**	**INTL$_{PT}$** **n = 48**	**WO$_{PT}$** **n = 42**	**BO$_{PT}$** **n = 34**	**INTL$_{PT}$** **n = 41**	**WO$_{PR}$** **n = 36**
E_{elast} (GPa)	35.2 ± 2.9	30.8 ± 2.1	25.1 ± 2.1	22.1 ± 2.6	20.9 ± 1.4	18.9 ± 2.7	20.3 ± 3.0	22.0 ± 2.7
E_{ve1} (GPa)	79.4 ± 14.4	79.2 ± 12.5	50.3 ± 7.4	45.6 ± 9.3	50.2 ± 9.8	35.8 ± 9.6	58.5 ± 9.8	43.1 ± 6.4
$\eta_{ve1} \times 10^2$ (GPa.s)	32.6 ± 10.1	39.8 ± 8.3	24.9 ± 5.8	17.1 ± 7.0	24.1 ± 5.9	15.6 ± 4.8	25.9 ± 5.9	17.2 ± 4.5
E_{ve2} (GPa)	124.3 ± 18.1	115.2 ± 12.6	78.0 ± 13.2	86.3 ± 19.1	85.4 ± 10.3	61.0 ± 14.9	106.0 ± 15.8	77.2 ± 13.3
$\eta_{ve2} \times 10^3$(GPa.s)	72.7 ± 23.2	84.4 ± 16.4	51.1 ± 7.1	41.1 ± 11.5	52.5 ± 9.1	39.4 ± 12.9	53.2 ± 14.3	39.1 ± 12.0
H (GPa)	0.84 ± 0.06	0.76 ± 0.07	0.58 ± 0.05	0.64 ± 0.07	0.63 ± 0.04	0.50 ± 0.1	0.67 ± 0.07	0.57 ± 0.06
η_{vp} (GPa.s)	308.7 ± 35.8	293.4 ± 28.9	218.6 ± 15.6	240.5 ± 32.6	229.7 ± 22.4	189.8 ± 35.0	236.8 ± 32.9	208.7 ± 23.5

PL: posterior longitudinal, PT: posterior transverse, PR: posterior radial, n= number of successful indentation

Table 5.4 Statistical significant differences for the mechanical response of each sample at each direction in the lamellar bone and a significance level for the p-value (p <0.05)

	Interstitial lamellae in the longitudinal direction																			
	E_{elast}			**E_{ve1}**			**η_{ve1}**			**E_{ve2}**			**η_{ve2}**			**Hardness**			**η_{vp}**	
Sample	MED	POS		MED	POS		MED	POS		MED	POS		MED	POS		MED	POS		MED	POS
LAT	ND	≠	LAT	ND	ND	LAT	≠	ND	LAT	≠	≠	LAT	ND	ND	LAT	≠	≠	LAT	≠	≠
MED		≠	MED		ND	MED		ND	MED		ND	MED		≠	MED		ND	MED		ND

	Interstitial lamellae in the transverse direction																			
	E_{elast}			**E_{ve1}**			**η_{ve1}**			**E_{ve2}**			**η_{ve2}**			**Hardness**			**η_{vp}**	
Sample	MED	POS		MED	POS		MED	POS		MED	POS		MED	POS		MED	POS		MED	POS
LAT	ND	≠	LAT	≠	ND	LAT	≠	ND	LAT	≠	≠	LAT	≠	≠	LAT	≠	≠	LAT	≠	≠
MED		≠	MED		≠	MED		≠	MED		≠	MED		≠	MED		ND	MED		≠

	Interstitial lamellae in the radial direction																			
	E_{elast}			**E_{ve1}**			**η_{ve1}**			**E_{ve2}**			**η_{ve2}**			**Hardness**			**η_{vp}**	
Sample	MED	POS		MED	POS		MED	POS		MED	POS		MED	POS		MED	POS		MED	POS
LAT	ND	ND	LAT	≠	≠	LAT	≠	≠	LAT	≠	≠	LAT	≠	≠	LAT	≠	≠	LAT	≠	≠
MED		ND	MED		≠	MED		ND	MED		≠	MED		ND	MED		ND	MED		ND

Symbol ≠ indicates a statistically significant difference while ND represents the absence of statistical significant differences

Table 5.5 Statistical significant differences for the mechanical response of each sample at each direction in the white osteons and a significance level for the p-value (p <0.05)

	White osteons in the longitudinal direction																			
	E_{elast}			**E_{ve1}**			**η_{ve1}**			**E_{ve2}**			**η_{ve2}**			**Hardness**			**η_{vp}**	
Sample	MED	POS		MED	POS		MED	POS		MED	POS		MED	POS		MED	POS		MED	POS
LAT	ND	ND	LAT	≠	≠	LAT	≠	≠	LAT	≠	≠	LAT	≠	≠	LAT	≠	≠	LAT	≠	≠
MED		ND	MED		≠	MED		ND	MED		≠	MED		ND	MED		≠	MED		ND

	White osteons in the transverse direction																			
	E_{elast}			**E_{ve1}**			**η_{ve1}**			**E_{ve2}**			**η_{ve2}**			**Hardness**			**η_{vp}**	
Sample	MED	POS		MED	POS		MED	POS		MED	POS		MED	POS		MED	POS		MED	POS
LAT	ND	≠	LAT	≠	ND	LAT	≠	ND	LAT	ND	≠	LAT	ND	≠	LAT	ND	≠	LAT	ND	≠
MED		≠	MED		ND	MED		≠	MED		ND	MED		≠	MED		ND	MED		ND

	White osteons in the radial direction																			
	E_{elast}			**E_{ve1}**			**η_{ve1}**			**E_{ve2}**			**η_{ve2}**			**Hardness**			**η_{vp}**	
Sample	MED	POS		MED	POS		MED	POS		MED	POS		MED	POS		MED	POS		MED	POS
LAT	≠	ND	LAT	ND	≠	LAT	ND	≠	LAT	ND	≠	LAT	ND	≠	LAT	ND	ND	LAT	ND	ND
MED		≠	MED		≠	MED		≠	MED		≠	MED		ND	MED		ND	MED		ND

Symbol ≠ indicates a statistically significant difference while ND represents the absence of statistical significant differences.

Table 5.6 Statistical significant differences for the mechanical response of each sample at each direction in the black osteons and a significance level for the p-value ($p < 0.05$)

	Black osteons in the longitudinal direction																			
	E_{elast}			E_{ve1}			η_{ve1}			E_{ve2}			η_{ve2}			**Hardness**			η_{vp}	
Sample	MED	POS		MED	POS		MED	POS		MED	POS		MED	POS		MED	POS		MED	POS
LAT	ND	ND	LAT	ND	ND	LAT	≠	ND	LAT	ND	≠	LAT	≠	ND	LAT	ND	≠	LAT	ND	≠
MED		≠	MED		≠	MED		≠	MED		≠	MED		≠	MED		≠	MED		≠

	Black osteons in the transverse direction																			
	E_{elast}			E_{ve1}			η_{ve1}			E_{ve2}			η_{ve2}			**Hardness**			η_{vp}	
Sample	MED	POS		MED	POS		MED	POS		MED	POS		MED	POS		MED	POS		MED	POS
LAT	≠	≠	LAT	≠	≠	LAT	≠	≠	LAT	≠	≠	LAT	≠	≠	LAT	≠	≠	LAT	≠	≠
MED		≠	MED		≠	MED		≠	MED		≠	MED		≠	MED		≠	MED		≠

Symbol ≠ indicates a statistically significant difference while ND represents the absence of statistical significant differences

Results of the elastic property E_{elast} are presented in figure 5.3. This property is plotted as a function of the indentation direction, the anatomical quadrant of sample and the element of the bone microstructure.

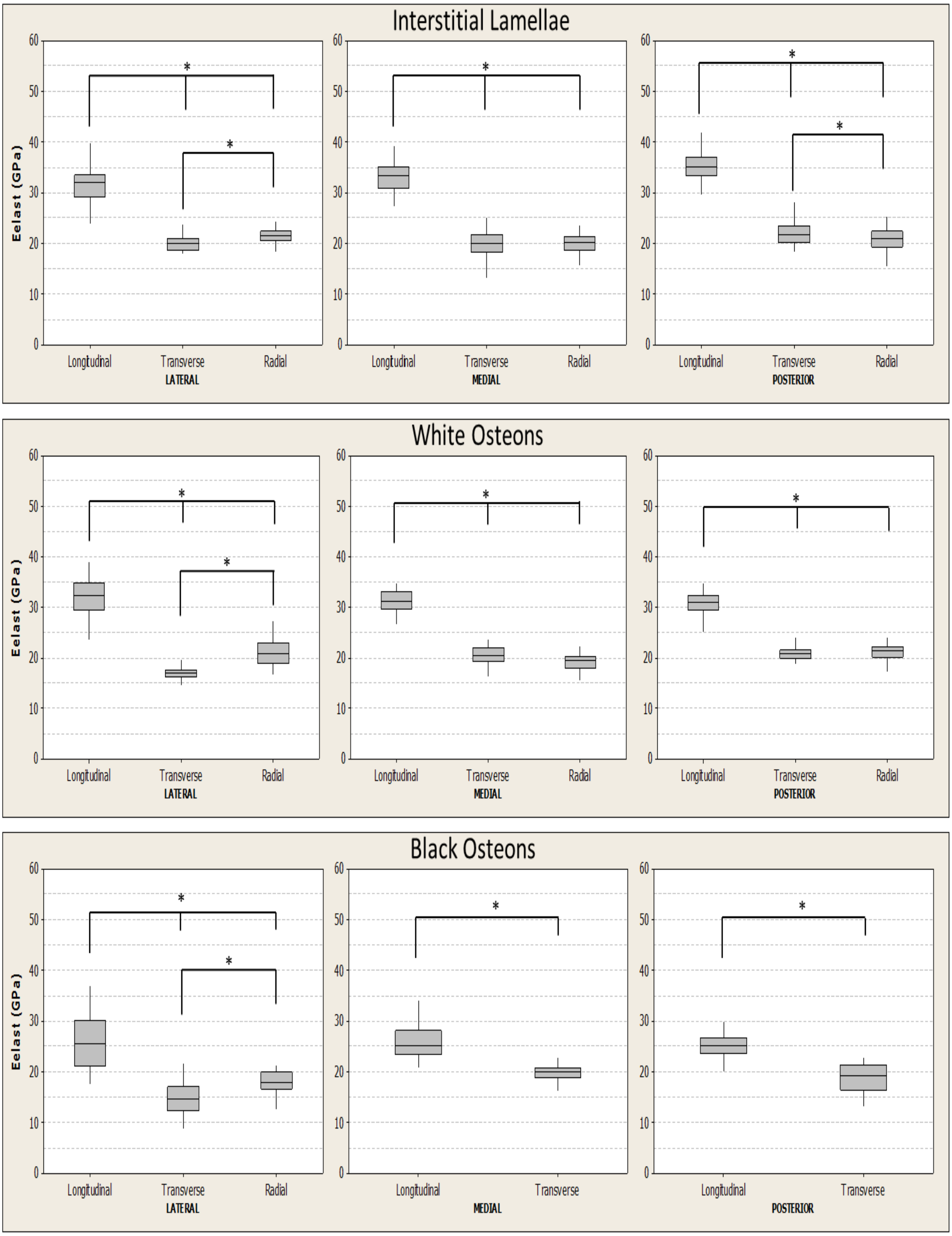

Figure 5.3 Elastic properties for human femoral cortical bone. The * represent a statistical significant difference between the results. The significance level for the *p*-value is ($p<0.05$).

Each element of the viscoelastic property is presented separately. First elastic component E_{ve1} is represented in figure 5.4.

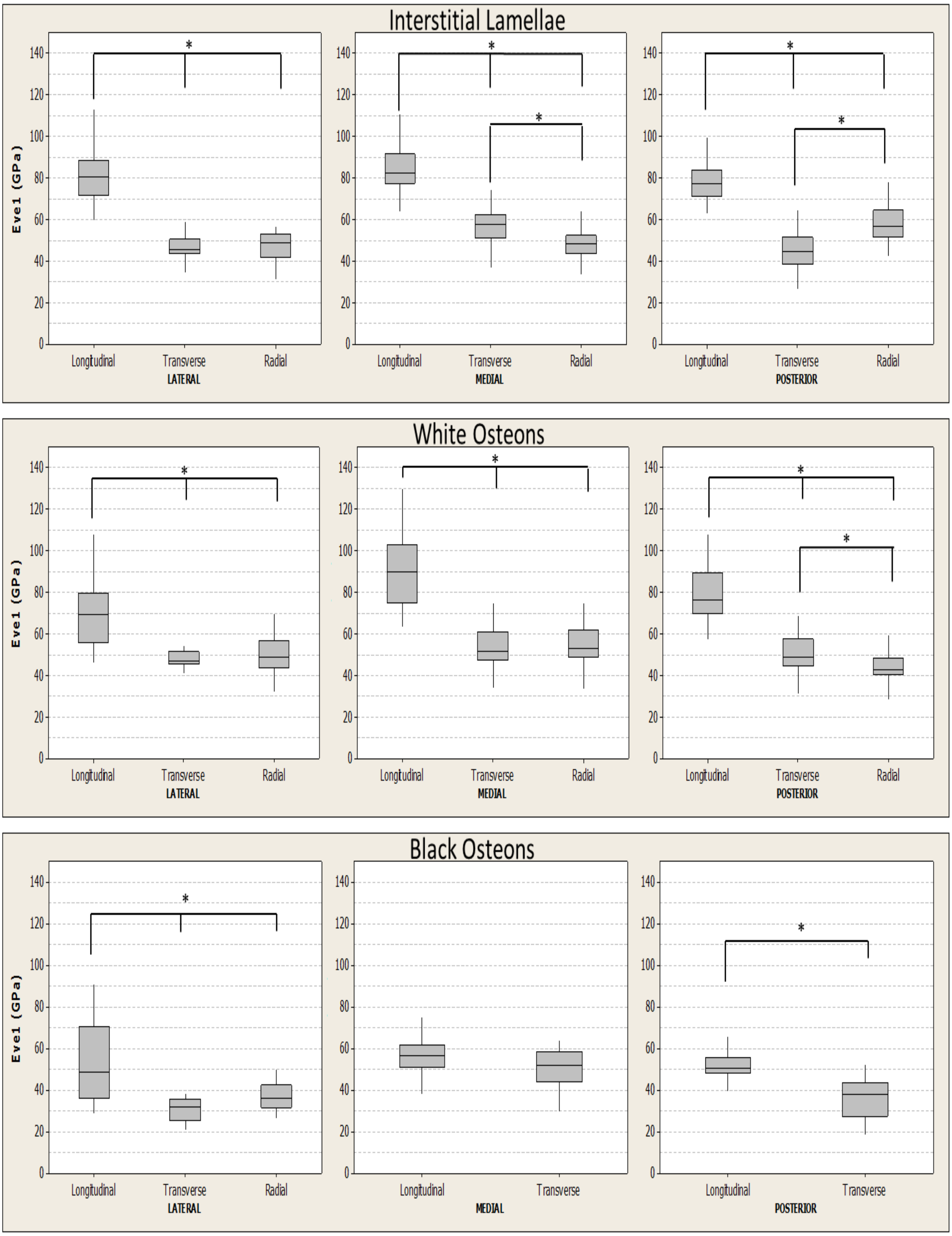

Figure 5.4 First Elastic component of the viscoelasticity for human femoral cortical bone. The * represent a statistical significant difference between the results. The significance level for the *p*-value is ($p<0.05$).

Then, the first viscous component η_{ve1} of viscoelasticity is represented in figure 5.5.

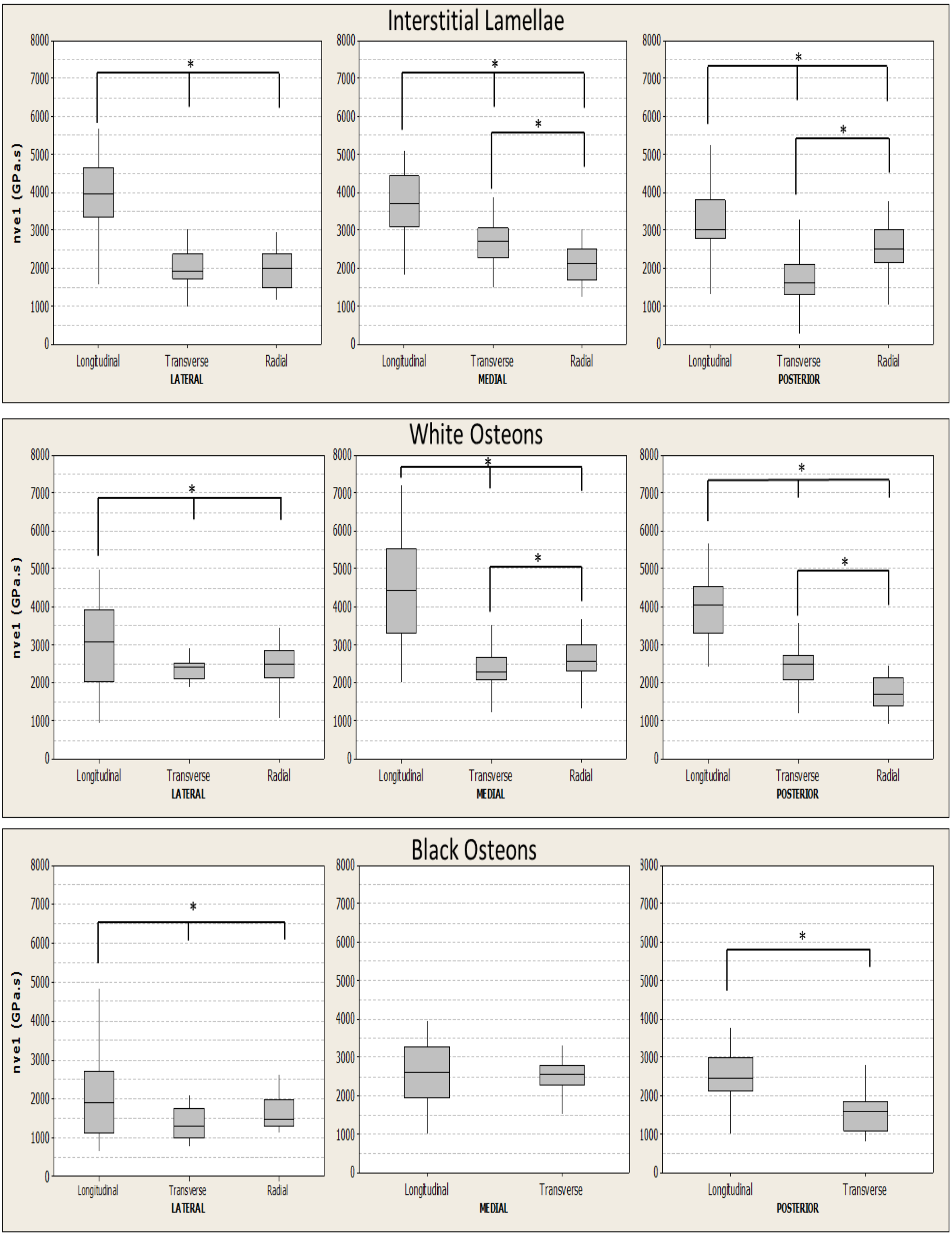

Figure 5.5 First viscous component of the viscoelasticity for human femoral cortical bone. The * represent a statistical significant difference between the results. The significance level for the *p*-value is ($p<0.05$).

The second elastic component Eve2 of viscoelasticity is represented in figure 5.6

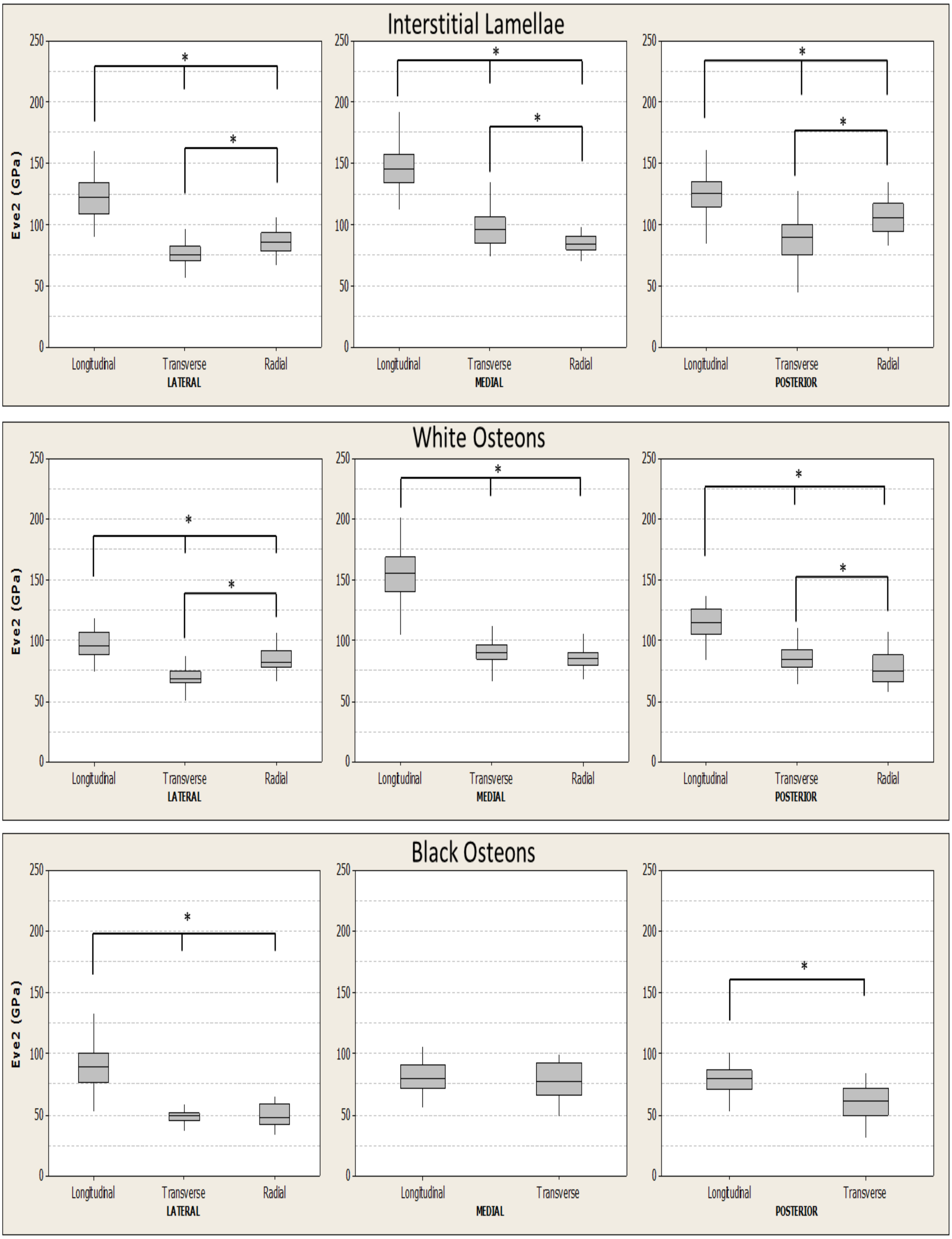

Figure 5.6 Second elastic component of the viscoelasticity for human femoral cortical bone. The * represent a statistical significant difference between the results. The significance level for the *p*-value is ($p<0.05$).

In addition, the final element of viscoelasticity is the second viscous component η_{ve2} which is presented in figure 5.7.

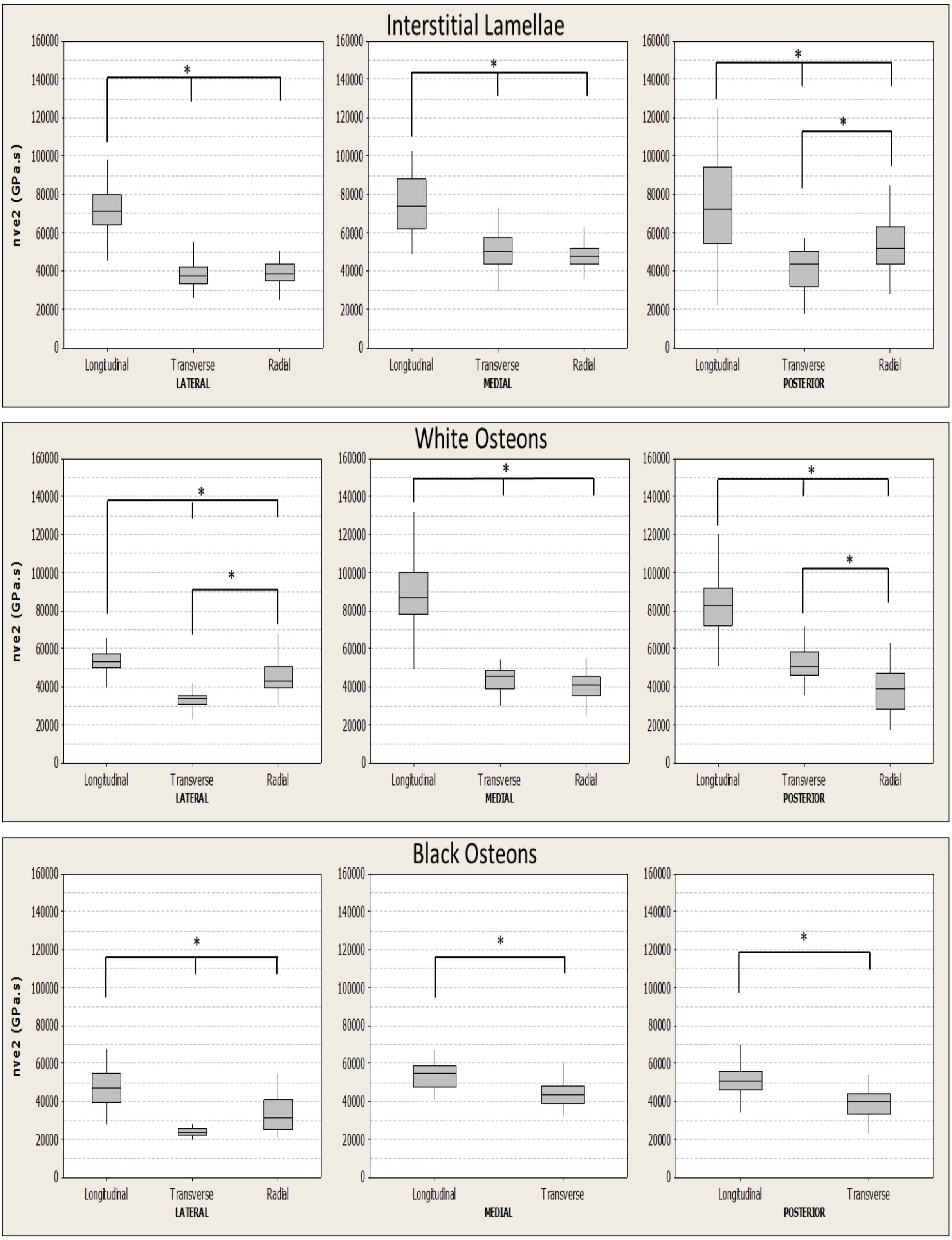

Figure 5.7 Second viscous component of viscoelasticity for human femoral cortical bone. The * represent a statistical significant difference between the results. The significance level for the *p*-value is ($p<0.05$).

Hardness H results are represented in figure 5.8.

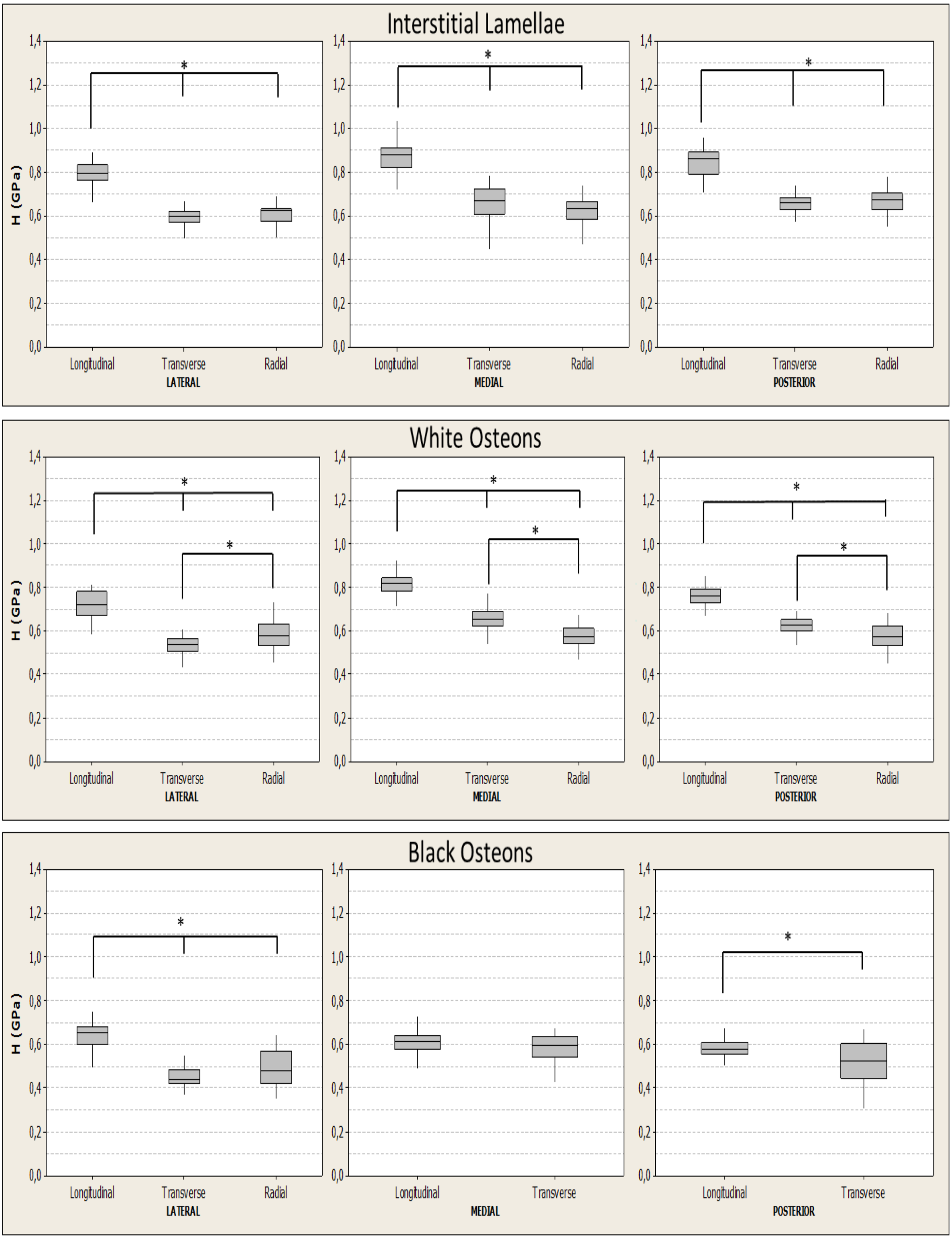

Figure 5.8 Hardness for human femoral cortical bone. The * represent a statistical significant difference between the results. The significance level for the *p*-value is ($p<0.05$)

Finally, viscoplasticity η_{vp} results are represented in figure 5.9.

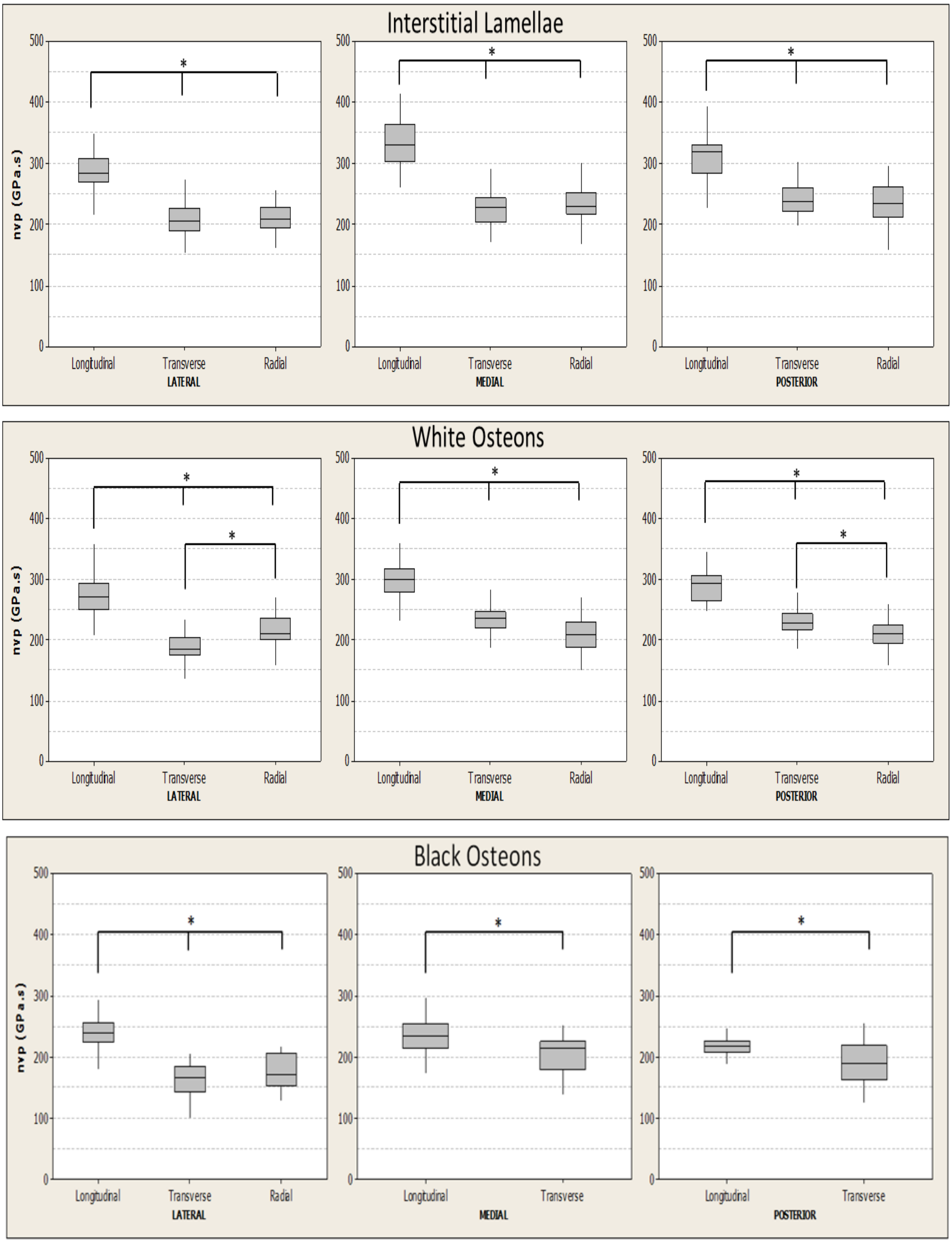

Figure 5.9 Viscoplasticity for human femoral cortical bone. The * represent a statistical significant difference between the results. The significance level for the *p*-value is ($p<0.05$).

The variation in the results of the nanoindentation tests for each of the three directions demonstrates the anisotropy of the mechanical response of bone at the micro scale. However, data analysis of the measured modulus must be performed carefully. Since nanoindentation tests are sensitive to the mechanical properties in the three-dimensions of the space, so the modulus reported in this study are not specific for each direction and it could be reflecting a combined modulus of a composite material.

In this work, the highest values of the mechanical response were found in the longitudinal direction. Values found on the transverse and radial direction were between 30% and 50% lower than those for the longitudinal direction. This behaviour is in good agreement with the results reported earlier by (Carnelli et al., 2011; Fan et al., 2002; Franzoso and Zysset, 2009) who found a similar difference in the bone mechanical response while changing the tests direction. Additionally, our findings are in good agreement with the results of (Ashman et al., 1984; van Buskirk et al., 1981). According to these authors, differences in the mechanical properties between the three directions reflect the orthotropic behaviour of bone that could be described by nine independent constants.

A possible explanation of the anisotropy in the mechanical response might be the structure of the tissues in the three directions. In the longitudinal direction, bone lamellar boundaries are approximately straight and parallel to the long axis of the sample. For the transverse and radial tissue, the lamellar boundaries are slightly curved and sometimes perpendicular to the sample long axis.

Based on the statistical comparisons the mechanical differences are evidenced for all tested anatomical quadrants (lateral, medial or posterior) of the cortical shell. In this work, bone sample of posterior zone do not have the lowest mechanical response as reported at the macro scale. These results are differ from those reported by (Bensamoun et al., 2004a, 2004b; Espinoza Orías et al., 2009; Yamamoto et al., 2012; Ziv et al., 1996) using ultrasound in cortical bone samples. They found a spatial distribution of the elastic and plastic mechanical properties of bone lower in the posterior zone than on the others zones. According to (Bensamoun et al., 2004a; Dong and Guo, 2004) the mechanical response of bone in the longitudinal direction is highly correlated to the porosity present in the different anatomical zones of the cortical shell. In the precise case of the posterior zone, macro porosity is about 47% in the zone near to the proximal femoral neck and about 15% in the distal zone.

By contrast, (Abdel-Wahab et al., 2011) used tensile tests to compute an elastic modulus of cortical bone. They found that in the longitudinal direction specimens from the lateral anatomical position demonstrated the lowest values. This fact suggests that special distribution of the mechanical response of bone could be linked to other structural phenomena or experimental conditions.

Nevertheless, most of the macroscopic measures (ultrasounds or tensile tests) do not discriminate the contribution of the different typologies of bone tissue. As we evidence in this work, at the microstructural level each of these structural components plays an important role in the variability of the mechanical response of bone. This means, the mechanical response of bone material could change according to the proportion of lamellar and osteonal bone and according to the kind of osteons present in the sample. This is important because some defects of human cortical bone result from cyclic dynamic loading and are originated at the microstructural level.

Another considerable result was that wherever the anatomical origin of bone samples; the mechanical response of the interstitial lamellae and the white osteons was very similar. As it has been suggest before, this fact can be associated to two factors: the maturity degree of the Haversian system and the distal origin of the femoral samples.

Black osteons were not tested in the radial direction of the lateral and posterior samples. This is because this kind of osteons (low apparent mineral content) had not been identified from the ESEM images. This fact could be linked to the aging of bone samples and to the diminution of the amount of young osteons.

One should note that as reported in chapter 3, the results reflect the heterogeneity of the mechanical response of the Haversian systems of cortical bone. In addition, for many mechanical properties results of black osteons in the longitudinal and transverse direction were not very different. Black osteons also known as young osteons are characterized by their low mineral content. From our results, this fact suggests that mineral phase plays an important role in bone anisotropy at the microstructural level (osteon lamellae).

As done in previous chapters, the elastic and viscoelastic mechanical properties are used to compute an apparent elastic modulus as a function of given strain rates (see chapter II section B). The mean values and the standard deviation (SD) as a function of the anatomical quadrant and the structural location (interstitial lamellae or Haversian system) are summarized in tables 5.7 to 5.9.

Table 5.7 Apparent elastic modulus of each microstructural element measured in the three directions of the LATERAL bone sample

Apparent elastic modulus (GPa)	Longitudinal direction			Transverse direction			Radial Direction		
	INTL_{LL}	W OL_{LL}	BO_{LL}	INTL_{PT}	WO_{PT}	BO_{PT}	INTL_{PR}	WO_{PR}	BO_{PR}
$\dot{\varepsilon} = 0$	17.3 ± 1.6	16.0 ± 1.4	12.4 ± 1.4	10.7 ± 0.7	9.7 ± 0.6	7.5 ± 0.9	11.5 ± 1.0	11.5 ± 1.2	8.8 ± 1.3
$\dot{\varepsilon} = 0.05s^{-1}$	25.6 ± 2.2	24.7 ± 2.1	18.8 ± 2.8	15.9 ± 1.3	14.0 ± 1.1	11.4 ± 1.8	17.0 ± 1.7	17.1 ± 2.3	14.2 ± 2.2
$\dot{\varepsilon} = \infty$	28.8 ± 2.8	29.2 ± 3.5	23.2 ± 4.8	18.4 ± 2.0	15.7 ± 1.6	13.6 ± 2.8	19.9 ± 2.4	19.7 ± 3.5	16.6 ± 2.8

LL: lateral longitudinal, LT: lateral transverse, LR: lateral radial

Table 5.8 Apparent elastic modulus of each microstructural element measured in the three directions of the MEDIAL bone sample

Apparent elastic modulus (GPa)	Longitudinal direction			Transverse direction			Radial Direction	
	INTL_{ML}	W O_{ML}	BO_{ML}	INTL_{MT}	WO_{MT}	BO_{MT}	INTL_{MR}	WO_{MR}
$\dot{\varepsilon} = 0$	18.6 ± 1.5	18.4 ± 1.6	13.0 ± 1.2	11.5 ± 1.5	11.5 ± 1.4	10.9 ±1.2	11.0 ± 0.8	11.1 ± 0.9
$\dot{\varepsilon} = 0.05s^{-1}$	26.5 ± 2.2	25.9 ± 2.3	20.1 ± 1.8	16.1 ± 2.2	16.4 ± 1.8	15.9 ± 1.5	15.9 ± 1.1	15.7 ± 1.1
$\dot{\varepsilon} = \infty$	30.3 ± 3.1	28.9 ± 2.9	23.6 ± 3.1	17.9 ± 2.7	18.6 ± 2.1	17.9 ± 1.8	18.2 ± 1.6	17.8 ± 1.6

ML: medial longitudinal, MT: medial transverse, MR: medial radial

Table 5.9 Apparent elastic modulus of each microstructural element measured in the three directions of the POSTERIOR bone sample

Apparent elastic modulus (GPa)	Longitudinal direction			Transverse direction			Radial Direction	
	INTL_{PL}	W O_{PL}	BO_{PL}	INTL_{LT}	WO_{LT}	BO_{LT}	INTL_{LR}	WO_{LR}
$\dot{\varepsilon} = 0$	18.4 ± 1.7	16.8 ± 1.2	12.4 ± 1.0	11.3 ± 1.1	11.3 ± 0.8	9.3 ± 1.7	11.9 ± 1.4	11.0 ± 1.0
$\dot{\varepsilon} = 0.05s^{-1}$	27.5 ± 2.2	25.0 ± 1.6	19.7 ± 1.4	16.7 ± 1.3	16.7 ± 0.9	14.6 ± 2.2	16.5 ± 2.2	16.8 ± 1.6
$\dot{\varepsilon} = \infty$	32.1 ± 2.7	28.0 ± 1.9	22.9 ± 2.0	20.2 ± 2.3	19.0 ± 1.3	17.3 ± 2.4	18.5 ± 2.7	20.0 ± 2.4

PL: posterior longitudinal, PT: posterior transverse, PR: posterior radial

Results of the apparent elastic modulus suggest that bone heterogeneity of the Haversian systems is kept in all the directions. As reported in previous chapters 3 and 4; values of the apparent elastic modulus were found to increase by almost a factor between 1.60 to 1.85 in the longitudinal and between 1.51 and 1.89 for the transverse and radial directions when the strain rate increase from 0 s^{-1} to infinite.

At the micro scale using nanoindentation tests in lamellar bone (Hengsberger et al., 2005; Middleton et al., 2010) found that apparent elastic modulus is higher in the posterior zone than the lateral and medial locations. In this work, apparent elastic modulus is lightly higher in the posterior zone than in the lateral and medial regions. This fact may be related to bone ability to thick differentially in specific region of the cortex.

Black osteons were found more frequently in the lateral zone of the cortical shell. This fact suggests a possible remodelling direction in the cortical shell. Black osteons are normally associated to newer bone and they are proving bone remodelling activity.

The previous experimental studies including the characterization of the mechanical effects of the strain rate used different methods such as air-guns (McElhaney, 1966), tension with DMA technique (Abdel-Wahab et al., 2011) and nanoindentation (Fan and Rho, 2003; Vanleene et al., 2006). However, including this work, all the results converge to the increase of the elastic modulus as the strain rate increases. Nevertheless, further physico-chemical analysis could be useful to understand this behaviour and to propose deeper interpretations.

C. Anisotropy ratio

The anisotropy ratio has been widely quantified for the elastic properties (Fan et al., 2002; Rho et al., 2001; Turner et al., 1995). However, to our knowledge, the influence of the time-dependent mechanical properties in the average anisotropy ratio of cortical bone has never been quantified.

The mean values of the anisotropy ratio for each mechanical property according to their anatomical location and structural typology are summarized in Table 5.10. In addition, an average anisotropy ratio of the mechanical properties was computed for the lamellar bone and the Haversian systems. These anisotropy ratios are compared with those reported in the literature. This anisotropic ratio is also useful to assess separately the variation and influence of the time-dependent mechanical properties according to the tested directions.

Table 5.10 Mean anisotropy ratio for each mechanical property of cortical bone for all anatomical quadrants. An average anisotropy ratio and the standard deviation are reported for each typology of the cortical bone.

Mechanical Property	***Interstitial lamellae***			***White Osteons***			***Black Osteons***		
	T/R	L/R	L/T	T/R	L/R	L/T	T/R	L/R	L/T
$\mathbf{E_{elast}}$	1.00	1.62	1.62	0.93	1.50	1.62	0.81	1.39	1.46
$\mathbf{E_{ve1}}$	0.97	1.60	1.66	1.05	1.65	1.56	0.84	1.41	1.38
$\boldsymbol{\eta}_{\mathbf{ve1}}$	0.99	1.69	1.75	1.09	1.78	1.64	0.82	1.26	1.39
$\mathbf{E_{ve2}}$	0.95	1.46	1.53	0.99	1.46	1.48	0.97	1.75	1.38
$\boldsymbol{\eta}_{\mathbf{ve2}}$	0.93	1.60	1.72	1.05	1.84	1.76	0.73	1.43	1.46
H	0.99	1.31	1.33	1.06	1.33	1.27	0.92	1.29	1.20
$\boldsymbol{\eta}_{\mathbf{vp}}$	0.99	1.36	1.38	1.03	1.37	1.33	0.94	1.38	1.26
$\mathbf{E}_{\mathbf{app\ at}\ \dot{\varepsilon}\mathbf{=0.05}}$	0.99	1.62	1.64	0.95	1.53	1.61	0.80	1.32	1.42
Average SD	**0.98 (0.02)**	**1.55 (0.13)**	**1.59 (0.14)**	**1.01 (0.10)**	**1.55 (0.16)**	**1.55 (0.15)**	**0.85 (0.1)**	**1.40 (0.13)**	**1.38 (0.1)**

R=Radial. T=Transverse. L=Longitudinal, SD = Standard deviation

The quantification of the anisotropic ratio of cortical bone is still being an open problem. Considering that macroscopic assessment of the mechanical response of bone is sensitive to composition of all the microstructural elements that are present in bone architecture as lamellar bone and osteons; microscopic assessment are important because they allow one to quantify the individual contribution of each microstructural component of the cortical bone. Generally, the anisotropic behaviour of bone at the macro scale is linked to its porosity degree (Ho Ba Tho et al., 2012, Bensamoun et al. 2004a).

In this study, the anisotropy ratio was computed for each mechanical property calculated from the nanoindentation data. Because values of the mechanical properties were meaningfully highest in the longitudinal direction, the coefficients of the anisotropy ratio were the greatest along the relations (longitudinal/radial and longitudinal/transverse). Meanwhile this ratio was found to be close to 1 for the other directions (transverse/radial) indicating a possible mechanical similarity between these two directions.

The highest values of the anisotropy ratio were found for the viscous component η_{ve} of the viscoelasticity assessed in the lamellar bone and white osteons. For lamellar bone, the anisotropy ratio found was 1.75 for η_{ve1} and 1.72 for η_{ve2}. For white osteons, the ratio of these elements was 1.78 for η_{ve1} and 1.84 η_{ve2}. Viscoelasticity is a mechanical property that depends of the orientation of collagen and mineral phases and the layered fluid inside bone. Strong variation in the viscous component could be also related to the highest bone capacity to dissipate energy in the longitudinal direction. According to Katz. 1980 this capacity of bone is mostly due to cement lines and to the boundaries between the lamellae within osteons. The average anisotropy ratio of black osteons was lower than white osteons. This fact could be due to the lower amount of mineral content present in black osteons.

In this study the computed average values of the anisotropy ratio of the apparent elastic modulus were found to be E_{TRANS}/E_{RAD} 0.99, E_{LONG}/E_{RAD} 1.62 and E_{LONG}/E_{TRANS} 1.64 for the lamellar bone; E_{TRANS}/E_{RAD} 0.95, E_{LONG}/E_{RAD} 1.53 and E_{LONG}/E_{TRANS} 1.61 for white osteons and E_{TRANS}/E_{RAD} 0.80, E_{LONG}/E_{RAD} 1.32 and E_{LONG}/E_{TRANS} 1.42 for the black osteons. These coefficients are in agreement with the range of values reported in the literature and which have been summarized in Table 1.7.

Anisotropy ratios for hardness and viscoplasticity were found to be similar for the entire bone microstructure. This fact suggests that independent of the typology, all the mineral-organic relationship have similar non-recoverable deformations.

The anisotropy ratio of cortical bone has been also quantified using macroscopic methods (tensile tests and ultrasounds) and crystallographic analysis (Abdel-Wahab et al.. 2011; Katz and Meunier. 1987; Sasaki et al.. 1991. 1989; Turner et al.. 1999. 1995; Wagner and Weiner. 1992; Yamamoto et al.. 2012). In order to explain these anisotropy ratios, different models have been proposed to predict different elastic symmetries for the osteon and the whole bone. Most of these models consider bone as an assembly of orthotropic lamellae bent into cylindrical structures having a constant, alternating angle between successive lamellae. These authors suggest also that bone anisotropy ratio is affected by its ultrastructural composition and its hierarchical architecture. They suggest that inhomogeneity and anisotropic behaviour of bone are related to the amount and preferred orientation of hydroxyapatite crystallites and collagen fibrils.

Furthermore, morphology of the mineral crystallites is commonly represented by a hexagonal system with c-axes mostly oriented along the bone longitudinal direction and rarely oriented in transverse and radial directions (Sasaki et al.. 1989). Thus, hydroxyapatite crystals orientation could play an important role in bone longitudinal higher mechanical response. This has been proved by Saber-Samandari and Gross, 2009 who suggest that hydroxyapatite crystals have a higher mechanical response in the basal plane (hardness 7.1 GPa and elastic modulus 150.4 GPa) than in the side plane (hardness 6.4 GPa and elastic modulus 143.6 GPa).

Chapter synthesis

The anisotropic mechanical behaviour of bone has been proved at the microscopic level as reflected by the significant anisotropic ratio of the mechanical properties of all the microstructural components.

The highest values computed for the mechanical properties were obtained in the longitudinal direction. Values computed in the transverse and radial direction are between 30 and 40% lower than those computed in the longitudinal direction.

Values of the mechanical properties for the medial anatomical quadrant were slightly higher than that of posterior and lateral anatomical quadrants.

The anisotropy ratios of the elastic properties reported in table 5.10 are in agreement and within the range of values reported in the literature for cortical bone. Nevertheless small differences with those reported in the literature may be explained by facts as: 1) our average values are computed including more mechanical properties, 2) studies reported in the literature compute the anisotropy ratio just from the elastic response 3) some of them used several assumptions to perform a data fusion of the lamellar and osteons experimental results in order to have an average anisotropic ratio for cortical bone and 4) the experimental conditions as the indentation protocol (indentation depth, strain rates, hold times) and the mechanical model used to quantify the mechanical properties (Oliver and Pharr, Swadener and Pharr, Mazeran et al. 2012).

The anisotropic ratio was higher in the viscous components of the viscoelasticity. Elastic properties are anisotropic for all the typologies meanwhile viscoplasticity and hardness have the lowest anisotropic ratio.

The anisotropic ratio computed for black osteons was lower than for the others microstructural typologies. This fact highlights that bone typologies with low mineral content could be less anisotropic. This result suggests that mineral could play an important role in bone anisotropic behaviour due to the possible orientation of the hydroxyapatite crystals.

The next chapter deals with the effects of demineralized process in the mechanical properties of bone. AFM imaging of the collagen fibrils exposed after demineralization could highlight more explanations about the structural organization of bone at the nano scale.

Chapter 6: Mechanical properties of demineralized cortical bone

In this chapter, the mechanical properties and morphological characteristics of bovine bone before and after demineralization process are characterized. The aims of this chapter are to assess the effects of mineral loss in the mechanical response and to examine the structural organization and orientation of the remaining collagen fibrils of bovine femoral bone. We performed two different demineralization processes that remove the largest quantity of mineral content and expose the collagen fibrils. The mechanical assessments were carried out in the three directions (longitudinal, transverse and radial) in order to examine the impact of mineral loss in the anisotropic behaviour of bone material.

A. Demineralization protocols

For protocol I, the chemical attack was performed in bone samples (~5×5×1.5 mm^3 size). Demineralization was carried out during 20 min by putting a small amount of acid on the polished face of bone sample (figure 6.1).

Protocol I:

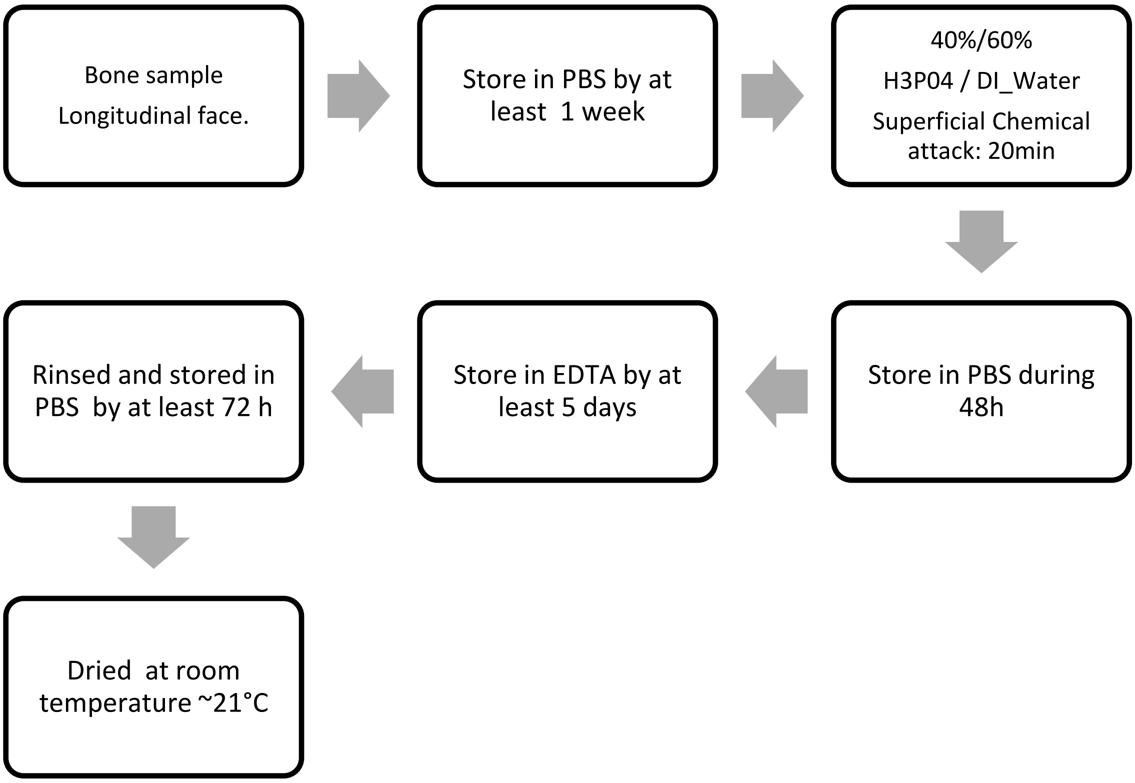

Figure 6.1 Demineralization protocol I performed over bovine cortical bone samples

As it has been informed in chapter 2, protocol II was performed and the results are part of a M.Sc. research project (W. Primaningtyas, 2014) in which the author was a co-advisor. Because of protocol I take more time for sample preparation (at least 3 weeks) the protocol II was developed (sample preparation ~1.2 week). Nevertheless, both protocols produce similar morphological and mechanical results.

For protocol II, the chemical attack was performed in bone samples (~5×5×5 mm^3 size) by total immersion throughout 24h.

Protocol II:

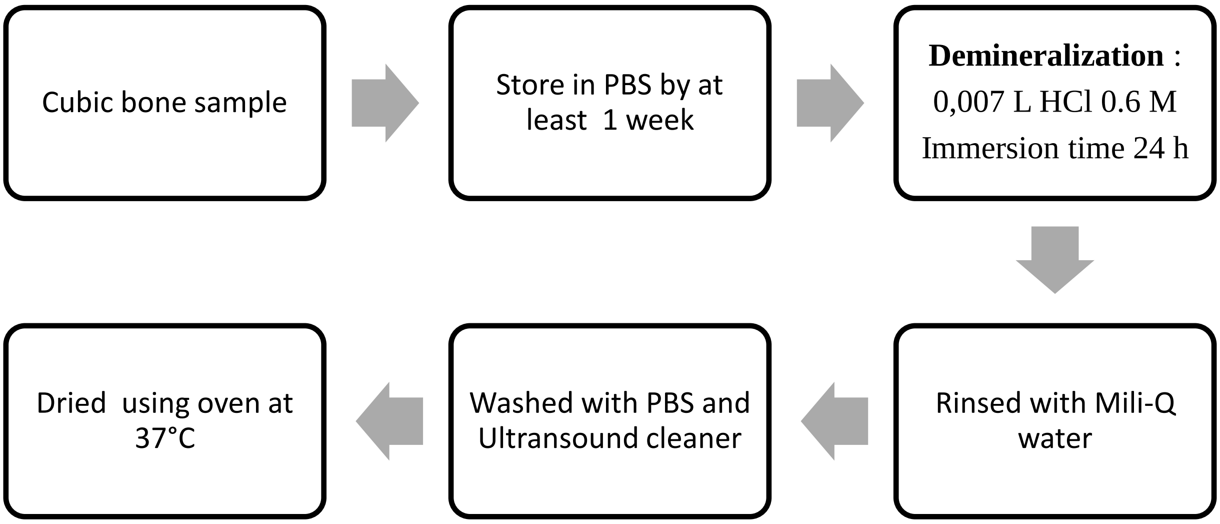

Figure 6.2 Demineralization protocol II performed over bovine cortical bone samples

B. Structural effects of the demineralization process

The bone surface before demineralization is presented in figure 6.3. After the nanoindentation tests, the surface was exposed to the different demineralization processes.

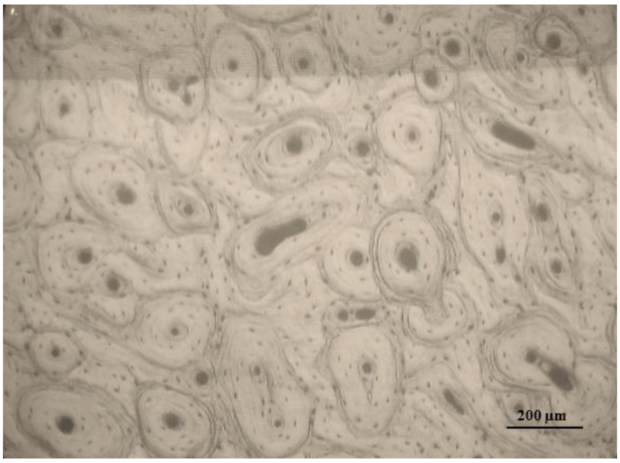

Figure 6.3 Microscopy image of the longitudinal face of the native sample of bovine femoral cortical bone.

In the demineralized samples, the apparent morphological effects are represented by the elimination of the surface boundaries between lamellar and concentric bone (see figure 6.4).

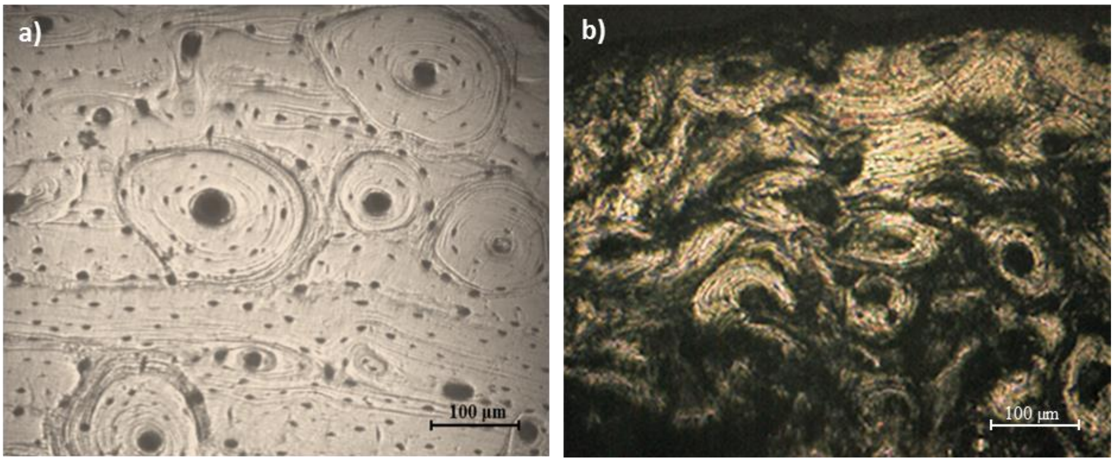

Figure 6.4 Optical microscopy image of bone surface a) before demineralization process and b) after demineralization process. One should note the compaction of bone microstructure

With protocol I, the most important effects were found near to the medullary cavity during the drying process. It was found that these cavities could increase their diameter from 60 µm to ~89 µm after 15 min of drying time.

For protocol II, the important morphological effect was the volume contraction after oven drying. The apparent volume of the sample decrease by about 30% after demineralization.

A common effect found for both protocols is production of apparent pores on the sample surface. Non-significant effects as cracks, apparent brittle or significant change in volume were observed in bone structure. Morphological results for each protocol are presented in figure 6.5.

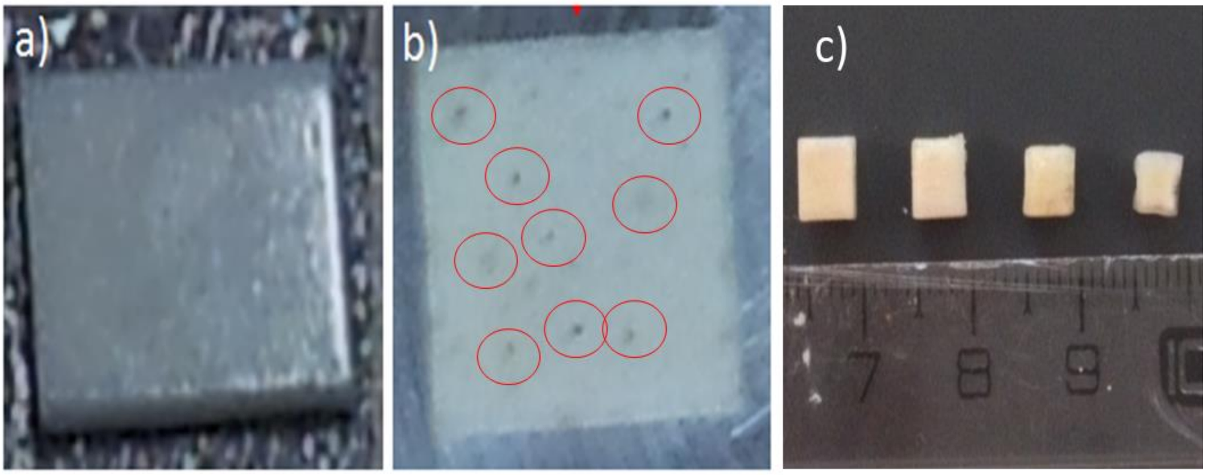

Figure 6.5 Demineralization effects on sample surface at the macroscopic level. a) Bone before demineralization; b) bone after demineralization with protocol I; and c) bone after demineralization with protocol II.

Bone density was found to decrease after demineralization process. The volumetric mass density was computed by the classical mass per unit volume method. The mean values are summarized in table 6.1. The decrease of bone density is a possible consequence of the increase of porosity and mass loss. The apparent percentage of mass loss was higher with the second protocol.

Table 6.1Values of sample's density before and after demineralization process

	Immersion Time	**Density (kg/m^3)**		**Δ Density (%)**
		Before	**After**	
Protocol I	20 min	1980.2 ± 10.9	1194.7 ± 16.5	39.7
Protocol II	24 hours	2019.5 ± 9.54	1002.1 ± 12.2	50.4

C. Mechanical properties

Nanoindentation tests were performed using the protocol and data analysis method proposed by Mazeran et al 2012 (see chapter 2 section B). Mechanical assessments were carried out in sample prepared with two demineralization protocols. Nanoindentation tests were performed in the same sample after and before demineralization process. For the demineralized sample, indentations were performed only in the flatter regions far enough of the large pore regions (as determined by optical microscopy). Tests were performed in different typologies of bone surface: the interstitial lamellae and the osteons.

Protocol I

A total of 30 indentations were performed before and after demineralization process in the lamellar bone and osteons. The mean values and the standard deviation (SD) are summarized in table 6.2.

These values found of each mechanical property were represented in figures 6.6 to 6.9. The statistical difference were assessed by non-parametric statistical tests with a significant *p* value (p <0 .05).

Table 6.2 Mechanical properties of bovine cortical bone after and before demineralization computed in he longitudinal direction using protocol I.

Mechanical properties	Before demineralization		After demineralization	
	Interstitial lamellae n = 20	Osteons n = 20	Interstitial lamellae n = 10	Osteons n = 10
E_{elast} (GPa)	40.4 ± 2.6	29.2 ± 3.2	4.1 ± 1.0	4.6 ± 0.9
E_{ve1} (GPa)	80.5 ± 21	55.0 ± 6.3	7.8 ± 1.7	7.2 ± 1.2
$\eta_{ve1} \times 10^2$ (GPa.s)	35.7 ± 12.4	21.7 ± 5.6	4.2 ± 0.9	3.7 ± 0.8
E_{ve2} (GPa)	150.7 ± 22.5	79.8 ± 21.1	10.4 ± 2.5	10.3 ± 1.6
$\eta_{ve2} \times 10^3$(GPa.s)	79.7 ± 15.0	50.6 ± 14.5	4.8 ± 0.9	5.6 ± 1.1
H (GPa)	0.89 ± 0.04	0.66 ± 0.06	0.15 ± 0.03	0.16 ± 0.02
η_{vp} (GPa.s)	336.1 ± 33	243.0 ± 27	50.5 ± 8.2	52.4 ± 8.0
E_{app} (GPa)	31.5 ± 1.7	22.4 ± 2.0	3.2 ± 0.7	3.5 ± 0.6

Mean values ± standard deviation

Before demineralization all the mechanical properties for interstitial lamellae and osteons were statistically and significantly different ($p<0.05$). After demineralization process, bone mechanical response does not show significant statistical differences between lamellar bone and osteons.

The elastic response was found to be quite different for interstitial lamellae and osteons before demineralization (figure 6.6).

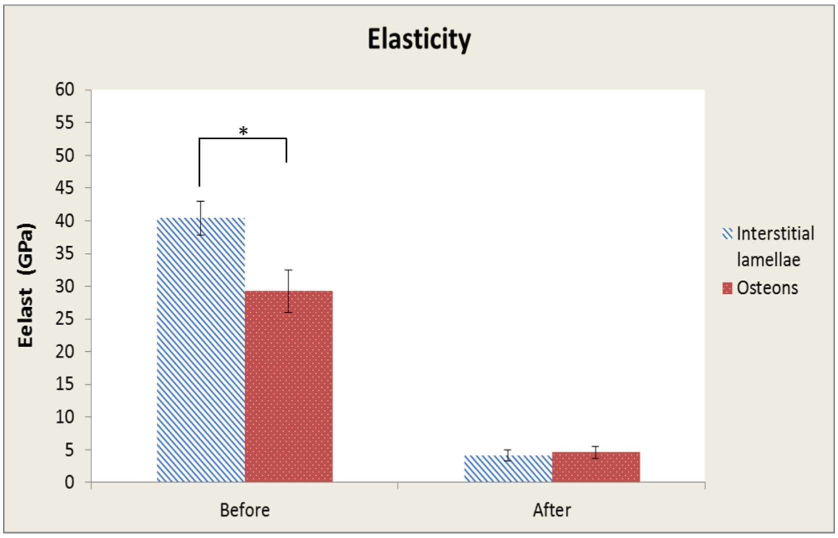

Figure 6.6 Elastic response of bovine femoral cortical bone before and after demineralization process. The * represents a significant statistical difference between the results with a significant p value ($p<0.05$)

Before demineralization, the elastic response of interstitial lamellae is higher than the one of osteons. This elastic response shows that lamellar bone present a more mineralized structure. After demineralization, values decreased about 90% for the lamellar bone and about 80% for osteons.

The results of viscoelasticity before and after demineralization process are represented in figure 6.7.

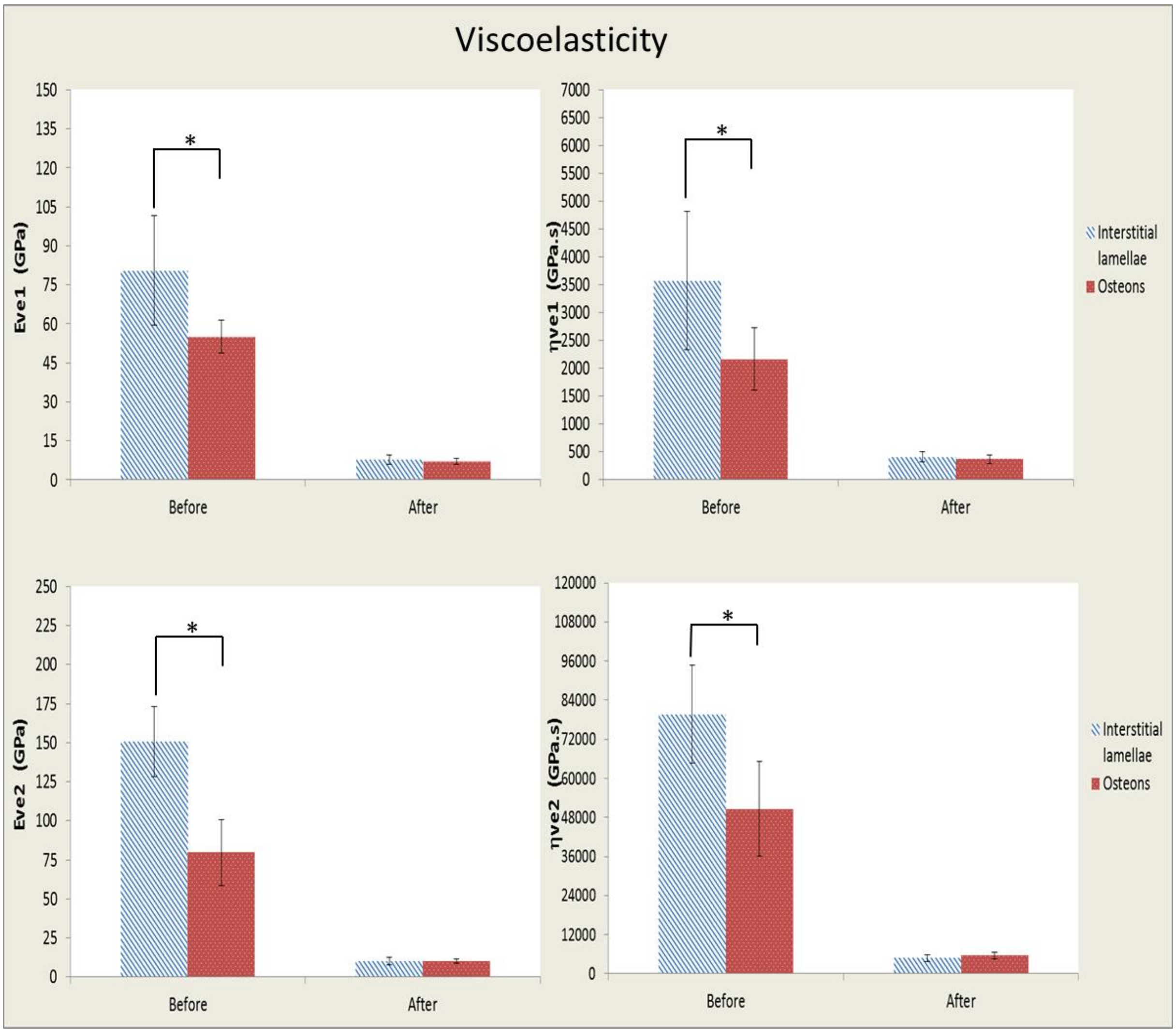

Figure 6.7 Viscoelastic response of bovine femoral cortical bone before and after demineralization process. The * represents a significant statistical difference between the results with a significant p value ($p<0.05$)

The most important decrease of the viscoelastic response was found for the second Kelvin-Voigt element. Indeed, values decrease about 94% for the lamellae bone and about 87% for osteons.

The results of hardness and viscoplasticity before and after demineralization process are represented in figure 6.8. Hardness of bone was found to decrease by 83% for lamellar bone and by 75% for osteons. Similar situation was found for viscoplastic response, for lamellar bone and osteons the values decrease by 85% and 79% respectively after demineralization process.

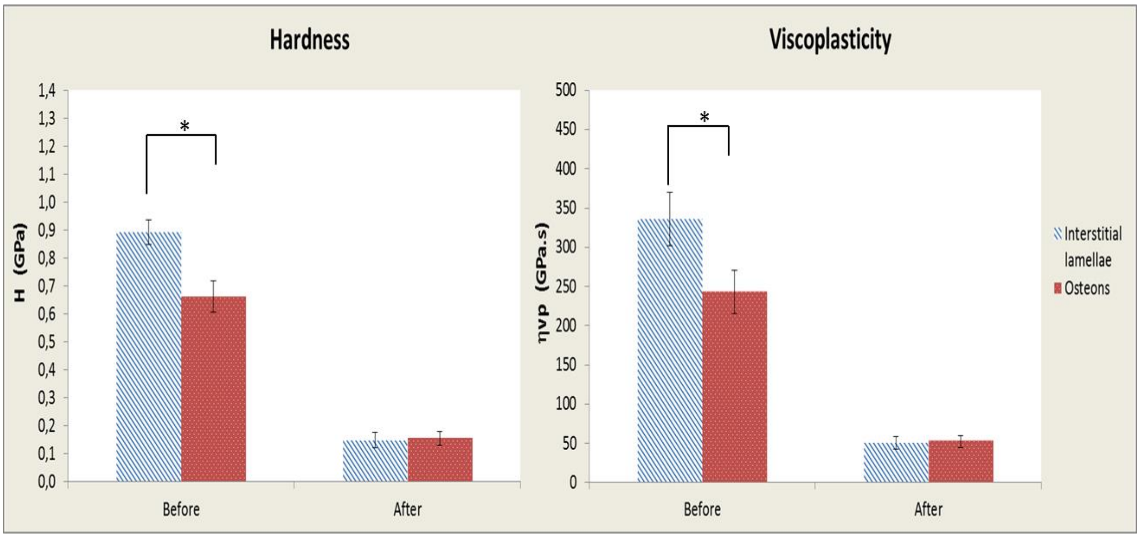

Figure 6.8 Hardness and viscoplasticity of bovine femoral cortical bone before and after demineralization process. The * represents a significant statistically difference between the results with a significant *p* value ($p<0.05$)

Using the elastic and viscoelastic mechanical properties, the apparent elastic modulus of bone after and before demineralization was computed. This modulus was computed for a given strain rate of $0.05 s^{-1}$ which is the strain rate used during the nanoindentation tests. The mean values and the SD were reported in table 6.3 and they are represented in figure 6.9.

The values after demineralization decrease by 90% for the lamellar bone and 84% for the osteonal region.

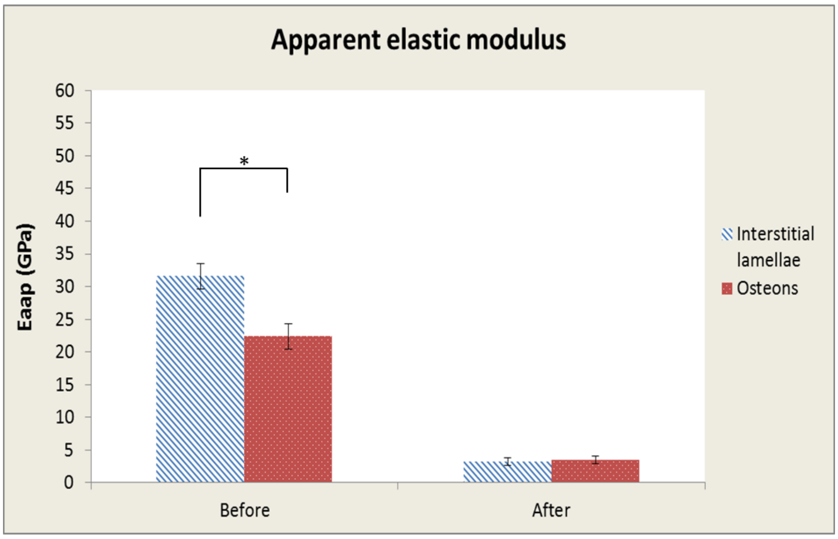

Figure 6.9 Apparent elastic modulus of bovine femoral cortical bone at a given strain rate of $0.05 s^{-1}$ before and after demineralization process. The * represents a significant statistical difference between the results with a significant p value ($p<0.05$)

Protocol II

Nanoindentation tests were performed in the three principal directions (longitudinal, transverse and radial) of bone axis. A total of 10 indentations per direction were performed in the lamellar bone and osteons before and after demineralization process. The mean values and the standard deviation computed from the experimental data are reported in Table 6.3. The apparent elastic modulus for a given strain rate of 0.05s^{-1} are also reported. This strain rate is the value used during the nanoindentation tests. These values of each mechanical property were represented in figures 6.10 to 6.13. The statistical tests were performed before and after demineralization process.

Table 6.3 Mechanical properties of bovine cortical bone after and before demineralization computed in the longitudinal direction using protocol II.

Before demineralization

Mechanical properties	**Longitudinal direction**		**Transverse direction**		**Radial Direction**	
	Lamellar Bone	**Osteons**	**Lamellar bone**	**Osteons**	**Lamellar bone**	**Osteons**
E_{elast} (GPa)	31.4 ± 1.6	27.9 ± 2.0	18.5 ± 0.2	17.3 ± 1.7	21.2 ± 1.2	20.6 ± 1.5
E_{ve1} (GPa)	65.5 ± 6.7	52.8 ± 2.3	39.9 ± 2.7	26.8 ± 2.0	31.8 ± 6.7	39.6 ± 5.4
η_{ve1} ×10^2(GPa.s)	28.4 ± 3.6	24.5 ± 2.7	20.2 ± 2.1	9.2 ± 1.2	10.4 ± 3.0	14.3 ± 2.7
E_{ve2} (GPa)	70.0 ± 11.9	74.3 ± 10.4	59.3 ± 2.7	58.1 ± 0.4	51.4 ± 9.8	50.6 ± 5.9
η_{ve2} ×10^3(GPa.s)	59.4 ± 7.0	58.5 ± 4.3	43.6 ± 6.9	31.3 ± 2.7	35.9 ± 3.8	29.8 ± 4.3
H (GPa)	0.69 ± 0.04	0.64 ± 0.03	0.54 ± 0.01	0.51 ± 0.03	0.55 ± 0.02	0.53 ± 0.06
η_{vp} (GPa.s)	263.4 ± 30.9	242.4± 15.0	196.0 ± 7.3	198.6 ± 23.0	197.4 ± 9.4	192.7 ± 12.4
Eapp (GPa)	24.5 ± 0.8	21.7± 1.2	14.8 ± 0.23	12.7 ± 0.6	15.1 ± 0.2	14.9 ± 1.7

After demineralization

Mechanical properties	**Longitudinal direction**		**Transverse direction**		**Radial Direction**	
	Lamellar Bone	**Osteons**	**Lamellar bone**	**Osteons**	**Lamellar bone**	**Osteons**
E_{elast} (GPa)	4.9 ± 1.7	3.4 ± 2.3	5.0 ± 0.5	5.1 ± 0.5	5.1 ± 0.9	5.3 ± 1.4
E_{ve1} (GPa)	7.4 ± 5.4	7.6 ± 1.9	6.2 ± 0.6	6.0 ± 0.8	6.2 ± 1.8	4.5 ± 1.3
η_{ve1} ×10^2(GPa.s)	3.6 ± 1.2	3.5 ± 2.0	2.4 ± 0.1	2.6 ± 0.1	3.0 ± 0.7	2.4 ± 0.4
E_{ve2} (GPa)	11.3 ± 7.2	8.0 ± 1.4	9.4 ± 0.7	8.8 ± 0.3	8.3 ± 2.8	6.4 ± 2.2
η_{ve2} ×10^3(GPa.s)	5.3 ± 0.8	2.6 ± 1.0	4.0 ± 0.3	5.0 ± 0.2	4.3 ± 1.1	3.7 ± 1.6
H (GPa)	0.11 ± 0.03	0.11 ± 0.03	0.14 ± 0.01	0.15 ± 0.03	0.12 ± 0.03	0.10 ± 0.03
η_{vp} (GPa.s)	40.8 ± 11.8	47.2 ± 21.3	57.0 ± 5.1	53.3 ± 6.0	42.2 ± 11.0	41.1 ± 9.9
Eapp (GPa)	3.7 ± 1.3	2.7 ± 1.6	3.5 ± 0.3	3.6 ± 0.3	3.6 ± 0.7	3.6 ± 0.9

mean values ± standard deviation

The values of the elastic response are represented in figure 6.10. In the longitudinal direction, before demineralization the elastic response was found to be different for interstitial lamellae and osteons.

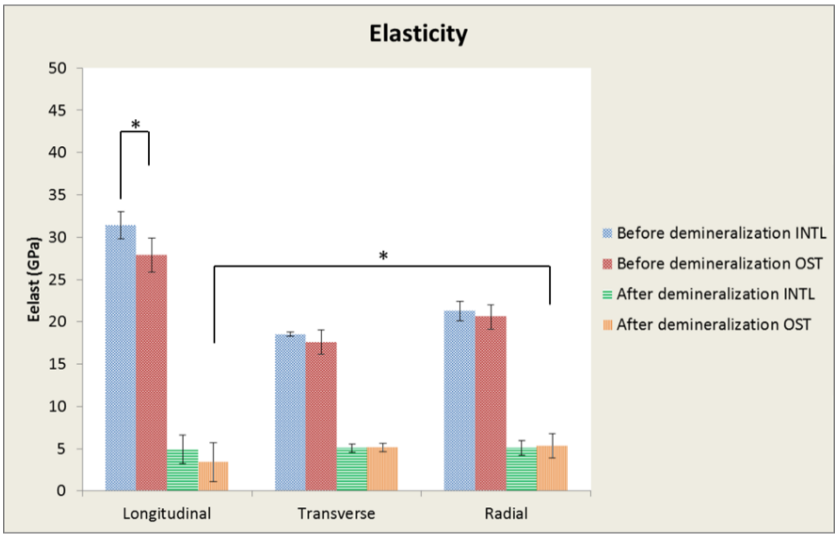

Figure 6.10 Elastic response of bovine femoral cortical bone before and after demineralization process assessed in the three main directions. The * represents a significant statistically difference between the results with a significant p value ($p<0.05$)

Non-significant statistical differences were found in the values computed for the transverse and radial direction. After demineralization process, in the longitudinal direction the values of the elastic response were found to decrease by about 90% for the lamellar bone and by about 80% for osteons. In addition, for the transverse and radial directions the values decrease by around 70% for lamellar bone and osteons. Complementary, non-statistical significant differences ($p<0.05$) were found between lamellar and osteonal bone after demineralization for any tested direction.

The results of viscoelasticity before and after demineralization process are represented in figure 6.11.

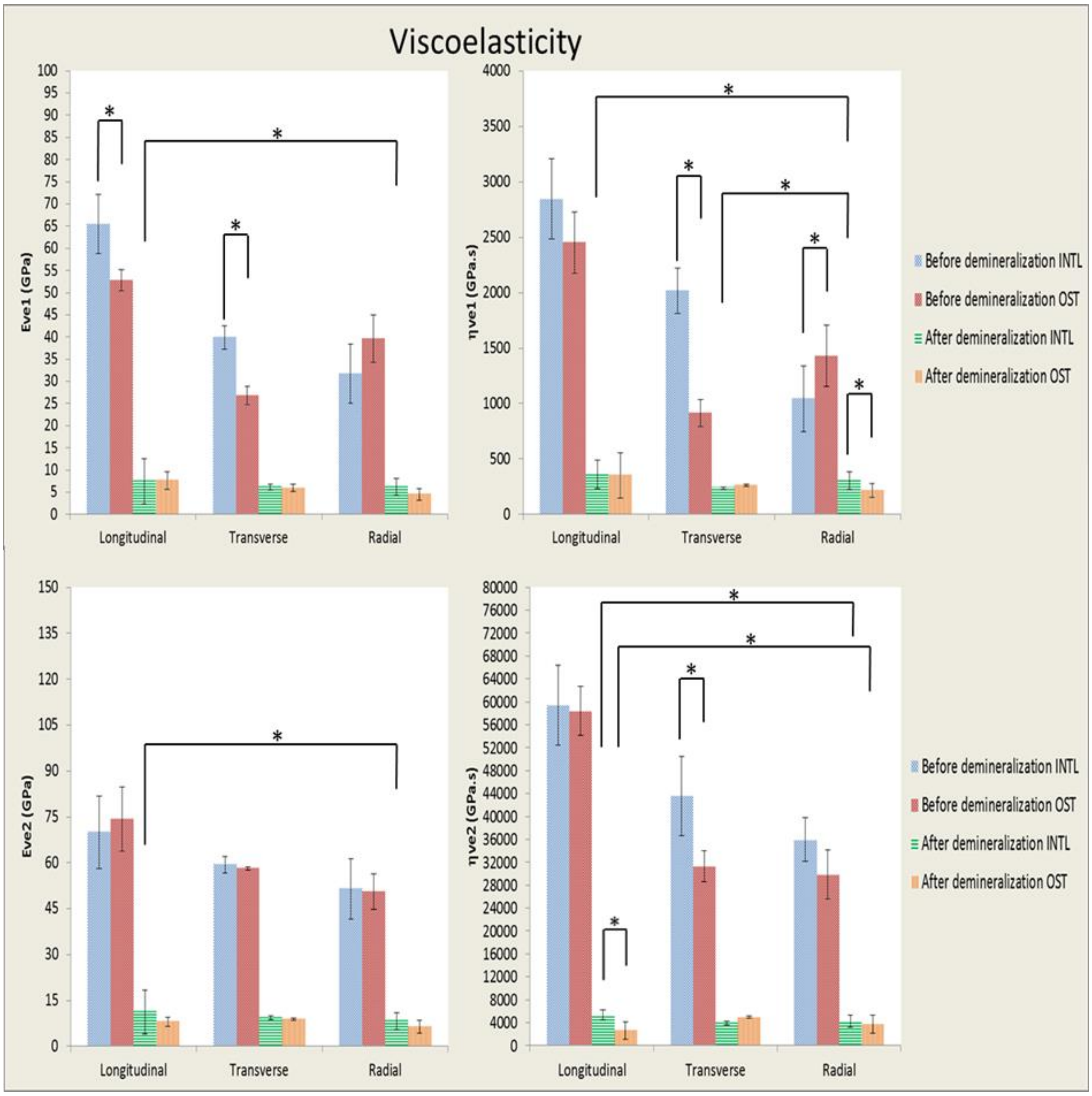

Figure 6.11 Viscoelastic response of bovine femoral cortical bone before and after demineralization process assessed in the three main directions. The * represents a significant statistical difference between the results with a significant p value ($p<0.05$)

Higher values of the viscoelastic response were found in the longitudinal direction. Before demineralization, the viscoelastic response is different for osteons and interstitial lamellae. After demineralization the elastic component E_{ve} have the same mechanical response for all the tested direction. In addition, the mechanical difference between osteons and lamellar bone is not evident for this component. The viscous components have important variations in the computed values. Significant statistical differences were found after demineralization between values of lamellar bone and osteons for η_{ve1} computed in the radial direction and for η_{ve2} computed in the longitudinal direction. Nevertheless, globally it is possible to affirm that the viscoelastic response of osteons and interstitial lamellae seem very similar after demineralization process.

Hardness and viscoplastic mechanical response are represented in figure 6.12

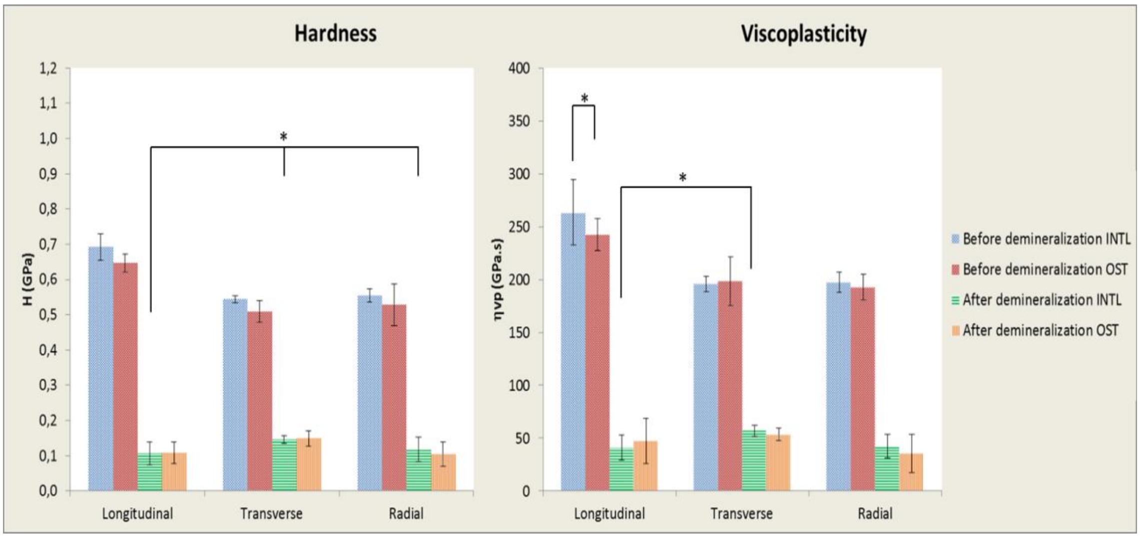

Figure 6.12 Hardness and viscoplasticity of bovine femoral cortical bone before and after demineralization process assessed in the three main directions. The * represents a significant statistical difference between the results with a significant *p* value ($p<0.05$)

The results show that before demineralization longitudinal direction presents the higher values. In addition, hardness values do not show statistical significant differences between osteons and lamellar bone at any testes direction. For viscoplasticity, statistical differences are presented between osteons and lamellar bone only in the longitudinal direction.

After demineralization, values of hardness and viscoplasticity decrease and become close to similar for all the directions. After mineral loss, interstitial lamellae of the longitudinal direction present statistical significant differences with the lamellar bone of the radial face. Meanwhile viscoplasticity values for interstitial lamellae of the longitudinal face are significantly statistically different of the lamellar bone of the transverse direction.

Using the elastic and viscoelastic mechanical properties, the apparent elastic modulus of bone after and before demineralization was computed for each direction. As performed for protocol I, this modulus was computing for a given strain rate of $0.05s^{-1}$.

The values obtained for this apparent elastic modulus at each direction are represented in figure 6.13.

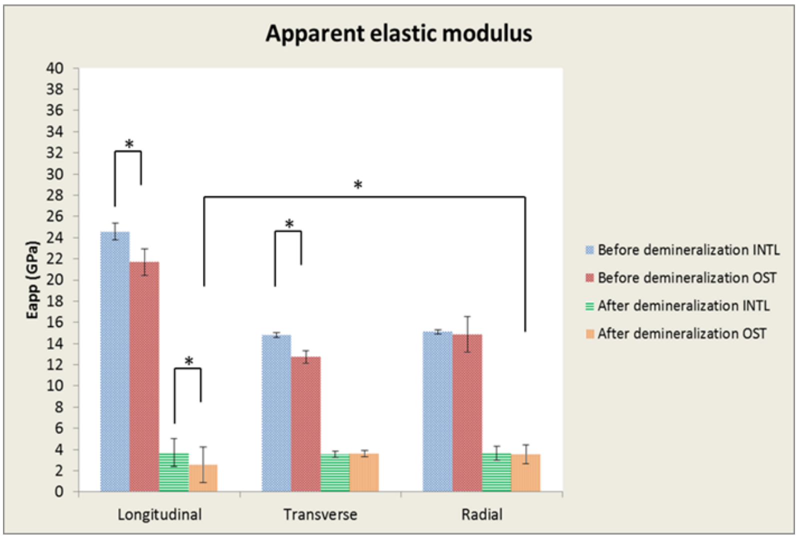

Figure 6.13 Apparent elastic modulus of bovine femoral cortical bone at a given strain rate of 0.05s^{-1} before and after demineralization process assessed in the three main directions. The * represents a significant statistical difference between the results with a significant p value (p<0.05)

As happened with protocol I, before demineralization the higher values of the apparent elastic modulus were found in the longitudinal direction. After demineralization, differences between values for the different directions are no longer evident. Only in the longitudinal direction, the differences between osteons and interstitial lamellae were statistically significant (*p*=0.049).

The values after demineralization decrease by about 88% in the longitudinal direction and about 80% in the transverse and radial directions. Statistical significant differences were found between osteons of the longitudinal and radial direction.

The anisotropic ratio was computed for bone samples before and after demineralization process. These values are summarized in Tables 6.4 and 6.5. Values reported allow one to highlight the impact of the mineral loss in the mechanical properties of bone. This fact suggests that bone become a quasi-isotropic material while mineral component is out.

Table 6.4 Mean anisotropy ratio for each mechanical property of bovine cortical bone BEFORE demineralization. An average anisotropic ratio and the standard deviation are reported for each typology of the cortical shell.

Mechanical Property	*Interstitial lamellae*			*Osteons*		
	T/R	L/R	L/T	T/R	L/R	L/T
$\mathbf{E_{elast}}$	0.87	1.48	1.70	0.84	1.35	1.61
$\mathbf{E_{ve1}}$	1.25	2.06	1.64	0.68	1.33	1.97
$\boldsymbol{\eta_{ve1}}$	1.94	2.73	1.41	0.64	1.71	2.66
$\mathbf{E_{ve2}}$	1.15	1.36	1.18	1.15	1.47	1.28
$\boldsymbol{\eta_{ve2}}$	1.21	1.65	1.36	1.05	1.96	1.87
H	0.98	1.25	1.28	0.96	1.21	1.25
$\boldsymbol{\eta_{vp}}$	0.99	1.33	1.34	1.03	1.26	1.22
$\mathbf{E_{app\ at\ \dot{\varepsilon}=0.05}}$	0.98	1.62	1.66	0.85	1.46	1.71
Average	**1.17**	**1.69**	**1.45**	**0.90**	**1.47**	**1.70**
SD	**(0.34)**	**(0.49)**	**(0.19)**	**(0.18)**	**(0.25)**	**(0.48)**

R=Radial. T=Transverse. L=Longitudinal, SD = Standard deviation

Table 6.5 Mean anisotropy ratio for each mechanical property of bovine cortical bone AFTER demineralization. An average anisotropic ratio and the standard deviation are reported for each typology of the cortical shell.

Mechanical Property	*Interstitial lamellae*			*Osteons*		
	T/R	L/R	L/T	T/R	L/R	L/T
$\mathbf{E_{elast}}$	0.98	0.96	0.98	0.96	0.64	0.67
$\mathbf{E_{ve1}}$	1.00	1.19	1.19	1.33	1.69	1.27
$\boldsymbol{\eta_{ve1}}$	0.80	1.20	1.50	1.08	1.46	1.35
$\mathbf{E_{ve2}}$	1.13	1.36	1.20	1.38	1.25	0.91
$\boldsymbol{\eta_{ve2}}$	0.93	1.23	1.33	1.35	0.70	0.52
H	1.17	0.92	0.79	1.50	1.10	0.73
$\boldsymbol{\eta_{vp}}$	1.35	0.97	0.72	1.30	1.15	0.89
$\mathbf{E_{app\ at\ \dot{\varepsilon}=0.05}}$	0.97	1.03	1.06	1.00	0.75	0.75
Average	**1.04**	**1.11**	**1.09**	**1.24**	**1.09**	**0.88**
SD	**(0.17)**	**(0.16)**	**(0.27)**	**(0.2)**	**(0.38)**	**(0.29)**

R=Radial. T=Transverse. L=Longitudinal, SD = Standard deviation

Even if physico-chemical analyses has not been performed yet, complete demineralization process could be confirmed for the values reported in Tables 6.3 and 6.4. The values computed for osteons and interstitial lamellae are close enough to validate the apparent absence of a vast part of the mineral component.

It was noted that changes in the mineral structure underlie a reduction in bone mechanical properties. The values computed for samples before and after demineralization process suggest that the presence of mineral phase in bone structure, increase their elastic, plastic and viscoplastic response by about five-times. Meanwhile the viscoelastic response increases about ten-times thank to the apatite.

According to the literature (see table 1.10), the elastic modulus of collagen fibrils type I computed using indentation tests is frequently found in a range between 1.2 and 6.2 GPa. This variation is commonly linked to the state and origin of the collagen fibrils, the experimental conditions and the method to quantify the values of the elastic response.

Moreover, in this study the elastic modulus computed for demineralized samples are in a range between 3.2 and 3.5 GPa for protocol I in the longitudinal direction and between 2.7 and 3.6 GPa for protocol II in any tested direction. These values are in agreement with the results reported by (Tai et al., 2005) who found an elastic modulus in the transverse direction of 3.8 GPa for samples with a mineral content ~4 Wt%. This remaining mineral content could be the reason why bone kept the frame after demineralization. In addition, the values obtained in this study are very similar to the values reported by (Andriotis et al., 2014; Grant et al., 2012; Wenger et al., 2008, 2007) with computed values of isolated collagen fibrils using AFM (~3.5 Gpa).. This fact could confirm two possibilities. On one hand, that both demineralization protocols allow one to obtain samples composed mostly by collagen and others organic components. On the other hand, this situation could confirm that mechanical properties obtained from this study could be attributed to the organic components of bone matrix.

The results obtained for samples demineralized with protocol II suggest that bone heterogeneity and its anisotropic behaviour could be mostly due to their mineral phase. This fact could be linked to the non-significant statistical differences between the values computed at the different directions for lamellar and osteonal bone.

As occurs for human bone in the previous chapter, the higher anisotropy ratios were found for bone viscoelastic components. One should note that without its mineral component, the values reported suggest that bone sample become a more homogeneous material with a quasi-isotropic mechanical behaviour. These facts could be verified by the two following points:

first, the anisotropic ratio after demineralization becomes ~1 for all the mechanical properties. Second, the mechanical differences between osteons and lamellar bone are no longer evident after demineralization.

The demineralized samples seem to lose its anisotropic behaviour. This suggests the role of minerals in the anistropic behaviour at the microscopic level. .

Nevertheless, it is necessary to perform complementary physico-chemical analysis in order to quantify the remained mineral content present in the samples. These analyses could improve and support better the interpretations about the contribution of the organic and mineral phases to the anisotropic behaviour of bone.

D. Morphological characterization by AFM

AFM characterization was performed before and after demineralization in samples obtained only by protocol I (cubic samples of protocol II are not size-adapted for multimode AFM). Images were obtained using contact AFM mode. AFM tips NP-S10 were used. These cantilevers are less stiff than other cantilevers used for contact mode. AFM images performed in different zones of the samples surface are presented in figures 6.14 to 6.16.

Before demineralization process, the collagen fibrils were never observed in native state. Frequently, they were masked for dense layers of mineral crystallites (figure 6.14).

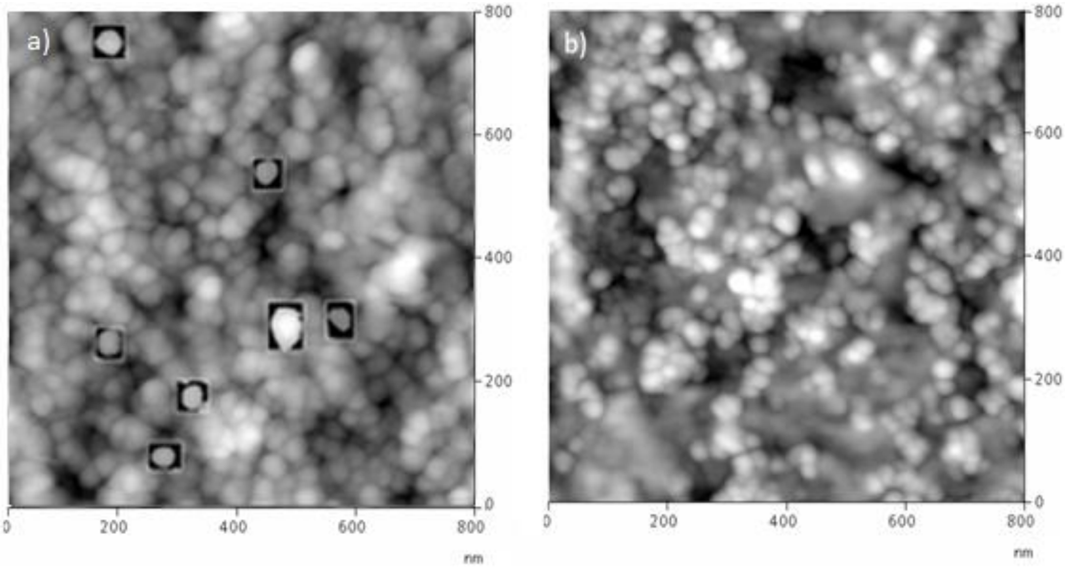

Figure 6.14 Contact mode height AFM images of mineral crystallites of bovine bone. Scan rate ~1.7 Hz and data scale 35 nm. a) Crystal shape is highlighted

From these images, it should be noted that crystal form small groups. These groups have an organization similar to bunch of grapes. This information could be useful for nanoscale bone models. Similar images were used to perform particle analysis in order to quantify some geometrical characteristics of the mineral crystals. Values found are reported in Table 6.6.

Table 6.6 Values of particle size acquired by AFM particle analysis for all bone samples

	Bovine bone before demineralization		
	Minimum (nm)	**Maximum (nm)**	**Mean (nm)**
Height	0.5	42.7	3.4
Diameter	11.0	443	50.2
Length	13.8	857	51.0
Width	13.8	318	34.2

After demineralization process, the remaining collagen fibrils are exposed and privileged orientation could be highlighted (figure 6.15 and 6.16).

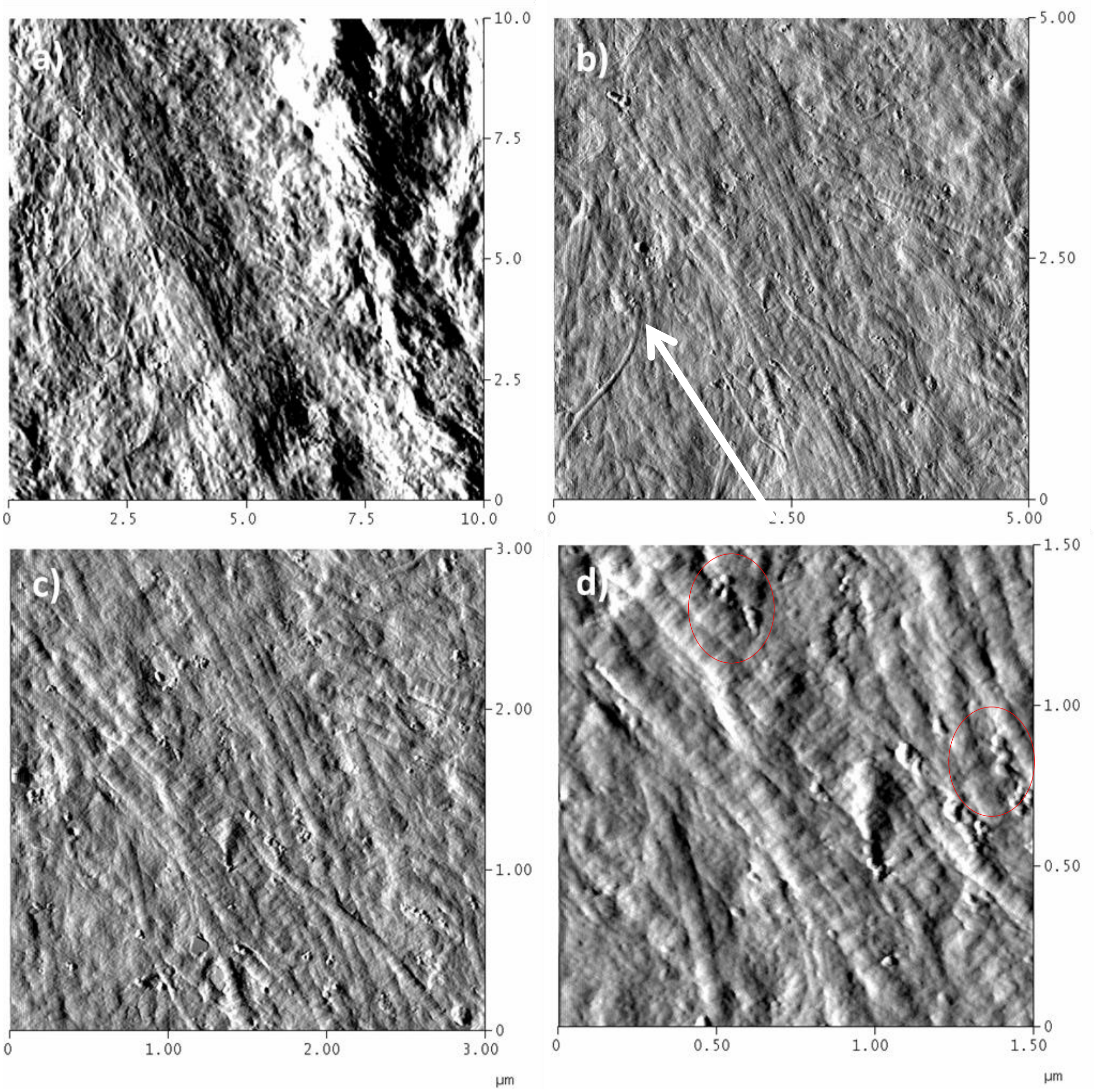

Figure 6.15 Deflection images of contact AFM mode of the demineralized sample obtained at different scales. Scan rate 2.2 Hz and data scale 45mV. White arrow displayed in all the figures signal the possible privileged orientation of the collagen fibrils. The circles point out possible remaining mineral crystals.

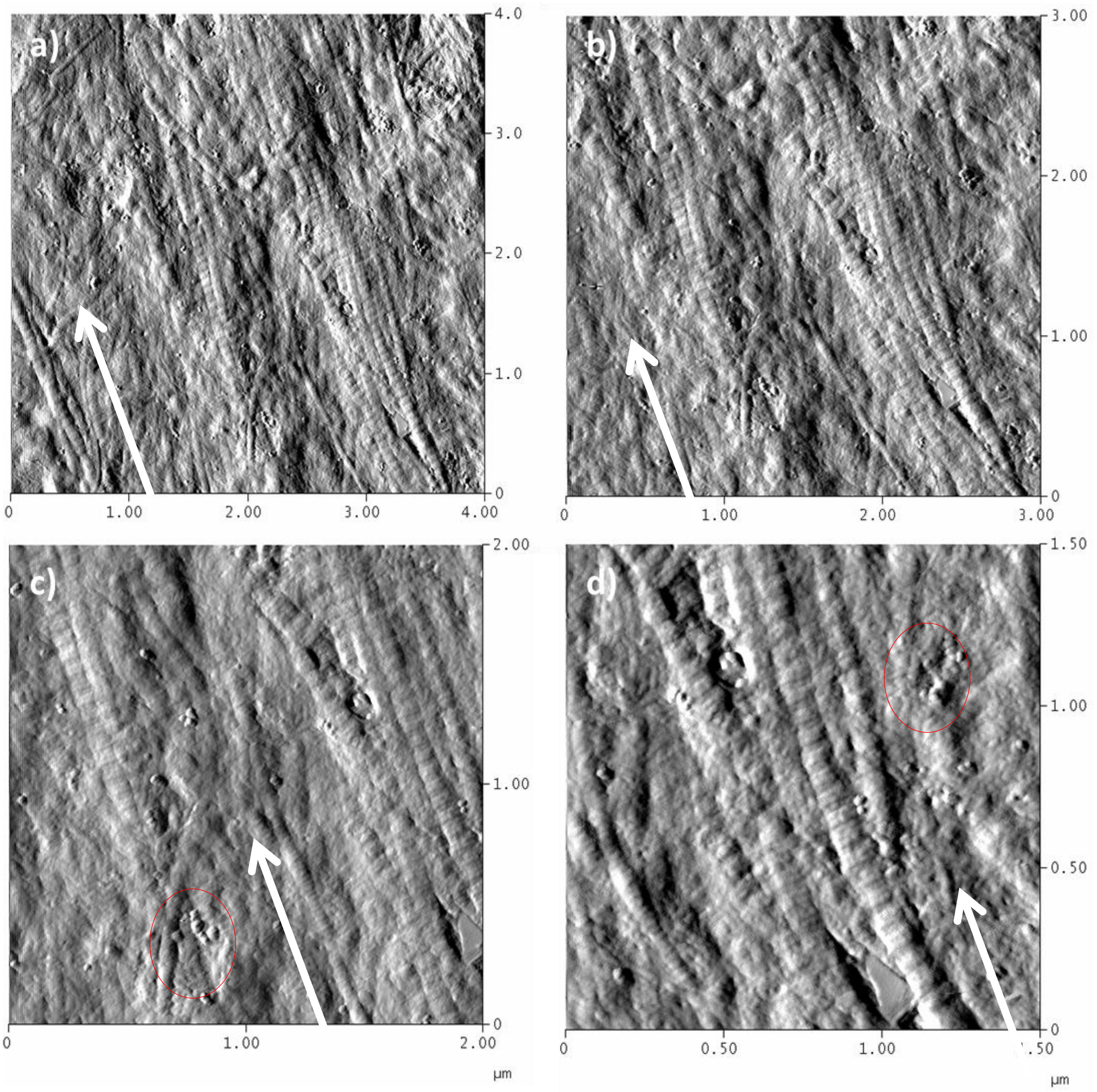

Figure 6.16 Deflection images of contact AFM mode of the demineralized sample obtained at different scales. Scan rate 2.2 Hz and data scale= 45mV. White arrow displayed in the entire figures signal the possible privileged orientation of the collagen fibrils. The circles point out possible remaining mineral crystals or particles debris.

The AFM images confirm the presence of collagen fibrils on bone surface. The fibrils were found frequently in the region of the lamellar bone and less recurrently near to the osteons region. From these AFM images collagen fibrils orientation were measured and found to be between 45° and 70° to the transverse plane of the bone. They are mostly aligned, running in the same direction, oriented mostly to ~60°. However, it is unknown if this privileged orientation is the original configuration of the collagen matrix or if is the consequence of the new reorganization due to the demineralization process.

After demineralization, samples surface was not subject to further preparations. Because of this, the privileged orientation of the collagen fibrils could be a reflection of their natural organization.

Using AFM image section analysis, the D-band patron was computed over 8 bovine collagen fibrils. Values of D-band patron were found to be within the range of the collagen type I periodicity (~ 68nm). The average values computed was 68.8 ± 1.8 nm. This value is slightly higher than that reported in the literature for collagen fibrils. However, this fact could be due to the manual placement of the markers used to measure the D-band patron. This placement depend a lot of the viewer perspective and that could induce small miscalculations. Despite this, the values computed are within the range of those reported in the literature (Hassenkam et al., 2004).

Analyses of the AFM images show that values of D-band patron for demineralized bone are very close of those found in this study for human (~67.9nm) and rat bone (~68.5nm). In addition, collagen fibrils of rat and demineralized bovine bone are aligned in a very similar way.

The structural organization and alignment of the collagen fibrils obtained from the demineralized bone was similar to the general topographical characteristics reported in literature for bovine and human trabecular bone (Hassenkam et al., 2005, 2004).

Mineral crystallites with their typical platelet-shape (see previous chapters) were rarely distinguished on the sample surface. Most of the particles found in the AFM images were associated to artefacts such as dust particles and other debris.

According to these results, one could affirm that collagen type I is an inner material common for all the species with most of their collagen fibrils oriented in a privileged direction.

Bone is a two-phase porous composite material composed of collagen type I and mineral. which together provide the structural and mechanical properties of bone (Burr. 2002). Most hard tissues have as their primary purpose to be stiff. According to the results obtained in this work after demineralization process, it is possible to confirm the hypothesis proposed by (Currey, 1999, 1969a, 1969b) who affirmed that mineralization of a soft organic matrix is the almost universal method of producing high stiffness and that mechanical properties of bone are very sensitive to the degree of mineralization of the bone matrix.

Chapter synthesis

Even if the mineral loss is extrapolated from the density diminution reported in Table 6.1, results proved that from both demineralization protocols produce similar mechanical response in bone sample.

Without an apparent mineral component, the remaining organic components present a mechanical behaviour close to 90% lower than the native bone.

After demineralization, the mechanical differences between osteons and lamellar bone are no longer evident.

As happened for human bone in chapter 5, the values of the mechanical response are highest in the longitudinal direction meanwhile in the transverse and radial directions are about 35% lower than in the longitudinal direction.

Before demineralization, the higher coefficients of the anisotropic ratio were found for the elastic and viscous components of viscoelasticity. The morphological assessments showed that collagen fibrils present a D-band of 68.8 ± 1.8 nm and present a privileged orientation around ~60° to the long axis of bone.

The average diameter of the mineral crystals was found to be 50nm, this values is quite similar that those obtained for mineral crystals in adult cortical bone of rats (chapter 3) and humans (chapter 4).

It was also noted from the anisotropic ratios computed in Table 6.4 and 6.5, that after demineralization process, the remaining “organic” component has a quasi-isotropic mechanical behaviour.

These results support the hypothesis presented in chapter 5, which suggests that bone anisotropy could be strongly linked to the mineral content and the collagen fibrils organization.

Conclusions and Outlook

Cortical bones present a very complex and hierarchical architecture given from the interaction between the mineral and collagen components. According to our knowledge, few investigations have been performed simultaneously on mechanical, morphological and physico-chemical properties of cortical bone. Thus, the aim of this thesis was to pursue the previous works performed in our laboratory by investigating the time-dependent mechanical properties at the microscopic scale and to correlate them to structural interactions at the nanometre scale thanks to the improvement realized by nanoindentation and atomic force microscopy.

In chapter 3, the time-dependent mechanical properties were assessed in a life span model of Wistar rat femoral cortical bones from growth to senescence.

- The results demonstrate that at the tissue level the mechanical properties varied with age. The elastic response increases from 1 to 4 months; the viscoelastic response increases from 1 to 9 months old and the plastic and viscoplastic response over the whole period covered by our experiments.
- The apparent elastic modulus increases by a factor ~2 while strain rate increases from 0 s^{-1} to infinite.
- The prediction equations computed to envisage the evolution of the mechanical properties with age could be useful for others fields as bone modelling and remodelling models.
- Elastic properties have a maturation age earlier and a growth rate faster than the other mechanical properties. Maturation age was found to be 2.7 months for the elastic properties meanwhile a range between ~9 to 11 months old was found for the time-dependent mechanical properties and hardness.
- The correlations between the time-dependent mechanical response and the physico-chemical properties suggest a strong correlation to micro porosity and to tissue composition (mineral content and protein weight). Nitrogen content was found to be strongly correlated to bone mechanical response.
- The morphological characterization performed by AFM shows collagen fibrils with their characteristic D-band patron which are mostly found in the endosteum zone.
- The mineral crystals size were found to increase with age meanwhile collagen fibrils were found to be privileged oriented between 45° and 60° in the transverse plane of the bone.

In chapter 4 and 5, human femoral bone were used. On one hand, three samples with different apparent densities and on the other hand, three samples from three different anatomic quadrants were tested.

- The time-dependent mechanical response of bone was not different between the high-density sample and the normal sample meanwhile bone with low density has a lower mechanical response especially for the elastic response.
- High mechanical response is found in the longitudinal direction of the femoral axis.
- Bone mechanical heterogeneity of the Haversian systems is related to their mineral content. Black osteons have a weaker mechanical response than white osteons in the longitudinal, transverse and radial direction.
- Independently of the tested direction, the apparent elastic modulus increases by a factor ~2 while the strain rate increases from a quasi-static to infinite strain rate.
- Even if few collagen fibers are observed, they were found to be oriented mostly of 45° in the transverse plane of the bone.
- In this work the apatite crystals shape were found to be predominantly platelet-like shape.
- The mechanical response was found to be higher in the longitudinal direction.
- Anisotropy behaviour was found in the entire microstructural component
- Bone mechanical response was slightly higher in the medial anatomical quadrant than in lateral and posterior quadrant of the cortical shell. Nevertheless, the influence of the anatomical quadrant is less obvious at the micro scale than at the macro scale.
- Viscous component of viscoelasticity have a higher anisotropic ratio; meanwhile viscoplasticity and hardness have a lower anisotropic ratio.
- The higher anisotropic behaviour was found to be greater for the viscoelastic properties. This situation could be associated to the possible orientation of the mineral crystallites.

In chapter 6, the mechanical and morphological characterization of the organic component of bone is presented. The mineral component was removed from bone structure by a chemical attack.

- Microscopic images after demineralization show the morphological compaction of bone microstructural boundaries between lamellar and osteonal bone.
- The AFM images were used to confirm the presence of collagen fibrils over most of the sample’s surface.
- Collagen fibrils are morphologically similar to those found in chapter 4 and 5 with a privileged orientation of 60° in the transverse plane of the bone.
- Mechanical properties after demineralization decreased between 75% and 95% in all directions.
- Mechanical results suggest that after demineralization bone become a homogeneous and mostly quasi-isotropic material. This fact suggests mineral phase of bone could be responsible for bone anisotropic behaviour.

From all the mechanical and morphological assessment at the micro and nano scale performed in human, rat and bovine bone, the follow common denominators are found:

- The mechanical properties for the adult femoral cortical bone are within the same range of values.
- Bone mechanical properties are strongly affected by its structural properties including pores and typology, the nitrogen content, the amount of hydroxyapatite crystallites and the orientation of the mineralized collagen fibrils.
- Bone increases its apparent elastic modulus by a factor ~2 while the strain rate passes from quasi-static to infinite.
- Morphological characteristics of the collagen fibrils type I and its D-band periodicity are similar for human, rat and bovine bone with privileged orientations between 45° and 60° to the transverse plane of the bone.
- Mineral crystals were found to have mostly a platelet-like shape with a diameter in a range between 37 to 68 nm.

In our concern, the new contributions of this work are:

- The assessment of the time-dependent mechanical properties that provide better description of bone mechanical properties providing new bone data characterizations.

- The preposition pooled for new prediction models to describe the evolution of the mechanical properties first as a function of age and then as a function of the physico-chemical characteristics.
- The assessments performed of bone mechanical and structural heterogeneity and anisotropic behaviour at the micro scale.
- The quantification done about the effects of a possible mineral loss in the mechanical response, structural and morphological characteristics of bone at the micro scale.
- The descriptions provided in the morphological characterization at the nanoscale, the mineral crystals size and shape and the apparent values for D-band periodicity and the privileged orientation of the collagen fibrils.

Because of its clinical relevance, a natural addition of this work may include the use of more human samples and the nanoindentation tests in hydrated conditions. New challenges will be addressed to investigate the mechanical properties of bone at the nano scale and their implications at the organ level. Another further work is the proposition of new multi-scale bone modelling in order to provide a new threshold in bone numerical simulations.

Clearly, a further extension of the present work may also contain deeper physico-chemical analyses in order to extrapolate; as far as possible; the mechanical properties of rat and bovine bone to human. Nevertheless, all the morphological data computed at the nanoscale (mineral crystals size, shape and collagen fibrils orientation) could be useful to propose new models of the bone remodelling and structural organization within the bone marrow.

Moreover, all the data reported in this work among different species could provide a better comprehension of the evolution of the mechanical properties with age, structure-property relationship and consequences of mineral loss. All this new understanding could be useful to develop new biomimetic materials and to propose new multi-scale constitutive laws of bone mechanical behaviour. In that context, a confidential report has been provided to the CNRS to identify the potential industrial transfer of the results of the PhD (Jaramillo 2014).

References

Abdel-Wahab, A. a, Alam, K., Silberschmidt, V. V, 2011. Analysis of anisotropic viscoelastoplastic properties of cortical bone tissues. J. Mech. Behav. Biomed. Mater. 4, 807–20.

Akkus, O., Adar, F., Schaffler, M.B., 2004. Age-related changes in physicochemical properties of mineral crystals are related to impaired mechanical function of cortical bone. Bone 34, 443–53.

Andriotis, O.G., Manuyakorn, W., Zekonyte, J., Katsamenis, O.L., Fabri, S., Howarth, P.H., Davies, D.E., Thurner, P.J., 2014. Nanomechanical assessment of human and murine collagen fibrils via atomic force microscopy cantilever-based nanoindentation. J. Mech. Behav. Biomed. Mater. 39C, 9–26.

Aoubiza, B., Crolet, J.M., Meunier, a, 1996. On the mechanical characterization of compact bone structure using the homogenization theory. J. Biomech. 29, 1539–47.

Ascenzi, a, Baschieri, P., Benvenuti, a, 1990. The bending properties of single osteons. J. Biomech. 23, 763–71.

Ascenzi, a, Benvenuti, A., Bonucci, E., 1982. The tensile properties of single osteonic lamellae: technical problems and preliminary results. J. Biomech. 15, 29–37.

Ashman, R.B., Cowin, S.C., Van Buskirk, W.C., Rice, J.C., 1984. A continuous wave technique for the measurement of the elastic properties of cortical bone. J. Biomech. 17, 349–361.

Balooch, M., Habelitz, S., Kinney, J.H., Marshall, S.J., Marshall, G.W., 2008. Mechanical properties of mineralized collagen fibrils as influenced by demineralization. J. Struct. Biol. 162, 404–10.

Bensamoun, S., 2003. Determination of mechanical and morphological properties of musculo skeletal tissue. Université de Technologie de Compiègne.

Bensamoun, S., Fan, Z., Brice, I., Rho, J.Y., Ho Ba Tho, M.-C., 2008. Assessment of Mechanical Properties of Human Osteon Lamellae Exhibiting Various Degrees of Mineralization By Nanoindentation. J. Musculoskelet. Res. 11, 135–143.

Bensamoun, S., Gherbezza, J., de Belleval, J.-F., Ho Ba Tho, M.-C., 2004a. Transmission scanning acoustic imaging of human cortical bone and relation with the microstructure. Clin. Biomech. (Bristol, Avon) 19, 639–47.

Bensamoun, S., Ho Ba Tho, M.-C., Luu, S., Gherbezza, J.-M., de Belleval, J.-F., 2004b. Spatial distribution of acoustic and elastic properties of human femoral cortical bone. J. Biomech. 37, 503–10.

Beyaoui, M., Mazeran, P.-E., Arvieu, M.-F., Bigerelle, M., Guigon, M., 2009. Analysis of nanoindentation curves in the case of bulk amorphous polymers. Int. J. Mater. Res. 100, 943–949.

Beyaoui, P.M., 2009. Nanoindentation de polymères amorphes, contribution à la détermination des propriétés quasi-statiques et dynamiques. Université de Technologie de Compiègne.

Bone Biology and Mechanics Lab [WWW Document], 2012. URL http://www.iupui.edu/~bbml/boneintro.shtml (accessed 5.25.14).

Bonucci, E., 1999. Basic composition and structure of bone. In: An, Y.H., Draughn, R.A. (Eds.), Mechanical Testing of Bone and the Bone-Implant Interface. CRC Press, pp. 3–22.

Bonucci, E., 2013. The mineralization of bone and its analogies with other hard tissues. In: Ferreira, S. (Ed.), Advance Topics on Crystal Growth. InTech.

Boussinesq, J., 1885. Applications des potentiels à l'étude de équilibre et du mouvement des solides élastiques. Gauthier-Villars, Paris.

Bozec, L., Groot, J. De, Odlyha, M., Nicholls, B., Nesbitt, S., Flanagan, A., Horton, M., 2005. Atomic force microscopy of collagen structure in bone and dentine revealed by osteoclastic resorption. Ultramicroscopy 105, 79–89.

Brockaert, H., 2010. Characterization of bone anisotropy at the microscopic scale. Université de Technologie de Compiègne.

Bromage, T.G., Goldman, H.M., McFarlin, S.C., Warshaw, J., Boyde, A., Riggs, C.M., 2003. Circularly polarized light standards for investigations of collagen fibre orientation in bone. Anat. Rec. B. New Anat. 274, 157–68.

Buckwalter, J.A., Glimcher, M.J., Cooper, R.R., Recker, R., 1995. Bone Biology. J. Bone Jt. Surg. 77, 1256–1275.

Budyn, E., Hoc, T., Jonvaux, J., 2008. Fracture strength assessment and aging signs detection in human cortical bone using an X-FEM multiple scale approach. Comput. Mech. 42, 579–591.

Budyn, E., Jonvaux, J., Funfschilling, C., Hoc, T., 2012. Bovine Cortical Bone Stiffness and Local Strain are Affected by Mineralization and Morphology. J. Appl. Mech. 79, 011008.

Burket, J., Gourion-Arsiquaud, S., Havill, L.M., Baker, S.P., Boskey, A.L., van der Meulen, M.C.H., 2011. Microstructure and nanomechanical properties in osteons relate to tissue and animal age. J. Biomech. 44, 277–84.

Burr, D.., 2002. The contribution of the organic matrix to bone's material properties. Bone 31, 8–11.

Burstein, a H., Currey, J.D., Frankel, V.H., Reilly, D.T., 1972. The ultimate properties of bone tissue: the effects of yielding. J. Biomech. 5, 35–44.

Busa, B., Miller, L.M., Rubin, C.T., Qin, Y.-X., Judex, S., 2005. Rapid establishment of chemical and mechanical properties during lamellar bone formation. Calcif. Tissue Int. 77, 386–94.

Butt, H.-J., Cappella, B., Kappl, M., 2005. Force measurements with the atomic force microscope: Technique, interpretation and applications. Surf. Sci. Rep. 59, 1–152.

Calabri, L., Pugno, N., Menozzi, C., Valeri, S., 2008. AFM nanoindentation: tip shape and tip radius of curvature effect on the hardness measurement. J. Phys. Condens. Matter 20, 474208.

Cappella, B., Dietler, G., 1999. Force-distance curves by atomic force microscopy. Surf. Sci. Rep. 34, 1–104.

Carnelli, D., Lucchini, R., Ponzoni, M., Contro, R., Vena, P., 2011. Nanoindentation testing and finite element simulations of cortical bone allowing for anisotropic elastic and inelastic mechanical response. J. Biomech. 44, 1852–1858.

Chen, W., Li, M., Zhang, T., Cheng, Y., Cheng, C., 2007. Influence of indenter tip roundness on hardness behavior in nanoindentation. Mater. Sci. Eng. A 445-446, 323–327.

Cook, S.M., Lang, K.M., Chynoweth, K.M., Wigton, M., Simmonds, R.W., Schäffer, T.E., 2006. Practical implementation of dynamic methods for measuring atomic force microscope cantilever spring constants. Nanotechnology 17, 2135–2145.

Cowin, S.C., 1983. The mechanical and stress adaptive properties of bone. Ann. Biomed. Eng. 11, 263–295.

Crolet, J.M., Aoubiza, B., Meunier, A., 1993. Compact bone: Numerical simulation of mechanical characteristics. J. Biomech. 26, 677–687.

Crowninshield, R.D., Pope, M.H., 1974. The response of compact bone in tension at various strain rates. Ann. Biomed. Eng. 2, 217–225.

Currey, J., 2008. Collagen and the Mechanical Properties of Bone and Calcified Cartilage. In: Bone. pp. 398 – 420.

Currey, J.D., 1969a. The relationship between the stiffness and the mineral content of bone. J. Biomech. 2, 477–480.

Currey, J.D., 1969b. The mechanical consequences of variation in the mineral content of bone. J. Biomech. 2, 1–11.

Currey, J.D., 1984. What should bones be designed to do? Calcif. Tissue Int. 36, S7–S10.

Currey, J.D., 1999. The design of mineralised hard tissues for their mechanical functions. J. Exp. Biol. 202, 3285–94.

Currey, J.D., Brear, K., Zioupos, P., 1996. The effects of ageing and changes in mineral content in degrading the toughness of human femora 29, 257–260.

Dall’Ara, E., Schmidt, R., Zysset, P., 2012. Microindentation can discriminate between damaged and intact human bone tissue. Bone 50, 925–9.

Dempster, D.W., 2006. Anatomy and functions of the adult skeleton. In: Favus MJ et al. (Ed.), Primer on the Metabolic Bone Diseases and Disorders of Mineral Metabolism. American Society for Bone and Mineral Research, Washington, pp. 7–11.

Dent, C.E., Smellie, J.M., Watson, L., 1965. Studies in osteopetrosis. Arch. Dis. Child. 40, 7–15.

Destresse, B., 1998. Mechanical and morphological studies of human spongious bone. Université Paul Sabatier.

Dominguez, L.J., Di Bella, G., Belvedere, M., Barbagallo, M., 2011. Physiology of the aging bone and mechanisms of action of bisphosphonates. Biogerontology 12, 397–408.

Dong, X.N., Guo, X.E., 2004. The dependence of transversely isotropic elasticity of human femoral cortical bone on porosity. J. Biomech. 37, 1281–7.

Donnelly, E., Boskey, A.L., Baker, S.P., van der Meulen, M.C.H., 2010. Effects of tissue age on bone tissue material composition and nanomechanical properties in the rat cortex. J. Biomed. Mater. Res. A 92, 1048–56.

Eberhardsteiner, L., Hellmich, C., Scheiner, S., 2014. Layered water in crystal interfaces as source for bone viscoelasticity: arguments from a multiscale approach. Comput. Methods Biomech. Biomed. Engin. 17, 48–63.

El Kirat, K., Burton, I., Dupres, V., Dufrene, Y.F., 2005. Sample preparation procedures for biological atomic force microscopy. J. Microsc. 218, 199–207.

El Kirat, K., Morandat, S., Dufrêne, Y.F., 2010. Nanoscale analysis of supported lipid bilayers using atomic force microscopy. Biochim. Biophys. Acta 1798, 750–65.

Eppell, S.J., Smith, B.N., Kahn, H., Ballarini, R., 2006. Nano measurements with micro-devices: mechanical properties of hydrated collagen fibrils. J. R. Soc. Interface 3, 117–21.

Espinoza Orías, A. a, Deuerling, J.M., Landrigan, M.D., Renaud, J.E., Roeder, R.K., 2009. Anatomic variation in the elastic anisotropy of cortical bone tissue in the human femur. J. Mech. Behav. Biomed. Mater. 2, 255–63.

Evans, F.G., Vincentelli, R., 1974. Relations of the compressive properties of human cortical bone to histological structure and calcification. J. Biomech. 7, 1–10.

Evans, G., 1973. Bone issue. pp. 341–384.

Eyden, B., Tzaphlidou, M., 2001. Structural variations of collagen in normal and pathological tissues: role of electron microscopy. Micron 32, 287–300.

Fan, Z., Rho, J.-Y., 2003. Effects of viscoelasticity and time-dependent plasticity on nanoindentation measurements of human cortical bone. J. Biomed. Mater. Res. A 67, 208–14.

Fan, Z., Swadener, J.G., Rho, J.Y., Roy, M.E., Pharr, G.M., 2002. Anisotropic properties of human tibial cortical bone as measured by nanoindentation. J. Orthop. Res. 20, 806–10.

Ferguson, V.L., 2009. Deformation partitioning provides insight into elastic, plastic, and viscous contributions to bone material behavior. J. Mech. Behav. Biomed. Mater. 2, 364–74.

Fischer-Cripps, a. C., 2004. A simple phenomenological approach to nanoindentation creep. Mater. Sci. Eng. A 385, 74–82.

Fischer-Cripps, A.C., 2009. The Handbook of f Nanoindentation, Analysis. Fischer-Cripps Laboratories Pty Ltd, Forestville NSW 2087 Australia.

Franzoso, G., Zysset, P.K., 2009. Elastic anisotropy of human cortical bone secondary osteons measured by nanoindentation. J. Biomech. Eng. 131, 021001.

Fratzl, P., Gupta, H.S., Paschalis, E.P., Roschger, P., 2004. Structure and mechanical quality of the collagen-mineral nano- composite in bone. J. Mater. Chem. 14, 2115.

Gautieri, A., Vesentini, S., Redaelli, A., Ballarini, R., 2013. Modeling and measuring visco-elastic properties: From collagen molecules to collagen fibrils. Int. J. Non. Linear. Mech. 56, 25–33.

Geisse, N. a., 2009. AFM and combined optical techniques. Mater. Today 12, 40–45.

Gibson, L.J., 1985. The mechanical behaviour of cancellous bone. J. Biomech. 18, 317–328.

Goldstein, S.A., 1987. The mechanical properties of trabecular bone: Dependence on anatomic location and function. J. Biomech. 20, 1055–1061.

Goodwin, K.J., Sharkey, N. a, 2002. Material properties of interstitial lamellae reflect local strain environments. J. Orthop. Res. 20, 600–6.

Grant, C. a, Brockwell, D.J., Radford, S.E., Thomson, N.H., 2009. Tuning the elastic modulus of hydrated collagen fibrils. Biophys. J. 97, 2985–92.

Grant, C.A., Phillips, M.A., Thomson, N.H., 2012. Dynamic mechanical analysis of collagen fibrils at the nanoscale. J. Mech. Behav. Biomed. Mater. 5, 165–70.

Gross, L., Mohn, F., Moll, N., Liljeroth, P., Meyer, G., 2009. The chemical structure of a molecule resolved by atomic force microscopy. Science 325, 1110–4.

Gupta, H.S., 2008. Nanoscale Deformation Mechanisms in Collagen. In: Fratzl, P. (Ed.), Collagen: Structure and Mechanics. pp. 155–173.

Gupta, H.S., Zioupos, P., 2008. Fracture of bone tissue: The “hows” and the “whys”. Med. Eng. Phys. 30, 1209–26.

Hadjidakis, D.J., Androulakis, I.I., 2006. Bone remodeling. Ann. N. Y. Acad. Sci. 1092, 385–96.

Hansma, P.K., Fantner, G.E., Kindt, J.H., Thurner, P.J., Schitter, G., Turner, P.J., Udwin, S.F., Finch, M.M., 2005. Sacrificial bonds in the interfibrillar matrix of bone. J. Musculoskelet. Neuronal Interact. 5, 313–5.

Hardin, J., Bertoni, G.P., Kleinsmith, L.J., 2010. Becker’s World of the Cell (8th Edition). Benjamin/Cummings Publishing Company, Inc., San Francisco.

Hassenkam, T., Fantner, G.E., Cutroni, J.A., Weaver, J.C., Morse, D.E., Hansma, P.K., 2004. High-resolution AFM imaging of intact and fractured trabecular bone. Bone 35, 4–10.

Hassenkam, T., Jørgensen, H.L., Pedersen, M.B., Kourakis, A.H., Simonsen, L., Lauritzen, J.B., 2005. Atomic force microscopy on human trabecular bone from an old woman with osteoporotic fractures. Bone 36, 681–687.

Hay, J., Agee, P., Herbert, E., 2010. Continuous stiffness measurement during instrumented indentation testing. Exp. Tech. 34, 86–94.

Hengsberger, S., Ammann, P., Legros, B., Rizzoli, R., Zysset, P., 2005. Intrinsic bone tissue properties in adult rat vertebrae: modulation by dietary protein. Bone 36, 134–41.

Hengsberger, S., Kulik, A., Zysset, P., 2001. A combined atomic force microscopy and nanoindentation technique to investigate the elastic properties of bone structural units. Eur. Cell. Mater. 1, 12–7.

Hengsberger, S., Kulik, A., Zysset, P., 2002. Nanoindentation discriminates the elastic properties of individual human bone lamellae under dry and physiological conditions. Bone 30, 178–84.

Herring, G.M., 1977. Methods for the study of the glycoproteins and proteoglycans of bone using bacterial collagenase. Calcif. Tissue Res. 24, 29–36.

Hertz, H., 1882. Ueber die Berührung fester elastischer Körper. J. für die reine und Angew. Math. (Crelle’s Journal) 1882, 156–171.

Hillier, M.L., Bell, L.S., 2007. Differentiating human bone from animal bone: a review of histological methods. J. Forensic Sci. 52, 249–63.

Ho Ba Tho, M.-C., Ashman, R.B., Darmara, R., Morucci, J., 1991a. Assesment of the elastic properties of human tibial cortical bone by ultrasonic measurements. In: Van der Perre, G., Lowet, G., Borgwardt Christensen, A. (Eds.), In Vivo Assessment of Bone Quality by Vibration and Wave Propagation Techniques. Part I. Leuven, Durham, pp. 45–56.

Ho Ba Tho, M.-C., Mazeran, P.-E., El-Kirat, K., Bensamoun, S., 2012. Multiscale Characterization of Human Cortical Bone. Comput. Model. Eng. Sci. 87, 557–577.

Ho Ba Tho, M.-C., Rho, J.-Y., Ashman, R.B., 1991b. Atlas of mechanical properties of human cortical and cancellous bone.pdf. In: In Vivo Assessment of Bone Quality by Vibration and Wave Propagation Techniques. Part II. Durham, pp. 7–38.

Hoc, T., Henry, L., Verdier, M., Aubry, D., Sedel, L., Meunier, a, 2006. Effect of microstructure on the mechanical properties of Haversian cortical bone. Bone 38, 466–74.

Hochstetter, G., Jimenez, A., Loubet, J.L., 1999. Strain-rate effects on hardness of glassy polymers in the nanoscale range. Comparison between quasi-static and continuous stiffness measurements. J. Macromol. Sci. Part B 38, 681–692.

Hodgskinson, R., Currey, J.D., 1992. Young's modulus, density and material properties in cancellous bone over a large density range. J. Mater. Sci. Mater. Med. 3, 377–381.

Hoffler, C.E., Moore, K.E., Kozloff, K., Zysset, P.K., Brown, M.B., Goldstein, S.A., 2000. Heterogeneity of bone lamellar-level elastic moduli. Bone 26, 603–9.

Hutter, J.L., Bechhoefer, J., 1993. Calibration of atomic-force microscope tips. Rev. Sci. Instrum. 64, 1868.

Iida, H., Fukuda, S., 2002. Age-related changes in bone mineral density, cross-sectional area and strength at different skeletal sites in male rats. J. Vet. Med. Sci. 64, 29–34.

Isaksson, H., Malkiewicz, M., Nowak, R., Helminen, H.J., Jurvelin, J.S., 2010a. Rabbit cortical bone tissue increases its elastic stiffness but becomes less viscoelastic with age. Bone 47, 1030–8.

Isaksson, H., Nagao, S., Małkiewicz, M., Julkunen, P., Nowak, R., Jurvelin, J.S., 2010b. Precision of nanoindentation protocols for measurement of viscoelasticity in cortical and trabecular bone. J. Biomech. 43, 2410–7.

Jämsä, T., Rho, J.-Y., Fan, Z., MacKay, C. a, Marks, S.C., Tuukkanen, J., 2002. Mechanical properties in long bones of rat osteopetrotic mutations. J. Biomech. 35, 161–5.

Jarvis, D.R., 1997. Nitrogen levels in long bones from coffin burials interred for periods of 26-90 years. Forensic Sci. Int. 85, 199–208.

Jiang, W., Pan, H., Cai, Y., Tao, J., Liu, P., Xu, X., Tang, R., 2008. Atomic force microscopy reveals hydroxyapatite-citrate interfacial structure at the atomic level. Langmuir 24, 12446–51.

Jørgensen, P.H., Bak, B., Andreassen, T.T., 1991. Mechanical properties and biochemical composition of rat cortical femur and tibia after long-term treatment with biosynthetic human growth hormone. Bone 12, 353–9.

JPK Instruments AG, n.d. Determining the elastic modulus of biological samples using atomic force microscopy. Appl. Note 1–9.

Katsamanis, F., Raftopoulos, D.D., 1990. Determination of mechanical properties of human femoral cortical bone by the Hopkinson bar stress technique. J. Biomech. 23, 1173–1184.

Katz, J.L., 1980. Anisotropy of Young’s modulus of bone. Nature 283, 106–107.

Katz, J.L., Meunier, A., 1987. The elastic anisotropy of bone. J. Biomech. 20, 1063–1070.

Katz, J.L., Yoon, H.S., Lipson, S., Maharidge, R., Meunier, a, Christel, P., 1984. The effects of remodeling on the elastic properties of bone. Calcif. Tissue Int. 36 Suppl 1, S31–6.

Kim, M.-S., Choi, J.-H., Kim, J.-H., Park, Y.-K., 2010. Accurate determination of spring constant of atomic force microscope cantilevers and comparison with other methods. Measurement 43, 520–526.

Kohles, S.S., Cartee, G.D., Vanderby, R., 1996. Cortical elasticity in aging rats with and without growth hormone treatments. J. Med. Eng. Technol. 20, 157–63.

Li, X., Bhushan, B., 2002. A review of nanoindentation continuous stiffness measurement technique and its applications. Mater. Charact. 48, 11 – 36.

Liebschner, M. a. K., 2004. Biomechanical considerations of animal models used in tissue engineering of bone. Biomaterials 25, 1697–1714.

Lin, D.C., Dimitriadis, E.K., Horkay, F., 2007. Robust strategies for automated AFM force curve analysis-II: adhesion-influenced indentation of soft, elastic materials. J. Biomech. Eng. 129, 904–12.

Lipson, S.F., Katz, J.L., 1984. The relationship between elastic properties and microstructure of bovine cortical bone. J. Biomech. 17, 231–240.

Loubet, J.L., Bauer, M., Tonck, A., Bec, S., Gauthier-Manuel, B., 1993. Nanoindentation with a Surface Force Apparatus. In: Nastasi, M., Parkin, D.M., Gleiter, H. (Eds.), Mechanical Properties and Deformation Behavior of Materials Having Ultra-Fine Microstructures. Springer Netherlands, Dordrecht, pp. 429–447.

Lucas, B.N., Oliver, W.C., Pharr, G.M., Loubet, J.-L., 1996a. Time Dependent Deformation During Indentation Testing. MRS Proc. 436, 233.

Lucas, B.N., Oliver, W.C., Pharr, G.M., Loubet, J.-L., 1996b. Time Dependent Deformation During Indentation Testing. MRS Proc. 436, 233.

Lucca, D. a., Herrmann, K., Klopfstein, M.J., 2010. Nanoindentation: Measuring methods and applications. CIRP Ann. - Manuf. Technol. 59, 803–819.

Markiewicz, P., Goh, M.C., 1995. Atomic force microscope tip deconvolution using calibration arrays. Rev. Sci. Instrum. 66, 3186.

Mazeran, P.-E., Beyaoui, M., Bigerelle, M., Guigon, M., 2012. Determination of mechanical properties by nanoindentation in the case of viscous materials. Int. J. Mater. Res. 103, 715–722.

McElhaney, J.H., 1966. Dynamic response of bone and muscle tissue. J. Appl. Physiol. 21, 1231–6.

Middleton, K.M., Goldstein, B.D., Guduru, P.R., Waters, J.F., Kelly, S. a, Swartz, S.M., Garland, T., 2010. Variation in within-bone stiffness measured by nanoindentation in mice bred for high levels of voluntary wheel running. J. Anat. 216, 121–31.

Minary-Jolandan, M., Yu, M.-F., 2009. Nanomechanical heterogeneity in the gap and overlap regions of type I collagen fibrils with implications for bone heterogeneity. Biomacromolecules 10, 2565–70.

Monclus, M. a., Young, T.J., Di Maio, D., 2010. AFM indentation method used for elastic modulus characterization of interfaces and thin layers. J. Mater. Sci. 45, 3190–3197.

Odegard, G.M., Gates, T.S., Herring, H.M., 2005. Characterization of viscoelastic properties of polymeric materials through nanoindentation. Exp. Mech. 45, 130–136.

Ohler, B., 2007. Cantilever spring constant calibration using laser Doppler vibrometry. Rev. Sci. Instrum. 78, 063701.

Olesiak, S.E., Oyen, M.L., Ferguson, V.L., 2009. Viscous-elastic-plastic behavior of bone using Berkovich nanoindentation. Mech. Time-Dependent Mater. 14, 111–124.

Oliver, W.C., Pharr, G.M., 1992. An improved technique for determining hardness and elastic modulus using load and displacement sensing indentation experiments. J. Mater. Res. 7, 1564–1583.

Oliver, W.C., Pharr, G.M., 2004. Measurement of hardness and elastic modulus by instrumented indentation: Advances in understanding and refinements to methodology. J. Mater. Res. 19, 3–20.

Oyen, M.L., 2005. Chapter 4 : Time-Dependent Indentation. In: University of Minnesota (Ed.), Ultrastructural Characterization of Time-Dependent, Inhomogeneous Materials and Tissues. Minnesota, pp. 122–157.

Oyen, M.L., 2006. Nanoindentation hardness of mineralized tissues. J. Biomech. 39, 2699–702.

Oyen, M.L., 2006. Analytical techniques for indentation of viscoelastic materials. Philos. Mag. 86, 5625–5641.

Oyen, M.L., Cook, R.F., 2003. Load–displacement behavior during sharp indentation of viscous–elastic–plastic materials. J. Mater. Res. 18, 139–150.

Oyen, M.L., Ko, C.-C., 2007. Examination of local variations in viscous, elastic, and plastic indentation responses in healing bone. J. Mater. Sci. Mater. Med. 18, 623–8.

Passeri, D., Bettucci, a., Germano, M., Rossi, M., Alippi, a., Orlanducci, S., Terranova, M.L., Ciavarella, M., 2005. Effect of tip geometry on local indentation modulus measurement via atomic force acoustic microscopy technique. Rev. Sci. Instrum. 76, 093904.

Pithioux, M., Lasaygues, P., Chabrand, P., 2002. An alternative ultrasonic method for measuring the elastic properties of cortical bone. J. Biomech. 35, 961–8.

Potes, J.C., Reis, C., Capela, F., Relvas, C., Cabrita, S., Simões, J.A., 2008. The Sheep as an Animal Model in Orthopaedic Research. Interface 2, 29–32.

Raisz, L.G., Seeman, E., 2001. Causes of age-related bone loss and bone fragility: an alternative view. J. Bone Miner. Res. 16, 1948–52.

Reilly, D.T., Burstein, A.H., 1975. The elastic and ultimate properties of compact bone tissue. J. Biomech. 8, 393–405.

Reilly, D.T., Burstein, A.H., Frankel, V.H., 1974. The elastic modulus for bone. J. Biomech. 7, 271–275.

Revenko, I., Sommer, F., Minh, D.T., Garrone, R., Franc, J.M., 1994. Atomic force microscopy study of the collagen fibre structure. Biol. Cell 80, 67–9.

Rho, J.Y., Currey, J.D., Zioupos, P., Pharr, G.M., 2001. The anisotropic young’s modulus of equine secondary osteones and interstitial bone determined by nanoindentation. J. Exp. Biol. 1781, 1775–1781.

Rho, J.Y., Kuhn-Spearing, L., Zioupos, P., 1998. Mechanical properties and the hierarchical structure of bone. Med. Eng. Phys. 20, 92–102.

Rho, J.Y., Pharr, G.M., 1999. Effects of drying on the mechanical properties of bovine femur measured by nanoindentation. J. Mater. Sci. Mater. Med. 10, 485–8.

Rho, J.Y., Roy, M.E., Tsui, T.Y., Pharr, G.M., 1999. Elastic properties of microstructural components of human bone tissue as measured by nanoindentation. J. Biomed. Mater. Res. 45, 48–54.

Rho, J.Y., Tsui, T.Y., Pharr, G.M., 1997. Elastic properties of human cortical and trabecular lamellar bone measured by nanoindentation. Biomaterials 18, 1325–30.

Rho, J.Y., Zioupos, P., Currey, J.D., Pharr, G.M., 2000. Variations in the individual thick lamellar properties within osteons by nanodentation. Bone 25, 295–300.

Rho, J.Y., Zioupos, P., Currey, J.D., Pharr, G.M., 2002. Microstructural elasticity and regional heterogeneity in human femoral bone of various ages examined by nano-indentation. J. Biomech. 35, 189–98.

Rice, J.C., Cowin, S.C., Bowman, J. a, 1988. On the dependence of the elasticity and strength of cancellous bone on apparent density. J. Biomech. 21, 155–68.

Rodriguez-Florez, N., Oyen, M.L., Shefelbine, S.J., 2013. Insight into differences in nanoindentation properties of bone. J. Mech. Behav. Biomed. Mater. 18, 90–9.

Rosen, L.B., Ginty, D.D., Weber, M.J., Greenberg, M.E., 1994. Membrane depolarization and calcium influx stimulate MEK and MAP kinase via activation of Ras. Neuron 12, 1207–21.

Rosen, V.B., Hobbs, L.W., Spector, M., 2002. The ultrastructure of anorganic bovine bone and selected synthetic hyroxyapatites used as bone graft substitute materials. Biomaterials 23, 921–8.

Roy, M.E., Rho, J.Y., Tsui, T.Y., Evans, N.D., Pharr, G.M., 1999. Mechanical and morphological variation of the human lumbar vertebral cortical and trabecular bone. J. Biomed. Mater. Res. 44, 191–7.

Saber-Samandari, S., Gross, K.A., 2009. Micromechanical properties of single crystal hydroxyapatite by nanoindentation. Acta Biomater. 5, 2206–12.

Sader, J.E., Chon, J.W.M., Mulvaney, P., 1999. Calibration of rectangular atomic force microscope cantilevers. Rev. Sci. Instrum. 70, 3967.

Sakamoto, M., Kobayashi, K., 2009. Viscoelastic Properties of Microstructural Components of Rat Cortical Bone Tissue as Measured by Dynamic Nanoindentation. J. JSEM 9, 151–155.

Saladin, K., 2002. Bone Tissue. In: Anatomy & Physiology: The Unity of Form and Function,. McGraw Hill, pp. 217–240.

Sansalone, V., Naili, S., Bousson, V., Bergot, C., Peyrin, F., Zarka, J., Laredo, J.D., Haïat, G., 2010. Determination of the heterogeneous anisotropic elastic properties of human femoral bone: from nanoscopic to organ scale. J. Biomech. 43, 1857–63.

Sasaki, N., Ikawa, T., Fukuda, A., 1991. Orientation of mineral in bovine bone and the anisotropic mechanical properties of plexiform bone. J. Biomech. 24, 57–61.

Sasaki, N., Matsushima, N., Ikawa, T., Yamamura, H., Fukuda, A., 1989. Orientation of bone mineral and its role in the anisotropic mechanical properties of bone—Transverse anisotropy. J. Biomech. 22, 157–164.

Schaffler, M.B., Burr, D.B., 1988. Stiffness of compact bone: effects of porosity and density. J. Biomech. 21, 13–6.

Seeman, E., 2002. Pathogenesis of bone fragility in women and men. Lancet 359, 1841–50.

Seeman, E., 2003. Bone quality. Osteoporos. Int. 14 Suppl 5, S3–7.

Seeman, E., Delmas, P.D., 2006. Bone quality--the material and structural basis of bone strength and fragility. N. Engl. J. Med. 354, 2250–61.

Senden, T.J., 2001. Force microscopy and surface interactions. Curr. Opin. Colloid Interface Sci. 6, 95–101.

Shen, Z.L., Dodge, M.R., Kahn, H., Ballarini, R., Eppell, S.J., 2008. Stress-strain experiments on individual collagen fibrils. Biophys. J. 95, 3956–63.

Shen, Z.L., Kahn, H., Ballarini, R., Eppell, S.J., 2011. Viscoelastic properties of isolated collagen fibrils. Biophys. J. 100, 3008–15.

Smith, J.W., 1960. Collagen fibre patterns in mammalian bone. J. Anat. 94, 329–44.

Sneddon, I.N., 1965. The relation between load and penetration in the axisymmetric boussinesq problem for a punch of arbitrary profile. Int. J. Eng. Sci. 3, 47–57.

Strasser, S., Zink, A., Janko, M., Heckl, W.M., Thalhammer, S., 2007. Structural investigations on native collagen type I fibrils using AFM. Biochem. Biophys. Res. Commun. 354, 27–32.

Svensson, R.B., Hassenkam, T., Hansen, P., Peter Magnusson, S., 2010. Viscoelastic behavior of discrete human collagen fibrils. J. Mech. Behav. Biomed. Mater. 3, 112–5.

Tabor, D., 1970. The hardness of solids. Rev. Phys. Technol. 1, 145–179.

Tai, K., Qi, H.J., Ortiz, C., 2005. Effect of mineral content on the nanoindentation properties and nanoscale deformation mechanisms of bovine tibial cortical bone. J. Mater. Sci. Mater. Med. 16, 947–59.

Thalhammer, S., Heckl, W.M., Zink, A., Nerlich, A.G., 2001. Atomic Force Microscopy for High Resolution Imaging of Collagen Fibrils—A New Technique to Investigate Collagen Structure in Historic Bone Tissues. J. Archaeol. Sci. 28, 1061–1068.

The Shape of Inorganic Particles, 2007. . In: Biological Calcification. Springer Berlin Heidelberg, pp. 105–144.

The Size of Inorganic Particles, 2007. . In: Biological Calcification. Springer Berlin Heidelberg, pp. 145–165.

Thurner, P.J., 2009. Atomic force microscopy and indentation force measurement of bone. Wiley Interdiscip. Rev. Nanomed. Nanobiotechnol. 1, 624–49.

Thurner, P.J., Oroudjev, E., Jungmann, R., Kreutz, C., Kindt, J.H., Schitter, G., Okouneva, T.O., Lauer, M.E., Fantner, G.E., Hansma, H.G., Hansma, P.K., 2007. Imaging of Bone Ultrastructure using Atomic Force Microscopy. In: Mendez-Vilas, A., Diaz, J. (Eds.), Modern Research and Educational Topics in Microscopy. pp. 37–48.

Timmins, P.A., Wall, J.C., 1977. Bone water. Calcif. Tissue Res. 23, 1–5.

Tjhia, C.K., Odvina, C. V, Rao, D.S., Stover, S.M., Wang, X., Fyhrie, D.P., 2011. Mechanical property and tissue mineral density differences among severely suppressed bone turnover (SSBT) patients, osteoporotic patients, and normal subjects. Bone 49, 1279–89.

Turner, C.H., Chandran, a, Pidaparti, R.M., 1995. The anisotropy of osteonal bone and its ultrastructural implications. Bone 17, 85–9.

Turner, C.H., Rho, J., Takano, Y., Tsui, T.Y., Pharr, G.M., 1999. The elastic properties of trabecular and cortical bone tissues are similar: results from two microscopic measurement techniques. J. Biomech. 32, 437–41.

Tzaphlidou, M., 2005. The role of collagen in bone structure: an image processing approach. Micron 36, 593–601.

Van Buskirk, W.C., Cowin, S.C., Ward, R.N., 1981. Ultrasonic measurement of orthotropic elastic constants of bovine femoral bone. J. Biomech. Eng. 103, 67–72.

Vanleene, M., 2006. Caractérisation Multi-Echelle des Propriétés Mécaniques de l'Os. Université de Technologie de Compiègne.

Vanleene, M., Mazeran, P.-E., Tho, M.-C.H.B., 2006. Influence of strain rate on the mechanical behavior of cortical bone interstitial lamellae at the micrometer scale. J. Mater. Res. 21, 2093–2097.

Vanleene, M., Rey, C., Ho Ba Tho, M.C., 2008. Relationships between density and Young's modulus with microporosity and physico-chemical properties of Wistar rat cortical bone from growth to senescence. Med. Eng. Phys. 30, 1049–56.

Villarrubia, J.S., 1997. Algorithms for scanned probe microscope image simulation, surface reconstruction, and tip estimation. J. Res. Natl. Inst. Stand. Technol. 102, 425.

Wagner, H.D., Weiner, S., 1992. On the relationship between the microstructure of bone and its mechanical stiffness. J. Biomech. 25, 1311–1320.

Wallace, J.M., 2012. Applications of atomic force microscopy for the assessment of nanoscale morphological and mechanical properties of bone. Bone 50, 420–7.

Wallace, J.M., Erickson, B., Les, C.M., Orr, B.G., Banaszak, M.M., 2010. Distribution of type I collagen morphologies in bone : Relation to estrogen depletion. Bone 46, 1349–1354.

Wang, X.J., Chen, X.B., Hodgson, P.D., Wen, C.E., 2006. Elastic modulus and hardness of cortical and trabecular bovine bone measured by nanoindentation. Trans. Nonferrous Met. Soc. China 16, 744–748.

Weiner, S., Arad, T., Sabanay, I., Traub, W., 1997. Rotated plywood structure of primary lamellar bone in the rat: orientations of the collagen fibril arrays. Bone 20, 509–14.

Weiner, S., Traub, W., Wagner, H.D., 1999. Lamellar bone: structure-function relations. J. Struct. Biol. 126, 241–55.

Wenger, M.P.E., Bozec, L., Horton, M. a, Mesquida, P., 2007. Mechanical properties of collagen fibrils. Biophys. J. 93, 1255–63.

Wenger, M.P.E., Horton, M. a, Mesquida, P., 2008. Nanoscale scraping and dissection of collagen fibrils. Nanotechnology 19, 384006.

Wenk, H.-R., Houtte, P. Van, 2004. Texture and anisotropy. Reports Prog. Phys. 67, 1367–1428.

Wheeler, J.M., 2006. Nanoindentation under Dynamic Conditions. University of Cambridge.

Winsor, C.P., 1932. The Gompertz Curve as a Growth Curve. Proc. Natl. Acad. Sci. 18, 1–8.

Wong, C., West, P.E., Olson, K.S., Mecartney, M.L., Starostina, N., 2007. Tip dilation and AFM capabilities in the characterization of nanoparticles. JOM 59, 12–16.

Yamamoto, K., Nakatsuji, T., Yaoi, Y., Yamato, Y., Yanagitani, T., Matsukawa, M., Yamazaki, K., Matsuyama, Y., 2012. Relationships between the anisotropy of longitudinal wave velocity and hydroxyapatite crystallite orientation in bovine cortical bone. Ultrasonics 52, 377–86.

Yang, L., van der Werf, K.O., Fitié, C.F.C., Bennink, M.L., Dijkstra, P.J., Feijen, J., 2008. Mechanical properties of native and cross-linked type I collagen fibrils. Biophys. J. 94, 2204–11.

Zioupos, P., Currey, J.D., 1998. Changes in the stiffness, strength, and toughness of human cortical bone with age. Bone 22, 57–66.

Ziv, V., Wagner, H.D., Weiner, S., 1996. Microstructure-Microhardness Relations in Parallel-Fibered and Lamellar Bone. Bone 18, 417–428.

Communications

A. Article

S. Jaramillo Isaza. P.-E. Mazeran. K. El-Kirat. and M.-C. Ho Ba Tho. *"Time-dependent mechanical properties of rat femoral cortical bone by nanoindentation: An age-related study."* **J. Mater. Res..** vol. 29. no. 10. pp. 1135–1143. Jun. 2014.

doi : 10.1557/jmr.2014.104

B. International communications

S. Jaramillo-Isaza. P-E. Mazeran. K. El-Kirat and M-C. Ho Ba Tho. *"Assessment of anisotropic viscoelastic and viscoplastic mechanical behavior of human cortical bone by nanoindentation ".* World Congres of Biomechanics. Boston. USA. Juillet 2014. ***Poster***

S. Jaramillo-Isaza. P-E. Mazeran. K. El-Kirat and M-C. Ho Ba Tho. *"Time dependent mechanical properties of human osteons and insterstitial lamellae by nanoindentation".* 19th Congress of the European Society of Biomechanics. Patras. Greece. Août 2013. ***Oral presentation***

S. Jaramillo-Isaza. P-E. Mazeran. K. El-Kirat and M-C. Ho Ba Tho. *"Time dependent mechanical properties of rat femoral cortical bone by nanoindentation".* 19th Congress of the European Society of Biomechanics. Patras. Greece. Août 2013. ***Oral presentation***

C. National communications

S. Jaramillo-Isaza. P-E. Mazeran. K. El-Kirat and M-C. Ho Ba Tho. *"Bone as a multilevel and multiphysical optimized structure : Micro-Nano characterization of cortical bone".* 1st International Workshop Labex MS2T. Compiègne. France. Septembre 2013. ***Poster with oral presentation.***

S. Jaramillo-Isaza. P-E. Mazeran. K. El-Kirat and M-C. Ho Ba Tho. "*Effect of bone density in the time-dependent mechanical properties of human cortical bone by* *nanoindentation*. ". Congress of La Societé de Biomécaniques. Valenciennes. France. Août 2014. ***Oral presentation and Acte in Computer Methods in Biomechanics and Biomedical Engineering***

D. Ad-joint research projects

M.Sc. degree research project: "*Effects of mineral content in the mechanical properties of bone tissue at the macro-micro scale"*. BMBI Laboratory, Université de Technologie de Compiègne, France.

Student**:** Widya PRIMANINGTYAS

Advisors: M-C. Ho Ba Tho – K. El-Kirat and **S. Jaramillo Isaza**

Engineer degree research project: "*Quantification of the time-dependent mechanical properties of bovine femoral bone by nanoindentation"*. BMBI Laboratory, Université de Technologie de Compiègne, France.

Student**:** Marco MARINO

Advisors: M-C. Ho Ba Tho and **S. Jaramillo Isaza**

E. Valorization project for the Centre National de Recherche Scientifique (CNRS)

Objectives : To identify potential industrial applications, technology transfer, patent of the results of the PhD.

Topic: *"Protocols and database for the nano mechanical characterization of bone by Atomic Force Microscopy at the nano scale and the time-dependent mechanical properties by nanoindentation at the micro scale".*

Responsible: **S. Jaramillo Isaza**

Advisors: M-C. Ho Ba Tho; P.-E. Mazeran; K. El-Kira